Spring 1-1-2016

A Topology Optimization Method for Structural Designs Reliant on Contact Phenomena

Matthew W. Lawry
University of Colorado at Boulder, mr.matt.lawry@gmail.com

A topology optimization method for structural designs reliant on contact phenomena

by

M. W. Lawry

M.S., University of Colorado, 2013

B.S., University of New Mexico, 2010

A thesis submitted to the

Faculty of the Graduate School of the

University of Colorado in partial fulfillment

of the requirements for the degree of

Doctor of Philosophy

Department of Aerospace Engineering

2016

This thesis entitled:
A topology optimization method for structural designs reliant on contact phenomena
written by M. W. Lawry
has been approved for the Department of Aerospace Engineering

Prof. Kurt Maute

Prof. John Evans

Date

The final copy of this thesis has been examined by the signatories, and we find that both the content and the form meet acceptable presentation standards of scholarly work in the above mentioned discipline.

Lawry, M. W. (Ph.D., Aerospace Engineering)

A topology optimization method for structural designs reliant on contact phenomena

Thesis directed by Prof. Kurt Maute

This thesis introduces a comprehensive computational methodology for the topology optimization of contact problems, which is relevant to a broad range of engineering applications. The proposed methodology is capable of handling geometric and material nonlinearities, unilateral and bilateral contact behavior, small and large contact surface sliding, various contact constitutive relations, and the analysis of both two and three dimensional problems. The Level Set Method (LSM) in combination with the eXtended Finite Element Method (XFEM) is used to provide geometry control while maintaining precise definition of the interface. Contact constitutive relations are enforced weakly at the interface using a surface-to-surface integration method. A nonlinear programming scheme is used to solve the optimization problem, and sensitivities are determined using the adjoint method. To demonstrate mechanical model accuracy and explore the defining characteristics of the proposed method, verification and optimization studies were performed on small strain frictionless contact problems in two dimensions, small strain cohesive problems in two and three dimensions, and large strain frictionless contact problems in two dimensions. The proposed method has shown great promise to achieve optimized geometry for a wide variety of contact behavior. Numerical examples demonstrate that in general, optimal geometry for contact problems depends heavily on the interface constitutive behavior. Three dimensional studies reveal design traits that cannot be characterized in two dimensions. Finally, numerical examples with large sliding contact behavior demonstrate that non-intuitive design solutions can be achieved for surfaces which experience contact over a broad range of motion. Mechanical model accuracy and optimization reliability concerns are discussed for a variety of contact behavioral assumptions and stabilization techniques.

Acknowledgements

Many thanks to my advisor, Kurt Maute, for his support, guidance, and patience throughout my doctoral program. I would like to acknowledge the members of my committee: Alireza Doostan, Carlos Felippa, John Evans, and Jeong-Hoon Song, for their feedback, suggestions, and help. I would also like to acknowledge the support of the National Science Foundation under grant CMMI-1235532 and support through Sandia National Laboratories under Contract Agreement 1396470. I thank my fellow PhD colleagues Steven Buck and Kyle Woolwine for their continual support and encouragement. I would like to express my deepest gratitude to my family for their reassurance and motivation throughout many years of education. Finally, I thank my faithful four-legged companion who has been by my side throughout graduate school, Mina, for always keeping morale high.

Contents

Chapter

Tables

Table

Figures

Figure

Chapter 1

Introduction

1.1 Research Overview

Mechanical devices which leverage contact behavior to perform certain tasks are prevalent in everyday living. From transportation, to energy production, agriculture, manufacturing, medical devices, electronics, and other essential processes, contact behavior plays an important role. Contact phenomena between multi-component structures can be utilized to re-direct motion, regulate potential and kinetic energy, control fluid-flow, provide a mechanical advantage, or provide traction.

The emergence of classical contact mechanics is often associated with Heinrich Hertz, who in 1882 provided a solution for frictionless contact between two curved elastic bodies [41]. Nearly a century later, surface energy was characterized for material adhesion in [47] and subsequently refuted by an alternative formulation [27]. Other forms of contact phenomena, such as friction, lubrication, and wear are well studied aspects of tribology. Frictional contact problems have been characterized throughout history, notably Da Vinci in the 15th century who deduced that frictional forces are proportional to the normal pressure exerted, and not the surface area between bodies (see Dowson, 1979 [29]). Subsequent studies by Coulomb (1785) developed frictional coefficients for various materials in sliding contact.

Research in the field of contact mechanics grew tremendously with the emergence of the Finite Element Method and modern computers: notable first forays include [112] and [20] in which treatments of contact were provided using geometrically linear theory, and [111] which defined a simple contact method capable of handling large strains. Since then, there is an abundance of lit-

erature on robust algorithms for handling various contact behavior such as contact dynamics [36], thermo-mechanical friction [114], frictional wear phenomena [25], and fluid-structure contact problems [86].

Provided that contact phenomena affords the functionality of many devices over a broad range of applications, and that abundant computational tools exist to model this behavior, the natural progression in the design of such devices would be through optimization. The optimization of contact related problems has received much interest within the scientific community. A wealth of literature exists for unilateral (i.e. rigid-elastic) contact optimization problems; for review of advances prior to the turn of the century, the reader is referred to [42]. In more recent studies, shape optimization excluding contact surface geometry has been achieved using adaptive mesh refinement techniques for small strain [43] and large strain problems [40].

Departing from conformal mesh optimization methods, topology changes have been afforded through density methods in small strain [4], [94] and large strain [64], excluding the contact surface from geometry control. The optimization of unilateral contact surface geometries have been achieved with the level set method for small strain theory problems, for example [74]. Optimization including the material interface geometry has been achieved for cohesive interface phenomena in multi-material problems using small strain theory [63].

While the topic of contact problem optimization is nothing new, previous examples rely on simplifications of the contact model (e.g. unilateral contact), exclusion of the contact interface from geometry changes, or small sliding approximations, which limit the applicability of such methods. The motivation of this research is to produce a robust optimization method for contact problems, affording the greatest flexibility in allowable geometry changes, while expressing high fidelity contact behavior between elastic materials. The framework must be carefully constructed to allow for geometric and material nonlinearities, large sliding behavior, and eventual extension to multi-phase (e.g. fluid-structure) contact problems.

1.2 Original Work

This thesis contributes to the state of the art in the following research focus areas:

Optimization of Geometrically Linear Structures, Frictionless Contact: Previously, the application of topology optimization methods to shape surfaces in contact with deformable substrates had not been achieved. Relevant publications have focused on lightening materials surrounding the region of contact [4], [94], or optimizing the shape of surfaces in contact with a rigid planar surface [74], [75], [77], [76]. For contact behavior between two deformable bodies, the optimization of surface geometries involved requires a crisp definition of interfaces, robust treatment of underlying physics, and a strong correlation of how changes of geometry affect a particular design objective. To produce clearly defined interfaces and a high level of geometry control, this work incorporates a level-set representation of object geometries and forward analysis using the eXtended Finite Element Method. A gradient based optimization scheme and adjoint sensitivity analysis allow for a high resolution of geometry sensitivities. This original work, summarized in Chapter 8, led to a publication on the topology optimization of bilateral contact problems with a frictionless interface in two dimensions [59].

Optimization of Geometrically Linear Structures, Material Cohesion: Material cohesion provides resistance to shear and normal separation of joined materials, but can result in rapid delamination when the cohesive limit is surpassed. Due to the complex behavior at the interface, prior to [59], the optimization of problems with material cohesion had not been explored. This work expanded the optimization framework developed for frictionless contact to include treatment of material cohesion [57]. Recently, [63] leveraged a similar optimization method to minimize the compliance of multi-material structures with interface cohesion in two dimensions. The presented work summarized in Chapter 9 led to the first optimization of problems with interface cohesion between two materials in three dimensions[9].

Optimization of Geometrically Nonlinear structures, Large Sliding Frictionless Contact: In finite strain contact mechanics, the kinematic and constitutive nonlinearities which

describe equilibrium are smooth and differentiable, whereas the interface conditions for contact and separation introduce a sharp discontinuity. Contact forces only act to prevent the interpenetration of bodies but vanish if the bodies separate. In addition to this sharp discontinuity, contact forces depend on surface orientation. For problems exhibiting large relative motion between components, care must be taken to identify overlapping regions along either respective surface. This imposes a dependency of coincident surface location from either body in contact on the displacement field, complicating the evaluation of design sensitivities. Due to these complexities, to date finite strain and large sliding bilateral contact topology optimization has not been published. Chapter 10 presents this first topology optimization of finite strain, large sliding contact problems in two dimensions.

1.3 Manuscript Organization

This manuscript is organized as follows. In Chapter 2 the concept of design optimization is described, and the subset in which this research resides is identified. In Chapter 3, a brief introduction to continuum mechanics is provided, followed by the definition of the physical behavior which characterizes the problems studied in this work. A description of the physical behavior at the contact interface is defined in Chapter 4. Chapter 5 defines the eXtended Finite Element numerical model. A detailed description of immersed boundary numerical implementation of small sliding and large sliding contact behavior is provided in Chapter 6. Mechanical model stabilization techniques are the topic of Chapter 7.

The following three chapters focus on the exploration of a particular subset of contact behavior. Each chapter includes an overview of related state of the art optimization studies, definition of the particular contact behavior, model verification, optimization examples, and discussion of results. Chapter 8 explores infinitesimal strain, small sliding frictionless contact behavior for two dimensional problems. Chapter 9 studies infinitesimal strain, small sliding cohesive contact behavior for two and three dimensional problems. Two dimensional problems involving finite strain, frictionless contact are explored in Chapter 10. Finally, conclusions of research contributions and

suggestions for future work are provided in Chapter 11.

Chapter 2

Design Optimization

2.1 General Theory

In a brief qualitative description, geometry optimization in the context of engineering is a systematic approach to determining the best arrangement of materials to satisfy a particular design objective. This approach can be expressed generically as a minimization of an objective function, z, subject to a set of both inequality constraints, g_j and equality constraints, h_k.

$$\begin{aligned} \min\ & z(\mathbf{s}, \mathbf{U}) \\ \text{s.t.}\ & \mathbf{g}(\mathbf{s}, \mathbf{U}) \leq 0 \\ & \mathbf{h}(\mathbf{s}, \mathbf{U}) = 0 \\ & \mathbf{s} \in \mathbb{R} \end{aligned} \tag{2.1}$$

Where the objective function and constraints are functions of real-valued abstract optimization parameters, $\mathbf{s}$, and the set of any state variable, $\mathbf{U}$. For structural design optimization the set of state variables must at minimum include structural displacements, but may also include additional components such as fluid state variables or temperature fields depending upon the physics involved.

This research relies solely on computational treatment of physical problems, where the response of an explicitly defined model is determined from equations of equilibrium, $\mathbf{R} = \mathbf{0}$. When the optimization problem defined in Equation 2.1 is applied to computational models, the equations of equilibrium reside within the equality constraints, $\mathbf{h}$. Instead of including the equilibrium equations

formally within the optimization problem, this research uses a technique known as nested analysis and design (NAND), where the state variables are expressed as functions of the optimization variables.

$$\mathbf{U} = \mathbf{U}(\mathbf{s}) \tag{2.2}$$

This allows the equilibrium equations to be solved independent from the optimization algorithm, reducing the overall size of the optimization problem. Additionally, NAND provides the analyst freedom to choose the best framework for solving the equations of equilibrium, which is commonly referred to as the "forward" analysis during the optimization process. Consequently, this added modularity can cause an increased solution time and non-smooth behavior.

2.2 Optimization Algorithm

To solve the optimization problem, this work relies strictly on gradient based algorithms. This requires the calculation of the gradients of the objective function and constraints with respect to the optimization variables. The objective function and constraints can be expressed collectively as the optimization problem, $\mathbf{q}$.

$$\mathbf{q} = \mathbf{q}(\mathbf{s}, \mathbf{U}(\mathbf{s})) \tag{2.3}$$

$$\frac{\mathrm{d}\mathbf{q}}{\mathrm{d}\mathbf{s}} = \frac{\partial \mathbf{q}}{\partial \mathbf{s}} + \frac{\partial \mathbf{q}}{\partial \mathbf{U}} \frac{\mathrm{d}\mathbf{U}}{\mathrm{d}\mathbf{s}} \tag{2.4}$$

The equations of equilibrium used in the forward portion of analysis, $\mathbf{R}(\mathbf{s}, \mathbf{U}(\mathbf{s}))$, provide the necessary correlation between state and objective variables to determine the last term of Equation 2.4.

$$\frac{\mathrm{d}\mathbf{R}}{\mathrm{d}\mathbf{s}} = \frac{\partial \mathbf{R}}{\partial \mathbf{s}} + \frac{\partial \mathbf{R}}{\partial \mathbf{U}} \frac{\mathrm{d}\mathbf{U}}{\mathrm{d}\mathbf{s}} = 0 \tag{2.5}$$

$$\frac{\mathrm{d}\mathbf{U}}{\mathrm{d}\mathbf{s}} = \left[\frac{\partial \mathbf{R}}{\partial \mathbf{U}}\right]^{-1}\left[-\frac{\partial \mathbf{R}}{\partial \mathbf{s}}\right] \tag{2.6}$$

Substituting back into Equation 2.4 results in the following analytical sensitivity expression.

$$\frac{\mathrm{d}\mathbf{q}}{\mathrm{d}\mathbf{s}} = \frac{\partial \mathbf{q}}{\partial \mathbf{s}} + \frac{\partial \mathbf{q}}{\partial \mathbf{U}}\left[\frac{\partial \mathbf{R}}{\partial \mathbf{U}}\right]^{-1}\left[-\frac{\partial \mathbf{R}}{\partial \mathbf{s}}\right] \tag{2.7}$$

Equation 2.7 provides an analytical sensitivity expression in terms of gradients that can be readily evaluated. However, depending on the number of design criteria and the number of optimization variables, the order of evaluation can have a significant impact on the overall computational cost. If the number of design criteria outweighs the number of optimization variables, then the direct method is employed. If the number of design criteria are less than the number of optimization variables, the adjoint method is preferable. The order of operations for each method are depicted in Figure 2.1.

$$\frac{\mathrm{d}\mathbf{q}}{\mathrm{d}\mathbf{s}} = \frac{\partial \mathbf{q}}{\partial \mathbf{s}} + \underbrace{\frac{\partial \mathbf{q}}{\partial \mathbf{U}}}_{\text{Adjoint}}\overbrace{\left[\frac{\partial \mathbf{R}}{\partial \mathbf{U}}\right]^{-1}\left[-\frac{\partial \mathbf{R}}{\partial \mathbf{s}}\right]}^{\text{Direct}}$$

Figure 2.1: First operation to be performed depending upon the method employed.

For the design problems analysed in this work, the number of optimization variables often outweigh the number of design criteria. Consequently, this work exclusively uses the adjoint method of solving for sensitivities.

Numerous gradient based algorithms have been developed to solve general optimization problems. This work relies on the Method of Moving Asymptotes (MMA) algorithm for its effectiveness in solving larger optimization problems. The MMA algorithm builds a local approximation based on asymptotic limits defined relative to current optimization variable values. For more information regarding the MMA algorithm, please refer to the works of Svanberg [95],[96].

2.3 Optimization Classification

Having a general understanding of how design optimization is employed, we now move on to the classification of the optimization problem. The classification of the optimization problem is defined by the choice of how optimization variables, s_i, relate to the structural design. Relating optimization variables to extrinsic properties such as cross sectional areas or length of a truss member is referred to as size optimization. Using optimization variables to change the shape of a structural domain is known as shape optimization. Both of these classes of optimization are constrained to specific variations of the initial design.

To allow a more open ended design problem, we must first introduce the concept of topological equivalence. Consider the three design domains illustrated in Figure 2.3. Two domains are considered topologically equivalent if there exists a continuously differentiable mapping between the two, with a positive Jacobian determinant throughout. This mapping may distort the domain, but any two adjacent points must remain adjacent after the transformation. Topology optimization

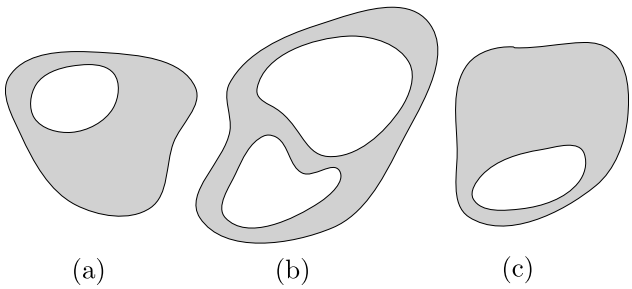

Figure 2.2: Example of topological equivalence. (a) and (c) are topologically equivalent, whereas (b) is topologically inequivalent to both (a) and (c).

facilitates the creation of conceptually new designs by not requiring topological equivalence during the the optimization process. This class of optimization provides a high level of design freedom, which is advantageous for complex problems where the general solution topology is unknown.

Further distinction of optimization classification can be made with regards to problems involving contact phenomena. Figure 2.3 illustrates an initial design configuration and four distinct options for geometry control. The shape of external geometry excluding the interface can be al-

tered (Fig. 2.3a), the shape of interface geometry (Fig. 2.3b) can be optimized, the topology of the design including interface geometry can be altered (Fig. 2.3c), and design topology excluding interface geometry can be optimized (Fig. 2.3d). The combination of options (c) and (d) lead to the greatest flexibility in geometry control. Towards the goal of producing a robust methodology for optimization of designs involving contact interactions, this work studies option (c) for two and thee dimensional problems, and a combination of options (b) and (d) for two dimensional problems. Chapter 2.4 briefly discusses various methods of relating optimization variables to structural design and provides justification for the method of choice.

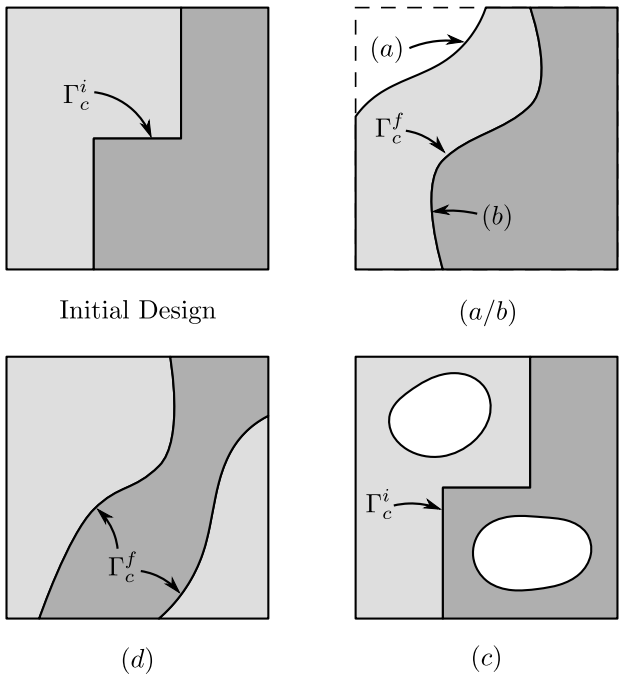

Figure 2.3: Classifications of geometry control in contact optimization problems; Γ_c^i and Γ_c^f represent the initial and final contact interface geometry, respectively.

2.4 Geometry Model

Density methods, such as the Solid Isotropic Material with Penalization (SIMP) method, have become popular for a wide variety of problems. Originally developed by [14] and [83] for structural topology optimization, the SIMP method describes the geometry of a body by a material

distribution within the design domain. A fictitious porous material with density, ρ, is introduced to allow a continuous transition between two or more material phases. For more information and an overview of recent developments, the reader is referred to [13]; [92] and [26]. Density methods approximate the phase boundaries via spatial gradients in the material distribution, effectively smearing the interface geometry. This issue has been studied for modeling design dependent surface loads. A popular approach is to convert the surface load into a volumetric body force; see for example [52], [91], and [118]. This approach does not explicitly define the interface geometry and is of limited applicability to modeling contact. Alternatively, [39] apply loads on surfaces described by iso-volumetric density curves. This technique introduces approximation errors in interface position and orientation, rendering it unsuited for treatment of contact interactions. The only studies on density methods for contact are restricted to problems where the geometry of the contact interface is not altered in the optimization process; see Fig. 2.3a. In the work of [94] and [4] the contact conditions are imposed on the same surface in a body-fitted mesh, independent of the density distribution which may change in the elements next to the contact surface.

Level set methods (LSM) provide a promising alternative approach for topology optimization problems where the structural response strongly depends on the geometry of the interface. The interface is defined explicitly using an iso-contour of the level set function ϕ at a particular value, commonly $\phi = 0$. For a review of recent developments of LSMs, the reader is referred to [104]. The interface geometry is represented in the discretized mechanical model either via a body fitted mesh, an Ersatz material approach, or immersed boundary techniques. For this work, geometry control is defined by the LSM to maintain a precise definition of interface position and orientation.

2.4.1 Two-Phase Problems

The material layout of a two-phase problem is described by a Level Set Function (LSF), $\phi(\mathbf{s}, \mathbf{x})$, as follows:

$$\begin{aligned} \phi(\mathbf{s}, \mathbf{x}) < 0, \quad \forall\ \mathbf{x} \in \Omega^A\ , \\ \phi(\mathbf{s}, \mathbf{x}) > 0, \quad \forall\ \mathbf{x} \in \Omega^B\ , \\ \phi(\mathbf{s}, \mathbf{x}) = 0, \quad \forall\ \mathbf{x} \in \Gamma_c\ , \end{aligned} \tag{2.8}$$

where $\mathbf{x}$ are the spatial coordinates. Instead of updating the LSF by the solution of the Hamilton-Jacobi equation, as proposed by [108] and [1], in this work the parameters of the discretized LSF are defined as explicit functions of the optimization variables.

The level set field can be parameterized to describe a set of geometric primitives, such as circles or rectangles. The optimization variables define the location and the dimensions of the primitives. This approach is used in the example provided in Section 8.4.2. To increase the design freedom, we follow the approach of [55] and discretize the design domain by finite elements and associate an optimization variable with each node, i.e. $N_s = N_n$, where N_n is the number of nodes. The level set value at the i^{th} node is defined by the following linear filter:

$$\phi_i = \left(\sum_{j=1}^{N_n} w_{ij} \right)^{-1} \sum_{j=1}^{N_n} w_{ij} s_j\ , \tag{2.9}$$

with

$$w_{ij} = max\left(0, (r - |\mathbf{x}_i - \mathbf{x}_j|)\right)\ , \tag{2.10}$$

where r is the filter radius, and $\mathbf{x}_j$ the position of the j^{th} node. The level set filter (2.9) widens the zone of influence of the optimization variables on the level set field and thus enhances the convergence of the optimization process [55]. This approach is used for select examples presented in Chapters 8,9, and 10.

2.4.2 Three-Phase Problems

A popular approach to defining the spatial distribution of multiple materials with the LSM is through the superposition of multiple LSFs. Originally developed for digital image processing [106],

this method describes the layout of 2^m materials with m LSFs. The individual phases are defined by the set of signs of the LSFs; the interfaces are described by one of the LSFs being zero. Also known as the 'color' level sets method, this method has been reported useful in several multi-phase optimization studies [28, 109, 119].

In this study we take a similar approach by using two LSFs to distinguish three material phases; however, we limit the spatial arrangement of these phases as follows:

$$\begin{aligned}
&\phi^1(\mathbf{s},\mathbf{X}) < 0, && && \forall\ \mathbf{X} \in \Omega^A,\\
&\phi^1(\mathbf{s},\mathbf{X}) > 0, && \phi^2(\mathbf{s},\mathbf{X}) > 0, && \forall\ \mathbf{X} \in \Omega^B,\\
&\phi^1(\mathbf{s},\mathbf{X}) > 0, && \phi^2(\mathbf{s},\mathbf{X}) < 0, && \forall\ \mathbf{X} \in \Omega^V,\\
&\phi^1(\mathbf{s},\mathbf{X}) = 0, && && \forall\ \mathbf{X} \in \Gamma_c,\\
&\phi^2(\mathbf{s},\mathbf{X}) = 0, && && \forall\ \mathbf{X} \in \Gamma_v.
\end{aligned} \tag{2.11}$$

This conditional treatment of the LSFs admits the definition of a third phase; however, Ω^V is restricted to reside within phase B through (2.11). For this work, the LSFs ϕ^1 and ϕ^2 are parameterized to describe a set of geometric primitives, such as circles or rectangles. The optimization variables define the location and the dimensions of the primitives. To avoid the emergence of triple junctions where $\phi^1 = \phi^2 = 0$, the limits s_{min} and s_{max} are carefully selected to ensure the geometric primitives in ϕ^1 do not intersect the geometric primitives in ϕ^2. For example, consider two level let fields used to define a two dimensional design, described by the following geometric primitives:

$$\phi^1 = s^1 - \sqrt{\mathbf{X}_1^2 + \mathbf{X}_2^2}, \qquad \phi^2 = \sqrt{\mathbf{X}_1^2 + \mathbf{X}_2^2} - s^2, \tag{2.12}$$

where design variables s^1 and s^2 control the radius of the zero level set contour of either respective field. The subscripts on $\mathbf{X}_1$ and $\mathbf{X}_2$ denote the cartesian x and y coordinates, respectively. With initial given values of $s^1 = 2$ and $s^2 = 1$, to avoid interactions between the zero level set contour of either field, one must choose optimization variable limits such that s^1_{min} is greater than s^2_{max}. This approach is used in two examples presented in Section 10.

Chapter 3

Physics Model

This chapter provides a brief overview of the relevant fundamentals of continuum mechanics, followed by the equilibrium relations used in this work. Greater detail of this topic can be found in abundant literature, for example [67], [45], and [10]. Contact behavior comes in many different forms, such as bonded, cohesive, frictionless, and frictional forms. The constitutive behavior of contact phenomena will be elaborated in subsequent chapters where they are used in optimization studies.

3.1 Kinematics

The motion and deformation of a homogenous body can be represented as a continuous field of material points. Figure 3.1 illustrates a continuum body in two different configurations: where $\mathcal{B}_0 \subset \mathbb{R}^3$ is the reference configuration of the body, and $\mathcal{B}_t \subset \mathbb{R}^3$ is the current configuration at time t. The transformation from reference to current configuration is defined by the unique and continuously differentiable map:

$$\boldsymbol{\varphi}_t : \mathcal{B}_0 \to \mathcal{B}_t. \tag{3.1}$$

At a particular time $t \in \mathbb{R}_+$, the material points $\mathbf{X} \in \mathcal{B}_0$ of the reference configuration can be mapped to the points $\mathbf{x} \in \mathcal{B}_t$ of the current configuration as follows:

$$\boldsymbol{\varphi}_t : \mathbf{X} \mapsto \mathbf{x} = \boldsymbol{\varphi}_t(\mathbf{X}) = \mathbf{x}(\mathbf{X}). \tag{3.2}$$

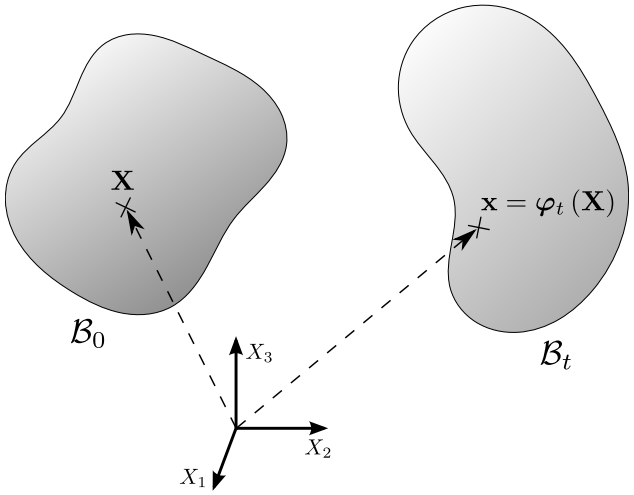

Figure 3.1: Continuum body in the reference and current configuration at time t.

Subsequently, the inverse map is uniquely defined as $\mathbf{X} = \boldsymbol{\varphi}_t^{-1}(\mathbf{x})$. The displacement vector is defined as the difference between the current and reference configuration:

$$\mathbf{u}(\mathbf{X}) = \mathbf{x}(\mathbf{X}) - \mathbf{X}. \tag{3.3}$$

The partial derivative of the deformation map $\mathbf{x} = \boldsymbol{\varphi}_t(\mathbf{X})$ with respect to the coordinates $\mathbf{X}$ is an essential kinematic quantity known as the deformation gradient:

$$\mathbf{F} = \nabla \mathbf{x} = \frac{\partial \mathbf{x}(\mathbf{X})}{\partial \mathbf{X}}. \tag{3.4}$$

The deformation gradient characterizes the behavior of motion in the neighborhood of a point. Uniqueness of mapping $\boldsymbol{\varphi}_t$ requires that $\mathbf{F}$ is continuous and nonsingular. Therefore the derivative of the inverse of motion $\mathbf{X}^{-1}$ with respect to the current position $\mathbf{x}$ exists so that

$$\mathbf{F}^{-1} = (\nabla \mathbf{x})^{-1} = \frac{\partial \mathbf{X}(\mathbf{x})}{\partial \mathbf{x}}. \tag{3.5}$$

We introduce the Jacobian determinant as $J = \det \mathbf{F}$, and the required smoothness of $\boldsymbol{\varphi}_t$ implies

$$J = \det \mathbf{F} > 0. \tag{3.6}$$

The deformation gradient maps an infinitesimal line element $\mathrm{d}\mathbf{X}$ at position $\mathbf{X}$ of the reference configuration to the infinitesimal line element $\mathrm{d}\mathbf{x}$ at $\mathbf{x}$ in the current configuration. The

transformation of infinitesimal line, area, and volume elements from the current configuration to the reference configuration are defined as:

$$\mathrm{d}\mathbf{x} = \mathbf{F}\mathrm{d}\mathbf{X}, \tag{3.7}$$

$$\mathrm{d}\mathbf{a} = J\mathbf{F}^{-T}\mathrm{d}\mathbf{A}, \tag{3.8}$$

$$\mathrm{d}v = J\mathrm{d}V. \tag{3.9}$$

The deformation gradient describes deformation uniquely, however, it still contains rigid body motions which are not suitable for describing the strain of a body. The deformation gradient can be separated into rigid body motion and stretch as

$$\mathbf{F} = \mathbf{RU} = \mathbf{vR}, \tag{3.10}$$

where $\mathbf{R}$ is an orthogonal rotation tensor, and the symmetric positive definite tensors $\mathbf{U}$ and $\mathbf{v}$ are the right and left stretch tensors, respectively.

The right Cauchy-Green tensor $\mathbf{C}$ defines strain quantities in the absence of rigid body motion as

$$\mathbf{C} = \mathbf{F}^T\mathbf{F} = (\mathbf{RU})^T\mathbf{RU} = \mathbf{U}^T\mathbf{R}^T\mathbf{RU} = \mathbf{U}^T\mathbf{U}. \tag{3.11}$$

In this work we assume a uniform, fixed Cartesian coordinate frame, and define the Green-Lagrangian strain tensor $\mathbf{E}$ as

$$\mathbf{E} = \frac{1}{2}\left(\mathbf{C} - \mathbf{I}\right), \tag{3.12}$$

where $\mathbf{I}$ is the identity matrix. Furthermore, we can describe Green-Lagrangian strain in terms of displacement gradients as

$$\mathbf{E} = \frac{1}{2}\left(\nabla\mathbf{u} + (\nabla\mathbf{u})^T + (\nabla\mathbf{u})^T\nabla\mathbf{u}\right) = \frac{1}{2}\left(\frac{\partial\mathbf{u}}{\partial\mathbf{X}} + \frac{\partial\mathbf{u}}{\partial\mathbf{X}}^T + \frac{\partial\mathbf{u}}{\partial\mathbf{X}}^T\frac{\partial\mathbf{u}}{\partial\mathbf{X}}\right) \tag{3.13}$$

For applications in which the displacement gradients are small, i.e. $\nabla\mathbf{u} << \mathbf{1}$, the Green-Lagrangian strain can be further reduced to its approximate form known as the infinitesimal strain

tensor

$$\boldsymbol{\varepsilon} = \frac{1}{2}\left(\nabla\mathbf{u} + (\nabla\mathbf{u})^T\right) = \frac{1}{2}\left(\frac{\partial\mathbf{u}}{\partial\mathbf{X}} + \frac{\partial\mathbf{u}}{\partial\mathbf{X}}^T\right) \approx \mathbf{E}. \tag{3.14}$$

The infinitesimal strain tensor is a linearized form of the Green-Lagrangian strain tensor.

With nonlinear strains defined and an approximate linearized version established, we now turn our attention to the definition of stress.

3.2 Stress

As a result of the deformation of continuum bodies, stress resides between material points within the body. In its most general form, stress can be defined as

$$\mathbf{t} = \frac{\mathrm{d}\mathbf{f}_a}{\mathrm{d}a}, \tag{3.15}$$

relating a resultant force vector $\mathrm{d}\mathbf{f}_a$ to the infinitesimal area $\mathrm{d}a$ in which it resides. Defining the spatial normal of the infinitesimal area $\mathrm{d}a$ as $\mathbf{n}$, by Cauchy theorem

$$\mathbf{t} = \boldsymbol{\sigma}\cdot\mathbf{n} \tag{3.16}$$

where $\boldsymbol{\sigma}$ is a symmetric spatial tensor field known as the Cauchy stress tensor, and $\mathbf{n}$ is the current configuration surface normal of the infinitesimal surface $\mathrm{d}a$. Note that

$$\mathbf{n}\mathrm{d}a = \mathrm{d}\mathbf{a}, \qquad \mathbf{n}_0\mathrm{d}A = \mathrm{d}\mathbf{A}. \tag{3.17}$$

The Cauchy stress tensor represents the real internal stress state within a body at its current configuration.

$$\mathrm{d}\mathbf{f}_a = \boldsymbol{\sigma}\cdot\mathbf{n}\mathrm{d}a = \boldsymbol{\sigma}\mathrm{d}\mathbf{a} \tag{3.18}$$

Using equation 3.8

$$\mathrm{d}\mathbf{f}_a = J\boldsymbol{\sigma}\mathbf{F}^{-T}\mathrm{d}\mathbf{A}, \tag{3.19}$$

we introduce the first Piola-Kirchhoff stress tensor as

$$\mathbf{P} = \frac{\mathrm{d}\mathbf{f}_a}{\mathrm{d}\mathbf{A}} = J\boldsymbol{\sigma}\mathbf{F}^{-T}, \tag{3.20}$$

which relates the resultant force vector within a body to the infinitesimal area in the reference configuration. The passage from $\boldsymbol{\sigma}$ to $\mathbf{P}$ is known as the Piola transformation. The first Piola-Kirchhoff stress tensor is non-symmetric by construction. By applying a pull-back operation on the resultant force, $\mathrm{d}\mathbf{F}_a = \mathbf{F}^{-1} \cdot \mathrm{d}\mathbf{f}_a$:

$$\mathrm{d}\mathbf{F}_a = J\mathbf{F}^{-1}\boldsymbol{\sigma}\mathbf{F}^{-T}\mathrm{d}\mathbf{A}, \tag{3.21}$$

we introduce the second Piola-Kirchhoff stress tensor as

$$\mathbf{S} = \frac{\mathrm{d}\mathbf{F}_a}{\mathrm{d}\mathbf{A}} = \mathbf{F}^{-1}\mathbf{P} = J\mathbf{F}^{-1}\boldsymbol{\sigma}\mathbf{F}^{-T}, \tag{3.22}$$

which relates a non-physical resultant force vector (i.e. pulled back to the reference configuration) to the infinitesimal area in the reference configuration. Although it does not admit any physical interpretation, the second Piola-Kirchhoff stress tensor is symmetric, and is parameterized by material coordinates only.

Expanding equation 3.8,

$$\mathbf{n}\mathrm{d}a = J\mathbf{F}^{-T} \cdot \mathbf{n}_0\mathrm{d}A, \tag{3.23}$$

we define the surface Jacobian as

$$\mathcal{J} = \frac{\mathrm{d}a}{\mathrm{d}A} = J\|\mathbf{F}^{-T} \cdot \mathbf{n}_0\|, \tag{3.24}$$

which scales surface quantities from the current to the reference configuration. The following transformation converts surface traction from the current to reference configuration:

$$\mathbf{P} \cdot \mathbf{n}^0 = \mathbf{F} \cdot \mathbf{S} \cdot \mathbf{n}^0 = \boldsymbol{\sigma} \cdot \mathbf{n}\mathcal{J}. \tag{3.25}$$

With the definitions of stress and mapping identities defined above, we turn our attention to the governing equations of equilibrium.

3.3 Conservation of Momentum

The local balance of momentum in the current configuration, $\mathcal{B}_t$, can be written as

$$\nabla \cdot \boldsymbol{\sigma} + \rho\mathbf{b} = \rho\dot{\mathbf{v}}, \tag{3.26}$$

where ρ is the material density, $\mathbf{b}$ is a body force (e.g. gravity force), and $\dot{\mathbf{v}}$ is acceleration. Frequently, one must evaluate equilibrium in the reference configuration, $\mathcal{B}_0$. By applying a pull-back operation and making use of Equations 3.20-3.22, the local balance of momentum referred to the reference configuration can be expressed as

$$\nabla \cdot \mathbf{P} + \rho_0 \mathbf{b}_0 = \rho_0 \dot{\mathbf{v}}, \tag{3.27}$$

or

$$\nabla \cdot (\mathbf{FS}) + \rho_0 \mathbf{b}_0 = \rho_0 \dot{\mathbf{v}}, \tag{3.28}$$

where

$$\mathbf{b}_0 = J\mathbf{b} \tag{3.29}$$

and

$$\rho_0 = J\rho. \tag{3.30}$$

Provided the admissible test function $\boldsymbol{\eta}$, the weak form in the current configuration can be expressed as

$$\int_{\mathcal{B}_t} \boldsymbol{\varepsilon}(\boldsymbol{\eta}) : \boldsymbol{\sigma} \, \mathrm{d}V + \int_{\mathcal{B}_t} \rho (\mathbf{b} - \dot{\mathbf{v}}) \cdot \boldsymbol{\eta} \, \mathrm{d}V = \mathbf{0}. \tag{3.31}$$

Through product rule differentiation and use of the divergence theorem, the weak form of equilibrium is expressed as

$$\int_{\mathcal{B}_t} \boldsymbol{\varepsilon}(\boldsymbol{\eta}) : \boldsymbol{\sigma} \, \mathrm{d}V - \int_{\mathcal{B}_t} \rho (\mathbf{b} - \dot{\mathbf{v}}) \cdot \boldsymbol{\eta} \, \mathrm{d}V - \int_{\partial \mathcal{B}_t} (\boldsymbol{n} \cdot \boldsymbol{\sigma}) \cdot \boldsymbol{\eta} \mathrm{d}a = \mathbf{0}. \tag{3.32}$$

Where $\partial \mathcal{B}_t$ represents the outer surface of the continuum body in its current configuration. Here we introduce surface traction $\bar{\boldsymbol{t}} = \boldsymbol{n} \cdot \boldsymbol{\sigma}$, which represents the Neumann boundary conditions prescribed along the specified outer surface $\partial \mathcal{B}_{\bar{\boldsymbol{t}}}$. For this paper, all problems analyzed are solved in a quasi-static manner, therefore the inertial term goes to zero, $\rho \dot{\boldsymbol{v}} = \mathbf{0}$. The weak form of equilibrium in the current configuration becomes

$$\int_{\mathcal{B}_t} \boldsymbol{\varepsilon}(\boldsymbol{\eta}) : \boldsymbol{\sigma} \, \mathrm{d}V - \int_{\mathcal{B}_t} \rho (\mathbf{b}) \cdot \boldsymbol{\eta} \, \mathrm{d}V - \int_{\partial \mathcal{B}_{\bar{t}}} \bar{\mathbf{t}} \cdot \boldsymbol{\eta} \, \mathrm{d}A = 0. \tag{3.33}$$

Similarly, the weak form of equilibrium can be expressed in the reference configuration as

$$\int_{\mathcal{B}_0} \mathbf{F}(\boldsymbol{\eta}) : \mathbf{P} \, \mathrm{d}V - \int_{\mathcal{B}_0} \rho_0(\mathbf{b}_0) \cdot \boldsymbol{\eta} \, \mathrm{d}V - \int_{\partial\mathcal{B}_{\bar{\mathbf{P}}}} \bar{\mathbf{t}}_0 \cdot \boldsymbol{\eta} \, \mathrm{d}A = 0. \tag{3.34}$$

Dirichlet boundary conditions are enforced strongly as

$$\mathbf{u} = \bar{\mathbf{u}} \text{ on } \partial\mathcal{B}_u, \tag{3.35}$$

where $\partial\mathcal{B}_u$ is a specified subset of $\partial\mathcal{B}_0$. The weak form of the governing equations are defined irrespective of the material constitutive behavior. For the related studies presented, the constitutive behavior of the material is discussed next.

3.4 Material Constitutive Behavior

3.4.1 Infinitesimal Strain, Elastic

The response of a material is characterized by the constitutive equation which defines stress as a function of deformation history of the body:

$$\boldsymbol{\sigma} = \mathbf{f}(\boldsymbol{\varepsilon}) \tag{3.36}$$

where for the current work $\mathbf{f}$ is assumed to be a monotonically increasing function. All materials used are elastic, meaning that there is no energy dissipation in deformation. The reversibility and path independence of elastic constitutive models implies that there exists a potential function $w(\varepsilon)$ such that

$$\boldsymbol{\sigma} = \mathbf{f}(\boldsymbol{\varepsilon}) = \frac{\mathrm{d}w(\boldsymbol{\varepsilon})}{\mathrm{d}\boldsymbol{\varepsilon}}, \tag{3.37}$$

where $w(\varepsilon)$ is the strain energy density per unit volume. For infinitesimal strain theory, the generalized Hooke's Law defines a linear relation among all components of the stress and strain tensor

$$w(\boldsymbol{\varepsilon}) = \frac{1}{2}\boldsymbol{\varepsilon}^T : \mathbb{C} : \boldsymbol{\varepsilon}, \tag{3.38}$$

where $\mathbb{C}$ is a fourth order stiffness tensor of material properties. This tensor has 81 terms in three-dimensional problems, and 16 components in two-dimensional problems. Thus, stress is defined as

$$\boldsymbol{\sigma} = \mathbb{C} : \boldsymbol{\varepsilon}. \tag{3.39}$$

In this work we assume isotropic material behavior and a plane strain assumption for two-dimensional problems.

3.4.2 Finite Strain, Hyperelastic

Elastic materials for which the work is independent of the load path are defined as hyperelastic. Hyperelastic material stress is often characterized by

$$\mathbf{S} = 2\frac{\partial \psi(\mathbf{C})}{\partial \mathbf{C}} = \frac{\partial w(\mathbf{E})}{\partial \mathbf{E}} \tag{3.40}$$

where ψ is the stored energy potential. When the potential is written in terms of the Cauchy-Green tensor $\mathbf{C}$, the notation ψ is used. The relation between scalar functions w and ψ is given by $w(\mathbf{E}) = \psi(\mathbf{E} + \mathbf{I})$ The stored energy function for a Neo-Hookean isotropic hyperelastic material is defined as

$$\psi(\mathbf{C}) = \frac{1}{2}\lambda_0 (\ln J)^2 - \mu_0 \ln J + \frac{1}{2}\mu_0 (\text{trace}\mathbf{C} - 3), \tag{3.41}$$

where λ_0 and μ_0 represent the Lamé constants of the linearized theory. Consequently, the second Piola-Kirchhoff stress as a function of the Cauchy-Green tensor is given by

$$\mathbf{S} = \lambda_0 \ln J \mathbf{C}^{-1} + \mu_0 \left(\mathbf{I} - \mathbf{C}^{-1}\right). \tag{3.42}$$

Thus far we have defined the physical model using both infinitesimal and finite strain theory; including kinematics, structural equilibrium, and constitutive relations. However, we have not yet defined the physical behavior at the interface in the presence of contact. Chapter 4 defines a generalized contact model, which is applicable to the various forms of contact behavior explored in this manuscript.

Chapter 4

Contact Model

This chapter defines contact kinematics, followed by a generalized form of contact contributions to equilibrium. While contact behavior comes in a variety of forms such as frictionless sliding, cohesion, frictional sliding, impact, lubrication, fatigue wear, etc., the scope of this paper is limited to the topology optimization of problems involving conservative (i.e. path independent) contact behavior in the absence of inertial effects. Therefore, rate-based kinematics and constitutive relations are omitted. For greater detail of contact phenomena, the reader is referred to [113].

4.0.1 Contact Kinematics

Often, contact problems involve large deformations and relative motion between two or more structural components. In this section contact kinematics are formulated for finite deformations, then further reduced to infinitesimal deformation problems. Figure 4.1 illustrates two continuum bodies in the reference, $\mathcal{B}_0^p$, and current configurations, $\mathcal{B}_t^p$, where $p = 1, 2$. In the current configuration, both bodies contact along the boundary Γ_c. It is observed that positions $\boldsymbol{\varphi}_t^1(\mathbf{X}_1, t)$ and $\boldsymbol{\varphi}_t^2(\mathbf{X}_2, t)$ are coincident in the current configuration. Hence, contact conditions must be formulated with respect to the current configuration.

4.0.1.1 Normal Contact

Irrespective of the material constitutive behavior, non-penetration conditions must be satisfied where $\boldsymbol{\varphi}_t^1\left(\mathbf{X}^1, t\right) = \boldsymbol{\varphi}_t^2\left(\mathbf{X}^2, t\right)$. By introducing convective coordinates $\boldsymbol{\xi}$ along the outer surface

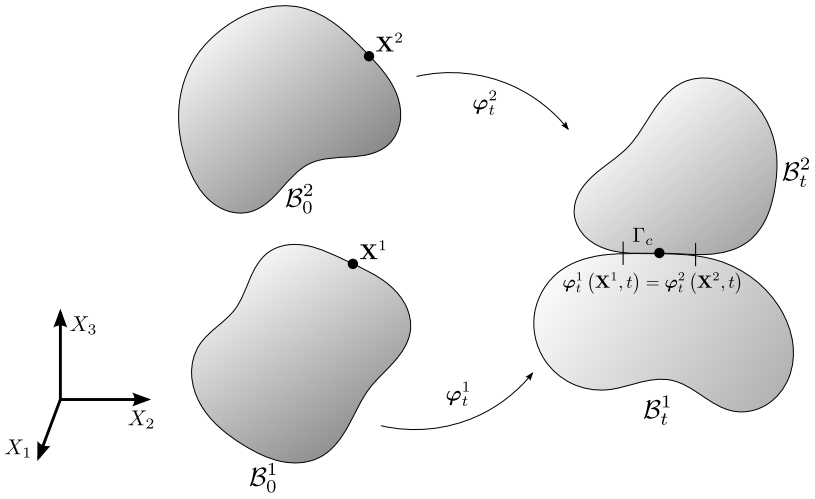

Figure 4.1: Contact between two continuum bodies.

of body $\mathcal{B}_t^1$, we can relate every point $\mathbf{x}^2$ on the surface of $\mathcal{B}_t^2$ to a point $\mathbf{x}^1(\boldsymbol{\xi})$ via the minimum distance problem

$$\min_{\mathbf{x}^1 \subseteq \Gamma_c^1} \left\| \boldsymbol{x}^2 - \boldsymbol{x}^1(\boldsymbol{\xi}) \right\|, \tag{4.1}$$

as depicted in Figure 4.2. With the associated position $\bar{\mathbf{x}}^1$ known, we define the tangent vectors on

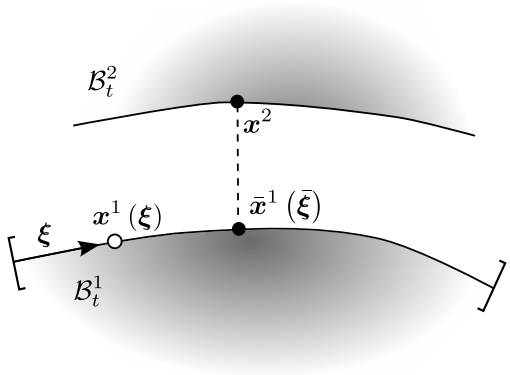

Figure 4.2: Coincident surface location along Γ_c.

the surface of $\mathcal{B}_t^1$ at this point as

$$\bar{\mathbf{a}}_1^1 = \frac{\partial \bar{\boldsymbol{x}}^1}{\partial \bar{\xi}_1}, \qquad \bar{\mathbf{a}}_2^1 = \frac{\partial \bar{\boldsymbol{x}}^1}{\partial \bar{\xi}_2}. \tag{4.2}$$

Subsequently, the surface normal at $\bar{\mathbf{x}}^1$ is defined as

$$\bar{\mathbf{n}}^1 = -\frac{\left(\bar{\mathbf{a}}_1^1 \times \bar{\mathbf{a}}_2^1\right)}{\left\|\bar{\mathbf{a}}_1^1 \times \bar{\mathbf{a}}_2^1\right\|}. \tag{4.3}$$

The normal gap value between both bodies is defined as

$$g_n = \left(\mathbf{x}^2 - \bar{\mathbf{x}}^1\right) \cdot \bar{\mathbf{n}}^1 \geq 0. \tag{4.4}$$

For infinitesimal strain theory, it is convenient to express the normal gap value as

$$g_n = \left(\boldsymbol{u}^2 - \bar{\boldsymbol{u}}^1\right) \cdot \bar{\boldsymbol{n}}^1 + g_X^n \geq 0, \tag{4.5}$$

where $g_X^n = \left(\mathbf{X}^2 - \bar{\mathbf{X}}^1\right) \cdot \bar{\boldsymbol{n}}^1$ represents the initial gap value.

Additionally, the definition of the normal gap can be further reduced if both surfaces are coincident in the reference configuration, i.e. $g_X^n = 0$, and small sliding is assumed. The convective coordinates $\boldsymbol{\xi}$ define the coincident position of both surfaces in the reference configuration, and define approximate coincident locations in the current configuration, rendering Equation 4.1 unnecessary. The normal gap value reduces to

$$g_n = \left(\boldsymbol{u}^2\left(\boldsymbol{\xi}\right) - \boldsymbol{u}^1\left(\boldsymbol{\xi}\right)\right) \cdot \boldsymbol{n}^1\left(\boldsymbol{\xi}\right) \geq 0. \tag{4.6}$$

4.0.1.2 Tangential Contact

The tangential relative motion between two continuum bodies is commonly used to describe constitutive behavior such as stiction, sliding friction, and material cohesion. The tangential gap between surfaces is defined as

$$g_T^1 = \left(\boldsymbol{x}^2 - \bar{\boldsymbol{x}}^1\right) \cdot \bar{\boldsymbol{a}}_1^1, \qquad g_T^2 = \left(\boldsymbol{x}^2 - \bar{\boldsymbol{x}}^1\right) \cdot \bar{\boldsymbol{a}}_2^1, \tag{4.7}$$

where $\bar{\boldsymbol{a}}_1^1$ and $\bar{\boldsymbol{a}}_2^1$ represent either tangent vector along the surface. Although beyond the scope of current work, it is worth noting that finite strain stiction and frictional relations are often constructed in terms of tangential relative displacements and velocities, respectively.

For infinitesimal strain theory, it is convenient to express the tangential gap value as

$$g_T^1 = \left(\boldsymbol{u}^2 - \bar{\boldsymbol{u}}^1\right) \cdot \bar{\boldsymbol{a}}_1^1 + g_X^{T1}, \qquad g_T^2 = \left(\boldsymbol{u}^2 - \bar{\boldsymbol{u}}^1\right) \cdot \bar{\boldsymbol{a}}_2^1 + g_X^{T2}, \tag{4.8}$$

where $\boldsymbol{g}_X^{Ti} = \left(\mathbf{X}^2 - \bar{\mathbf{X}}^1\right) \cdot \bar{\boldsymbol{a}}_i^1$ represents the initial tangential gap value for each tangent vector corresponding to $i = 1, 2$. The definition of the tangential gap can be further reduced if both surfaces are coincident in the reference configuration, i.e. $g_X^{Ti} = 0$, and small sliding is assumed. The convective coordinates $\boldsymbol{\xi}$ define the coincident position of both surfaces in the reference configuration, and define approximate coincident locations in the current configuration, rendering Equation 4.1 unnecessary. The tangential gap value reduces to

$$\boldsymbol{g}_T^1 = \left(\boldsymbol{u}^2\left(\boldsymbol{\xi}\right) - \boldsymbol{u}^1\left(\boldsymbol{\xi}\right)\right) \cdot \boldsymbol{a}_1^1\left(\boldsymbol{\xi}\right), \qquad \boldsymbol{g}_T^2 = \left(\boldsymbol{u}^2\left(\boldsymbol{\xi}\right) - \boldsymbol{u}^1\left(\boldsymbol{\xi}\right)\right) \cdot \boldsymbol{a}_2^1\left(\boldsymbol{\xi}\right), \tag{4.9}$$

where $\boldsymbol{\xi}$ defines coincident locations along the interface between both bodies. This form of defining the tangential gap is often used to construct cohesive constitutive relations at the interface.

4.0.2 Contact Boundary Value Problem

Contact behavior is represented as a boundary value problem, wherein surface traction exists at the area of contact along either respective surface as illustrated in Figure 4.3. Surface traction

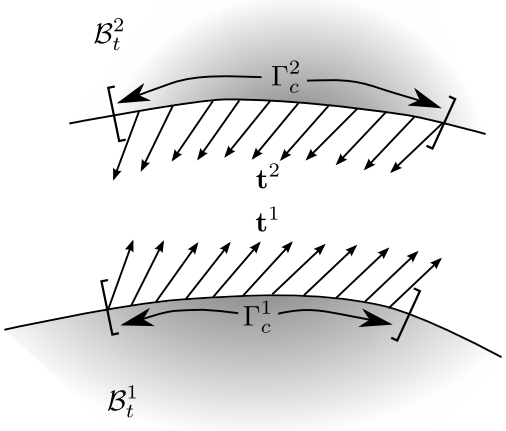

Figure 4.3: Surface traction along Γ_c.

$\mathbf{t}^b$ for body $b = 1, 2$ is decomposed into normal and tangential components

$$\mathbf{t}^b = \lambda^b \mathbf{n}^b + \tau_1^b \mathbf{a}_1^b + \tau_2^b \mathbf{a}_2^b, \tag{4.10}$$

where λ is the normal pressure at the surface, and τ_i is the tangential traction in the direction of $\mathbf{a}_i$. We define the contact contribution Π_c as

$$\Pi_c = \sum_{b=1}^{2} \int_{\Gamma_c^b} g_n \lambda^b + \boldsymbol{g}_t \cdot \boldsymbol{\tau}^b \mathrm{d}\Gamma. \tag{4.11}$$

Taking the variation of Equation 4.11 leads to the contact constraint formulation

$$\mathbf{r}_c = \sum_{b=1}^{2} \int_{\Gamma_c^b} \delta g_n \lambda^b + g_n \delta\lambda^b + \delta \boldsymbol{g}_t \cdot \boldsymbol{\tau}^b + \boldsymbol{g}_t \cdot \delta\boldsymbol{\tau}^b \mathrm{d}\Gamma, \tag{4.12}$$

Thus, the weak form of equilibrium in the current configuration 3.33 becomes

$$\sum_{b=1}^{2} \left[\int_{\mathcal{B}_t^b} \boldsymbol{\sigma}^b : \nabla \boldsymbol{\eta}^b \, \mathrm{d}V - \int_{\mathcal{B}_t^b} \rho^b \left(\mathbf{b}^b \right) \cdot \boldsymbol{\eta}^b \, \mathrm{d}V - \int_{\partial \mathcal{B}_\sigma^b} \bar{\mathbf{t}}^b \cdot \boldsymbol{\eta}^b \, \mathrm{d}A \right] - \mathbf{r}_c = 0, \tag{4.13}$$

and the weak form of equilibrium referred to the reference configuration 3.34 becomes

$$\sum_{b=1}^{2} \left[\int_{\mathcal{B}_0^b} \mathbf{P}^b : \nabla \boldsymbol{\eta}^b \, \mathrm{d}V - \int_{\mathcal{B}_0^b} \rho_0^b \left(\mathbf{b}_0^b \right) \cdot \boldsymbol{\eta}^b \, \mathrm{d}V - \int_{\partial \mathcal{B}_P^b} \bar{\mathbf{t}}_0^b \cdot \boldsymbol{\eta}^b \, \mathrm{d}A \right] - \mathbf{r}_c^0 = 0, \tag{4.14}$$

where $\boldsymbol{r}_c^0$ represents the contact constraint formulation referred to the reference configuration. The definition and variation of the normal and tangential gap depend on the underlying kinematic assumption and the choice of discretization. They are discussed in detail in Chapter 6. The constitutive behavior of λ and τ are presented for each Chapter that explores a particular interface condition. Specifically, small strain frictionless contact behavior is studied in Chapter 8, small strain cohesive contact behavior is explored in Chapter 9, and large strain frictionless contact behavior is examined in Chapter 10

Chapter 5

Numerical Implementation

Numerical simulation of interface phenomena may be carried out through different approaches, such as: the boundary element formulation [117], the element free Galerkin method [11], and the finite element formulation [116]. In standard finite element methods, a common approach is to introduce an interface element between volume elements. Remeshing may or may not be necessary depending on the magnitude of surface geometry changes in the mechanical deformation and design optimization processes [38, 100, 12, 46]. The XFEM has been developed to model arbitrary discontinuities in the finite element model without remeshing. This method leverages the partition of unity concept with appropriate enrichment functions to accurately resolve displacement fields along the interface [69, 70]. A variety of contact modeling methods have been explored in the XFEM. A penalty method has been employed to model small strain frictional contact problem using XFEM, for example, by [61, 73, 51]. The XFEM framework has been used to investigate interface cohesion effects on the mechanical performance of nano-structures [32]. A Lagrange multiplier formulation has been used in a few approaches, see [35] and [2]. A mixed Lagrange multiplier formulation has been applied for contact problems by [62] and mortar methods have been studied by [37], respectively. Finite deformations have been considered in a few contact problems, for example, by [79, 90, 50, 98, 15].

5.1 XFEM Discretization

We adopt an immersed boundary technique, specifically the extended finite element method (XFEM), for predicting the mechanical response. The reader is referred to [33] and [49] for an introduction and general overview of the XFEM. Modeling contact problems with the XFEM has shown great promise considering both friction and sliding contact. Assuming infinitesimal strains, [61] and [73] enforce the contact conditions by a penalty method. The approaches of [35] and [2] are based on a Lagrange multiplier formulation. Mixed Lagrange multiplier and mortar methods are studied by [62] and [37], respectively. Finite deformations are considered, for example, by [79], [90], [98] and [15]. In this study we adopt a Lagrange multiplier approach, similar to the one of [35], for modeling sliding contact problems assuming a linear elastic material behavior and infinitesimal strains. The particular framework for integrating the explicit LSM and the generalized formulation of the XFEM used in this study are described in detail in [66] and [107].

For problems involving sliding contact and separation, the solution field at material boundaries are discontinuous. Therefore, a Heaviside enrichment strategy is used exclusively for this work. For more information regarding different enrichment strategies, the reader is referred to [34]. The displacements, u_i, throughout the design domain are defined as follows:

$$u_i(\mathbf{x}) = \sum_{m=1}^{M} \left(H(-\phi(\mathbf{x})) \sum_{k=1}^{N_e} N_k(\mathbf{x})\ \delta_{mp}^{A,k}\ u_{i,k}^{A,m} + H(\phi(\mathbf{x})) \sum_{k=1}^{N_e} N_k(\mathbf{x})\ \delta_{mq}^{B,k}\ u_{i,k}^{B,m} \right) , \tag{5.1}$$

where the Heaviside step function is:

$$H(\phi) = \begin{cases} 1, & \text{if } \phi > 0, \\ 0, & \text{if } \phi \leq 0\ . \end{cases} \tag{5.2}$$

The shape functions are denoted as $N_i(\mathbf{x})$, M is the number of enrichment levels, N_e is the number of elemental nodes, $u_{i,k}^{p,m}$ is the degree of freedom of enrichment level m at node k corresponding to the displacement u_i in phase $p \in \{A, B\}$, and δ is the Kronecker delta. The Heaviside function

turns on/off the interpolation functions associated with each material. For each material, multiple enrichment functions may be necessary to interpolate the solution to multiple, disconnected regions to prevent fictitious coupling or load transferring. The Kronecker delta, $\delta_{mq}^{p,k}$, applies the active enrichment level q for node k such that the displacements at point $\mathbf{x}$ are interpolated by only one set of degrees of freedom defined at node k, satisfying the partition of unity principle. To maintain the continuity of the displacement field across the elemental boundaries, an appropriate enrichment level is chosen. The approach used in this study is adapted from [66], for more description the reader is referred to [66, 99, 101]. The XFEM allows the integration of the weak form of governing equations in an intersected element by decomposing into triangles (2D) and tetrahedrons (3D) while in non-intersected elements the displacement field is approximated by the standard finite element interpolation.

For three-phase problems, we approximate the displacements $u_i(\mathbf{X})$ in phases A and B as:

$$u_i(\mathbf{X}) = \sum_{m=1}^{M} \left(H(-\phi^1(\mathbf{X})) \sum_{k}^{N_e} N_k(\mathbf{X})\ \delta_{mq}^{A,k}\ u_{i,k}^{A,m} + H(\phi^2(\mathbf{X}))H(\phi^1(\mathbf{X})) \sum_{k}^{N_e} N_k(\mathbf{X})\ \delta_{mp}^{B,k}\ u_{i,k}^{B,m} \right). \tag{5.3}$$

The Heaviside function applied to the LSF ϕ^2 serves to turn off the approximation in the void phase. Aside from this deviation, the displacement field is approximated in the same manner as for two phase problems. For both two and three phase problems, the intersected elements in phases A and B are triangulated for integration purposes.

In this paper, the displacements are approximated by quad-4 and hex-8 elements in 2D and 3D, respectively. The stabilized Lagrange multiplier for the contact non-penetration condition described in Equation (9.7) is approximated as being element-wise constant. The Lagrange multipliers are condensed out locally to determine the structural response. To cure the ill-conditioning of the XFEM formulation associated with small intersections, the geometric preconditioning scheme detailed by [56] is employed.

Chapter 6

Numerical Implementation: Contact Contributions

The XFEM discretized model requires contact contributions defined in Equation 4.12 to be evaluated in a piece-wise fashion along immersed boundaries. This chapter provides detailed definition of how this is accomplished in small strain and large strain problems. Considering the mechanical response is solved via an iterative Newton-Raphson procedure, the generalized contact tangent stiffness contributions are defined as

$$\boldsymbol{J}_c = \frac{\partial \boldsymbol{r}_c}{\partial \boldsymbol{u}} = \sum_{b=1}^{2} \Big[\int_{\Gamma_c^b} \frac{\partial}{\partial \boldsymbol{u}} \left(\delta g_n \lambda^b + g_n \delta \lambda^b + \delta \boldsymbol{g}_t \cdot \boldsymbol{\tau}^b + \boldsymbol{g}_t \cdot \delta \boldsymbol{\tau}^b \right) \mathrm{d}\Gamma + \oint_{\acute{\Gamma}_c^b} \left(\delta g_n \lambda^b + g_n \delta \lambda^b + \delta \boldsymbol{g}_t \cdot \boldsymbol{\tau}^b + \boldsymbol{g}_t \cdot \delta \boldsymbol{\tau}^b \right) \frac{\partial \Gamma_c^b}{\partial \boldsymbol{u}} \, \mathrm{d}\acute{\Gamma} \Big], \quad (6.1)$$

where $\acute{\Gamma}_c^b$ is the boundary along the area of contact. The tangent stiffness consists of two components: the first accounts for the derivative of the integrand, and the second accounts for changes in the area of contact with respect to displacements. The following sections define how small sliding and large sliding assumptions affect the residual and Jacobian contributions from contact. In Section 6.1, we define the discretized mechanical model where relative sliding between surfaces is negligible. In Section 6.2, two distinct approaches are provided for the discretized contact model considering non-negligible sliding.

6.1 Small Sliding

For two-phase material geometry prescribed by a single level set field, contact surfaces are always coincident in the undeformed configuration. Considering small sliding contact kinematics,

a typical XFEM intersected is illustrated in the current configuration in Figure 6.1. With a small

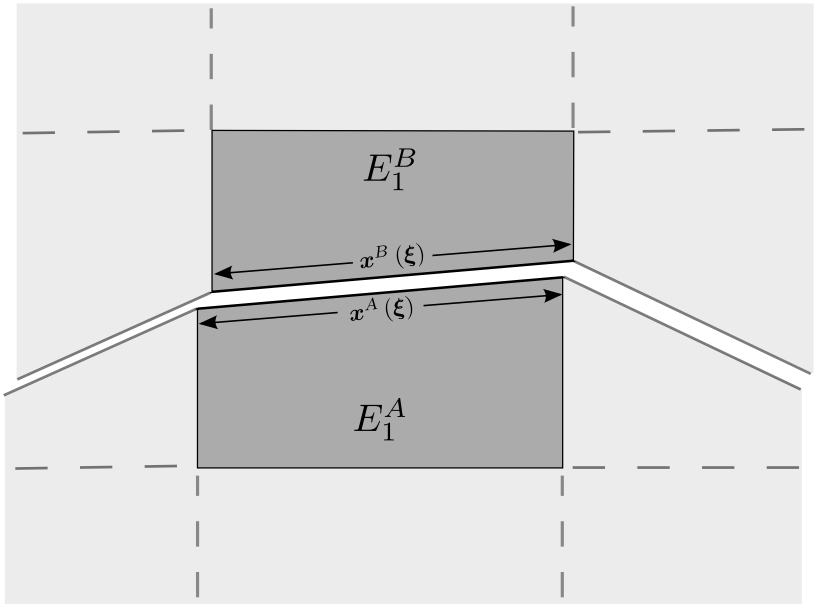

Figure 6.1: XFEM intersected element in current configuration, small sliding.

sliding assumption, the convective coordinates $\boldsymbol{\xi}$ describe coincident location along the interface in the reference configuration, and approximate coincident location in the current configuration. This affords the use of the normal and tangential gap as defined in Equations 4.6 and 4.9. With the XFEM, the solution at the immersed interface is defined as

$$\boldsymbol{u}^A(\boldsymbol{\xi}) = \sum_{i=1}^{N_s^A} \boldsymbol{\eta}_i^A(\boldsymbol{\xi})\,\hat{\boldsymbol{u}}_i^A, \qquad \boldsymbol{u}^B(\boldsymbol{\xi}) = \sum_{i=1}^{N_s^B} \boldsymbol{\eta}_i^B(\boldsymbol{\xi})\,\hat{\boldsymbol{u}}_i^B, \tag{6.2}$$

where $\boldsymbol{\eta}_i$ are the shape functions associated with the solution field of either phase, and $\hat{\boldsymbol{u}}_i$ are the discrete solution vectors for either phase.

With infinitesimal strain theory, the current configuration surface tangential and normal vectors are assumed to be approximately constant, i.e.

$$\delta\boldsymbol{a}_1^A \approx \boldsymbol{0}, \qquad \delta\boldsymbol{a}_2^A \approx \boldsymbol{0}, \qquad \delta\boldsymbol{n}^A \approx \boldsymbol{0}. \tag{6.3}$$

With Equations 6.2 and 6.3, the variation of the normal and tangential gap components in the contact constraint formulation 4.12 are defined as

$$\delta g_n = \left(\boldsymbol{\eta}_i^B(\boldsymbol{\xi}) - \boldsymbol{\eta}_i^A(\boldsymbol{\xi})\right) \cdot \boldsymbol{n}^A(\boldsymbol{\xi}) \tag{6.4}$$

$$\delta \boldsymbol{g}_T = \left(\boldsymbol{\eta}_i^B\left(\boldsymbol{\xi}\right) - \boldsymbol{\eta}_i^A\left(\boldsymbol{\xi}\right)\right) \cdot \boldsymbol{a}_\alpha^A\left(\boldsymbol{\xi}\right) \tag{6.5}$$

where $\alpha = 1, 2$ corresponds to either surface tangent vector. Additionally, the small sliding assumption implies

$$\frac{\partial \Gamma_c^b}{\partial \boldsymbol{u}} \approx \mathbf{0}, \tag{6.6}$$

which eliminates the second term in the tangent stiffness contribution from contact (Equation 6.1).

6.2 Large Sliding

As material strains exceed the small strain limit or the relative displacements between surfaces surpass the element side length, the ability to compute a structural response accurately becomes increasingly difficult. Contact search algorithms, nonlinear kinematics, irrotational stress-strain relations, and reference configuration mapping are well studied aspects of evaluating a correct physical response. While nonlinear kinematics, irrotational stress, and reference configuration mapping are all tractable with regards to evaluating gradient based design sensitivities, large sliding behavior imposes a dependency of the location of contact on the displacement field. The transportive relationship between the displacement field and coincident surface location must be carefully evaluated to ensure the tangent stiffness, and subsequently design sensitivities, are accurate.

In the context of Finite Element based mechanical models, there are a number of methods for constructing coincident mesh entity pairs to evaluate contact related governing equations. These methods include Node-to-Node (NTN), Node-to-Surface (NTS), and Surface-to-Surface (STS) pairing. The XFEM preserves the definition of the interface and is extensible to any of these methods. The main departure from FEM is that instead of constructing contact relations between element nodes and surfaces, the XFEM must interpolate the solution to intersection points and the zero level set iso-surfaces within elements. To integrate the weak form of contact governing equations uniformly, this work relies solely on the STS pairing of intersected element surfaces.

Presented in this chapter are two distinct methods for constructing and integrating STS pairs

for two dimensional problems: the segmented approach, and the coupled parametric approach. The segmented approach assumes a piecewise-linear discretization of the surface, and recovers a globally consistent tangent system by constructing auxiliary contact variables related to the limits of integration for each STS pair. The coupled parametric approach is generalized to any surface discretization, and accounts for the transportive relationship between surfaces inherently.

6.2.1 Segmented Approach

When the relative motion between two bodies in contact approaches the scale of the elemental side length, the assumption of coincident structural facets is no longer valid. An illustration of how this would appear in the framework of the XFEM is provided in Figure 6.2, where subscripts denote the element number and superscripts represent the phase. Contact contributions between surfaces can no longer be determined at the elemental level. Instead, we must determine the deformed configuration overlap of continuous regions along the immersed interface. The segmented approach

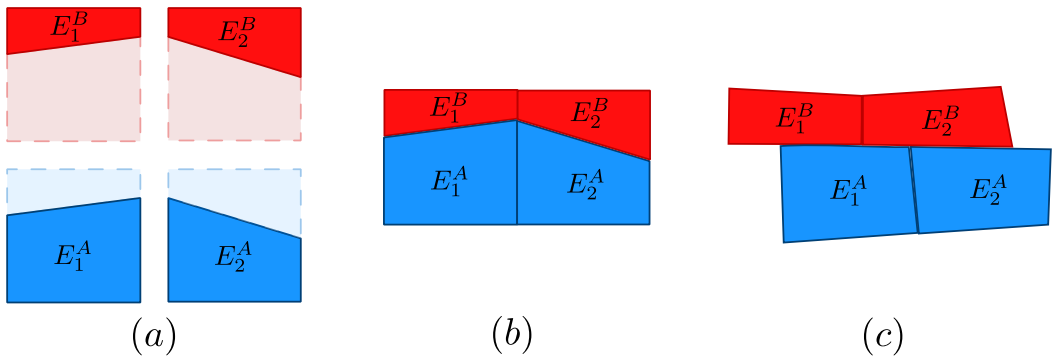

Figure 6.2: Visualization of large sliding contact within the XFEM: (a) illustrates a disassembled view, whereas (b) and (c) depict the elements in their undeformed and deformed configurations, respectively.

assumes each surface is piece-wise linear, and coincident surface location is linearly distributed throughout the domain of integration.

6.2.1.1 Contact Search Algorithm

For large relative motion, a two-step search algorithm is employed during each Newton-Raphson iteration throughout the analysis to determine surface projections. A global search gathers all intersected elements, and interpolates the solution field from either respective phase to the zero level set iso surface. With the deformed position of the interface known, a local search algorithm cycles through continuous regions of the deformed interface to construct STS pairs. For each pair of elements that successfully project onto one another within a specified search radius, a STS contact element pairing is constructed as shown in Figure 6.3.

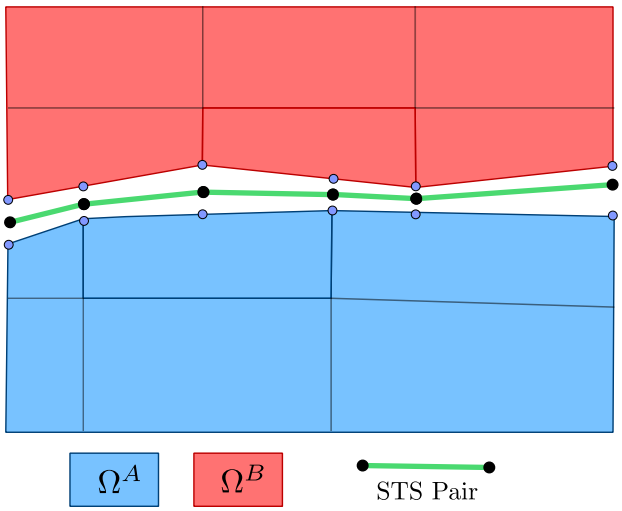

Figure 6.3: Contact element pairing between intersected elements.

The local search algorithm begins by cycling through all immersed boundary segments from material Ω^A and comparing them to every boundary segment from material Ω^B. An initial geometric proximity check is performed. If both segments are within a specified distance from each other, typically h to $3h$ where h is the element side length, the search algorithm then determines if a viable STS pair can be constructed. This process begins by transforming the coordinate system of both segments to one aligned with the surface of Ω^A. This process is illustrated in Figure 6.4. The intersected element edge locations in the current configuration are evaluated in the new coordinate system. Coordinates ξ_{1-2} are compared to ξ_{3-4} to determine the configuration of overlap. A total

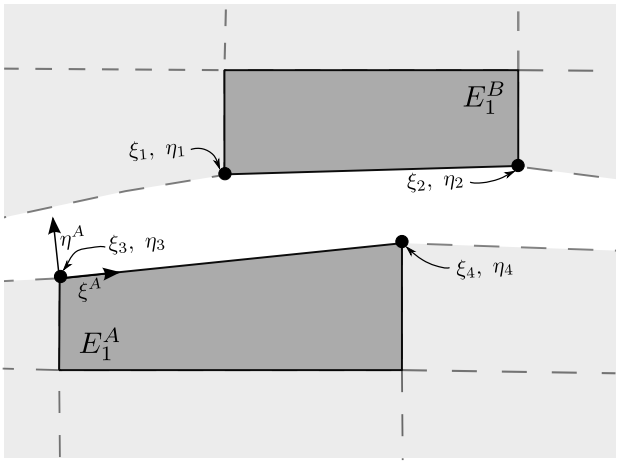

Figure 6.4: Contact element pairing between intersected elements.

of nine configurations exist for how these segments may overlap, illustrated in Figure 6.5. Positions

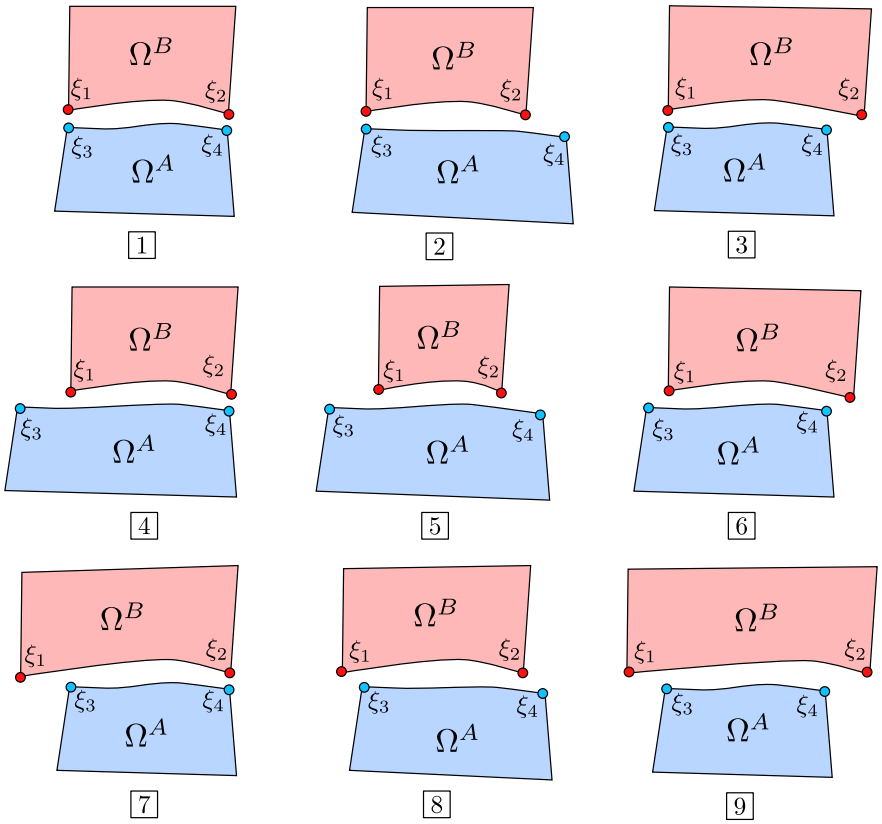

Figure 6.5: Configurations of overlap.

ξ_1 and ξ_2 from Ω^B are either equivalent, greater, or less than ξ_3 and ξ_4, respectively. Based on

the particular configuration encountered, the deformed surface normal of material Ω_A is used to project and evaluate new limits of integration if necessary. The integration limits in the reference configuration are recorded and stored with each STS pair created.

Re-entrant corners take careful consideration to ensure that incorrect STS pairs are avoided. As an example, consider the configuration illustrated in Figure 6.6. In this particular example, surface segment Γ^A is to be compared to segments Γ^B_{1-5} to determine the appropriate contact pairs. The local search algorithm detects Γ^B_1 through Γ^B_5 as overlapping with Γ^A after transforming

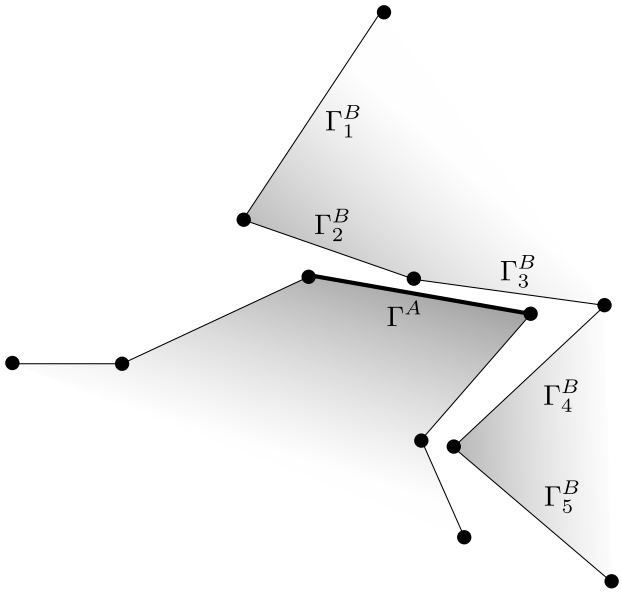

Figure 6.6: Re-entrant corner example.

to the new coordinate system aligned with Γ^A. To remove incorrect surface pairing, each surface segment is numbered in successive order along the interface perimeter. After determining the closest proximity surface segment (Γ^B_3), all other contact pairs with Γ^A are revisited. If the other contact pairs are a topological neighbor to Γ^B_3, e.g. Γ^B_2 and Γ^B_4, they are still candidates for being kept as correct contact pairs. The deformed surface normals n^A and n^B_i are compared, where n^B_i is the surface normal of candidate segment Γ^B_i. If the surface normals are not opposing, the candidate is rejected. Thus, Γ^B_4 is determined to be an incorrect STS pair and removed. Since Γ^B_5 is not a topological neighbor of Γ^B_3, it is also considered an incorrect STS pair. This process is repeated

for each accepted candidate. Thus, Γ_1^B would also be removed as a pair with Γ^A. Although it is a topological neighbor of Γ_2^B, which was an accepted surface pairing, the surface normal does not oppose that of Γ^A.

6.2.1.2 Coincident Surface Location

The contact search algorithm imposes a dependency of surface overlap on the displacement field. While an infinitesimal sliding assumption yields only intrinsic tangent stiffness contributions, finite sliding introduces transportive tangent stiffness contributions. To attain global tangent stiffness consistency, and subsequently accurate design sensitivities, one must consider how the contact search algorithm affects the equilibrium of the system. In two dimensions, the contact search algorithm determines four distinct limits of integration per element pair: two along the interface of either respective body as shown in Figure 6.7. These convective coordinate integration domain limits are treated as additional degrees of freedom.

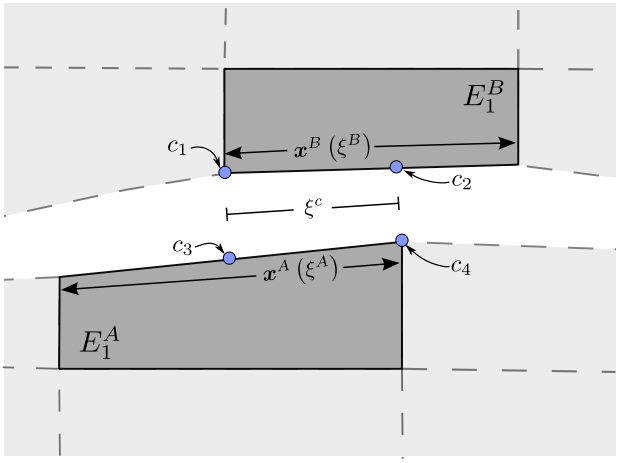

Figure 6.7: Each pair of contacting elements introduce 4 additional degrees of freedom: the intersection locations of each surface.

Provided that c_1 projects onto c_3, and c_2 projects onto c_4, with a linear discretized interface, we assume that the distributed points from either surface in between the limits of integration are relatable by:

$$\xi^c = \frac{\left(\xi^A - c_3\right)}{c_4 - c_3} = \frac{\left(\xi^B - c_1\right)}{c_2 - c_1}, \qquad 0 \leq \xi^c \leq 1, \tag{6.7}$$

and the displacements along either surface are known to be

$$\boldsymbol{u}^A\left(\xi^c\right) = \sum_{i=1}^{N_s^A} \boldsymbol{\eta}_i^A \left(\frac{\left(\xi^A - c_3\right)}{c_4 - c_3} \right) \hat{\boldsymbol{u}}_i^A, \tag{6.8}$$

$$\boldsymbol{u}^B\left(\xi^c\right) = \sum_{i=1}^{N_s^B} \boldsymbol{\eta}_i^B \left(\frac{\left(\xi^B - c_1\right)}{c_2 - c_1} \right) \hat{\boldsymbol{u}}_i^B. \tag{6.9}$$

With Equations 6.2 and 6.3, and with constant normal and tangential vectors for each segment of the interface, the variation of the normal and tangential gap components in the contact constraint formulation 4.12 are defined as

$$\delta g_n = \left(\boldsymbol{\eta}_i^B\left(\xi^c\right) - \boldsymbol{\eta}_i^A\left(\xi^c\right)\right) \cdot \boldsymbol{n}^A \tag{6.10}$$

$$\delta \boldsymbol{g}_T = \left(\boldsymbol{\eta}_i^B\left(\xi^c\right) - \boldsymbol{\eta}_i^A\left(\xi^c\right)\right) \cdot \boldsymbol{a}_\alpha^A \tag{6.11}$$

To overcome rank deficiency caused by the additional variables, residual equations are constructed with respect to the limits of integration:

$$\boldsymbol{r}_s = \begin{bmatrix} c_1 - S.A.\left(c_1\right) \\ c_2 - S.A.\left(c_2\right) \\ c_3 - S.A.\left(c_3\right) \\ c_4 - S.A.\left(c_4\right) \end{bmatrix}, \tag{6.12}$$

where c_{1-4} represents the integration limit variables in the convective coordinate system of either surface, and $S.A.\left(c_{1-4}\right)$ represents the search algorithm's determined location for c_{1-4} based on the displacements of either respective surface. This yields the coupled system of equations

$$\begin{bmatrix} \frac{\partial \boldsymbol{r}_c}{\partial \boldsymbol{u}} & \frac{\partial \boldsymbol{r}_c}{\partial \boldsymbol{c}} \\ \frac{\partial \boldsymbol{r}_s}{\partial \boldsymbol{u}} & \frac{\partial \boldsymbol{r}_s}{\partial \boldsymbol{c}} \end{bmatrix} \begin{bmatrix} \Delta \boldsymbol{u} \\ \Delta \boldsymbol{c} \end{bmatrix} = \begin{bmatrix} \boldsymbol{r}_c \\ \boldsymbol{r}_s \end{bmatrix}. \tag{6.13}$$

The residual equations ($\boldsymbol{r}_s$) are created in a manner that is least computationally intensive. Considering the search algorithm updates integration limits every Newton iteration, $\boldsymbol{r}_s$ is

conveniently always zero. The tangent stiffness matrix term $\frac{\partial \boldsymbol{r}_s}{\partial \boldsymbol{c}}$ becomes the identity matrix. By condensing out the added degrees of freedom, the tangent stiffness for state variables becomes

$$\left[\frac{\partial \boldsymbol{r}_c}{\partial \boldsymbol{u}} - \frac{\partial \boldsymbol{r}_c}{\partial \boldsymbol{c}}\frac{\partial \boldsymbol{r}_s}{\partial \boldsymbol{u}}\right]\Delta \boldsymbol{u} = \boldsymbol{r}_u. \tag{6.14}$$

Through condensation, it is clear from Equation 6.14 that $\frac{\partial \boldsymbol{r}_c}{\partial \boldsymbol{u}}$ is the intrinsic portion of the tangent stiffness, and $-\frac{\partial \boldsymbol{r}_c}{\partial \boldsymbol{c}}\frac{\partial \boldsymbol{r}_s}{\partial \boldsymbol{u}}$ is the transportive term of the tangent stiffness.

6.2.1.3 Summary

Although this method recovers global tangent stiffness consistency, it is heavily limited by the assumptions made. It is only suitable for linear interpolation of the zero level set iso-contour, and is not extensible to three dimensional cases. Additionally, due to the assumption of linearly distributed surface overlap within each contact element pair, the terms $\frac{\partial \boldsymbol{r}_c}{\partial \boldsymbol{c}}$ and $\frac{\partial \boldsymbol{r}_s}{\partial \boldsymbol{u}}$ do not easily yield an analytical expression and are evaluated through a finite difference method. The associated computational expense is compounded for evaluating design sensitivities, rendering this method ill-suited for optimization problems.

6.2.2 Coupled Parametric Approach

Structural response due to contact phenomena is also highly sensitive to surface geometry. A linear discretization of a surface yields sharp corners at element boundaries. These sharp corners often result in high response prediction error for surface to surface contact formulations. To allow for a continuous description of a broad range of surface geometries and derive the influence of the search algorithm on the physical response, contact mechanics are built from a parametric representation of each surface.

6.2.2.1 Surface Parametrization

Geometric parametrization is a method of describing the location of all points which reside on a particular object. It is especially useful to parameterize domain entities of reduced dimensionality.

For example, a one dimensional curve existing in a higher dimensional space can be defined by a single parameter, or a two dimensional surface in a higher dimensional space can be defined by two surface parameters.

The cartesian coordinates for any given point on a surface can be defined as a general function of curve parameters and control variables:

$$X_i = f_i\left(\alpha_j, c_k\right) \tag{6.15}$$

where f_i is an arbitrary function of curve parameters α_j and control variables c_k for dimension X_i. In the context of defining structural surfaces for contact, subscript $i = 1-3$, $j = 1-2$, and k can be any number of surface control variables. Surface tangent vectors and normal vector can be defined at any given point as follows:

$$\vec{t_1^0} = \frac{\partial X_i}{\partial \alpha_1}, \qquad \vec{t_2^0} = \frac{\partial X_i}{\partial \alpha_2}, \qquad \vec{n^0} = t_i^1 \times t_i^2 \tag{6.16}$$

where $\vec{t_1^0}$, $\vec{t_2^0}$, and $\vec{n^0}$ are the two surface tangents and surface normal respectively. For the derivation of surface quantities such as normal pressure or tangential traction, it is necessary to normalize normal and tangent vectors. For large strain contact relations, it is often necessary to know surface information in both the reference and deformed configuration. The lagrangian description of the deformed surface position is as follows:

$$x_i\left(\alpha_j, c_k\right) = X_i\left(\alpha_j, c_k\right) + u_i\left(X_i\left(\alpha_j, c_k\right)\right) \tag{6.17}$$

where x_i is the deformed position of the surface at location α_j. The same relations for determining surface tangents and surface normal vectors can be applied to the deformed position x_i.

$$\vec{t_1} = \frac{\partial X_i}{\partial \alpha_1} + \frac{\partial u_i}{\partial X_j}\frac{\partial X_j}{\partial \alpha_1}, \qquad \vec{t_2} = \frac{\partial X_i}{\partial \alpha_2} + \frac{\partial u_i}{\partial X_j}\frac{\partial X_j}{\partial \alpha_2}, \qquad \vec{n} = t_i^1 \times t_i^2 \tag{6.18}$$

As an example, consider the surface defined by:

$$X = \alpha_1, \qquad Y = \alpha_2, \qquad Z = \sin\left(c_1\alpha_1\right) + \cos\left(c_1\alpha_2\right) \tag{6.19}$$

with a known solution field of:

$$u_x = 0, \qquad u_y = 0, \qquad u_z = XY \tag{6.20}$$

where $c_1 = 2\pi$. For the range $0 \leq \alpha_1 \leq 1$ and $0 \leq \alpha_2 \leq 1$, the parametric surface is illustrated in Figure 6.8. Reference configuration surface tangents and normals can be continuously described

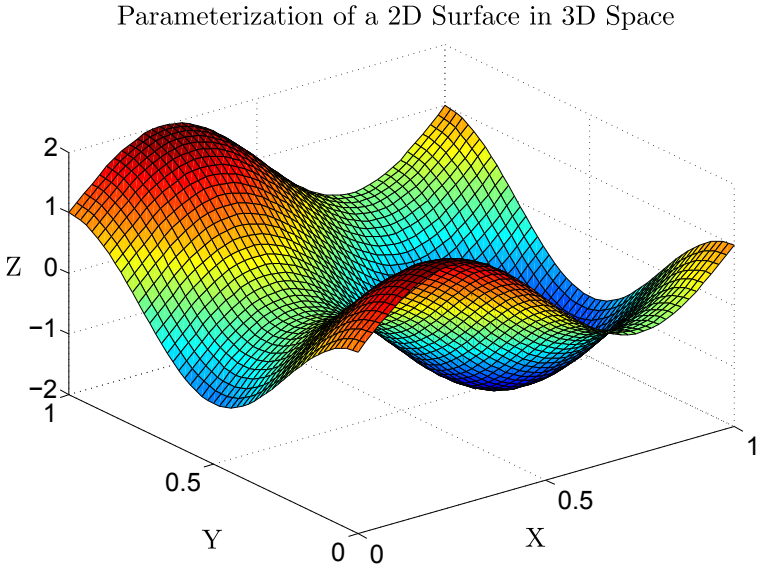

Figure 6.8: Parametric surface defined by sine and cosine functions.

as:

$$\vec{t_1^0} = \begin{bmatrix} 1 \\ 0 \\ c_1 \cos(c_1\alpha_1) \end{bmatrix}, \quad \vec{t_2^0} = \begin{bmatrix} 0 \\ 1 \\ -c_1 \sin(c_1\alpha_2) \end{bmatrix}, \quad \vec{n^0} = \begin{bmatrix} c_1 \cos(c_1\alpha_1) \\ c_1 \sin(c_1\alpha_2) \\ 1 \end{bmatrix} \tag{6.21}$$

and the deformed configuration tangent and normal vectors become:

$$\vec{t_1} = \begin{bmatrix} 1 \\ 0 \\ c_1 \cos(c_1\alpha_1) + \alpha_2 \end{bmatrix}, \quad \vec{t_2} = \begin{bmatrix} 0 \\ 1 \\ -c_1 \sin(c_1\alpha_2) + \alpha_1 \end{bmatrix}, \quad \vec{n} = \begin{bmatrix} -c_1 \cos(c_1\alpha_1) - \alpha_2 \\ c_1 \sin(c_1\alpha_2) - \alpha_1 \\ 1 \end{bmatrix} \tag{6.22}$$

This method of defining surface location and orientation through parametrization is easily applied to two dimensional domains with one dimensional surfaces. Only one surface parameter exists, and the second tangent vector is orthogonal to the design domain. Within the framework of XFEM, it is convenient to allow the intersection points along element edges to be control variables for each parametric surface segment. With a parameterized surface framework, the user may define

any continuous representation between element boundaries. Ideally, this definition would include additional control variables which maintain C^1 continuity across element boundaries.

6.2.2.2 Continuous Coupling of Overlapping Structures

To provide a continuous representation of overlapping structures, we wish to couple both surface parametrization schemes. Thereby defining two surface locations with a single set of parameters. Consider two continuum bodies approaching contact in the deformed configuration as seen in Figure 6.9: where X_i and u_i are the position and displacements along the surface of con-

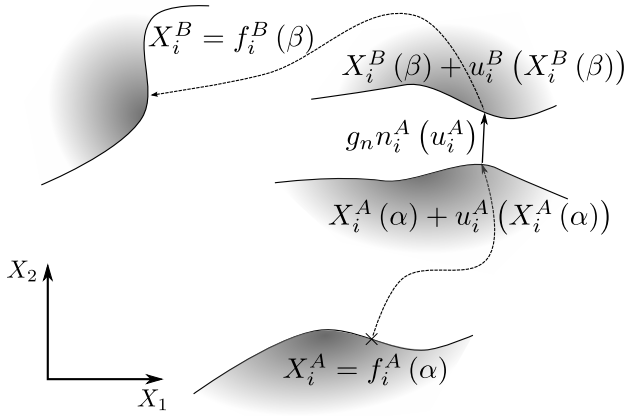

Figure 6.9: Parametric representation of Surfaces A and B.

tinuum bodies A and B. Surface geometries of either body can be expressed as arbitrary functions of curve parameters α and β. To establish a relationship between surface parametric locations α and β, one can restrict the deformed locations of either surface to be coincident provided some projection based on surface orientation. Arbitrarily, surface normal n_i^A is chosen as a projection direction, and the following surface relationship is established:

$$\boldsymbol{r}_p = X_i^A(\alpha) + u_i^A\left(X_i^A(\alpha)\right) + g_n n_i^A\left(X_i^A, u_i^A\right) - X_i^B(\beta) - u_i^B\left(X_j^B(\beta)\right) = \mathbf{0} \tag{6.23}$$

where g_n is the unknown scalar projection distance. Conveniently, this by definition is the normal gap value between surfaces. For the two-dimensional case presented in Figure 6.9, this equation must be satisfied in both X_1 and X_2 dimensions. Currently the system of equations is under-

determined, since α, β, and g_n are unknown. This illustrates in the most basic sense the need for a 'master-slave' approach. By choosing position α, we can solve for the remaining two unknowns. This method is scalable to three dimensions, resulting in 3 equations and four surface parameters:$\alpha_1, \alpha_2, \beta_1, \beta_2$. With α_1 and α_2 known, we can solve for β_1, β_2, and g_n. For the remainder of this topic, superscript A will be changed to m and superscript B will be changed to s to identify master and slave objects.

For a chosen position α, it can be observed that if either displacements are perturbed, the scalar gap g_n and slave surface position β must change for Equation 6.23 to hold true. While describing contact interactions using parametric representation of surfaces is common practice within the field of computational mechanics [113], describing both surface positions with one set of parameters requires careful consideration when the state equilibrium drives geometry optimization.

6.2.2.3 Master-Slave Surface Dependencies

Normal Position Relations Consider a continuous solution field that is defined as a function of discrete variables. For a finite element based mechanical model, a locally continuous solution of either surface can be defined as some spatial interpolation of discrete state variables:

$$u_i^p(\psi) = \sum_k N_k\left(X_i^p\left(\psi, c_j^p\right)\right)\hat{u}_{i_k}^p \tag{6.24}$$

where superscript p denotes the master or slave body,ψ represents the parametric coordinate for either surface, subscripts i and k represent dimension and interpolation space, N denotes an appropriate interpolation function, c_j are the parametric control variables, and $\hat{u}$ represents the discrete solution. We wish to uniquely describe the position and solution of both surfaces given one parametric coordinate (α). While the master surface spatial interpolation remains as defined in Equation 6.24, through continuous mapping the slave surface spatial interpolation becomes a function of the master surface position.

$$u_i^s(\alpha) = \sum_k N_k\left(X_i^s\left(\beta\left(\alpha, c_j^m, c_j^s, \hat{u}_i^m, \hat{u}_i^s\right), c_j^s\right)\right)\hat{u}_{i_k}^s \tag{6.25}$$

Note that the slave surface solution u_i^s for a given master surface location α is now a function of the discrete solution of both bodies. These dependencies can be intuitively expressed by taking the variation of the continuous slave surface solution.

$$\delta\left(u_i^s\right) = \left(\frac{\partial u_i^s}{\partial X_j^s}\frac{\partial X_j^s}{\partial \beta}\frac{\partial \beta}{\partial \hat{u}_k^m}\right)\delta\hat{u}_k^m + \left(\frac{\partial u_i^s}{\partial X_j^s}\frac{\partial X_j^s}{\partial \beta}\frac{\partial \beta}{\partial \hat{u}_k^s} + \frac{\partial u_i^s}{\partial \hat{u}_k^s}\right)\delta\hat{u}_k^s \tag{6.26}$$

The parametric control variables c_j^p are related to geometry description, and are independent of the mechanical response during the forward analysis. Sensitivity dependencies will be discussed in Section 6.2.2.7. The first term can be interpreted as the transportive relationship between the master surface solution and the corresponding slave location. The second term contains both transportive and intrinsic relations to the slave surface discrete solution. However, the dependencies of the slave surface parameter β and normal gap g_n on the discretized solution have not yet been evaluated. These dependencies can be derived by taking the total derivative of Equation 6.23:

$$\frac{\mathrm{d}\boldsymbol{r}_p}{\mathrm{d}\hat{u}_i^p} = \frac{\partial \boldsymbol{r}_p}{\partial \hat{u}_i^p} + \frac{\partial \boldsymbol{r}_p}{\partial g_n}\frac{\partial g_n}{\partial \hat{u}_i^p} + \frac{\partial \boldsymbol{r}_p}{\partial \beta}\frac{\partial \beta}{\partial \hat{u}_i^p} = \mathbf{0} \tag{6.27}$$

which is solved for the dependency of the normal gap and slave position on the discretized solution $\partial g_n/\partial \hat{u}_i^p$ and $\partial \beta/\partial \hat{u}_i^p$.

During the evaluation of the tangent stiffness, many contact constitutive relations (Penalty, Stabilized Lagrange, Nitsche, etc.) require the second order derivatives $\partial^2 g_n/\partial \hat{u}_i^p \partial \hat{u}_j^p$ and $\partial^2 \beta/\partial \hat{u}_i^p \partial \hat{u}_j^p$ to be consistent. These dependencies can be derived by taking the second total derivative of Equation 6.23.

$$\begin{aligned}\frac{\mathrm{d}^2\boldsymbol{r}_p}{\mathrm{d}\hat{u}_i^p \mathrm{d}\hat{u}_j^p} &= \frac{\partial^2 \boldsymbol{r}_p}{\partial \hat{u}_i^p \partial \hat{u}_j^p} + \frac{\partial^2 \boldsymbol{r}_p}{\partial g_n \partial \hat{u}_i^p}\frac{\partial g_n}{\partial \hat{u}_j^p} + \frac{\partial^2 \boldsymbol{r}_p}{\partial \beta \partial \hat{u}_i^p}\frac{\partial \beta}{\partial \hat{u}_j^p} + \frac{\partial^2 \boldsymbol{r}_p}{\partial g_n \partial \hat{u}_j^p}\frac{\partial g_n}{\partial \hat{u}_i^p} + \frac{\partial^2 \boldsymbol{r}_p}{\partial g_n^2}\frac{\partial g_n}{\partial \hat{u}_i^p}\frac{\partial g_n}{\partial \hat{u}_j^p} \cdots \\ &+ \frac{\partial^2 \boldsymbol{r}_p}{\partial g_n \partial \beta}\frac{\partial g_n}{\partial \hat{u}_i^p}\frac{\partial \beta}{\partial \hat{u}_j^p} + \frac{\partial \boldsymbol{r}_p}{\partial g_n}\frac{\partial^2 g_n}{\partial \hat{u}_i^p \partial \hat{u}_j^p} + \frac{\partial^2 \boldsymbol{r}_p}{\partial \beta \partial \hat{u}_j^p}\frac{\partial \beta}{\partial \hat{u}_i^p} + \frac{\partial^2 \boldsymbol{r}_p}{\partial g_n \partial \beta}\frac{\partial \beta}{\partial \hat{u}_i^p}\frac{\partial g_n}{\partial \hat{u}_j^p} + \frac{\partial^2 \boldsymbol{r}_p}{\partial \beta^2}\frac{\partial \beta}{\partial \hat{u}_i^p}\frac{\partial \beta}{\partial \hat{u}_j^p} + \frac{\partial \boldsymbol{r}_p}{\partial \beta}\frac{\partial^2 \beta}{\partial \hat{u}_i^p \partial \hat{u}_j^p} = \mathbf{0}\end{aligned} \tag{6.28}$$

With a continuous framework established coupling both master and slave surface position to a single parametric coordinate α, we now turn our attention to defining tangential velocities between surfaces.

Tangential Motion Relations

By construction, the master and slave surface positions defined by parameter α project onto one another in the direction of n_i^m. The tangential relative gap can be defined as:

$$g_t = (x_i^s - x_i^m)\, t_i^m \tag{6.29}$$

where g_t is the scalar tangential gap, x_i is the deformed position of material p, and t_i^m is the master surface tangent vector in the deformed configuration. Equation 6.29 will always be zero due to Equation 6.23, however, the variation of the tangential gap is defined as follows:

$$\begin{aligned}\delta g_t = &\left[\left(\frac{\partial x_i^s}{\partial \hat{u}_k^s} + \frac{\partial x_i^s}{\partial X_j^s}\frac{\partial X_j^s}{\partial \beta}\frac{\partial \beta}{\partial \hat{u}_k^s}\right) t_i^m\right]\delta \hat{u}_k^s \\ &+ \left[\left(\frac{\partial x_i^s}{\partial X_j^s}\frac{\partial X_j^s}{\partial \beta}\frac{\partial \beta}{\partial \hat{u}_k^m} - \frac{\partial x_i^m}{\partial \hat{u}_k^m}\right) t_i^m + (x_i^s - x_i^m)\frac{\partial t_i^m}{\partial u_j^m}\frac{\partial u_j^m}{\partial \hat{u}_k^m}\right]\delta \hat{u}_k^m\end{aligned} \tag{6.30}$$

The relative tangent velocity can be described as:

$$\dot{g}_t = \left(\frac{\partial x_i^s}{\partial t} - \frac{\partial x_i^m}{\partial t}\right) n_i^m + (x_i^s - x_i^m)\frac{\partial n_i^m}{\partial t} \tag{6.31}$$

6.2.2.4 General Contact Equilibrium Enforcement

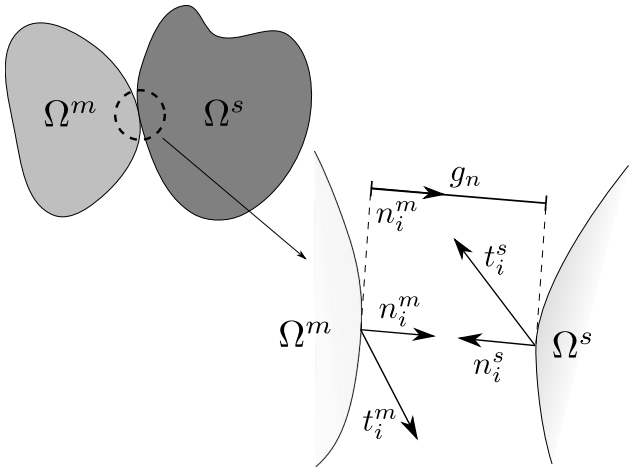

Figure 6.10: Interactions between two bodies in contact.

Consider two bodies, Ω^m and Ω^s, in contact as shown in Figure 6.10. For every point α on the master surface, the normal gap and slave surface position β are uniquely defined through rela-

tion 6.23. We wish to satisfy some equilibrium relation between both bodies to prevent penetration along the surface:

$$\boldsymbol{r}_c = \int_{\Gamma_c} f\left(g_n, u_i^m, u_i^s\right) \mathrm{d}\Gamma_c \tag{6.32}$$

where f is an arbitrary equilibrium condition based on the solution fields of either body and the relative gap between them, and Γ_c is the contact surface. Given the continuous relation afforded in Equation 6.23 everything can be mapped to the master surface parametric coordinates. Using identity 6.33 we can convert our integration space from cartesian to the parametric coordinates, yielding Equation 6.34. Note that Equation 6.33 holds for 2D problems, and would appear differently for 3D problems.

$$\lim_{n\to\infty} \sum_{i=1}^{n} f\left(c_i\right) \Delta_i = \int_a^b f\left(x, y\right) d\left(s\right) = \int_a^b f\left(x\left(\alpha\right), y\left(\alpha\right)\right) \sqrt{\left(\frac{\mathrm{d}x}{\mathrm{d}\alpha}\right)^2 + \left(\frac{\mathrm{d}y}{\mathrm{d}\alpha}\right)^2} \mathrm{d}\alpha \tag{6.33}$$

$$\boldsymbol{r}_c = \oint f\left(g_n\left(\alpha\right), u_i^m\left(\alpha\right), u_i^s\left(\alpha\right)\right) \left| \frac{\partial X_i^m}{\partial \alpha} \right| \mathrm{d}\alpha \tag{6.34}$$

If the solution field, parametric representation of either body, and equilibrium relations were entirely continuous and differentiable, Equation 6.34 could be resolved analytically. However, given the discontinuous nature of contact and piece-wise continuous spatial interpolation schemes of most mechanical models, in practice this is rarely the case. In the following section, integration limits are discussed for finite-element based mechanical models.

6.2.2.5 Integral Limit Dependencies

Piecewise continuous discretization necessitates the use of a search algorithm to find overlapping elements in contact. Integration of residual contributions from contact requires constructing elemental pairs from either surface that overlap. The pairing of contact surfaces and subsequent integration boundaries are now related to displacements through a search algorithm. To recover a fully consistent mechanical model, these integration boundary dependencies must be accounted for in the tangent stiffness derivation.

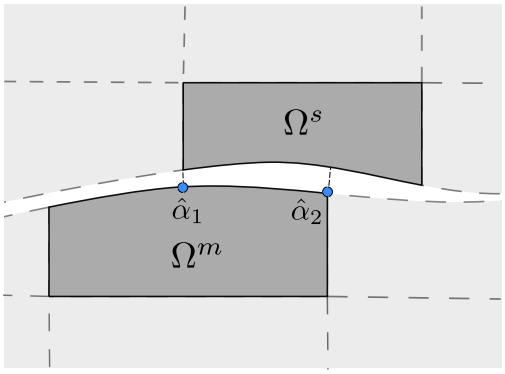

Figure 6.11: Limits of integration are dependent on elemental discretization of bodies in contact.

For a surface-to-surface formulation, we wish to integrate the residual and tangent stiffness contributions over the shared region between both elements. If the integration limit coincides with the master surface element boundary, as is the case for $\hat{\alpha_2}$ in Figure 6.11, it is solution independent. However, if the integration limit does not coincide with the master element boundary, as is the case for $\hat{\alpha}_1$, its position depends on how the slave element boundary projects onto the master element in the deformed configuration. In this case, the slave surface element boundary position in parametric coordinates β is known. The integration limit $\hat{\alpha}_1$ can be found through projection in the deformed configuration as seen in Figure 6.12.

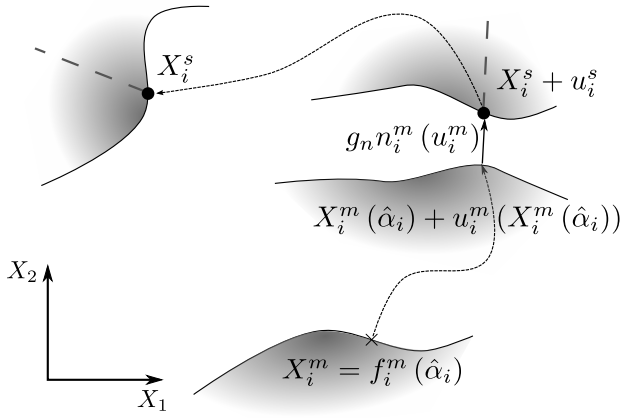

Figure 6.12: Determining limits of integration based on element boundary projection.

The parametric coordinate $\hat{\alpha}$ can be found through a change of dependencies in our continuous

mapping equation:

$$\boldsymbol{r}_p = X_i^m\left(\hat{\alpha}\right) + u_i^m\left(X_i^m\left(\hat{\alpha}\right)\right) - g_n n_i^m(\left(X_i^m\left(\hat{\alpha}\right), u_i^m\left(X_i^m\left(\hat{\alpha}\right)\right)\right) - X_i^s - u_i^s = \mathbf{0} \tag{6.35}$$

where X_i^s and u_i^s are the position and displacements at the slave element boundary. Similarly to the previous section solving integrand dependencies, we can take the total derivative to determine the relation between the limits of integration and the discrete solution field.

$$\frac{\mathrm{d}\boldsymbol{r}_p}{\mathrm{d}\hat{u}_i^p} = \frac{\partial \boldsymbol{r}_p}{\partial \hat{u}_i^p} + \frac{\partial \boldsymbol{r}_p}{\partial g_n}\frac{\partial g_n}{\partial \hat{u}_i^p} + \frac{\partial \boldsymbol{r}_p}{\partial \hat{\alpha}}\frac{\partial \hat{\alpha}}{\partial \hat{u_i^p}} = \mathbf{0} \tag{6.36}$$

While developing a large sliding contact framework, care must be taken to ensure that the search algorithm is consistent in defining limits of integration, as these dependencies will be accounted for in the evaluation of the tangent stiffness of the system.

6.2.2.6 Consistent Tangent Stiffness

With a piecewise continuous solution field, our local contribution to equilibrium becomes:

$$\boldsymbol{r}_c = \int_{\hat{\alpha}_1}^{\hat{\alpha_2}} f\left(g_n\left(\alpha\right), u_i^m\left(\alpha\right), u_i^s\left(\alpha\right)\right) \left| \frac{\partial X_i^m}{\partial \alpha} \right| \mathrm{d}\alpha \tag{6.37}$$

where $\hat{\alpha}_1$ and $\hat{\alpha}_2$ are the search algorithm defined limits of integration based on element boundaries. By derivation, our residual contribution has been fully mapped to a one dimensional space where coordinate α has no dependencies on the solution. Taking the total derivative of Equation 6.37 with respect to the discretized solution:

$$\frac{\mathrm{d}\boldsymbol{r}_c}{\mathrm{d}\hat{u}_i^p} = \frac{\partial \boldsymbol{r}_c}{\partial \hat{u}_i^p} + \frac{\partial \boldsymbol{r}_c}{\partial \hat{\alpha}_1}\frac{\partial \hat{\alpha}_1}{\partial \hat{u}_i^p} + \frac{\partial \boldsymbol{r}_c}{\partial \hat{\alpha}_2}\frac{\partial \hat{\alpha}_2}{\partial \hat{u}_i^p} \tag{6.38}$$

where:

$$\frac{\partial \boldsymbol{r}_c}{\partial \hat{u}_i^p} = \frac{\partial}{\partial \hat{u}_i^p}\int_{\hat{\alpha}_1}^{\hat{\alpha}_2} f_\alpha \, \mathrm{d}\alpha = \int_{\hat{\alpha}_1}^{\hat{\alpha}_2} \frac{\partial f_\alpha}{\partial \hat{u}_i^p} \, \mathrm{d}\alpha \tag{6.39}$$

$$\frac{\partial \boldsymbol{r}_c}{\partial \hat{\alpha}_1} = \frac{\partial}{\partial \hat{\alpha}_1}\int_{\hat{\alpha}_1}^{\hat{\alpha}_2} f_\alpha \, \mathrm{d}\alpha = -f_\alpha \Big|_{\hat{\alpha_1}} \tag{6.40}$$

$$\frac{\partial \boldsymbol{r}_c}{\partial \hat{\alpha}_2} = \frac{\partial}{\partial \hat{\alpha}_2}\int_{\hat{\alpha}_1}^{\hat{\alpha}_2} f_\alpha \, \mathrm{d}\alpha = f_\alpha \Big|_{\hat{\alpha_2}} \tag{6.41}$$

Variable f_α denotes the equilibrium integrand after mapping to parametric coordinate α. Pulling it all together, we arrive at our fully consistent tangent stiffness for a generalized contact equilibrium condition.

$$\frac{\mathrm{d}\boldsymbol{r}_c}{\mathrm{d}\hat{u}_i} = \int_{\hat{\alpha}_1}^{\hat{\alpha}_2} \frac{\partial f_\alpha}{\partial \hat{u}_i} \ \mathrm{d}\alpha + \left(f_\alpha \Big|_{\hat{\alpha_2}} \right) \frac{\partial \hat{\alpha}_2}{\partial \hat{u}_i} - \left(f_\alpha \Big|_{\hat{\alpha_1}} \right) \frac{\partial \hat{\alpha}_1}{\partial \hat{u}_i} \tag{6.42}$$

The first term on the right hand side of Equation 6.42 is tangent stiffness of the integrand, which is equivalent to the first term of Equation 6.1. The last two terms in Equation 6.42 account for the changes in the area of contact with respect to displacements, which is equivalent to the second term of Equation 6.1.

6.2.2.7 Design Sensitivities of the Parameterized Contact Model

For the gradient based design optimization outlined in Section 2.2, contact contributions to design sensitivities must be derived:

$$\frac{\partial \boldsymbol{r}_c}{\partial s_k} = \frac{\partial \boldsymbol{r}_c}{\partial c_i} \frac{\partial c_i}{\partial \phi_j} \frac{\partial \phi_j}{\partial s_k} \tag{6.43}$$

where c_i are the control variables related to surface geometry, ϕ_j are the discrete PDVs which influence the parametric control variables, and s_k are the ADVs which govern the PDVs. Derivatives $\frac{\partial c_i}{\partial \phi_j}$ and $\frac{\partial \phi_j}{\partial s_k}$ are solely related to the choice of parametric surface discretization (see Section 6.2.2.1) and level set field control (see Section 2.4). Provided a robust definition of parametric surface control variables, determining their sensitivities with respect to the ADVs is trivial. What follows is a generalized derivative of the residual contributions with respect to the parametric control variables.

The choice of parametric space is crucial to the way in which design sensitivities are evaluated. Perhaps the most convenient option is to allow the parametric space to be a fixed range, $0 \leq \alpha \leq 1$, which covers the local interface per element. Similar to the derivation of the consistent tangent stiffness in the previous section, the derivative of the residual contribution with respect to the design variables can be separated into integrand and integration limit contributions.

Integrand Design Dependencies

Revisiting Equations 6.24 and 6.25, the cartesian location and displacements along a surface are continuously described by the parametric parameters α_j.

$$u_i^m(\alpha) = \sum_k N_k\left(X_i^m\left(\alpha, c_j^m\right)\right)\hat{u}_{i_k}^m \tag{6.44}$$

$$u_i^s(\alpha) = \sum_k N_k\left(X_i^s\left(\beta\left(\alpha, c_j^m, c_j^s, \hat{u}_i^m, \hat{u}_i^s\right), c_j^s\right)\right)\hat{u}_{i_k}^s \tag{6.45}$$

What has been largely ignored until this point are the control parameters c_k which define structure geometry.

Equation 6.43 is a contribution to the total derivative from Equation 2.7. By definition, the derivative of residual contributions with respect to the ADVs is evaluated assuming the discrete solution $\hat{u}_i^p$ is fixed. The derivative of the continuous solution field u_i^p at the contact interface with respect to the control variables c_j^p can be derived as follows:

$$\frac{\partial u_i^m}{\partial c_k^m} = \frac{\partial u_i^m}{\partial X_j^m}\frac{\partial X_j^m}{\partial c_k^m}, \qquad \frac{\partial u_i^m}{\partial c_k^s} = \mathbf{0} \tag{6.46}$$

$$\frac{\partial u_i^s}{\partial c_k^m} = \frac{\partial u_i^s}{\partial X_j^s}\frac{\partial X_j^s}{\partial \beta}\frac{\partial \beta}{\partial c_k^m} \tag{6.47}$$

$$\frac{\partial u_i^s}{\partial c_k^s} = \frac{\partial u_i^s}{\partial X_j^s}\frac{\partial X_j^s}{\partial \beta}\frac{\partial \beta}{\partial c_k^s} + \frac{\partial u_i^s}{\partial X_j^s}\frac{\partial X_j^s}{\partial c_k^s} \tag{6.48}$$

The derivative of the slave surface parameter with respect to the control variables, $\frac{\partial \beta}{\partial c_k^p}$, and the derivative of the normal gap with respect to the control parameters, $\frac{\partial g_n}{\partial c_k^p}$ can be evaluated by taking the total derivative of Equation 6.23.

$$\frac{\mathrm{d}\boldsymbol{r}_p}{\mathrm{d}c_i^p} = \frac{\partial \boldsymbol{r}_p}{\partial c_i^p} + \frac{\partial \boldsymbol{r}_p}{\partial g_n}\frac{\partial g_n}{\partial c_i^p} + \frac{\partial \boldsymbol{r}_p}{\partial \beta}\frac{\partial \beta}{\partial c_i^p} = \mathbf{0} \tag{6.49}$$

With all relations derived necessary for evaluating design sensitivities within the integrand of the residual contribution from contact, we now turn our attention to the limits of integration.

Integral Limit Design Dependencies

For the non-coincident overlap of two elements, such as depicted in Figure 6.11, the control parameters (c_i^p) will affect some or all integration limits for that particular element pair. If the integration limit coincides with the master surface element boundary, it has no sensitivity with respect to the design variables. However, if the integration limit does not coincide with the master element boundary, it is dependent on the control variables c_i^p and subsequently the abstract design variables by chain rule (Equation 6.43).

The derivative of each parametric integration limit $\hat{\alpha}$ with respect to control variables c_j^p can be derived by taking the total derivative of Equation 6.35 with respect to the control variables:

$$\frac{\mathrm{d}\boldsymbol{r}_p}{\mathrm{d}c_j^p} = \frac{\partial \boldsymbol{r}_p}{\partial c_j^p} + \frac{\partial \boldsymbol{r}_p}{\partial g_n}\frac{\partial g_n}{\partial c_j^p} + \frac{\partial \boldsymbol{r}_p}{\partial \hat{\alpha}}\frac{\partial \hat{\alpha}}{\partial c_j^p} = \mathbf{0} \tag{6.50}$$

6.2.2.8 Complete Contact Residual Design Sensitivities

Recall the generalized local contribution to equilibrium from contact:

$$\boldsymbol{r}_c = \int_{\hat{\alpha}_1}^{\hat{\alpha_2}} f\left(g_n\left(\alpha\right), u_i^m\left(\alpha\right), u_i^s\left(\alpha\right)\right) \left| \frac{\partial X_i^m}{\partial \alpha} \right| \mathrm{d}\alpha \tag{6.51}$$

where $\hat{\alpha}_1$ and $\hat{\alpha}_2$ are the search algorithm defined limits of integration based on element boundaries. Taking the total derivative of Equation 6.37 with respect to the control variables which define our parametric space:

$$\frac{\mathrm{d}\boldsymbol{r}_c}{\mathrm{d}c_j^p} = \frac{\partial \boldsymbol{r}_c}{\partial c_j^p} + \frac{\partial \boldsymbol{r}_c}{\partial \hat{\alpha}_1}\frac{\partial \hat{\alpha}_1}{\partial c_j^p} + \frac{\partial \boldsymbol{r}_c}{\partial \hat{\alpha}_2}\frac{\partial \hat{\alpha}_2}{\partial c_j^p} \tag{6.52}$$

where:

$$\frac{\partial \boldsymbol{r}_c}{\partial c_j^p} = \frac{\partial}{\partial c_j^p}\int_{\hat{\alpha}_1}^{\hat{\alpha}_2} f_\alpha \, \mathrm{d}\alpha = \int_{\hat{\alpha}_1}^{\hat{\alpha}_2} \frac{\partial f_\alpha}{\partial c_j^p} \, \mathrm{d}\alpha \tag{6.53}$$

$$\frac{\partial \boldsymbol{r}_c}{\partial \hat{\alpha}_1} = \frac{\partial}{\partial \hat{\alpha}_1}\int_{\hat{\alpha}_1}^{\hat{\alpha}_2} f_\alpha \, \mathrm{d}\alpha = -f_\alpha \Big|_{\hat{\alpha_1}} \tag{6.54}$$

$$\frac{\partial \boldsymbol{r}_c}{\partial \hat{\alpha}_2} = \frac{\partial}{\partial \hat{\alpha}_2}\int_{\hat{\alpha}_1}^{\hat{\alpha}_2} f_\alpha \, \mathrm{d}\alpha = f_\alpha \Big|_{\hat{\alpha_2}} \tag{6.55}$$

Variable f_α denotes the equilibrium integrand after mapping to parametric coordinate α. Pulling it all together, we arrive at an analytical expression for the derivative of residual contributions with respect to the parametric space control parameters.

$$\frac{\mathrm{d}\boldsymbol{r}_c}{\mathrm{d}c_j^p} = \int_{\hat{\alpha}_1}^{\hat{\alpha}_2} \frac{\partial f_\alpha}{\partial c_j^p} \ \mathrm{d}\alpha + \left(f_\alpha \Big|_{\hat{\alpha_2}} \right) \frac{\partial \hat{\alpha}_2}{\partial c_j^p} - \left(f_\alpha \Big|_{\hat{\alpha_1}} \right) \frac{\partial \hat{\alpha}_1}{\partial c_j^p} \tag{6.56}$$

6.2.2.9 Summary

The coupled parametric approach yields a globally consistent tangent stiffness, is easily extensible to higher order interface geometry, and can be used directly for three dimensional problems. The transportive effects on the tangent stiffness are handled continuously, without any surface discretization assumptions. The derived tangent stiffness and design sensitivities are fully analytical, greatly reducing the computational expense when compared to the segmented approach. For all large strain examples presented in Chapter 10, the coupled parametric approach is employed. Appendix A provides detailed examples of deriving coupled parametric weak form equilibrium expressions from strong form contact constitutive relations.

Chapter 7

Stabilization Techniques

While the XFEM unburdens model geometry and discontinuous displacement fields from being mesh-conforming, it can result in an ill-conditioned system of equations when the ratio of volumes on either side of the interface in an element is small. During topological changes on a fixed mesh, this predicament is often unavoidable. For contact related problems, this ill conditioning often results in artificially high stress predictions in thinly intersected elements. This can lead to solution divergence for problems in which the contact constitutive equations rely on stress to satisfy non-penetration conditions.

This work makes use of two separate approaches to mitigate ill-conditioning. The first method of stabilization, presented in Section 7.1, is an XFEM-based geometric preconditioner, where a scaling matrix is constructed to balance the system[56]. The second approach presented in Section 7.2 is known as a ghost-penalty method, wherein the gradient jumps of the solution field are penalized along common facets of intersected elements[87].

Contact behavior can result in neutral and unstable equilibrium, hampering the convergence of iterative solvers. At the apex before release, snap-fit designs or material anchors can experience a brief moment of neutral stability. Rapid delamination of cohesive bonds can result in an abrupt release of strain energy. For these reasons, this work makes use of a Levenberg-Marquardt similar method of dynamic relaxation[72]. Described in Section 7.3, this method introduces an artificial damping term to the tangent stiffness that vanishes as convergence is achieved.

7.1 Geometric Preconditioner

As previously defined in Section 5.1, the degree of freedom $u_{i,k}^{p,m}$ interpolates the solution field of enrichment level m to topologically connected subdomains of phase p. As this particular subdomain vanishes, the numerical model becomes increasingly ill-conditioned. To mitigate this issue, we use the geometric conditioning approach of [56], which was introduced for 2D heat conduction and flow problems. Geometric preconditioning does not change the variational formulation of the problem, but makes the resulting linearized sub-problem easier to solve by balancing the influence of all degrees-of-freedom in the system through the following projection:

$$\tilde{\mathbf{u}} = \mathbf{T}\mathbf{u}, \tag{7.1}$$

where $\mathbf{u}$ is the vector of displacement variables, $\mathbf{T}$ is a transformation matrix, and $\tilde{\mathbf{u}}$ is the solution vector in the transformed space. Likewise, the residual and stiffness matrix in the transformed space are defined as

$$\tilde{\mathbf{R}} = \mathbf{T}^T\mathbf{R}, \tag{7.2}$$

$$\tilde{\mathbf{K}} = \mathbf{T}^T\mathbf{K}\mathbf{T}, \tag{7.3}$$

where $\mathbf{R}$ and $\mathbf{K}$ are the residual and stiffness equations resulting from the weak form of governing equations.

The preconditioner matrix $\mathbf{T}$ is a diagonal matrix constructed as a ratio of integrals of shape function derivatives:

$$\mathbf{T}_{i,m}^{p} = \left(\max_{\Omega_e \in \Omega_e^c} \frac{\int_{\Omega_e \cap \Omega_m^p} \nabla \boldsymbol{\nu}\left(\mathbf{x}\right) \cdot \nabla \boldsymbol{\nu}\left(\mathbf{x}\right) \mathrm{d}\Omega}{\int_{\Omega_e \cap \Omega^p} \nabla \boldsymbol{\nu}\left(\mathbf{x}\right) \cdot \nabla \boldsymbol{\nu}\left(\mathbf{x}\right) \mathrm{d}\Omega} \right)^{-1/2} \tag{7.4}$$

where $\mathbf{T}_{i,m}^{p}$ is the preconditioner value for the degree of freedom $u_{i,k}^{p,m}$ of node i, material phase p and enrichment level m. Volume Ω_e^c is the set of elements connected to node i, Ω_m^p is the volume of phase p that is integrated with enrichment level m with respect to node i, and $\boldsymbol{\nu}\left(\mathbf{x}\right)$ is the set of admissible test functions. The values of this matrix increase as the region of influence of a

particular degree-of-freedom decreases. To avoid very large values for the components of $\mathbf{T}$, the degrees of freedom associated with a particular diagonal entry $\mathbf{T}^p_{i,m}$ are constrained to zero if

$$\mathbf{T}^p_{i,m} \geq T_{tol}, \tag{7.5}$$

where T_{tol} is a specified tolerance. For this paper, the specified tolerance is set to a value of $T_{tol} = 1.0 \times 10^8$. In the context of large sliding and finite strain contact problems, performance studies related to geometric preconditioning are provided in Appendix B.2.

7.2 Ghost Penalization

As an alternative to the XFEM geometric preconditioner, ghost penalization mitigates ill-conditioning by penalizing the flux jump of a state variable related quantity across element borders in the vicinity of the material interface. For each material phase, ghost penalization is evaluated over the entire intersected element border. In contrast to geometric preconditioning, Ghost penalization augments the variational formulation of the physical model. It has proven successful for stabilizing incompressible Navier-Stokes fluid flow problems [18], fluid incompressibility constraints [87], and species field transport problems [17].

For the work presented in this paper, a geometric preconditioner proved adequate for the stabilization of infinitesimal strain problems. For two-dimensional finite strain problems, residual contributions for ghost penalization are evaluated as follows:

$$r^{GP} = \sum_{p\in\{A,B\}} \sum_{m=1}^{N_m} \int_{\Gamma^0_e} \gamma^L \left[\!\!\left[\frac{\partial \nu_i}{\partial X_j} \right]\!\!\right] n^0_j \left[\!\left[S_{ik} \right]\!\right] n^0_k \mathrm{d}\Gamma, \tag{7.6}$$

where the double bracket operator $[\![]\!]$ denotes the jump in a particular quantity. This form of ghost penalization seeks to minimize the flux jump in stress at the element boarders in the vicinity of the material interface. The local penalty parameter γ^L can be defined in two ways. First, it can be expressed as a global constant value:

$$\gamma^L = \gamma^G \ . \tag{7.7}$$

As a second approach, the local penalty parameter can be defined as:

$$\gamma^L = 10^{\epsilon}\gamma^G, \tag{7.8}$$

and scaling factor ϵ is bounded by

$$\epsilon^p = \begin{cases} 0 & \text{if } \phi_1\phi_2 \geq 0 \\ \left|\frac{\phi_{\phi\in p}}{\phi_1-\phi_2}\right| & \text{if } \phi_1\phi_2 < 0 \end{cases}, \tag{7.9}$$

where ϕ_1 and ϕ_2 are the level set values of the nodes for a particular element edge, $\phi_{\phi\in p}$ is the node whose level set value matches phase p, and γ^G is the global penalization value. This localized scaling places a stronger penalty on intersection configurations where the physical volume fraction occupying the element is small. For edges that are not intersected, but are a part of an intersected element, the scaling factor is set to $\epsilon = 0$. The global penalization term is often scaled with the element side length, i.e. $\gamma^G = ch$, where $0 < c < 1$. In the context of large sliding and finite strain contact problems, performance studies related to ghost penalization are provided in Appendix B.2.

7.3 Dynamic Relaxation

The discretized model yields a non-linear system of equations, which is solved in a quasi-static manner using a Newton-Raphson iterative procedure. Convergence difficulties often arise in Newton-Raphson based solvers when the solution approaches a strong material or geometric nonlinearity. To mitigate these convergence issues, we use dynamic relaxation. This method uses an artificial damping term which mitigates oscillations in the system response and increases the stability and convergence toward the steady state solution. The damping parameter is updated during the iterative solve based on convergence criteria, and vanishes as convergence is achieved. Dynamic relaxation has been successfully used for solving variety of nonlinear problems such as elasto-plasticity, wrinkling, large deflection analysis, simulation of atomic structures and materials [120, 85, 80].

For problems presented in Chapters 9 and 10, we adopt a Levenberg-Marquardt similar algorithm [72] for dynamic relaxation. Originally developed to solve non-linear least square problems,

the Levenberg-Marquardt algorithm has shown to be useful in density method topology optimization; specifically by reducing analysis instabilities caused by element distortion in large strain compliant mechanisms [48]. In this paper we follow a similar approach by modifying the Jacobian matrix as follows:

$$\tilde{\mathbf{J}} = \mathbf{J} + \tilde{\beta}\ \mathrm{diag}(\mathbf{J})\ , \tag{7.10}$$

where $\mathbf{J}$ is the original Jacobian of the system, $\tilde{\beta}$ is the damping parameter, and $\tilde{\mathbf{J}}$ is the modified Jacobian of the system, respectively. The basic algorithm and convergence criteria for computing the structural response using an adaptive dynamic relaxation method are presented in Algorithm 1.

Algorithm 1: A basic algorithm for computing the structural response using the adaptive dynamic relaxation method.

Input: damping parameter $\tilde{\beta}_{\text{int}}$

for $n \leftarrow 1$ **to maximum time iterations do**

  Restart damping parameter: $\tilde{\beta}^n = \tilde{\beta}_{\text{int}}$

  for $k \leftarrow 1$ **to maximum Newton's iteration do**

    for $m \leftarrow 1$ **to maximum dynamic relaxation iteration do**

      1) Compute new damping parameter for relaxation iteration

$$\tilde{\beta}^{n+1}_{(k+1)_m} = \begin{cases} 10\tilde{\beta}^n & \text{if} \quad \left|\mathbf{R}^{n+1}_{(k+1)_m}\right| > |\mathbf{R}^n_k| \\ \tilde{\beta}^n/10 & \text{if} \quad \left|\mathbf{R}^{n+1}_{(k+1)_m}\right| \leq |\mathbf{R}^n_k| \end{cases}$$

      2) Update the Jacobian matrix

$$\tilde{\mathbf{J}}^{n+1}_{(k+1)_m} = \mathbf{J}^{n+1}_{(k+1)_m} + \tilde{\beta}^{n+1}_{(k+1)_m}\ \mathrm{diag}(\mathbf{J}^{n+1}_{(k+1)_m})$$

      3) Solve for current relaxation iteration

$$\Delta\mathbf{u}^{n+1}_{(k+1)_m} = -(\tilde{\mathbf{J}}^{n+1}_{(k+1)_m})^{-1}\mathbf{R}^{n+1}_{(k+1)_m}$$
$$\hat{\mathbf{u}}^{n+1}_{(k+1)_m} = \mathbf{u}^n_k + \Delta\mathbf{u}^{n+1}_{(k+1)_m}$$

      4) Check the convergence of dynamic relaxation

      if $\left(\left|\mathbf{R}^{n+1}_{(k+1)_m}\right| < \left|\mathbf{R}^{n+1}_k\right|\right)$ **or** $\left(\left|\Delta\mathbf{u}^{n+1}_{(k+1)_m}\right| < \left|\Delta\mathbf{u}^{n+1}_k\right|\right)$ **then**

        accept current solution: $\mathbf{u}^{n+1}_{k+1} = \hat{\mathbf{u}}^{n+1}_{(k+1)_m}$

        go to next Newton's iteration: $k = k + 1$

        break

For each Newton step k, the physical response solver applies m dynamic relaxation iterations.

Damping parameter $\tilde{\beta}$ is either increased or decreased depending on whether or not the norm of the residual, $|\mathbf{R}|$, has reduced from the previous iteration. If the norm of the residual or the solution increment, $|\Delta\mathbf{u}|$, has decreased from the previous Newton iteration, the solution increment is accepted. However, if these convergence criteria are not met, the solution increment is rejected and dynamic relaxation continues to the next iteration. The reliable convergence behavior afforded by dynamic relaxation is offset by additional computational expense; for the numerical experiments presented, the computational time required for response prediction often doubled. In the context of large sliding and finite strain contact problems, performance studies related to dynamic relaxation are provided in Appendix B.2.2.

7.4 Solution Correction Scaling

For large sliding frictionless contact behavior, from the authors experience, stabilization of the physical response prediction is necessary primarily in situations of neutral instability and snap-through behavior. In these scenarios, convergence behavior can be erratic. Considering the contact search algorithm is performed with each Newton increment solution, this quickly can lead to divergence if the displacement field produces incorrect contact STS pairs. As an alternative approach to dynamic relaxation, this method of stabilization scales back the iterative displacement field to a specified maximal value. The procedure for solution correction scaling is presented in Algorithm 2.

As a minor deviation from the standard Newton-Raphson iterative procedure, this method scales back the solution adjustment $\Delta\mathbf{u}^{n+1}_{(k+1)}$ if the largest value exceeds a specified limit. For the large sliding contact problems considered here, a specified maximum value in the range of $h/2 \leq \delta_{max} \leq h$, where h is the element side length, proves adequate. In the context of large sliding and finite strain contact problems, performance studies related to solution correction scaling are provided in Appendix B.2.2.

Algorithm 2: A basic algorithm for computing the structural response using the solution correction scaling method.

Input: maximum allowable solution adjustment δ_{max}

for $n \leftarrow 1$ **to maximum time iterations do**

  for $k \leftarrow 1$ **to maximum Newton's iteration do**

    1) Solve for current Newton iteration:
    $\Delta \mathbf{u}_{(k+1)}^{n+1} = -(\mathbf{J}_{(k+1)}^{n+1})^{-1} \mathbf{R}_{(k+1)}^{n+1}$

    2) Scale back solution increment if necessary:

    if $\max |\Delta \mathbf{u}_{(k+1)}^{n+1}| > \delta_{max}$

    then
    $\Delta \mathbf{u}_{(k+1)}^{n+1} = \delta_{max} \Delta \mathbf{u}_{(k+1)}^{n+1} / \max |\Delta \mathbf{u}_{(k+1)}^{n+1}|$

    3) Accept solution increment:
    $\hat{\mathbf{u}}_{(k+1)}^{n+1} = \mathbf{u}_{k}^{n} + \Delta \mathbf{u}_{(k+1)}^{n+1}$
    go to next Newton's iteration: $k = k + 1$
    break

Chapter 8

Small Strain Frictionless Interface Studies

This chapter investigates topology optimization of infinitesimal strain theory, small sliding, frictionless bilateral contact problems in two dimensions. The material presented in this chapter are condensed from the resulting publication[59].

8.1 Introduction

The response of structures composed of multiple components and the behavior of heterogeneous materials with multiple constituents are often dominated by mechanical interface phenomena, such as contact, friction, and adhesion. The interface geometry typically has a strong influence on these phenomena and needs to be designed carefully, considering in addition external loading conditions and the material properties of the individual components and constituents. For example, the geometry of anchors differs significantly, depending on the properties of the host material. This chapter introduces a topology optimization method for problems involving sliding contact and separation. While adhesion and friction are ignored here, the proposed computational framework allows for the inclusion of other interface phenomena. Optimization of problems involving material cohesion is the topic of Chapter 9.

Irrespective of whether other forms of kinematic or material nonlinearities are considered, modeling contact leads to a nonlinear mechanical problem. Contact forces only act to prevent the interpenetration of bodies but vanish if the bodies separate. Furthermore, the geometry of the interfaces needs to be clearly defined, as the contact forces depend on both the location of

the boundary and the surface normal. Due to these complexities, to date contact has only been considered in very few topology optimization studies, following either a density or a level set approach.

Myślińsky pioneered level set methods for shape and topology optimization of unilateral contact problems where one of the bodies is rigid; see for example [74], [75], [77] and [76]. The finite element method in combination with an Ersatz material approach is used to model contact problems with and without friction. The contact interface location is defined by a Dirac function and the contact conditions are enforced via Lagrange multipliers. Topological derivatives are used to insert additional holes. The level set field is updated via the solution of the Hamilton-Jacobi equation, a reaction-diffusion equation, or a phase field approach. The method is illustrated with numerical examples where the shape of the contact interface and the internal layout are optimized. This corresponds to a combination of options (b) and (d) in Figure 2.3 where one of the bodies is rigid and does not change its topology.

In this chapter we build upon the work of Myśliński and expand it onto bi-lateral contact problems where all bodies in contact deform elastically. The proposed method allows altering the shape and topology of the contact interface. We use an explicit level set method to describe the interface geometry between two distinct material phases. In contrast to advancing the level set field by the Hamilton-Jacobi equations, explicit LSMs treat the parameters of the discretized level set function as explicit functions of the optimization variables [104]. This allows solving the resulting optimization problem by standard nonlinear programming algorithms.

The remainder of this chapter is organized as follows: in Section 8.2, we outline the formulation of the optimization problems considered in this study. In Section 8.3, the mechanical model of the contact problem is described. In Section 8.4, we study the main characteristics of the proposed LSM-XFEM method with numerical examples. Insight gained from the numerical studies and areas for future research are summarized in Section 8.4.4.

8.2 Optimization Problem

In this chapter we consider the interactions between two solid phases, A and B, with sliding, separable contact at the phase boundaries. A representative configuration of the problems discussed in this chapter is shown in Figure 8.1. The design domain Ω_D is composed by two non-overlapping subdomains, Ω^A and Ω^B, such that $\Omega_D = \Omega^A \cup \Omega^B$ and $\Gamma_C = \Omega^A \cap \Omega^B$ is the contact interface. The displacements in phase A are prescribed at the boundary Γ_U^A while the second phase is subjected to either a prescribed force or displacement controlled loading at the boundary $\Gamma_{U,N}^B$. Prescribed displacements are denoted by the subscript U and prescribed forces by the subscript N.

In the examples presented in Section 8.4 we seek to minimize either one of two objectives: for force controlled loading we seek to minimize the displacement at Γ_N^B, for displacement controlled loading we maximize the reaction load at Γ_U^B.

To discourage the emergence of small geometric features and oscillatory shapes, we introduce perimeter penalty term into the formulation of the objective function. The perimeter measures the interface between domains Ω_A and Ω_B and is computed as follows:

$$P = \int_{\Gamma_c} \mathrm{d}\Gamma \tag{8.1}$$

While a perimeter penalty does not allow explicitly controlling the local shape and the feature size, it has been reported effective in regularizing structural optimization problems [104]. In addition, we constrain the ratio of volumes occupied by either solid, V^A & V^B, to exclude trivial solutions. While the proposed optimization framework allows considering other objectives and constraints, such as strain energy and displacement and stress measures, we found that the formulations of the optimization problem used here are well suited to illustrate the influence of the interface condition on the optimized design.

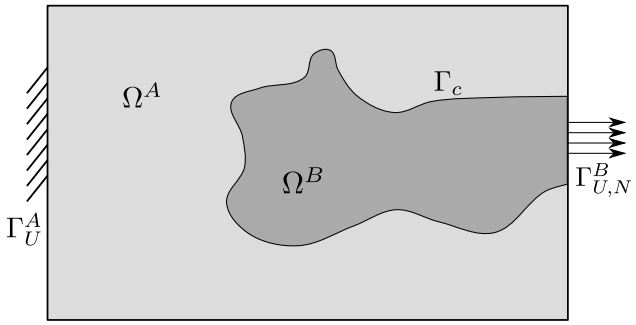

Figure 8.1: Generalized optimization problem.

The optimization problem is defined by the following nonlinear program:

$$\begin{aligned} &\min \big(c_u \; z(\mathbf{s},\mathbf{u}) + c_p \; P(\mathbf{s})\big), \\ &\text{s.t. } V^B(\mathbf{s}) - c_v \; V^A(\mathbf{s}) \leq 0 \\ &\mathbf{s} \in \mathbf{S} = \left\{\mathbb{R}^{N_s} | s_{min} \leq s_i \leq s_{max}, \; i = 1....N_s\right\} \; , \end{aligned} \tag{8.2}$$

where z denotes the contribution of the mechanical response to the objective, c_u is the associated weighting factor, c_p is the weight of the perimeter penalty, and c_v controls the desired volume ratio between the two solids. The number of optimization variables is N_s; the lower and upper bounds on the optimization variables are denoted by s_{min} and s_{max}, respectively.

The dependency of the objective function and constraints on the optimization variables, s_i, are defined by the framework described in Section 2.2. Note that the objective also depends on the structural response: $z(\mathbf{s},\mathbf{u})$, where $\mathbf{u}$ denotes the vector of discretized state variables that are considered dependent variables of $\mathbf{s}$. The discretized state equations are described in Section 8.3. The optimization problem is solved by a nonlinear programming (NLP) method, and the design sensitivities are calculated by the adjoint method.

8.3 Physical Model

We consider two bodies in contact as shown in Figure 8.2. The bodies occupy the volume Ω^A and Ω^B, respectively. Static equilibrium is described by the following state equations:

$$\sigma^p_{ij,j} + f^p_i = \mathbf{0} \text{ in } \Omega^p \; , \tag{8.3}$$

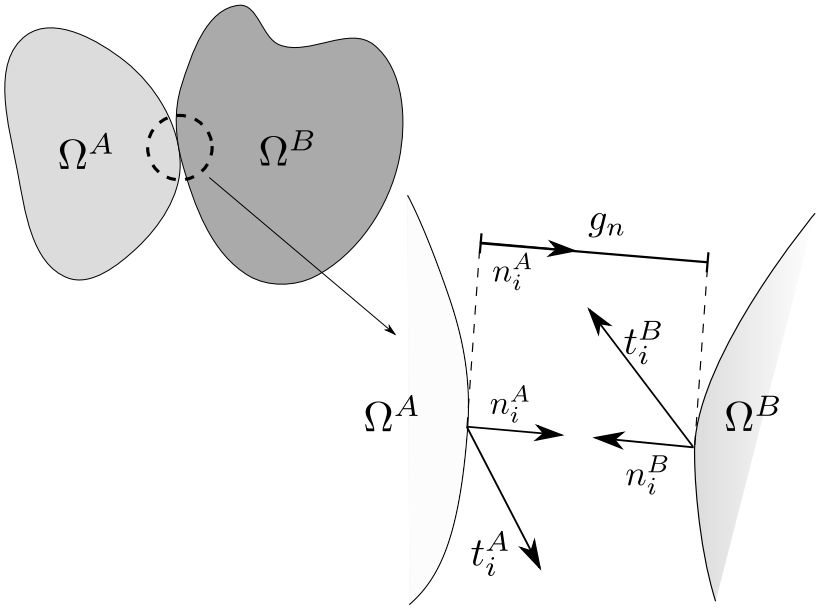

Figure 8.2: Continuum bodies in contact.

$$u_i^p = U_i^p \text{ on } \Gamma_U^p \ , \tag{8.4}$$

$$\sigma_{ij,j}^p n_j^p = F_i^p \text{ on } \Gamma_N^p \ , \tag{8.5}$$

where σ_{ij}^p denotes the stress tensor and f_i^p are the body forces in phase $p = A, B$. The prescribed displacements at Γ_U^p and the external surface loads acting on Γ_N^p are denoted by U_i^p and F_i^p, respectively. The outward pointing normal on phase p is n_j^p. We assume a linear elastic material behavior and a linear kinematic relationship:

$$\sigma_{ij}^p = C_{ijkl}^p \, \varepsilon_{kl}^p \tag{8.6}$$

$$\varepsilon_{ij}^p(u_i^p) = \frac{1}{2}\left(u_{i,j}^p + u_{j,i}^p\right), \tag{8.7}$$

where C_{ijkl}^p and ε_{kl}^p are the elastic and strain tensors in phase p.

At the phase boundaries, Γ_C, the non-penetration condition is described as follows:

$$g_n \ \lambda_n^p = 0, \ g_n \geq 0, \ \lambda_n^p \leq 0, \ p = A, B \ , \tag{8.8}$$

with

$$g_n = n_i^A \ \left(x_i^B + u_i^B\right) - n_i^A \ \left(x_i^A + u_i^A\right) \ , \tag{8.9}$$

$$\lambda_n^p = \sigma_{ij}^p \ n_i^p \ n_j^p, \ p = A, B \ , \tag{8.10}$$

where the g_n is the gap between the bodies and λ_n^p the surface traction in normal direction. To prevent interpenetration, the gap needs to be positive. The surface traction vanishes if the bodies are separated and is negative when the bodies are in contact. Thus, λ_n^p serves as Lagrange multiplier of the contact condition. As $\lambda_n^A = \lambda_n^B$, we drop the superscript for the phase in the following discussion. Restricting our study to two-phase problems, the initial gap, $n_i^A \ x_i^A + n^B \ x_i^B$, vanishes.

The XFEM discretization of the contact problem is based on the following stabilized weak form of the governing equations:

$$\sum_{p=A,B} \int_{\Omega^p} \varepsilon_{ij}(v_i^p) \ \sigma_{ij}^p \ d\Omega - \sum_{p=A,B} \int_{\Omega^p} v_i^p \ f_i^p \ d\Omega \\ - \sum_{p=A,B} \int_{\Gamma_N^p} v_i^p \ F_i^p \ d\Gamma - \int_{\Gamma_C} [v_i] \ \lambda_n \ n_i^A \ d\Gamma = 0 \ , \tag{8.11}$$

where v_i an admissible test function and $[v_i] = v_i^A - v_i^B$ denotes a jump across the contact interface. Following [113], if the contact conditions are active, i.e. $g_n \leq 0$, the Lagrange multiplier λ_n is governed by the following stabilized formulation of the contact conditions:

$$\int_{\Gamma_C} \mu \ \left(\lambda_n - \tilde{\lambda}_n - \gamma \ g_n\right) \ d\Gamma = 0 \ , \tag{8.12}$$

with

$$\tilde{\lambda}_n = \left(\kappa^A \ \sigma_{ij}^A + \kappa^B \ \sigma_{ij}^B\right) \ n_i^A \ n_j^A \ , \tag{8.13}$$

where μ is a test function for the non-penetration condition, $\tilde{\lambda}_n$ is a weighted average of the surface traction in normal direction and κ^p are weighting factors such that $\kappa^A + \kappa^B = 1$. The larger the penalty factor γ the better the non-penetration condition is satisfied, but the conditioning of the problem deteriorates for large γ values. The formulations for κ^p and γ used in this work are given below. If the interface separates and the contact condition is not active, i.e. $g_n > 0$, λ_n vanishes.

An active set strategy is used to handle the non-penetration condition when solving for the weak form of the equilibrium equations (B.11).

8.4 Numerical Examples

This section first begins by verifying the accuracy of the frictionless contact model in the XFEM to previously published results. Next, we illustrate the main characteristics of the proposed optimization approach and compare designs optimized for various interface models, excluding tangential behavior such as cohesion and friction. In the first example, we restrict the geometry to simple primitives and optimize the location of the primitives. This leads to tractable optimization problem with a small number of optimization variables. In the second example, we optimize the interface geometry of an anchor without restricting the geometry variations.

For all examples, we assume plain strain and a quasi-static response. The interface model describes sliding contact with separation, unless specified otherwise. Each example is discretized by bi-linear elements using the XFEM scheme outlined in Section 5. The nonlinear contact problems are solved by Newton's method using an active set strategy for the contact conditions. A drop of the residual of 10^{-9} relative to the initial residual is required. The external loads are applied in a single step. A direct solver is applied to the linearized sub-problems.

The parameter optimization problems are solved by the Globally Convergent Method of Moving Asymptotes (GCMMA) of [96]. The parameters for the initial, lower, and upper asymptote adaptation are set to 0.5, 0.7, and 1.2, respectively. The relative step size, Δs, is given with each example. The design sensitivities are computed with the adjoint method. The reader is referred to [7], [54] and [53] for an in depth discussion of sensitivity analysis for contact problems. In this work, the partial derivatives of the state equations and objective function with respect to the state variables are evaluated using analytically differentiated formulations. The partial derivatives of the objective, constraints, and element residuals with respect to the optimization variables are calculated by a finite difference scheme.

8.4.1 Verification of Small Strain Frictionless Contact

Consider two rectangular materials of the same properties under compression as seen in Figure 8.3. The square structural domain of side length $L = 1m$ is composed of two non-overlapping

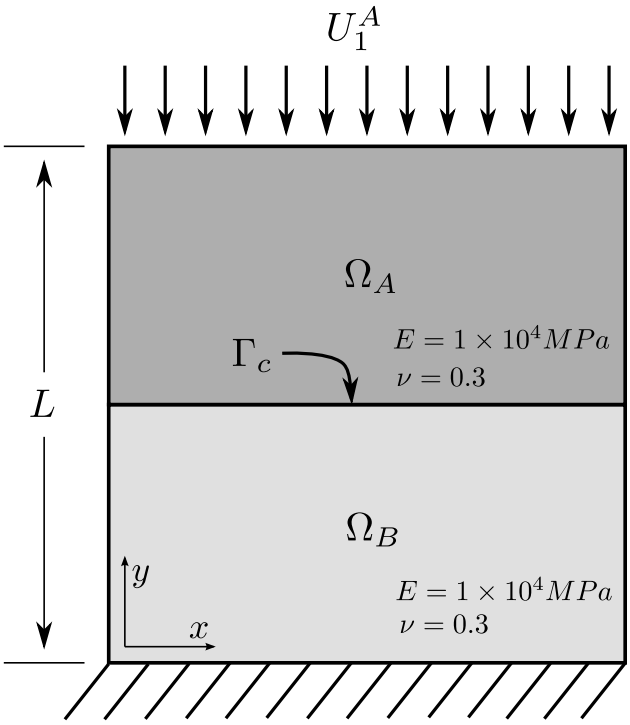

Figure 8.3: Small strain, frictionless contact benchmark setup.

subdomains Ω_A and Ω_B such that $\Gamma_c = \Omega_A \cap \Omega_B$ is the contact interface. Subdomains Ω_A and Ω_B are linear elastic hookean materials of the same properties, where frictionless contact is imposed at Γ_c via a stabilized Lagrange method. Displacements at the top edge of Ω_A are prescribed as $U_x^A = 0$ and $U_y^A = -0.1$, whereas the bottom edge of Ω_B is fixed. This example is chosen to demonstrate the convergence behavior of surface pressure and penetration error with mesh refinement, as well as to provide a direct comparison to previous publications.

To examine the convergence behavior of the mechanical model, the problem was run for four different mesh sizes: Mesh 1 consists of 5×5 elements, Mesh 2 contains 11×11 elements, Mesh 3 has 21×21 elements, and Mesh 4 consists of 41×41 elements. Surface pressures and normal penetration errors were extracted at the interface for all models. Figure 8.4 demonstrates the surface pressure

convergence with mesh refinement. Additionally, Figure 8.5 illustrates the normalized penetration

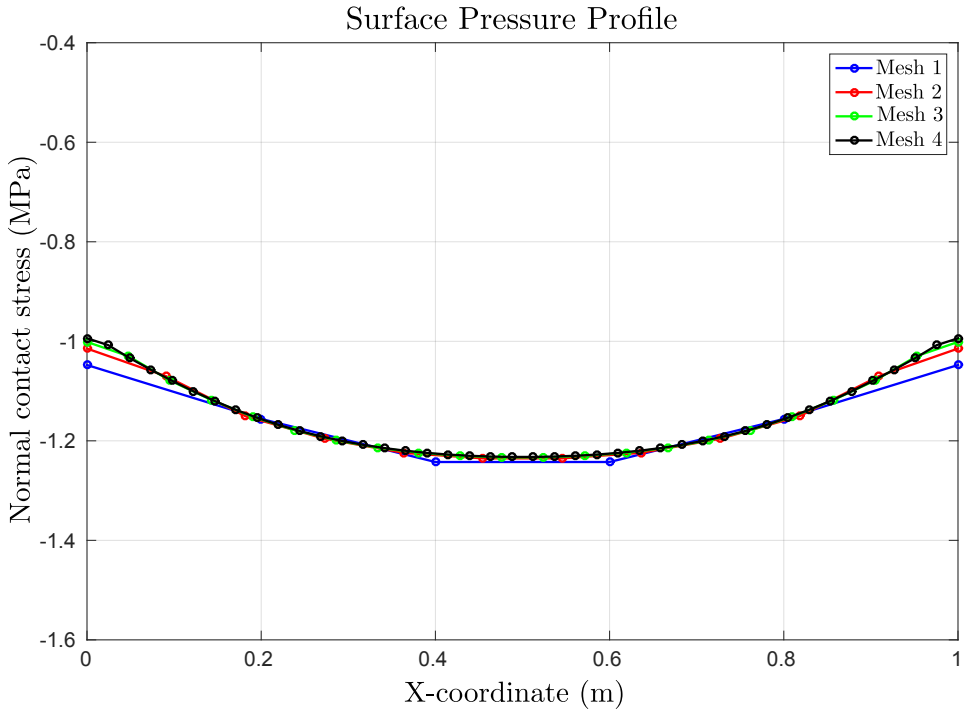

Figure 8.4: Surface pressure convergence with Mesh refinement. Mesh 1: 5×5, Mesh 2: 11×11, Mesh 3: 21×21, Mesh 4: 41×41,.

error as the mesh is refined. Penetration error is the measure of relative displacement between both surfaces in the direction of domain Ω_B interface undeformed normal. It is normalized by the domain length L. Finally, the integrated L2 error in the normalized penetration error is plotted in Figure 8.6 as a function of degrees of freedom used in each mesh.

A similar benchmark study was performed by [62] and [44] using the extended finite element method. For surface pressure stabilization the authors used an augmented Lagrange method enforced at intersection boundaries of element. To further restrict the interpolation space of the Lagrange multiplier, the authors used a Polynomial Pressure Projection technique (PPP) and a Vital Edges method respectively. The current work differs by allowing the Lagrange multiplier to be an element-wise constant variable, which is condensed out at the local level. Figures 8.7-8.8 compare the

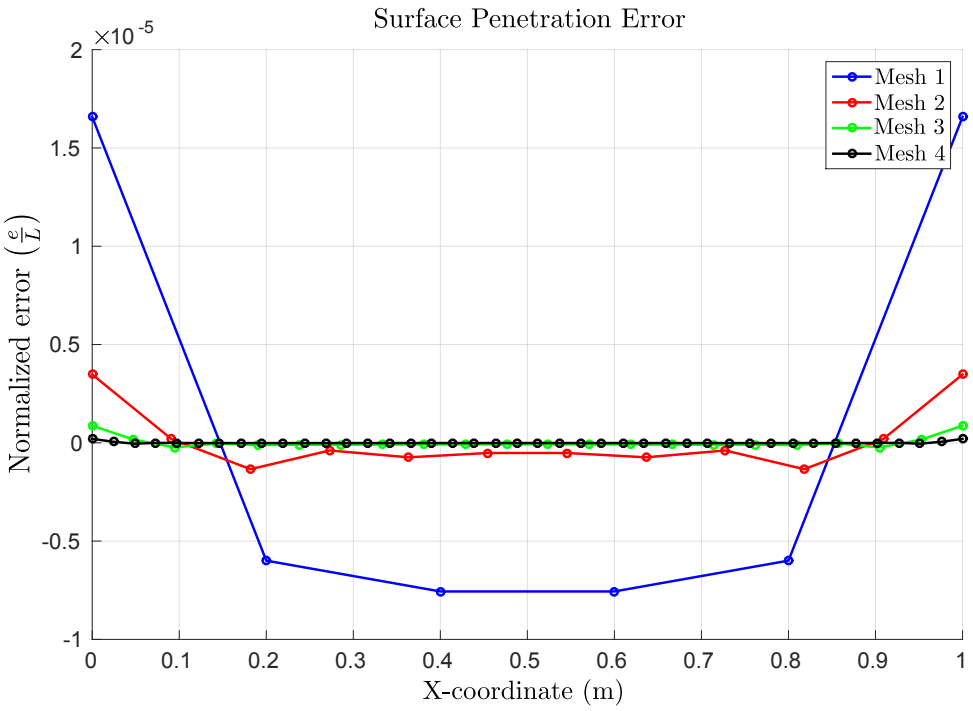

Figure 8.5: Penetration error convergence with mesh refinement. Mesh 1: 5×5, Mesh 2: 11×11, Mesh 3: 21×21, Mesh 4: 41×41,.

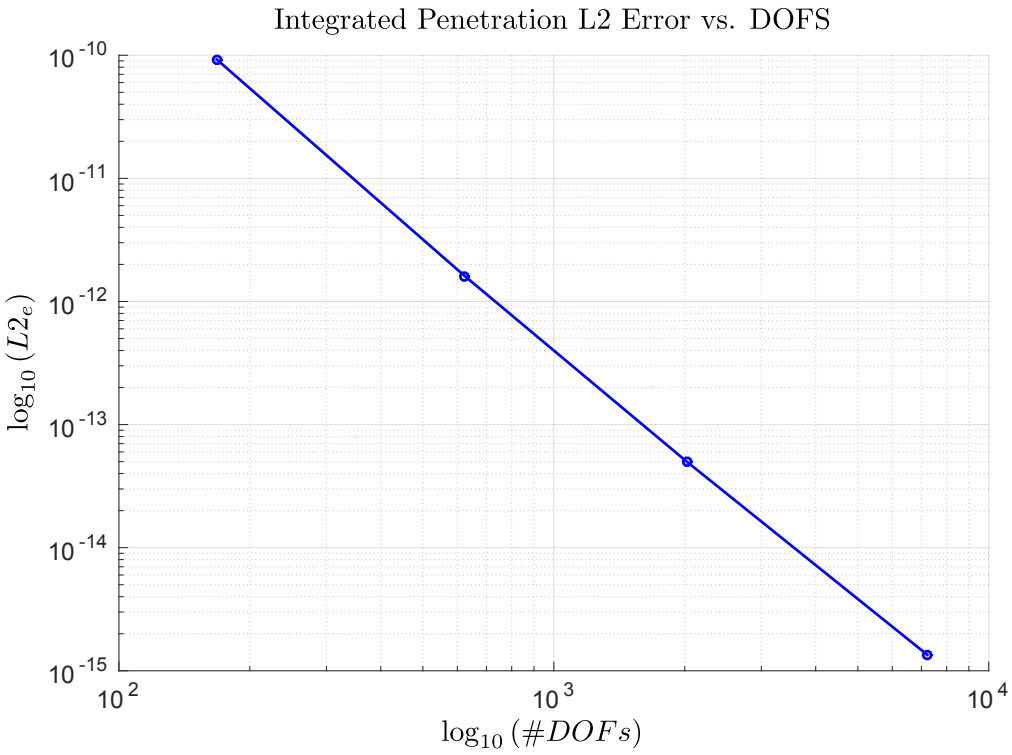

Figure 8.6: Integrated L2 error in surface penetration as a function of degrees of freedom used.

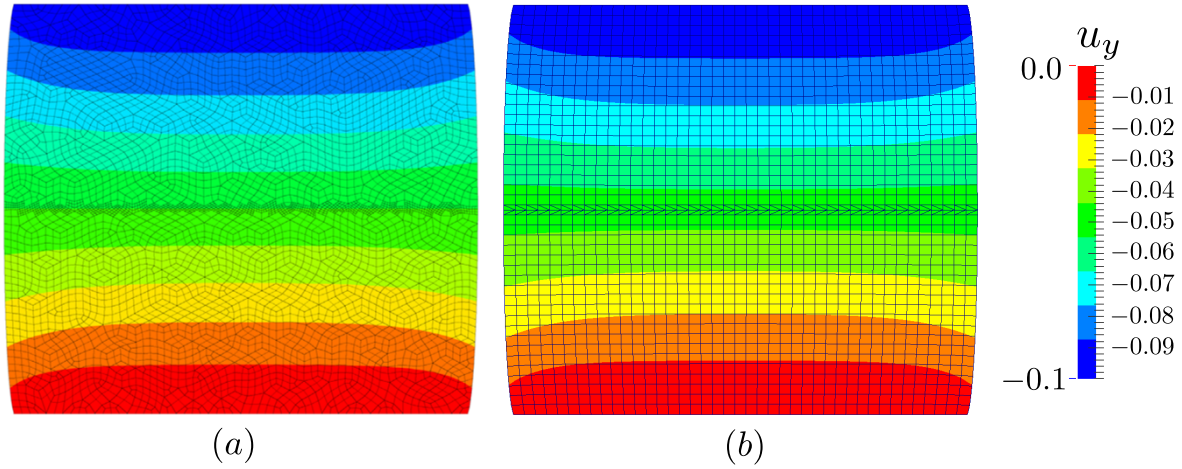

Figure 8.7: Contour plot of Y displacements for (a) [44] and (b) current work.

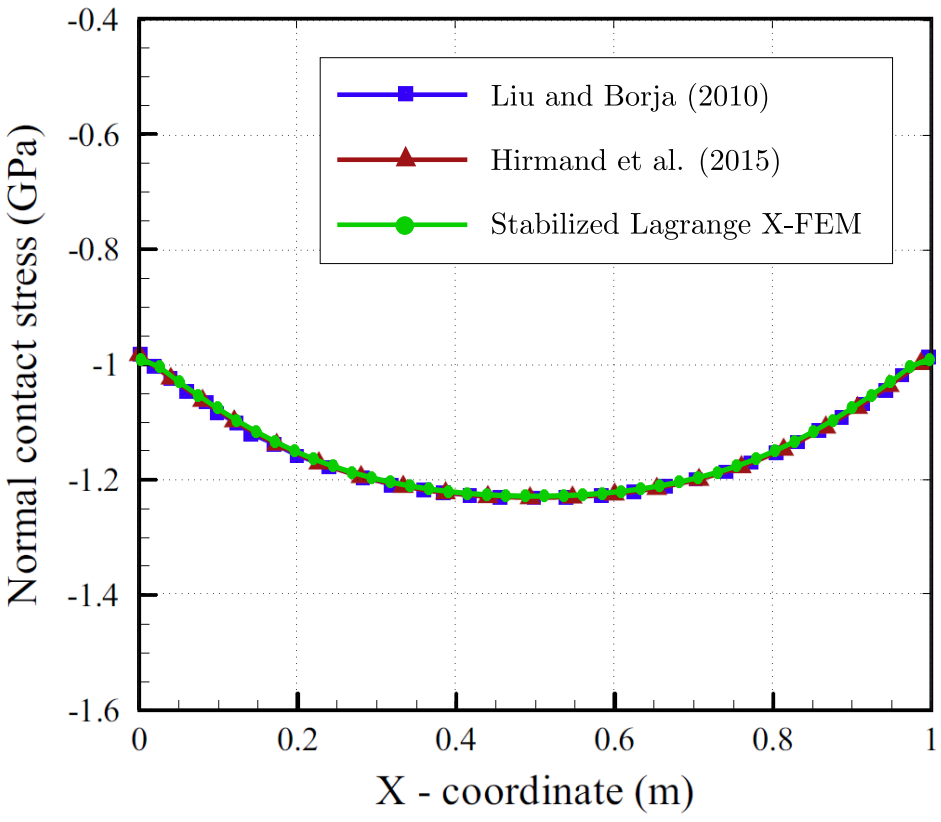

Figure 8.8: Pressure along the interface for [62], [44], and current work.

8.4.2 Bolted Plate

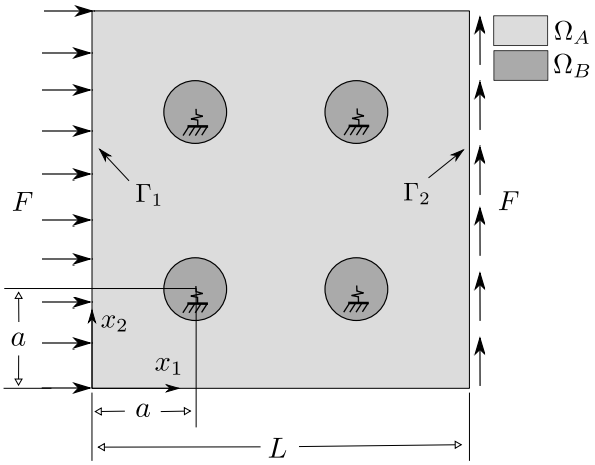

Figure 8.9: Bolted plate problem.

Plate Side Length	$L = 1.0$ m
Bolt Location	$a = 1/4$ m
Plate Thickness	$t = 1/15$ m
Bolt Radius	$r = 0.065$ m
Distributed Load	$F^A = 0.1$ N
Young's Modulus	$E^A = E^B = 10^4$ N/m^2
Poisson Ratio	$\nu^A = \nu^B = 0.3$
Spring Stiffness	$K = 10^6$ N/m^2
Response Weight	$c_u = 1.0$
Perimeter Weight	$c_p = 0$
GCMMA Step Size	$\Delta s = 0.05$

Table 8.1: Bolted plate parameters

A square plate of thickness t is fastened to a rigid surface by four bolts; see Figure 8.9. Phase A represents the plate and phase B the bolts. The plate is subject to a distributed horizontal force along the left edge and a distributed vertical force of the same magnitude along the right edge. First we consider sliding contact and separation at the bolt-plate interface. The result for this interface model is then compared against the solution assuming perfect bonding. The bolts are connected to the rigid surface via distributed springs. The latter allows for an elastic deformation of the bolts. The bolts and plate are made of the same material.

The optimization problem is to find the location of the bolts such that a weighted average of the displacements in the direction of the external loads is minimized:

$$z = \int_{\Gamma_1} 2\ u_1 \mathrm{d}\Gamma + \int_{\Gamma_2} u_2 \mathrm{d}\Gamma\ . \tag{8.14}$$

For this example, the volume ratio of the material phases and the interface perimeter are constant due to problem setup. The penalty for the perimeter, c_p, in (10.1) is set to zero and the constraint on volume ratio is omitted, i.e. $c_v = \infty$.

The spatial arrangement of the bolts are described by the following level set function:

$$\phi(\mathbf{x}) = \max_i \left(R_b - |\mathbf{x} - \mathbf{x}_i^b| \right) \quad i = 1, 2, 3, 4\ , \tag{8.15}$$

where R_b is the bolt radius and $\mathbf{x}_i^b$ the position of the bolt center. Varying $\mathbf{x}_i^b$ leads to a total of 8 independent optimization variables. The upper and lower bounds on the optimization variables are chosen such that the bolts cannot penetrate the outer edges of the plate. The domain is discretized with a uniform mesh of 60 elements along each edge. The problem parameters are given in Table 8.1.

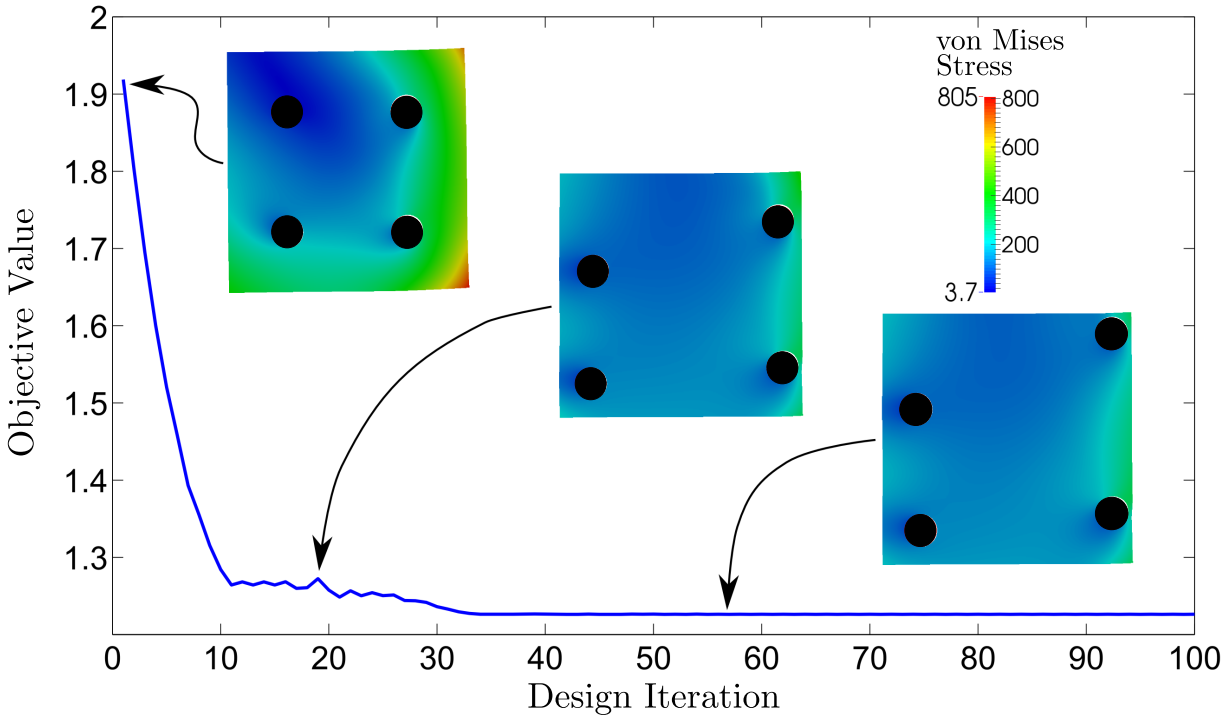

Figure 8.10: Evolution of objective in design process with select design iterations visualized.

The optimization process is started from the initial configuration shown in Figure 8.9. The evolution of the objective along with snapshots of the bolt configuration is depicted in Figure 8.10. The contour plot shows the von Mises stress in the plate. To better visualize the location of the bolts, they are colored black. As one can expect, the bolts spread outwards to resist the deformations near the applied loads.

The influence of the contact interface model can be observed when we compare to a design optimized with an interface model that assumes perfect bonding; see Figure 8.11. The formulation of the perfect bond model is described in detail in [66]. The design optimized with the contact model exhibits a larger degree of asymmetry to reduce compliance due to sliding and separation

Analyzed with	Optimized for	
	Separable	Fixed
Separable	1.2263	1.3656
Fixed	0.8998	0.8227

Table 8.2: Objective values of optimized designs when analyzed with different interface conditions.

at the interface. We quantify the dependency of the optimized design on the interface condition by cross-comparing the optimized designs. Table 8.2 provides objective values for the optimized geometries analyzed with the two interface models. Assuming sliding contact at the bolt-plate interface, the geometry optimized for a sliding contact yields an 11% reduction of compliance when compared to the geometry optimized for a perfectly bonded interface.

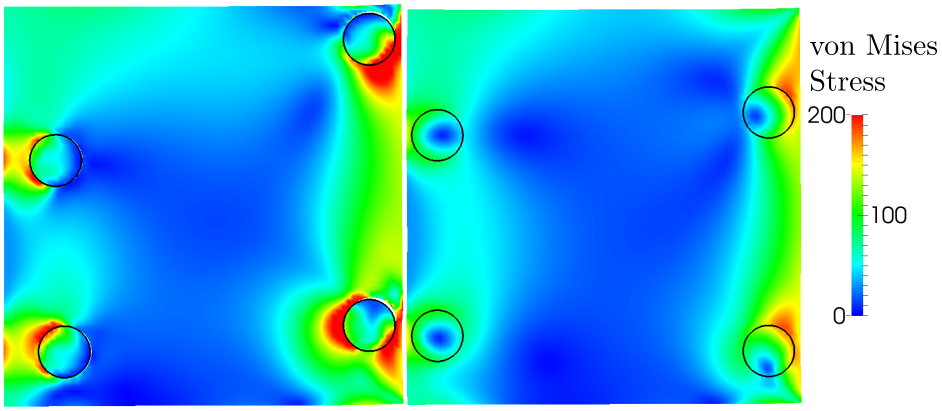

Figure 8.11: Contour plot of von Mises stress for optimized designs of (a) frictionless, separable and (b) bonded interface conditions.

8.4.3 Material Anchor

In this example we seek to determine the optimal geometry of an anchor encased within host material such that the holding force of the anchor is maximum. The problem setup along with the initial seed of the anchor material is shown in Figure 8.12.

Phase A represents the host and phase B the anchor material. The anchor is fixed along the boundary Γ_1 which is not part of the design domain and where the material is prescribed to phase B. The host material is pulled to the left by prescribing the displacements in x_1 direction at Γ_2,

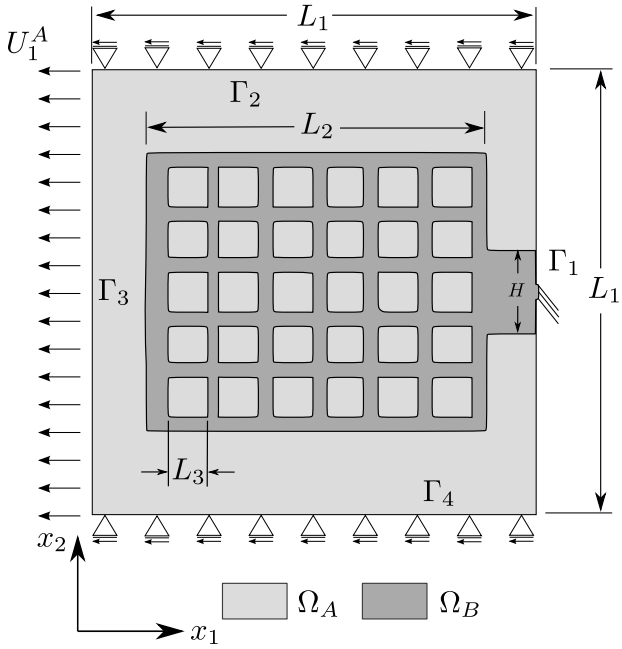

Figure 8.12: Material anchor design problem.

Host Side Length	$L_1 = 1.0$ m
Anchor Side Length	$L_2 = 0.79$ m
Cuboid Side Length	$L_3 = 0.0833$ m
Domain Thickness	$t = 1/15$ m
Applied Displacement on Γ_2	$U_1^A = -0.007$ m
Phase A Young's Modulus	$E^A = 10^4$ N/m^2
Phase B Young's Modulus	$E^B = 10^4$ N/m^2
Poisson Ratio	$\nu^A = \nu^B = 0.3$
Spring Stiffness	$K = 2 \times 10^3$ N/m^2
Response Weight	$c_u = 1/E^B$
Perimeter Weight	$c_p = 1/4$
GCMMA Step Size	$\Delta s = 0.008$

Table 8.3: Nominal parameters of anchor design problem.

Γ_3, and Γ_4, i.e. $\Gamma_U^A = \Gamma_2 \cap \Gamma_3 \cap \Gamma_4$. Note that the boundary Γ_U^A is constrained to zero in the x_2-direction, and is not part of the design domain. The material at Γ_U^A is set to phase A. Exploiting the symmetry of the problem, only one half of the problem is analyzed.

The holding force of the anchor in x_1-direction is measured by integrating the normal stress σ_{11} along Γ_1. The response dependent contribution, z, to the objective function in (10.1) is defined as follows:

$$z = -\int_{\Gamma_1} \sigma_{11} d\Gamma \ . \tag{8.16}$$

The optimization problem is regularized by applying a perimeter penalty, considering different values for the weight c_p. In the case of sliding and separable contact interface conditions, additional constraints are not necessary for this example. Only when studying the influence of interface models on the optimized design, a volume constraint is imposed to avoid trivial solutions.

The LSF is discretized by the same mesh used for the structural analysis. The nodal level set values are defined as functions of the optimization parameters using the linear filter described in Section 2.4. Discretizing half of the design domain with 120×60 mesh, the smoothing radius is

a factor of 4.5 times the element size. The lower and upper bounds for the optimization variables are set to $s_{min} = -h$ and $s_{max} = h$ where h is the element side length. The LSF is initialized by an 6×5 array of cuboids within a square inclusion as shown in Figure 8.12. Note that additional anchor material is placed to connect the patterned arrangement of material to Γ_1. This ensures that the boundary conditions along Γ_1 and displacement controlled loading along Γ_2 are applied to the anchor and host materials, respectively.

Structural inclusions that are only constrained by sliding contact may be able to rotate rigidly which cause an ill-conditioned system. To mitigate this issue, the host material is grounded elastically by a distributed system of weak linear springs with stiffness K.

In the following numerical experiments we first illustrate the convergence behavior for the nominal problem parameters, which are summarized in Table 8.3. We then consider different values of the weighting factor c_p for the perimeter term in (10.1) to illustrate its influence on the optimized design. The influence of the material properties of anchor and host material are studied by varying the ratio E^A/E^B. Finally, the optimized designs are compared for different interface conditions.

8.4.3.1 Nominal Problem Parameters

The optimization problem is solved for a response weight of $c_u = 10^{-4}$ and a perimeter penalty weight of $c_p = 1/4$. The volume constraint is omitted, i.e. $c_v = \infty$. The stiffness ratio between the anchor and host material is $E^A/E^B = 1$.

Figure 8.13 shows the evolution of the objective function and snapshots of material layout in the course of the optimization process. The snapshots show contour plots of the von Mises stress in the host and anchor; the interface between both materials is outlined in black. The cuboids of the initial LSF quickly merge to form a single anchor domain. The contact interface evolves into a barb-type shape maximizing the contact force. The holding force and perimeter of the initial and final design are given in Table 8.4.

While the geometry is visually converged, the objective oscillates slightly. The behavior is due to the stress approximation in the XFEM. In the presence of small intersections, the interface

	Holding Force (N)	Perimeter (m)
Initial	0.9979	2.7987
Final	1.0766	3.0336

Table 8.4: Holding force and perimeter of initial and final design for nominal configuration.

stress is very sensitive to small variation in the interface geometry; see also Section 7.2. Alternative formulation of the interface conditions that mitigate this issue will be explored in future studies.

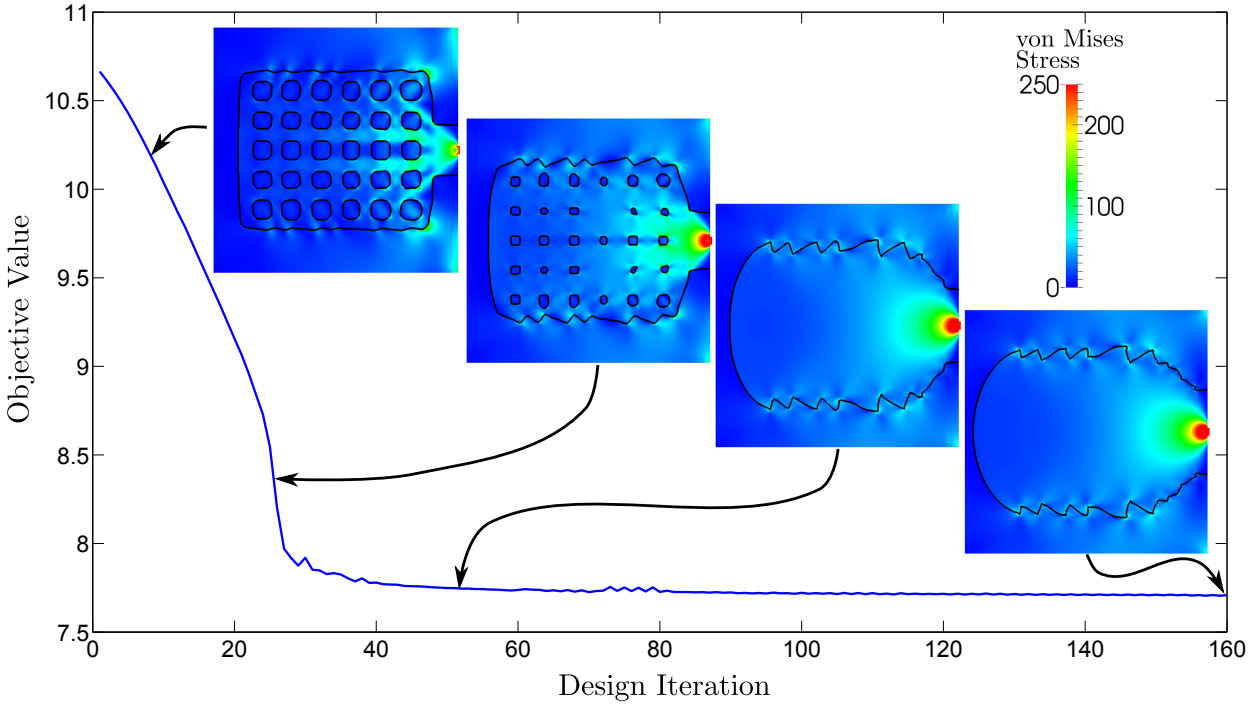

Figure 8.13: Evolution of objective function with select iterations visualized.

8.4.3.2 Influence of Perimeter Penalty

To investigate the influence of the perimeter penalty, the problem is solved for different values of the perimeter penalty weight, c_p. All other model parameters are set to the ones of the nominal configuration. The resulting geometries are shown in Figure 8.14 and the performance of the optimized designs is given in Table 8.5.

As the perimeter penalty is increased, the size of barb-type features are reduced and the maximum holding force of the anchor decreases, see Figure 8.15. Note that the maximum holding

Perimeter Weight c_p	Holding Force (N)	Perimeter (m)
3/4	1.0567	2.6039
1/2	1.0669	2.7918
1/4	1.0766	3.0336
1/5	1.0774	3.0458
1/10	1.0813	3.2608
0	1.0830	3.9574

Table 8.5: Holding force and perimeter of optimized designs for different perimeter penalty weights, c_p.

forces varies by less than 6% for the range of perimeter penalty weights considered here. This result suggests that the impact of the perimeter penalty on the mechanical response is low. However, it might be more pronounced for other problems.

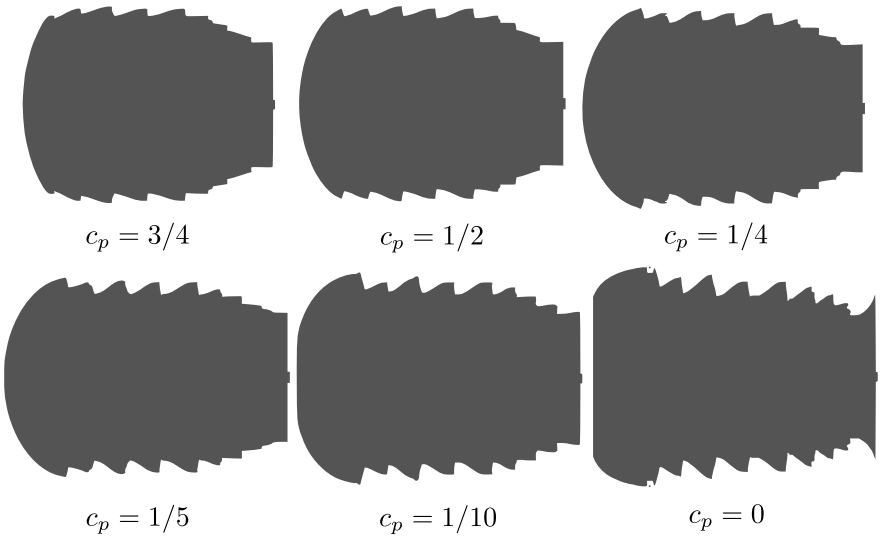

Figure 8.14: Optimized designs for varying perimeter penalty weights.

8.4.3.3 Influence of Material Stiffness

In the nominal configuration, we assumed the same material for both phases. To explore the dependency of the optimized design on the material properties of the individual phases, the optimization problem is solved for two additional stiffness ratios. We consider the case where the host material is softer than the anchor by assuming $E^A = 1/4\ E^B$ where E^B is the nominal value,

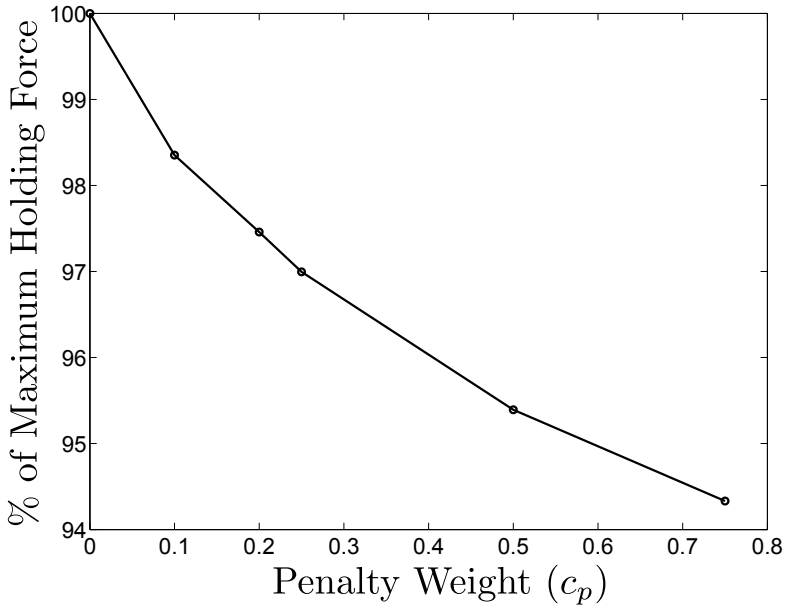

Figure 8.15: Effect of perimeter penalty on relative holding force of optimized designs; the reference value is the holding force for $c_p = 0.0$.

and the case of a soft anchor with $E^B = 1/16\ E^A$ where E^A is the nominal value. In the latter case, the weight of the response contribution to the objective is increased to $c_u = 1/E^B = 16/E^A$ in order to compensate for an expected smaller holding force. All other model parameters are set to the ones of the nominal configuration.

The optimized designs are shown in Figure 8.16 and their performance is reported in Table 8.6. Assuming sliding contact and separation, a stiff anchor embedded in a softer matrix material exhibits a tapering profile with barbs or tines to maximize resistance to a pull-out loading. For soft anchors embedded in a stiff host material, the formation of thin features and barbs is less pronounced, but a centralized mass and a thin neck provide an increased resistance to separation.

To quantify the effectiveness of each design, the anchor design optimized for the soft casing is analyzed assuming the stiff casing and vice versa. Table 8.7 shows the holding forces achieved by the optimized designs considering different material stiffness ratios in the analysis. The geometry optimized for a particular stiffness ratio yields an 9% to 22% increase in holding force when compared to geometry optimized with the other stiffness ratio. These results illustrate the importance

	Holding Force (N)	Perimeter (m)
soft casing	0.9348	3.4340
soft anchor	0.0929	2.9527

Table 8.6: Holding force and perimeter for soft and stiff casing configurations.

of accounting for the material properties of the individual phases when optimizing the interface geometry of contact problems.

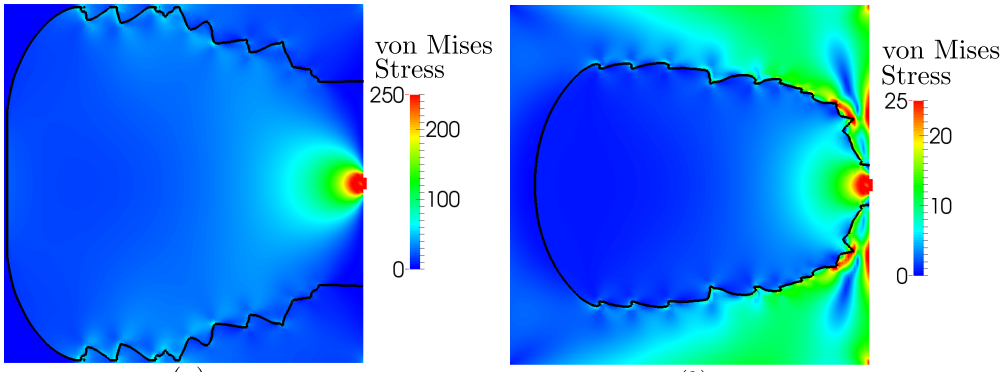

Figure 8.16: Optimized designs for material ratios: (a) $E^A = \frac{1}{4}E^B$ and (b) $E^B = \frac{1}{16}E^A$.

8.4.3.4 Influence of Interface Conditions

Finally, we study the influence of the interface condition on the optimal design. We compare the results for a sliding contact model that allows for separation against designs optimized with interface models that (a) assume perfect bonding and (b) allow sliding of the interface but prevent separation. The latter model describes, for example, the behavior of lubricated interfaces where the fluid allows sliding but not separation. To prevent separation, the contact model outlined in Section 8.3 is used but the normal gap is enforced to be zero, irrespective of the sign of the contact pressure λ_n.

Assuming a stiffness ratio of $E^A = 0.75\ E^B$ with E^B being the nominal value, a volume constraint is imposed with a weighting factor of $c_v = 1$ to prevent the trivial solution in which the anchor material Ω_B occupies the entire design domain for interface conditions (a) and (b). Aside

Analyzed with	Optimized for	
	soft casing	soft anchor
soft casing	0.9348	0.7324
soft anchor	0.0845	0.0929

Table 8.7: Holding forces (N) of optimized designs when analyzed with different stiffness ratios between anchor and holding material.

from the above mentioned stiffness ratio, volume constraint, and varying interface conditions, all other model parameters are consistent with that of the nominal configuration.

The optimized designs are shown in Figure 8.17. The anchor design strongly depends on the interface model. To further illustrate the importance of accounting for the appropriate interface conditions, we cross-compare the optimized designs assuming different interface models. The holding forces of the optimized designs are given in Table 8.8. For each interface condition, the geometry optimized specifically for that interface condition provides the highest holding force under applied displacements. These results suggest that designs optimized assuming a perfect bonding or sliding contact without separation are of little use for applications which exhibit contact with separation. While the design optimized for contact with separation performs well for the other interface models in this example, this result cannot be generalized to other boundary conditions and combinations of the materials with distinctly different properties.

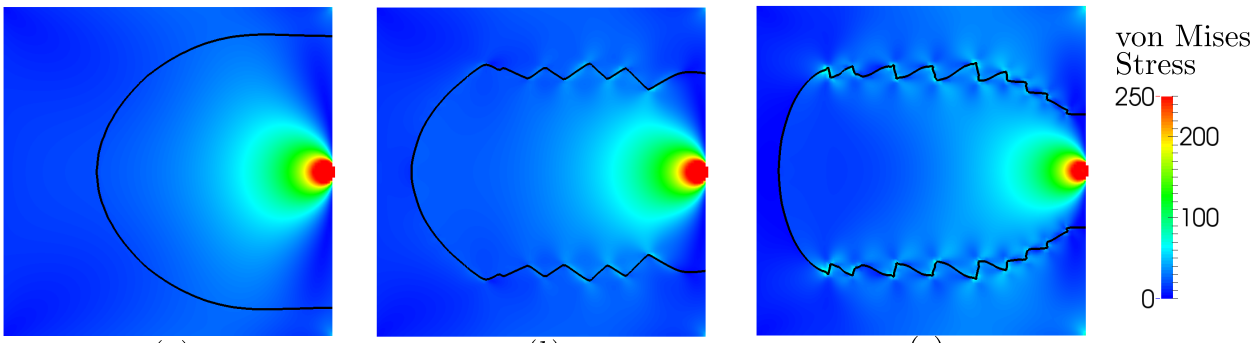

Figure 8.17: Optimized design for (a) fixed, (b) sliding, and (c) separable interface conditions.

Analyzed with	Optimized with		
	Fixed	Sliding	Separable
Fixed	1.2658	1.2624	1.2605
Sliding	1.2395	1.2626	1.2447
Separable	0.0	0.7445	1.0177

Table 8.8: Holding forces (N) of optimized designs analyzed with different interface models.

8.4.4 Discussion

This study introduced a LSM-XFEM topology optimization method for optimizing the geometry of interfaces of two elastic bodies. The method allows for optimizing the shape and topology of the phase boundaries. An explicit LSM is used to describe the geometry by explicit function of the optimization variables. The mechanical model assumes infinitesimal small strains and a linear elastic behavior. The contact conditions are enforced via a stabilized Lagrange multiplier method and an active set method. The XFEM is used to discretize the contact model and allows directly integrating the weak form of the contact conditions at the interface. A broad range of measures of the mechanical response can be considered in the formulation of the optimization problem. To regularize the problem a penalty on the perimeter is introduced into the objective function and a constraint on the volume ratio of the material phases is imposed. The optimization problem is solved by a nonlinear programming algorithm, computing the design sensitivities by the adjoint method.

The proposed optimization method was applied to a problem optimizing the location of four bolts supporting an elastic plate. This example illustrated the use of geometric primitives where only the location but not the shape of the primitives is optimized. The optimization method showed a satisfactory convergence rate. Comparing the optimized bolt locations assuming sliding contact and perfect bonding illustrated that the interface model may have a noticeable impact on the design, even when the number of design variables is small and the design freedom is limited.

In the second problem the interface geometry of an anchor embedded in a host material was optimized. The influences of the perimeter penalty, the stiffness ratio of the material phases, and the interface model on the optimized design were studied. The formation of barb-type features

was observed which increase the resistance of the anchor to external forces. In contrast to the bolt problem, minor convergence issues were observed due to stress oscillations along the interface. This issue is caused by the XFEM discretization of the stabilized Lagrange multiplier formulation of the contact conditions. Alternative formulations of the contact conditions need to be studied, such as the ghost penalty method of [17].

The study on the perimeter penalty showed that increasing the perimeter penalty reduces the size of the barb-type features without significantly affecting the maximum holding force of the anchor. The weak influence of the perimeter penalty on the mechanical response might be specific to the numerical example considered in this study but also due to the small strain assumption. The linear kinematic does not correctly capture the mechanical response if the local deformation is comparable to the feature size. Therefore, the resistance of the barb-type features is likely over-predicted. In future studies, finite strain models will be integrated in the proposed optimization framework.

The studies on the influence of the material stiffness ratio and the interface model demonstrated the significant impact of these physical parameters on the optimum design. These results suggest that the material properties of the individual phases as well as the interface conditions need be considered carefully when designing contact problems. Therefore, applying the proposed optimization method to specific engineering problems seems to be a promising endeavor.

This chapter explored topology optimization for bilateral contact problems with an infinitesimal strain assumption, small relative sliding, and frictionless interface conditions. In addition, the scope of this chapter was limited to two-phase solid-solid problems.

Chapter 9

Small Strain Cohesive Interface Studies

This chapter investigates topology optimization of infinitesimal strain theory, small sliding, cohesive bilateral contact problems in two and three dimensions. The material presented in this chapter are condensed from the resulting publication[9].

9.1 Introduction

Material cohesion represents a progressive nonlinear behavior along the interface. This phenomenon, which relates separation along the interface to surface traction, is also called the cohesive zone model. The cohesive zone model is frequently used to describe material failure and interfacial debonding in engineering structures. It was initially introduced by Dugdale [30] to analyze the damage evolution and material failure within a localized region surrounding the tip of a crack. During separation, the traction along the interface grows to a maximum value, then diminishes to zero. Numerical modeling of structural problems with cohesive zone models have received considerable attention, seminally introduced by Needleman [78]. Normal and tangential traction at the interface can be represented as either independent or coupled functions of normal and tangential separation. The constitutive relation between traction and separation has been described by exponential, bilinear, and polynomial forms of cohesive zone laws [19, 102, 103, 115]. The standard bilinear cohesive zone model is used often for the simulation of interfacial debonding, matrix cracking, delamination of fiber reinforced composites [31, 60], and failure in functionally graded materials [121]. This work considers an uncoupled, bilinear representation of the cohesive zone models. For more information

about cohesive zone models, the reader is referred to [81].

Many cohesive zone laws rely on a penalty method to prevent surface penetration during compression. To mitigate ill-conditioning and accuracy issues often caused by penalty formulations, in this work a stabilized Lagrange method is adopted for the enforcement of non-penetration. During the process of delamination, the mechanical model can experience instabilities. To mitigate this issue, a dynamic relaxation method is employed for the evaluation of the structural response. The interface geometry between two distinct material phases is described by an explicit LSM. Unlike an implicit level set method, which typically describes the evolution of the level set field in the optimization process by the Hamilton-Jacobi equation (e.g. [1]), explicit LSMs define the discretized level set field as explicit functions of the optimization variables [110, 65, 82]. To retain a sharp definition of the interface, we adopt the XFEM for predicting the mechanical response. The particular framework for integrating the explicit LSM and the generalized formulation of the XFEM used in this study are described in detail in [66] and [107].

Previously [59] applied the XFEM-LSM to topology optimization of structural problems with bilateral, frictionless sliding contact. Initially applied to two dimensional frictionless contact problems, it was subsequently extended to interface cohesion problems [57]. Liu et al. [63] recently leveraged the XFEM-LSM framework to minimize the compliance of multi-material structures with interface cohesion. Using adjoint sensitivities and the Hamilton-Jacobi equation to advance the structural boundary, optimal solutions were achieved for two dimensional problems. The presented method builds on the work of [57], extending it to the treatment of interface cohesion between two materials in three dimensions.

The remainder of this chapter is organized as follows: in Section 9.2, we outline the formulation of the optimization problems considered in this study. In Section 9.3, the mechanical model of problems with cohesive interfaces is described. In Section 9.4, we study the main characteristics of the proposed XFEM-LSM method with numerical examples. Insight gained from the numerical studies and areas for future research are summarized in Section 9.5.

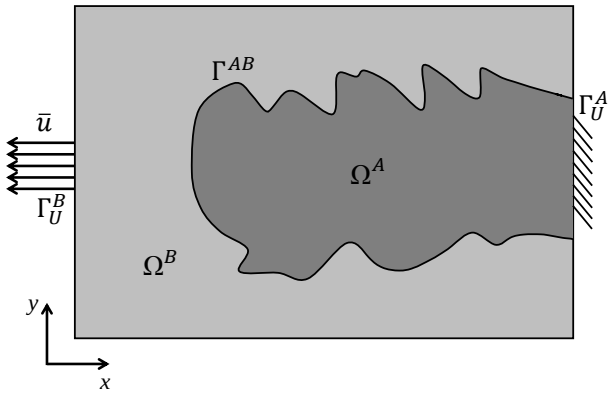

Figure 9.1: Representative configuration of an optimization problem.

9.2 Optimization Problem

In this study, we consider the interactions between two phases, A and B, in two and three dimensions. A representative configuration of the optimization problems relevant to this chapter is shown in Figure 9.1. The design domain Ω^D consists of two non-overlapping subdomains Ω^A and Ω^B, such that $\Omega^D = \Omega^A \cup \Omega^B$ and $\Gamma^{AB} = \Omega^A \cap \Omega^B$ is the interface between both subdomains. Frictionless sliding or a cohesive interface behavior is modeled at the material interface Γ^{AB}. Displacements are prescribed at the boundary Γ_U^B while material A is fixed at the boundary Γ_U^A. In the optimization examples presented in Section 9.4 we seek to maximize the reaction force at Γ_U^A.

To discourage the emergence of oscillatory shapes mimicking a rough surface, we introduce a perimeter penalty term into the formulation of the objective function. This penalty term measures the interface between domains Ω^A and Ω^B and is computed as follows:

$$P = \int_{\Gamma^{AB}} \mathrm{d}\Gamma \ . \tag{9.1}$$

While a perimeter penalty does not allow explicit control of the local shape and the size of geometric features, it has been reported effective in regularizing structural optimization problems [104]. For additional reading on the use of perimeter measures for regularization, the reader is referred to [68, 105, 59].

Geometric features that approach the length scale of element size can result in poor mechan-

ical response predictions. To suppress the formation of such features, a constraint is imposed on the integral measure, G, that is evaluated over the design domain as follows:

$$G = \int_{\Omega^D} e^{-\alpha^2} \left(|\nabla\phi| - 1\right)^2 \mathrm{d}\Omega \qquad \text{with} \qquad \alpha = e_p \frac{\phi}{\Delta\phi} \ , \quad \Delta\phi = \phi_{max} - \phi_{min} \ , \tag{9.2}$$

where e_p is the penalization parameter, and $\Delta\phi$ is the range of allowable level-set values within the design domain, with ϕ_{max} and ϕ_{min} denoting the upper and lower limits of the level set value, respectively. The first term in (9.2) vanishes away from the zero level set isosurfaces, but is unity in its vicinity. The second term encourages a signed distance-like level set field, i.e. $|\nabla\phi| = 1$. The combination of these two terms identifies level set gradients that do not match the desired value of 1 near the material interface. The use of the integral measure G for regularization is only successful in discouraging sub-element features with appropriate upper and lower bounds of the level set values, ideally $\phi_{max} = h/2$ and $\phi_{min} = -h/2$ where h corresponds to the element size. This approach was used successfully towards the optimization of convective heat dissipation problems [22, 21], where it was observed that the lower and upper bounds can be relaxed to $\mp h$ to improve the convergence of the optimization process. Regularization of the optimization problem by way of penalties is less restrictive, as opposed to imposing additional constraint equations. Through numerical studies the authors have found it easier to assign penalty values instead of constraint limits for regularization, especially for cases in which the optimum geometry is largely unknown. For more information about regularization of the optimization problem by way of constraints the reader is referred to [22]. Finally, we constrain the ratio of volumes occupied by either solid, V^A and V^B, to exclude trivial solutions.

The optimization problem is defined by the following nonlinear program:

$$\begin{aligned} &\min_{\mathbf{s}} \left(\frac{c_u}{z_0} z(\mathbf{u}(\mathbf{s})) + \frac{c_p}{P_0} P(\mathbf{s}) + \frac{c_g}{G_0} G(\mathbf{s}) \right) \\ \text{s.t.} \quad &V^A(\mathbf{s}) - c_v \, V^B(\mathbf{s}) \leq 0 \\ &\mathbf{s} \in \mathbf{S} = \left\{ \mathbb{R}^{N_s} | s_{min} \leq s_i \leq s_{max}, \ i = 1....N_s \right\} \ , \end{aligned} \tag{9.3}$$

where z denotes the contribution of the mechanical response to the objective, c_u is the associated weighting factor, z_0 is the initial mechanical response in objective, c_p is the weight of the material

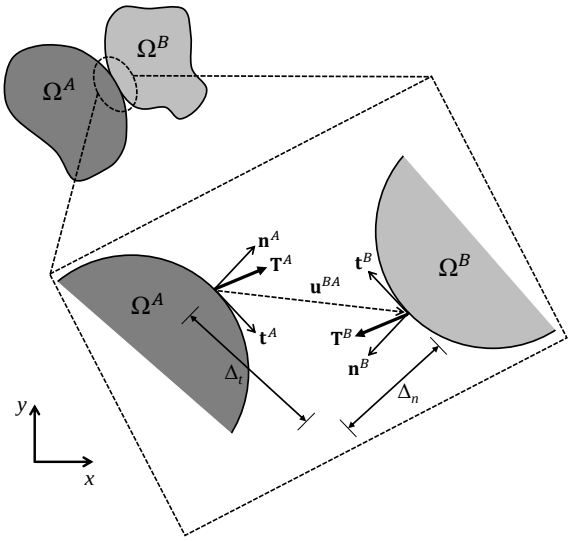

Figure 9.2: Contact relations between two continuum bodies.

interface penalty, P_0 is the initial measure of the material interface, c_g is the weight of gradient measure penalty, G_0 is the initial gradient measure, and c_v controls the desired volume ratio between the two solids, respectively. The number of optimization variables is N_s; the lower and upper bounds on the optimization variables are denoted by s_{min} and s_{max}, respectively. The structural response, $z(\mathbf{u}(\mathbf{s}))$, depends on the discretized state variables, $\mathbf{u}$, which are implicitly dependent on design variables, $\mathbf{s}$. While the proposed optimization framework allows considering other objectives and constraints, such as strain energy, displacement and stress measures, the formulations of the optimization problem used here are well suited to illustrate the influence of mechanical interface conditions on optimized designs. The optimization problem (9.3) is solved by a nonlinear programming method, and the design sensitivities are calculated by the adjoint method.

9.3 Physical Model

To describe the mechanical response at the interface between Ω^A and Ω^B, Figure 9.2 illustrates contact relations pertinent to the interface phenomena considered in this chapter. Here we introduce superscript p to represent either of phases A and B. Surface quantities $\mathbf{T}^p$, $\mathbf{n}^p$, and $\mathbf{t}^p$ are the traction, normal vector, and tangential vector for phase p, respectively. We define $\mathbf{u}^{BA}$ as

the displacement jump across the interface. The mechanical response at the interface depends on the traction and relative displacement across the interface. For any given point on the interface, the normal and tangential traction and separations are defined as:

$$\begin{aligned} \Delta_n = \mathbf{u}^{BA} \cdot \mathbf{n}^A, \qquad \Delta_t = \mathbf{u}^{BA} \cdot \mathbf{t}^A, \qquad \mathbf{n}^A = -\mathbf{n}^B, \qquad \mathbf{t}^A = -\mathbf{t}^B \ , \\ \tilde{T}_n = \mathbf{T}^A \cdot \mathbf{n}^A = -\mathbf{T}^B \cdot \mathbf{n}^A, \qquad \tilde{T}_t = \mathbf{T}^A \cdot \mathbf{t}^A = -\mathbf{T}^B \cdot \mathbf{t}^A \ , \end{aligned} \tag{9.4}$$

where Δ_n is the normal separation, Δ_t is the tangential separation, $\tilde{T}_n$ is the magnitude of normal traction, and $\tilde{T}_t$ is the magnitude of tangential traction. The relationship between surface traction and relative displacement are illustrated in Figure 9.3. The variables δ_c^n, δ_c^t, δ_f^n, and δ_f^t represent the critical normal separation, the critical tangential separation, the normal separation at which the normal traction vanishes, and the tangential separation at which the tangential traction vanishes, respectively. In our uncoupled bilinear cohesive zone law three distinct regions are defined. The bonded zone refers to the linear elastic region where $\Delta_n \leq \delta_c^n$ and $\Delta_t \leq \delta_c^t$. The reduced zone is defined as the region where $\delta_c^n \leq \Delta_n \leq \delta_f^n$ and $\delta_c^t \leq \Delta_t \leq \delta_f^t$. Finally, the debonded zone refers to the region in which cohesion has vanished, i.e. $\Delta_n \geq \delta_f^n$ and $\Delta_t \geq \delta_f^t$.

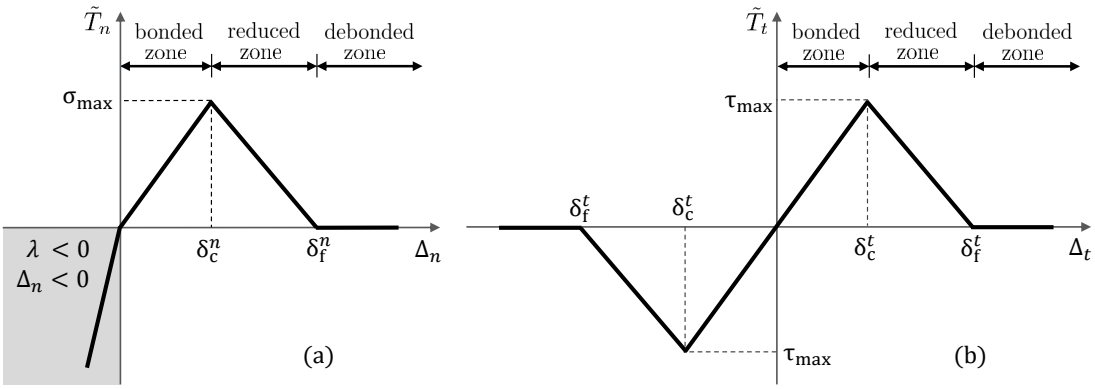

Figure 9.3: Uncoupled bilinear cohesive zone law, (a) normal response, (b) tangential response.

Departing from the frequently used penalty method to prevent surface penetration, the compressive region depicted in the lower left quadrant of Figure 9.3(a) is handled separately by a stabilized Lagrange formulation. This mitigates ill-conditioning and accuracy issues that can arise with the use of penalty methods. During separation, the magnitude of normal and shear traction

at the interface increases linearly to a prescribed maximum value, then falls to zero when separation has surpassed the cohesion limit. The governing equations for bilinear cohesion are defined as follows:

$$\tilde{T}_n(\Delta_n, \lambda) = \begin{cases} \lambda & \text{if } \lambda \leq 0 \\ \frac{\sigma_{\max}}{\delta_c^n}\Delta_n & \text{if } 0 \leq \Delta_n \leq \delta_c^n \\ \frac{\sigma_{\max}(\delta_f^n - \Delta_n)}{\delta_f^n - \delta_c^n} & \text{if } \delta_c^n < \Delta_n \leq \delta_f^n \\ 0 & \text{if } \Delta_n > \delta_f^n \end{cases} , \tag{9.5}$$

and

$$\tilde{T}_t(\Delta_t) = \begin{cases} \frac{\tau_{\max}}{\delta_c^t}\Delta_t & \text{if } -\delta_c^t \leq \Delta_t \leq \delta_c^t \\ \frac{\tau_{\max}(\delta_f^t - \Delta_t)}{\delta_f^t - \delta_c^t} & \text{if } \delta_c^t < \Delta_t \leq \delta_f^t \\ -\frac{\tau_{\max}(\delta_f^t - \Delta_t)}{\delta_f^t - \delta_c^t} & \text{if } -\delta_f^t \leq \Delta_t < -\delta_c^t \\ 0 & \text{if } |\Delta_t| > \delta_f^t \end{cases} , \tag{9.6}$$

where $\sigma_{\max}$ is the value of normal traction at the critical normal separation, δ_c^n; $\tau_{\max}$ is the tangential traction at the critical tangential separation, δ_c^t; λ is the Lagrange multiplier associated with the non-penetration condition. The constraint equation associated with the stabilized Lagrange multiplier is evaluated as follows:

$$\lambda - \bar{\mathbf{T}} \cdot \mathbf{n}^A - \gamma \Delta_n = 0 \ , \tag{9.7}$$

with

$$\bar{\mathbf{T}} = \bar{\boldsymbol{\sigma}} \cdot \mathbf{n}^A, \qquad \bar{\boldsymbol{\sigma}} = \omega^A \boldsymbol{\sigma}^A + \omega^B \boldsymbol{\sigma}^B \ , \tag{9.8}$$

where γ is a penalty factor. The penalty factor discourages penetration during the early stages of convergence but becomes insignificant as equilibrium is achieved and the relative normal separation goes to zero, i.e. $\Delta_n \approx 0$. The weighting factors, ω^p, are such that $\omega^A + \omega^B = 1$; in this work we assume that $\omega^A = \omega^B = 0.5$.

9.4 Numerical Examples

In this section, we first verify the accuracy of the implemented cohesive zone model for different modes of delamination through comparison against analytical reference solutions. To gain insight into the effectiveness and robustness of the optimization framework, both 2D and 3D optimization problems are considered. We study the influence of cohesive interface parameters on the optimized design through numerical examples. The effect of the gradient measure penalty on optimal performance is evaluated, and the impact of surface debonding on the optimized geometry is assessed by varying the magnitude of the applied loads.

The optimization problems are solved by the Globally Convergent Method of Moving Asymptotes (GCMMA) [96]. The optimization problem is considered converged if the change of the objective function relative to the initial objective value is less than 10^{-6} and the constraints are satisfied. The parameters controlling the adaptation of the lower and upper asymptotes are set to 0.5, 0.7, and 1.2, respectively. The relative step size, Δs, is provided for each example. The GCMMA constraint penalty is set to 50. For all optimization examples provided in this chapter, the upper and lower limits for the optimization variables are set to $s_{max} = h$ and $s_{min} = -h$, where h represents the length of the elements. For the sensitivity analysis we adopt a discrete formulation similar to that used by [21], which can be readily evaluated from the governing equations of the design problem. The partial derivatives of the objective function, the constraint, and the element residual with respect to the design variables are evaluated by a finite difference method. The linearized sub-problems within the Newton iterations and the adjoint sensitivity analysis are solved using the UMFPACK direct solver [24] for the 2D examples and a Generalized Minimal RESidual (GMRES) iterative solver with incomplete LU factorization [84] for the 3D examples.

9.4.1 Verification of cohesive zone model

The accuracy of the XFEM formulation of the cohesive zone model discussed above is validated through comparison against the analytical solution for mode I of delamination. For this

purpose, a double cantilever beam (DCB) is studied. The schematic of the DCB geometry is illustrated in Figure 9.4. Using linear elastic beam theory [3], the analytical solution for the crack length can be described as a function of cohesive fracture energy. The crack length is given by [93] as:

$$a = \sqrt[4]{\frac{3EH^3\Delta^2}{4G_c}} \ , \tag{9.9}$$

where E is the Young's modulus, Δ is the separation at the end, H is the beam height, and G_c is the cohesive fracture energy. We adapted the model parameters and problem configuration given by [93], provided in Table 9.1. For numerical modeling, the beam is discretized with 330×33 bilinear quadrilateral elements and the forward analysis is solved with a 2D plane strain condition. The measured crack length, a, is plotted as a function of end displacement, Δ, and compared to the analytical solution in Figure 9.5. The inset snapshots depict the initial and final deformed configuration of the DCB, with an expanded view of the mesh used. For visualization purposes, intersected elements are decomposed into triangles. Despite the influence of the fixed edge boundary condition, the measured relative error between two solutions is approximately 1%. This error is caused by unstable crack growth near the fixed edge of the beam, similarly observed by [3, 93].

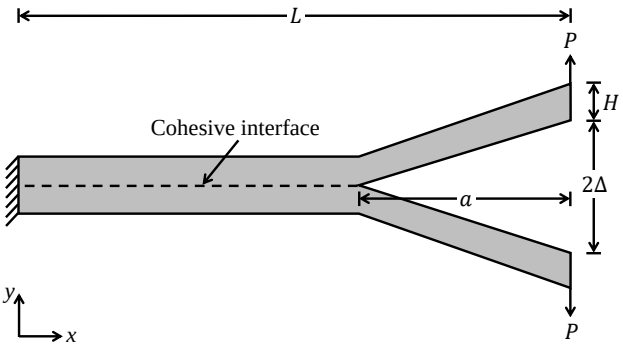

Figure 9.4: Schematic of double cantilever beam.

Description	Parameter	Value	Units
beam length	L	200	mm
beam height	H	10	mm
Young's modulus	E	14.2	GPa
Poisson's ratio	ν	0.35	
fraction energy	G_c	344	J/m^2
material strength	$\sigma_{\max}$	3.56	MPa
penalty factor	γ	20	

Table 9.1: Model parameters of double cantilever beam.

In addition to mode I verification, the structural response during mixed mode uniform delamination is verified by an analytical solution. A rectangular block with a horizontal cohesive interface is fixed along the bottom edge and subjected to a uniform displacement along the top edge. The schematic of the problem and the boundary conditions are shown in Figure 9.6. The

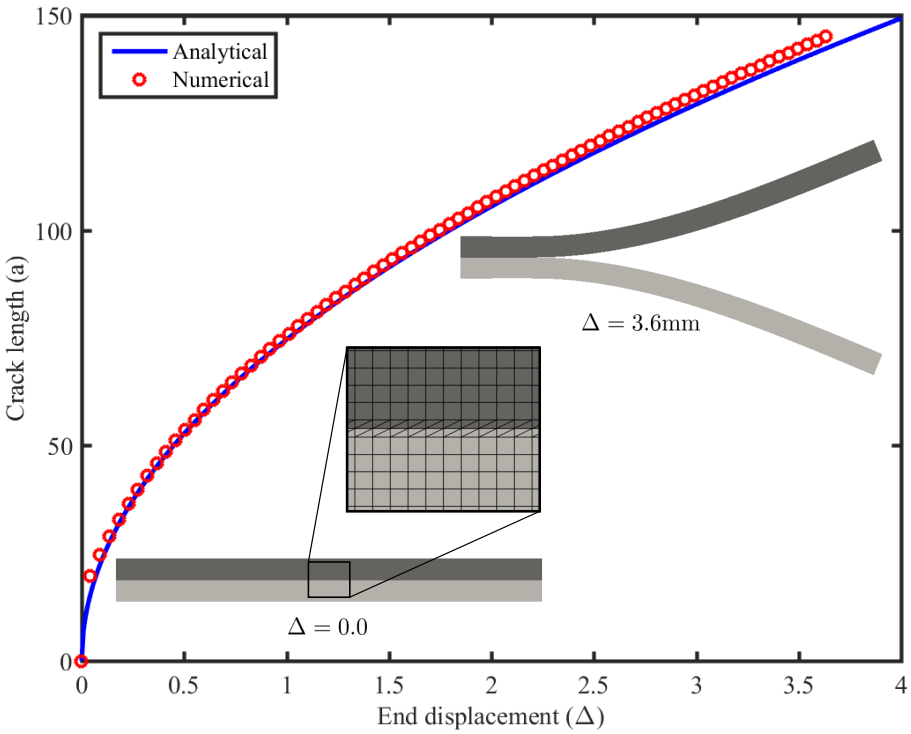

Figure 9.5: Comparison between analytical and numerical solutions for double cantilever beam. For visualization purpose, the displacement in the deformed configuration is shown with a scaling factor 10.

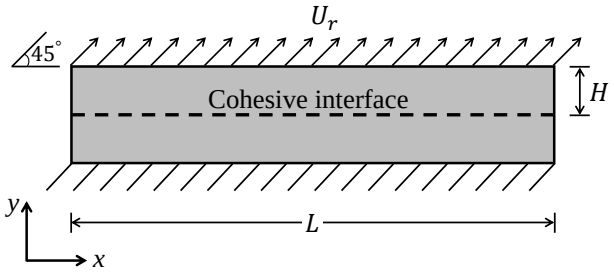

Figure 9.6: Loading and boundary conditions for laminated structure with cohesive interface.

material and cohesive zone model parameters for the mixed mode delamination model are given in Table 9.2. For any given uniform surface separation value, the analytical solution for the total delamination force is:

$$f = \int_{\Gamma_c} \left(T_n^2 + T_t^2\right)^{1/2} \mathrm{d}\Gamma \;\approx\; \left(T_n^2 + T_t^2\right)^{1/2} \times H \times t \;, \tag{9.10}$$

where f is the total force for uniform delamination along the cohesive interface Γ_c. For numerical

Description	Parameter	Value	Units
beam length	L	10	mm
beam height	H	0.1	mm
beam thickness	t	0.1	mm
applied displacement	U_r	0.15	mm
Young's modulus	E	2.0	GPa
Poisson's ratio	ν	0.3	
maximum normal traction	$\sigma_{\max}$	1.0	MPa
maximum tangential traction	$\tau_{\max}$	3.0	MPa
ultimate normal separation	δ_{f}^{n}	0.06	mm
ultimate tangential separation	δ_{f}^{t}	0.033	mm
critical normal separation	δ_{c}^{n}	0.006	mm
critical tangential separation	δ_{c}^{t}	0.0033	mm
penalty factor	γ	20	

Table 9.2: Material and cohesive zone parameters for mixed mode model.

modeling, the domain is discretized with 100×1 elements and the simulation is performed for 2D plane strain conditions. Since only the response at the interface is of interest, a single layer of elements in thickness direction is sufficient. A uniform displacement is applied with a magnitude of 0.15 mm in sequence of load increments. Figure 9.7 compares numerical and analytical results for the total delamination force as a function of the magnitude of separation between the surfaces. The inset snapshots illustrate the mechanical response of a segment of the laminated structure at specific loading stages, with the intersected elements decomposed into triangles for visualization purposes. The measured relative error in the uniform mixed mode example problem is 2.25×10^{-7} %.

9.4.2 Material anchor - 2D

To explore the characteristics of the proposed optimization method, we first introduce the 2D material anchor design problem shown in Figure 9.8. A structural anchor (represented by phase A) is embedded in a host material (designated as phase B) with frictionless and cohesive interface conditions, imposed at the boundary between both phases. In this problem, we wish to determine the optimal geometry such that the holding force of the anchor is maximized. Originally studied for frictionless contact by [59], this problem is extended to account for cohesion at the interface.

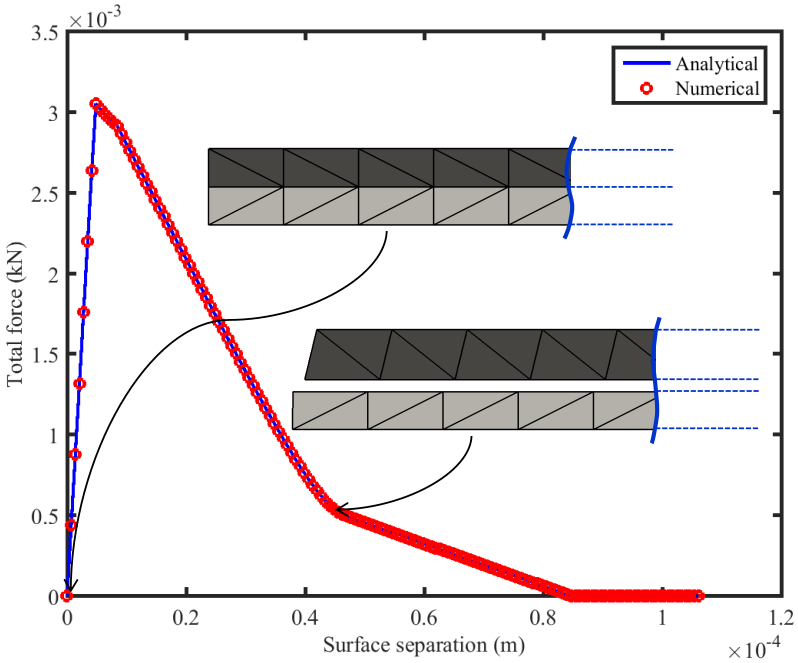

Figure 9.7: Force-separation curves for the analytical and numerical solutions.

The latticed initial configuration widens the prevalence of design sensitivities throughout the design domain, encouraging rapid convergence to an optimized geometry.

The anchor is fixed along the boundary Γ_1, and a prescribed displacement, U_x^B, is applied to the host material along Γ_{2-4}. Displacements in the y direction are constrained to zero along Γ_{2-4}. To exclude the trivial case in which the anchor material directly connects boundary Γ_1 to boundaries Γ_{2-4}, these boundaries are excluded from the design domain. Considering the symmetric nature of the problem, only one half of the design domain is analyzed. The response dependent contribution to the objective function in Equation (9.3) is defined through the holding force of the anchor in the x direction along Γ_1. The holding force is measured by integrating the normal stress σ_{xx} along Γ_1. This contribution to the objective function is defined as follows:

$$z = -\int_{\Gamma_1} \sigma_{xx} \, d\Gamma \ . \tag{9.11}$$

The optimization problem is regularized by applying a perimeter penalty and the level set gradient measure penalty along the interface. In order to ensure that the anchor material geometry does not occupy the entire design domain geometry, a volume constraint of 50% is imposed.

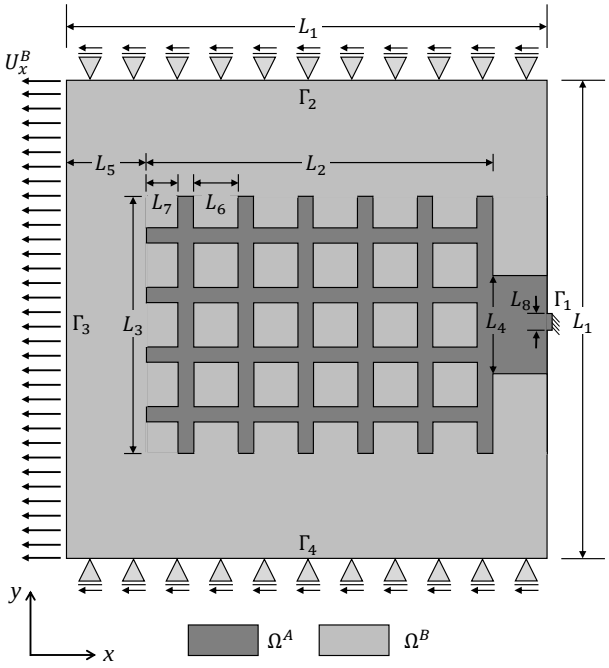

Figure 9.8: Initial design of the material anchor problem.

Description	Parameter
length of domain	$L_1 = 1.0$ m
length of anchor head	$L_2 = 0.715$ m
length of anchor width	$L_3 = 0.523$ m
anchor base width	$L_4 = 0.20$ m
anchor distance from end	$L_5 = 0.175$ m
inclusion width	$L_6 = 0.0833$ m
inclusion width	$L_7 = 0.0667$ m
fixed section width	$L_8 = 0.0333$ m
thickness	$t = 1/13$ m
applied displacement	$U_x^B = \text{var.}$
Young's modulus	$E^A = 10^4 \text{N/m}^2$
Young's modulus	$E^B = 10^4 \text{N/m}^2$
Poisson's ratio	$\nu^A = 0.3$
Poisson's ratio	$\nu^B = 0.3$
spring stiffness	$K = 2.0 \times 10^3 \text{N/m}^2$
response weight	$c_u = 5.0 \times E^A$
perimeter weight	$c_p = 0.25$
volume constraint weight	$c_v = 0.5$
gradient measure weight	$c_g = \text{var.}$
penalization parameter	$e_p = 1.0$
desired level set gradient	$\text{d}\phi_p = 1.0$
penalty factor	$\gamma = 20$
initial damping parameter	$\tilde{\beta}_{\text{int}} = 0.01$
GCMMA step size	$\Delta s = 3.0 \times 10^{-5}$

Table 9.3: Nominal parameters for the material anchor design problem.

Half of the design domain is discretized with 120×60 elements and the physical response is predicted assuming plane strain conditions. To mitigate mechanical response convergence issues due to material inclusions undergoing rigid body rotations, the host material is grounded elastically by a distributed system of weak linear springs with stiffness K. The LSF is discretized by the XFEM mesh and the nodal level set values are defined as the optimization variables. The LSF is initialized by an array of cuboids as shown in Figure 9.8. The smoothing radius of the linear filter in (2.9) is 0.0375m.

The effect of the perimeter penalty on optimized designs for frictionless contact was studied in [59]. The results showed that the perimeter penalty reduces the number and size of barbs, however it does not result in a large depreciation of the holding force. In this work, we study the

effectiveness of constraining the level set gradient measure to regularize the optimization problem and consider different values of the weighting factor c_g in Equation (9.3). The influence of the interface conditions and the cohesive zone parameters on the optimized design are studied by varying the normal and tangential interface resistance. An example designed to initially exhibit total debonding is optimized to recover interface cohesion. Finally, the influences of the applied load are investigated through the variation of the applied displacement magnitude.

9.4.2.1 Nominal design

We first illustrate the geometry evolution and convergence behavior of the nominal design. Design parameters are consistent with those given in Table 9.3, and we exclude the influence of the level set gradient measure by setting $c_g = 0.0$. The nominal model assumes frictionless sliding contact, excluding material cohesion, and the applied displacement is set to $U_x^B = 0.025$m. The evolution of the nominal design is shown in Figure 9.9. During the optimization process, the anchor material coalesces into a unified body. Interlocking tabs at the anchor head and barbs along the sides afford resistance to separation. The initial and optimized values for the holding force and the interface length are given in Table 9.4. While the general design traits are similar to that of [59], the increase of prescribed displacements in this study produces interlocking tabs at the head of the anchor.

Design iteration	Holding force (N)	Interface length (m)
Initial	1.1432	3.86387
Optimized	1.8835	1.36123

Table 9.4: Holding force and interface length in the initial and optimized designs for nominal configuration.

9.4.2.2 Influence of gradient measure penalty

Optimization problems involving sliding contact can lead to the formation of extremely sharp protrusions or periodic surface oscillations to maximize the resistance to surface separation. These small features can lead to poor mechanical response predictions when they approach the length

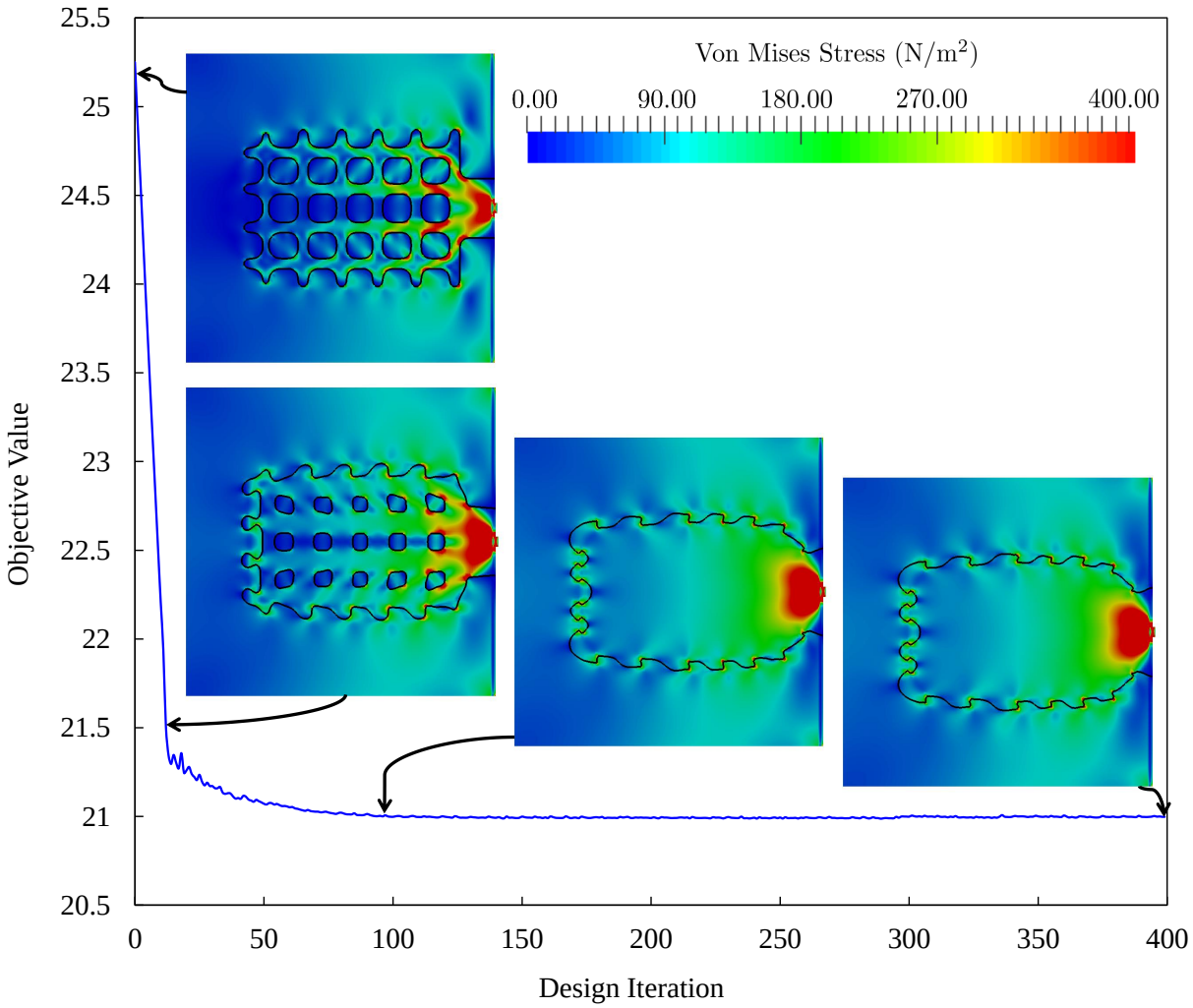

Figure 9.9: Objective evolution and convergence behavior of the nominal design.

scale of an element. Additionally, small features can be problematic for manufacturing. The level set gradient measure penalty helps to regularize the problem by discouraging small features. However, this form of regularization may lessen the formation of barbs along the side and separation resistant features if it is overemphasized in the objective function. To explore the impact of gradient measure regularization, the nominal design is solved for different values of the gradient measure penalty weight, c_g. The applied load is increased to $U_x^B = 0.05$m to amplify optimized geometry features, while all other model parameters and boundary conditions are the same as defined for the nominal design.

With an initial penalty weight of $c_g = 0.0$, the optimized geometry and subsequent holding force provide a reference value free of gradient measure regularization. The penalty weight is then increased incrementally to $c_g = 1.0$, and the percentage of the reduction in holding force is evaluated by comparison to the optimized design with no gradient measure penalty. The optimization results are given in Figure 9.10 and Table 9.5. The gradient measure regularization reduces the prevalence of small features at a minimal cost to the resulting holding force. For the remaining 2D examples provided in this chapter, a gradient measure penalty of $c_g = 0.01$ is used. Although contributions to the objective function are normalized by the initial response, it is not guaranteed that the optimal gradient measure penalty weight value is constant for all optimization problems considered in this chapter. However, in the author's experience, a gradient measure penalty weight of $c_g = 0.01$ reduces the prevalence of small features without altering general optimized design characteristics for problems presented in this chapter.

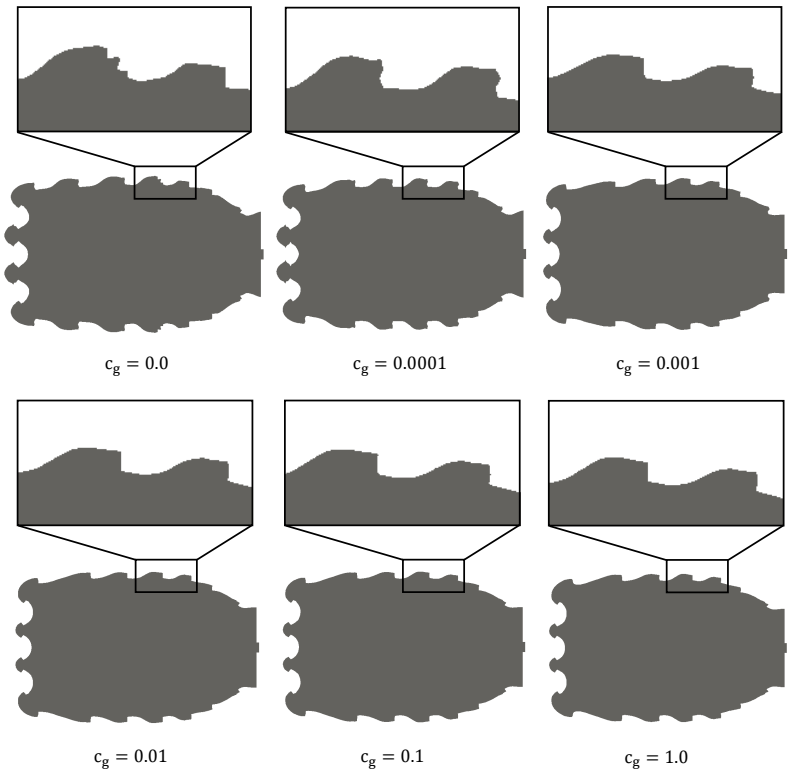

Figure 9.10: Effect of gradient measure penalty on the optimized design.

Gradient measure penalty c_g	Holding force (N)	Reduction in holding force (%)	Interface length (m)
0.0	4.0827	0.0	1.3885
0.0001	4.0830	0.009	1.4244
0.001	4.0728	0.242	1.2857
0.01	4.0739	0.216	1.2861
0.1	4.0806	0.052	1.2859
1.0	4.0805	0.053	1.4553

Table 9.5: Holding force, reduction in holding force and the interface length of the optimized design for different gradient measure penalty weights, c_g.

9.4.2.3 Influence of interface conditions

While optimized geometries for frictionless contact are somewhat intuitive, additional interface phenomena, such as cohesion and debonding, complicate design considerations. The optimized anchor design in the presence of cohesive interface conditions is investigated by varying the normal and tangential resistance at the interface. While the critical and final separation cohesion parameters are kept constant, $\delta_{\mathrm{c}}^n = \delta_{\mathrm{c}}^t = 0.007\mathrm{m}, \delta_{\mathrm{f}}^n = \delta_{\mathrm{f}}^t = 0.2\mathrm{m}$, the optimization problem is solved for different values of maximum normal and tangential traction, σ_{max} and τ_{max}. To provide an intuitive metric for the normal and tangential resistance experienced at the interface, we define the effective normal and shear cohesion modulus as follows:

$$E^N = \frac{\sigma_{max}}{\delta_c^n}, \qquad E^T = \frac{\tau_{max}}{\delta_c^t}\ , \tag{9.12}$$

where E^N is the effective normal cohesion modulus and E^T is the effective shear cohesion modulus. Figure 9.11 illustrates optimized geometries for various normal and shear cohesion moduli values normalized by the anchor material Young's modulus (E^A). As the tangential cohesion modulus is increased, the contact interface aligns with the direction of the applied displacement to maximize resistance. In the case of a large normal cohesion modulus, the trailing edges of barbs or tines flatten out to provide resistance to normal separation. For a design involving large shear and normal cohesion, analogous to perfect bonding at the interface, a reduction of surface features and consolidated anchor mass are observed. This design trend has also been observed by [59] for

the case of perfect bonding and separable interface. For all examples with cohesion presented in Figure 9.11, interface cohesion remains in the bonded zone; see Figure 9.3.

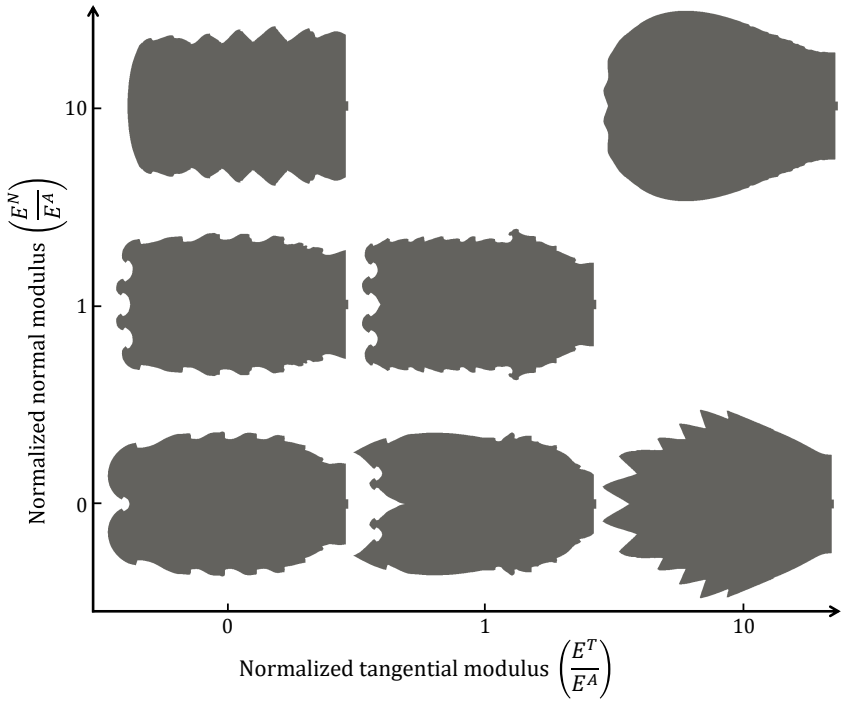

Figure 9.11: Influence of interface conditions on the optimized design, $U_x^B = 0.025$m.

9.4.2.4 Optimization of problems experiencing debonding

In the numerical studies above, the initial anchor geometry provides significant interface resistance. During the evolution of the anchor geometry, features quickly emerged to further increase the surface traction. This section considers the case where the optimization process is initialized with a design that experiences complete delamination. To this end, the optimized geometry for the highest pure tangential cohesion case, $E^N/E^A = 0.0$ and $E^T/E^A = 10.0$ from Figure 9.11, is chosen as the initial configuration. The final separation parameters are set to $\delta_{\mathrm{f}}^n = \delta_{\mathrm{f}}^t = 0.014$m, the maximum tangential traction parameter to $\tau_{max} = 140\mathrm{N/m}^2$ and the applied displacement to $U_x^B = 0.1$m. All other material parameters remain the same as the nominal design.

The objective history during optimization, supported by snapshots of the physical response and force-displacement curves for select iterations, are shown in Figure 9.12. During the ini-

tial stages of design evolution, full debonding occurs when the applied displacement surpasses 0.05m. This behavior is evident by the sudden drop in holding force at the applied displacement of $U_x^B \approx 0.05$m, shown in the inset of Figure 9.12. Within the first ten design iterations total debonding is mitigated. After optimization, the entirety of the material interface remains in the bonded zone of cohesion at the maximum applied displacement, as demonstrated by the linear force-displacement curve. Similar to the frictionless nominal design, the geometry produces barbs along the sides that provide resistance to the separation. This example also demonstrates that dynamic relaxation provides a reliable evaluation of the mechanical response experiencing rapid delamination, throughout design iterations.

9.4.2.5 Influence of applied load

In the previous example, complete debonding of the initial design was induced by selecting the initial geometry, load conditions, and interface properties favorable to such a response. To further investigate design traits associated with reduced cohesion, in this study we focus our attention on the influence of the magnitude of the applied displacement on the optimized geometry. Beginning with the optimized design and model parameters for the tangential resistance case $E^N/E^A = 0.0$ and $E^T/E^A = 1.0$ shown in Figure 9.11, the applied displacement is incrementally raised to match the final separation cohesion parameter, i.e. $U_x^B = \delta_{\mathrm{f}}^{\mathrm{t}} = 0.2m$. The optimization problem is solved at each load level using the initial design shown in Figure 9.8. The evolution of the optimized design as the applied displacement increases is shown in Figure 9.13.

For small displacements, the optimized design exhibits an interface that is predominantly aligned with the direction of applied load to afford cohesive resistance to separation. As the applied displacement increases, cohesion diminishes gradually in localized regions. The physical response in these regions is dominated by sliding contact interactions. At the highest loading case of $U_x^B = 0.2$m, the majority of interfacial separation is greater than the critical separation value. With a reduced influence of cohesion, the optimized design for the maximum load scenario shows a close resemblance to the nominal design without cohesion.

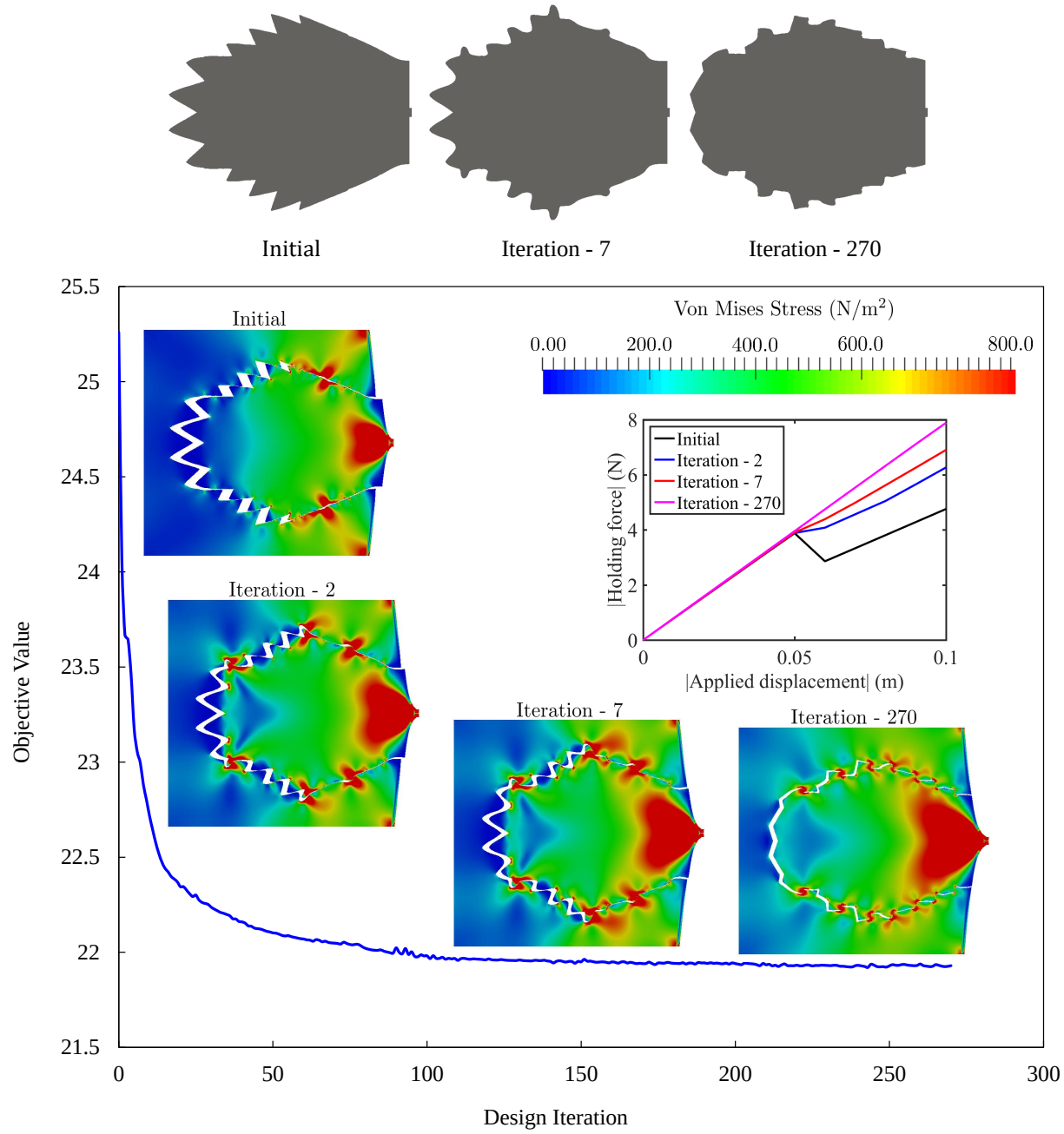

Figure 9.12: Evolution of design and load-displacement curve during optimization.

The highest loading level, i.e. $U_x^B = 0.2m$, is applied to the material interface configurations studied in Section 9.4.2.3, and the resulting optimized geometries are illustrated in Figure 9.14. The percentage of the interface which resides in the reduced zone of cohesion is provided above each case. Comparison between Figures 9.11 and 9.14 shows that under the maximum loading

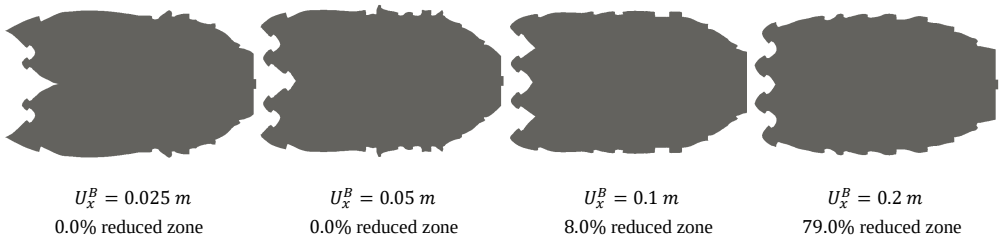

Figure 9.13: Influence of applied load on the optimized design, $E^T/E^A = 1.0$.

condition, there is a general trend towards the development of barbs or interlocking features to prevent separation. For this load case scenario, the benefit of such features outweighs the cost of the interface measure penalty. However, design problems in which the entire interface remains in the bonded zone of cohesion (Figure 9.3) remain relatively unchanged. The holding forces of each design illustrated in Figures 9.11 and 9.14 are provided in a Table 9.6. Increasing the interface resistance in both normal and tangential directions results in higher holding forces.

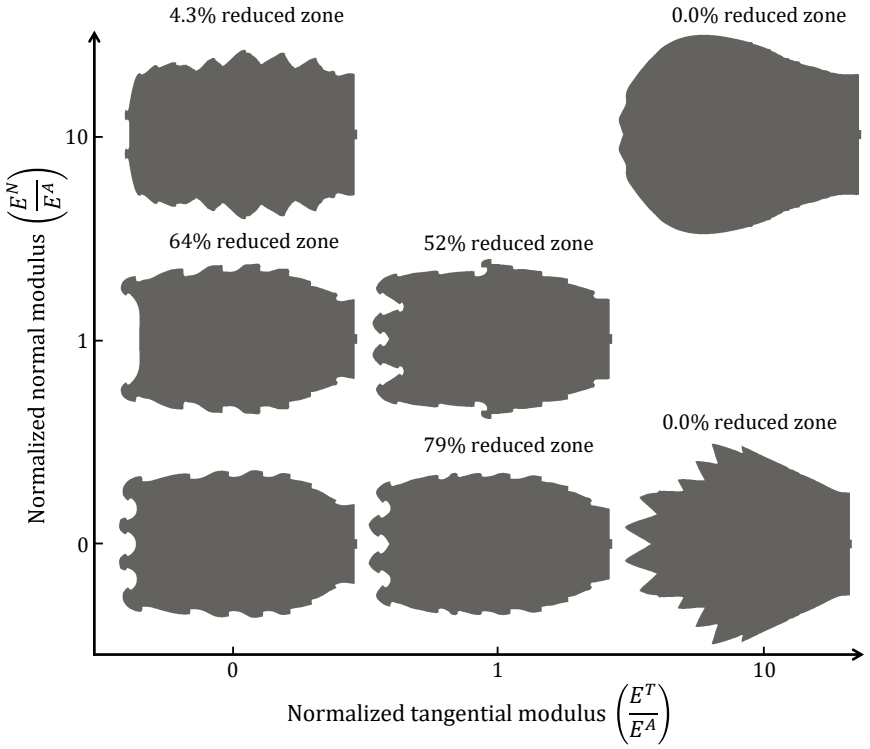

Figure 9.14: Influence of extreme loading condition on the optimized design, $U_x^B = 0.2$m.

To provide further insight to optimized design traits which may leverage material cohesion to increase holding force, the relative gap value and cohesive traction at the interface are illustrated for the two design cases experiencing the highest percentage of reduced cohesion. For the case of pure tangential cohesion, $E^T/E^A = 1,\ E^N/E^A = 0$, the tangential separation and traction at the interface are depicted in Figure 9.15. The tangential separation between the anchor and host material is less pronounced in the vicinity of the interlocking tabs at the head of the anchor, but exceeds the critical separation value along the sides of the anchor which are aligned with the direction of applied load. The state of surface traction at the interface suggests that interlocking tabs or barbs provide a greater advantage in localized regions experiencing minimal cohesive traction. While the interface geometry along the side of the anchor shows a slight decrease in barb size, the general profile closely resembles the optimized geometry without interface cohesion.

For the case of pure normal cohesion, $E^T/E^A = 0,\ E^N/E^A = 1$, the normal separation and traction are illustrated in Figure 9.16. The normal surface separation is most prominent along the trailing edge of the majority of barb-like features, and at the head of the anchor. The normal surface traction at the interface suggests that the smooth anchor head profile leverages cohesive resistance to increase the holding force of the design.

The studies performed on the 2D material anchor design problem demonstrate that the proposed optimization framework is sufficient to solve a broad range of problems, including those exhibiting complete debonding. Interfacial properties have shown to be a dominant design con-

Interface condition $(E^T/E^A, E^N/E^A)$	Holding force (N) $U_x^B = 0.025$m	Holding force (N) $U_x^B = 0.2$m
(0,0)	1.9814	16.3305
(1,0)	2.0598	16.5288
(10,0)	2.2429	17.9635
(0,1)	2.0856	15.8748
(0,10)	2.2135	17.7353
(1,1)	2.1344	16.9302
(10,10)	2.2491	17.9866

Table 9.6: Holding forces of each design illustrated in Figures 9.11 and 9.14.

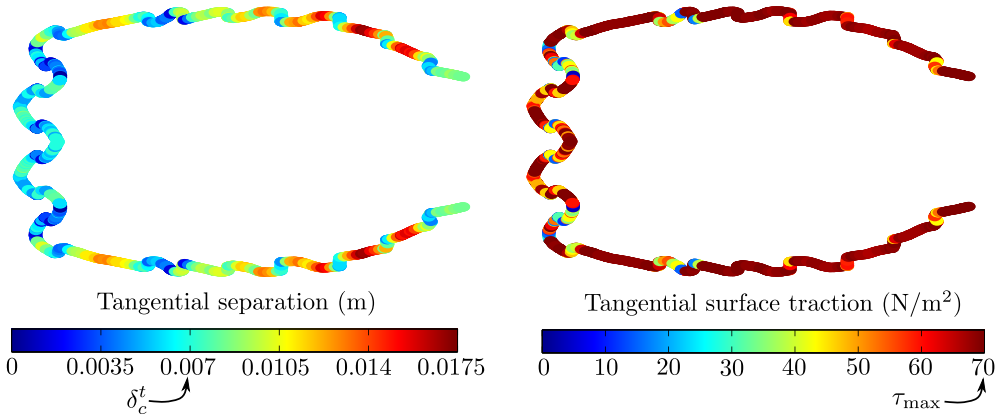

Figure 9.15: Interface separation and traction for case study: $E^T/E^A = 1,\ E^N/E^A = 0$.

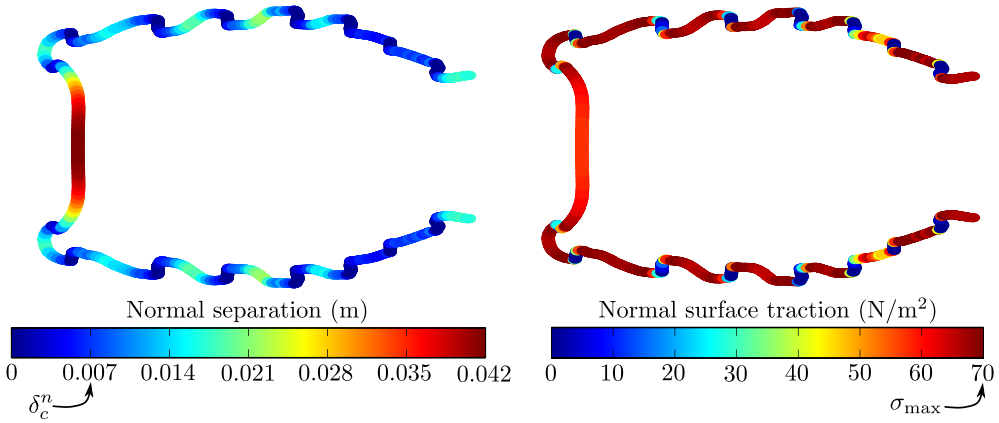

Figure 9.16: Interface separation and traction for case study: $E^T/E^A = 0,\ E^N/E^A = 1$.

sideration for material anchors. The study on varying the magnitude of the applied load showed that design characteristics can be tailored in localized regions where either cohesion or frictionless contact are prevalent.

9.4.3 Material anchor - 3D

The following examples extend the design domain to study three dimensional problems. The design domain of the 2D example in Figure 9.8 is repeated in the out-of-plane direction. The schematic of the 3D model initial configuration is shown in Figure 9.17. All material parameters and interface conditions are adopted from 2D example; see Table 9.3.

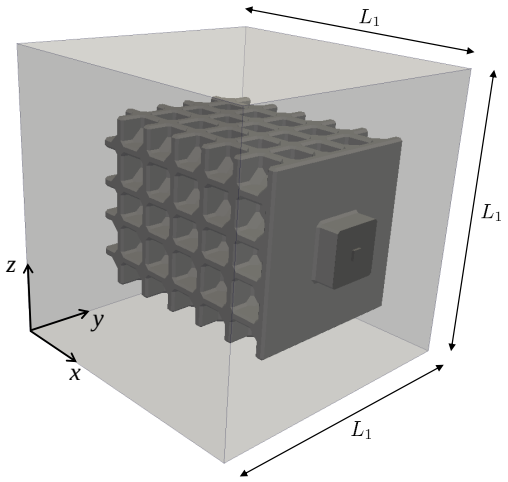

Figure 9.17: Schematic of the initial design in 3D anchor problem.

Similar to the 2D example, the objective is to maximize the holding force of the anchor. Line boundary Γ_1 is extended to a surface boundary where the 3D anchor exits the design domain. Line boundaries Γ_2 and Γ_4 are extended to the $x-y$ and $x-z$ planes at the design domain boundaries. Finally, line boundary Γ_3 is extended to a surface boundary at the $x = 0$ plane. Considering the symmetric nature of the problem, only one fourth of the domain is analyzed with $60\times30\times30$ elements. The optimization step size is set to $\Delta s = 0.001$. Similar to the 2D example, the response dependent contribution to the objective function in Equation (9.3) is defined through the holding force of the anchor in the x direction along Γ_1. The holding force is measured by integrating the normal stress σ_{xx} along Γ_1 (9.11). The optimization problem is regularized by applying a perimeter penalty and gradient measure penalty for the level set field along the interface. The response, perimeter, and volume constraint weights are the same as provided in Table 9.3, whereas the gradient measure weight is kept consistent with the 2D analog for each study. Specifically, the gradient measure weight is set to $c_g = 0.0$ for the nominal design and $c_g = 0.01$ for the remaining 3D examples.

We first illustrate the geometric evolution and convergence behavior of the nominal design. In all 3D examples, the applied displacement is set to $U_x^B = 0.007$m; higher loads resulted in numerical instabilities from complex geometric features. The evolution of the nominal design is

shown in Figure 9.18. Similar to the 2D problem, the anchor material evolves into a unified body. Ridges or spines along the outer face of the anchor provide resistance to separation.

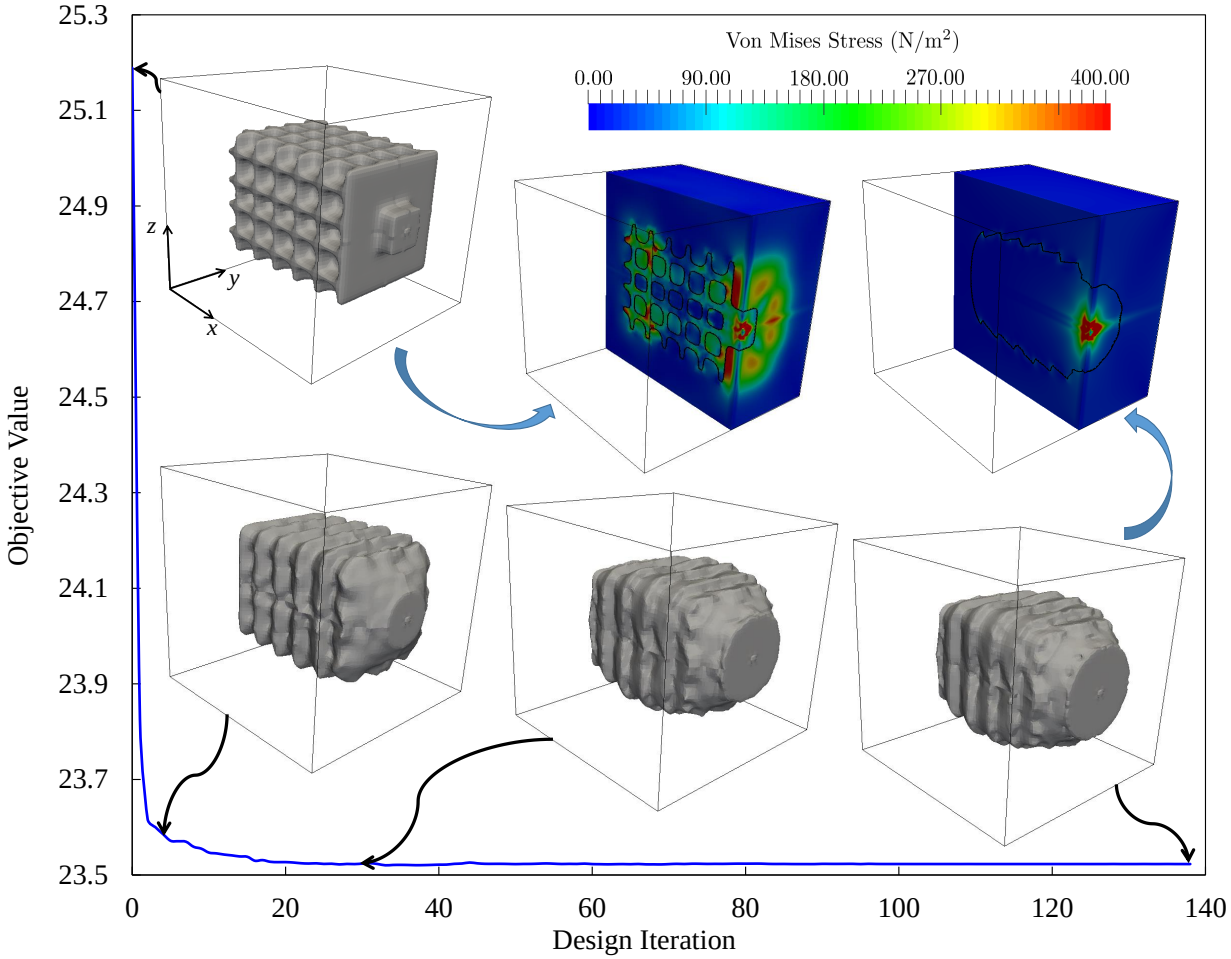

Figure 9.18: Objective evolution for 3D nominal design.

9.4.3.1 Influence of interface conditions

The 3D effects of interface cohesion on the optimized design are investigated for different levels of normal and tangential cohesive resistance. All cases of interfacial properties investigated in Section 9.4.2.3 are studied here for the three dimensional configuration. The resulting geometries for these sets of interface parameters are shown in Figure 9.19. For comparison, a cutaway view is provided in Figure 9.20.

Although 2D and 3D examples show design trend similarities, the 3D optimized geometries exhibit traits that cannot be fully represented in two dimensions. The relative size and placement of barbs in the x direction along the outer surface varies radially, which cannot be deduced from 2D examples. The non-uniform radial profile is likely a result of the square shaped design domain. The plain strain assumption used in 2D examples determines the physical response appropriate for an extruded 3D domain. Due to the cylindrical nature of the optimized geometry in 3D examples, the relative size of barbs is not directly comparable. For all 3D examples presented, the entirety of the interface remained in the bonded zone of cohesion. Note that the reduction of barbs size in the 3D examples when compared to 2D cases could be a result of the reduced applied load. However, these examples suggest that concluding 3D geometries from a 2D analysis may not be adequate depending on the intended application.

9.5 Discussion

This chapter presented a topology optimization framework for two-phase materials with cohesive interface phenomena. The interface condition is described by a bilinear cohesive zone model. To prevent surface penetration and to provide more accurate solution of the finite element analysis, the constitutive cohesive zone model is augmented by a stabilized Lagrange multiplier formulation. The material behavior of the mechanical model is described by linear elastic isotropic material and infinitesimal strains are assumed for the mechanical deformation. The XFEM is used to discretize and integrate the governing equations. To remedy the convergence difficulties for large separation and post delamination, an adaptive dynamic relaxation method is adopted for computing the static response.

An explicit LSM is used to describe the interface geometry between two distinct material phases. The LSF is defined by explicit functions of the optimization variables. The optimization problem is solved with a nonlinear programming method. The optimization problems studied in this chapter consider the mechanical response and penalty terms on the material interface surface area and a level set gradient measure to suppress sub-element geometric features. A constraint on

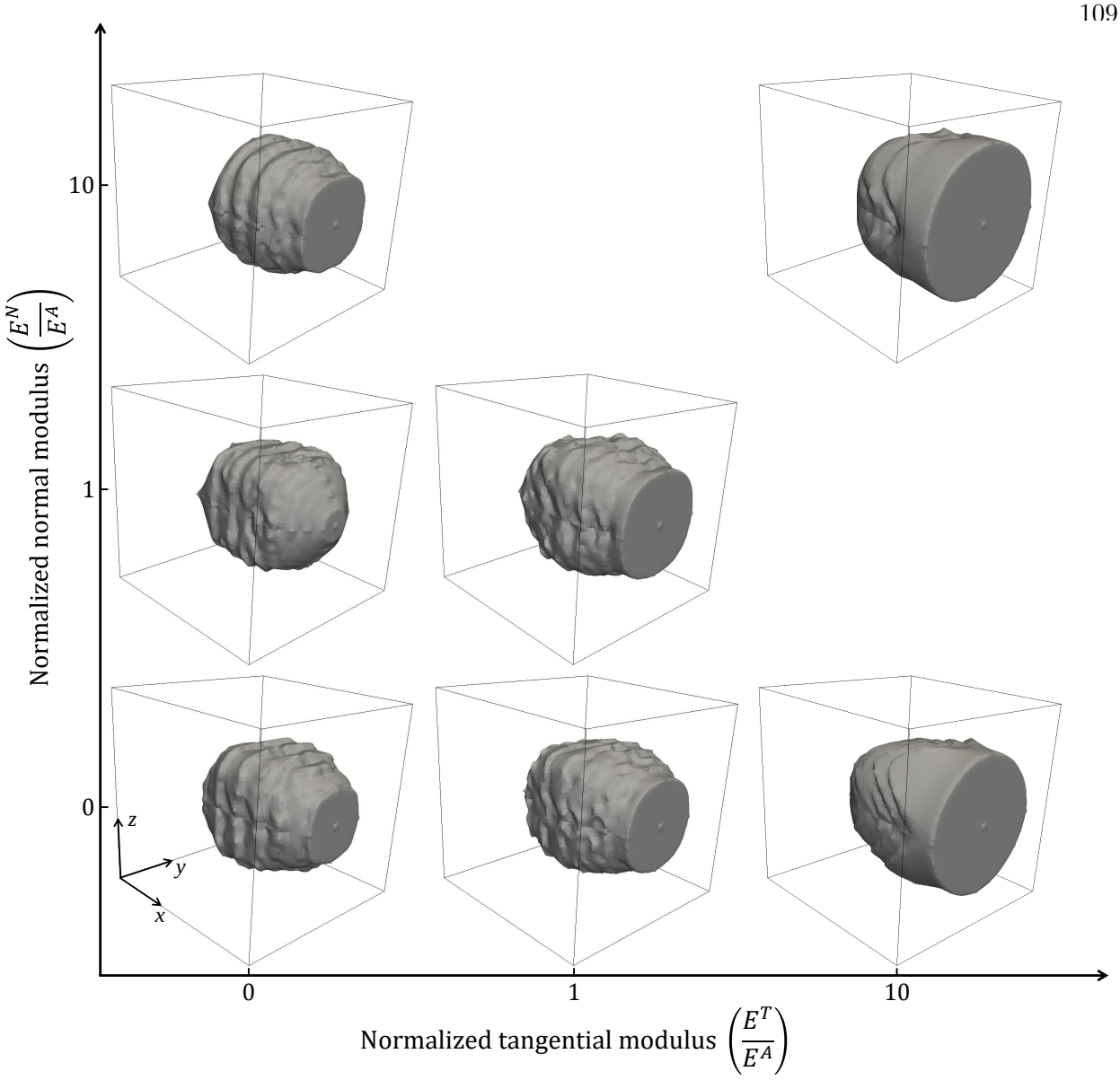

Figure 9.19: 3D view of the influence of interface conditions on the optimized design, $U_x^B = 0.007$m.

the volume ratio of the material phase is imposed. The design sensitivities are evaluated by the adjoint method.

The presented optimization framework proved reliable for a variety of 2D and 3D examples, optimizing the topology of a material anchor by maximizing the holding force. Perimeter measure regularization was employed, as it was shown in previous studies [59] to be effective in reducing the number and size of geometric features at a minimal cost to design performance. Gradient

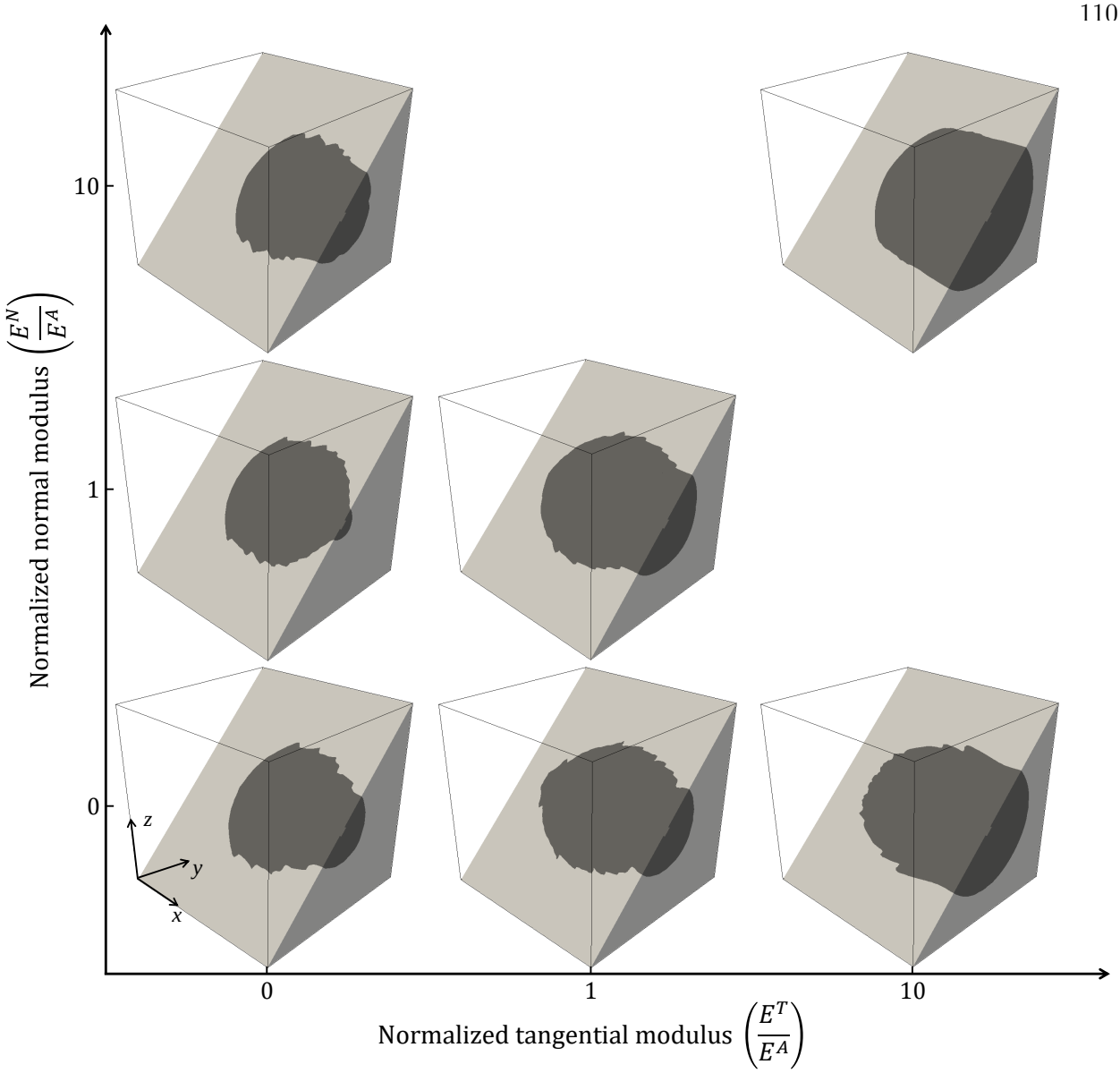

Figure 9.20: Inclined cross section view of the influence of interface conditions on the optimized design, $U_x^B = 0.007$m.

measure regularization was shown to be successful at removing small features that are problematic for accurate response prediction and for manufacturing considerations at a minimal cost to design performance. A volume constraint was imposed to prevent optimal geometries from being influenced by the outer design domain boundaries. Future studies on the effects of varied volume constraints should be explored. The interface conditions were shown to have a strong influence on optimized

geometry, as various levels of normal and tangential resistance yielded drastically different designs. An initial design experiencing total debonding was optimized to recover interface cohesion and a monotonic resistance to separation. The applied load study demonstrated that geometry can be tailored to localized regions where either cohesion or delamination are present. A three dimensional example revealed design traits that could not deduced from 2D studies, such as circumferential barb size and placement.

While only bilinear cohesion and frictionless contact were considered in this chapter, the developed method allows for the convenient extension of the framework for different interface constitutive relations. The applied load in three dimensional studies was reduced, as convergence difficulties in the mechanical model were encountered at higher loads.

Chapter 10

Large Sliding Frictionless Interface Studies

This chapter investigates topology optimization of finite strain theory, large sliding, frictionless bilateral contact problems in two dimensions. The material presented in this chapter are condensed from the resulting publication[58].

10.1 Introduction

Sliding contact phenomena between deformable structures play a crucial role in the functionality of many mechanical systems in commercial and industrial applications. Whether the desired functionality is to re-direct motion, provide a mechanical advantage, improve traction, or regulate stored energy, the performance of such systems is highly sensitive to interface geometry. Computational design optimization is well suited for these types of problems, as ideal design solutions can be non-intuitive. This chapter provides a shape and topology optimization method for problems involving large sliding, large deformation, frictionless contact and separation in two dimensions. While interfacial adhesion and friction are ignored in this chapter, the proposed framework allows for the inclusion of additional contact phenomena. As previously discussed, design optimization methods for contact related problems can be categorized by the type of geometry changes allowed during optimization (Figure 2.3). This chapter studies option (d) for two-phase problems, and a combination of options (b) and (c) for three-phase problems.

Analogous to Figure 2.3d, topology changes have been afforded through density methods in small strain [4, 94] and large strain [64], excluding the contact surface from geometry control. This,

however, severely restricts the optimal design solution space, as the functionality is often strongly correlated to the interface geometry. The optimization of unilateral contact surface geometries (similar to Fig. 2.3b) have been achieved with LSM for small strain theory problems; see for example [74]. Topology optimization including the material interface geometry has been achieved in a few small strain theory studies, namely for frictionless two-phase problems [59] and cohesive interface phenomena of multi-phase problems [63]. These two studies analyzed two dimensional problems and are comparable to option (d) and a combination of options (c) and (d) from Figure 2.3, respectively. In addition to the contact nonlinearities explored in Chapter 8, this chapter introduces large relative motion between components and large deformation of materials. Coincident surface location here is deformation dependent, complicating the solution of the physical response and evaluation of design sensitivities. These complexities pose interesting challenges for shape and topology optimization.

Previous studies of optimization in which the contact interface is altered rely on either small strain kinematics or unilateral contact to reduce the complexity of sliding contact behavior. In this chapter we expand the methods presented in [59] to the shape and topology optimization of bilateral contact problems with finite strain kinematics and large sliding contact. This marks a significant extension to the limits of accurate physical response prediction, which in turn grants access to a much broader scope of engineering problems.

The XFEM has been leveraged to analyze problems in which relative sliding is significant. Large sliding bilateral contact behavior was considered using an augmented Lagrange method and surface-to-surface (STS) integration in small strain [89] and hybrid elements in large strain theory [79]. In large strain theory, penalty methods have proven successful for unilateral contact problems [15] and bilateral contact problems with node-to-surface (NTS) integration [98]. In this chapter we adopt a large strain theory stabilized Lagrange multiplier method similar to the approach of [79]. However, instead of using hybrid elements, contact equilibrium is enforced weakly through STS integration at the immersed boundary.

The remainder of this chapter is organized as follows: in Section 10.2, we outline the formulation of the optimization problems considered in this study. In Section 10.3, the mechanical

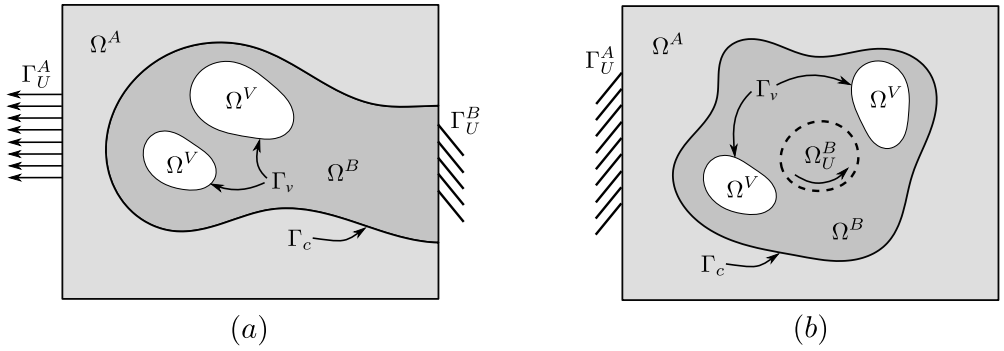

Figure 10.1: Representative configurations of optimization problems pertinent to this study.

model of the contact problem is described. In Section 10.4, the surface parametrisation scheme is outlined. In Section 10.5, we study the main characteristics of the proposed LSM-XFEM method with numerical examples. Insight gained from the numerical studies and areas for future research are summarized in Section 10.6.

10.2 Optimization Problem

In this chapter we consider the interactions between two solid phases, A and B, with sliding, separable contact at the phase boundaries. For select optimization problems, a void phase, V, is introduced within solid phase B. The optimization problems presented in this chapter can be illustrated by the representative configurations provided in Figure 10.1. The design domain Ω_D is composed by three non-overlapping subdomains, Ω^A, Ω^B, and Ω^V such that $\Omega_D = \Omega^A \cup \Omega^B \cup \Omega^V$. The contact interface Γ_C resides between the two solid phases such that $\Gamma_C = \Omega^A \cap \Omega^B$. The boundary between phase B and the void phase is denoted by $\Gamma_v = \Omega^B \cap \Omega^V$. To reduce interface complexities, such as triple junctions, the void subdomain, Ω^V, resides within Ω^B such that $\Omega^V \cap \Omega^A = 0$. The approach for restricting the void phase to reside within phase B is discussed in Section 2.4.2.

While the proposed optimization method is applicable to a broad range of problems, we focus in this chapter on two representative types of problems depicted in Figure 10.1 and studied in Section 10.5. The examples presented in Sections 10.5.4 and 10.5.5 are analogous to Figure 10.1(a),

wherein the displacements in phase B are prescribed along the boundary Γ_U^B and displacement controlled loading is applied at the boundary Γ_U^A. We seek to minimize an objective function related to the reaction load at Γ_U^B. The examples presented in Section 10.5.6 are analogous to Figure 10.1(b), wherein the displacements in phase A are prescribed along the boundary Γ_U^A and displacement controlled loading is applied within a subset of the domain occupied by phase B, Ω_U^B. For problems considered here, the objective is to minimize some function related to the reaction load at boundary Γ_U^A.

The design problems of interest are defined by the following nonlinear program:

$$\begin{aligned} &\min_{\mathbf{s}} q(\mathbf{s}), \\ \text{s.t. } &\frac{V^B(\mathbf{s})}{V^B(\mathbf{s}) + V^A(\mathbf{s})} - c_v \leq 0 \\ &\mathbf{s} \in \mathbf{S} = \left\{ \mathbb{R}^{N_s} | s_{min} \leq s_i \leq s_{max},\ i = 1....N_s \right\}, \end{aligned} \tag{10.1}$$

where q denotes the scalar objective, $\mathbf{s}$ is the vector of optimization variables, and the number of optimization variables is N_s; the lower and upper bounds on the optimization variables are denoted by s_{min} and s_{max}, respectively. For the scope of optimization problems studied in this chapter, the objective function, q, is defined as:

$$q(\mathbf{s}) = c_u \frac{z(\mathbf{s}, \hat{\mathbf{u}}(\mathbf{s}))}{z_0} + c_p \frac{P(\mathbf{s})}{P_0} \tag{10.2}$$

where z denotes the contribution of the mechanical response to the objective, c_u is the associated weighting factor, P is a measure of the perimeter, and c_p is the associated weighting factor. Both the contribution of the mechanical response and the perimeter measure are normalized by their initial value, z_0 and P_0 respectively. The perimeter penalty term, P, is introduced into the formulation of the objective function to discourage the emergence of small geometric features. The perimeter measure is the interface area of Γ_c and Γ_v, and is computed as follows:

$$P = \int_{\Gamma_c \cup \Gamma_v} \mathrm{d}\Gamma. \tag{10.3}$$

The mechanical response contribution and the perimeter measure penalty are normalized by the initial measures, z_0 and P_0, respectively. While a perimeter penalty does not explicitly control the

local shape and the feature size, it has been reported effective in regularizing structural optimization problems [104]. In addition, for specific problems we constrain the ratio of volumes occupied by either solid, V^A and V^B, to exclude trivial solutions. To provide control over the weighting of both the perimeter penalty and the volume inequality constraint, c_p is the weight of the perimeter penalty, and c_v controls the desired volume ratio between the two solids. While the proposed optimization framework allows considering other objectives and constraints, such as strain energy, displacement and stress measures, we found that the formulations of the optimization problem used here are well suited to illustrate the influence of the interface condition on the optimized design.

The dependency of the objective function and constraints on the optimization variables, $\mathbf{s}$, are defined by the framework described in Section 2.4. Note that the objective also depends on the structural response: $z(\mathbf{s}, \hat{\mathbf{u}})$, where $\hat{\mathbf{u}}$ denotes the vector of discretized state variables that are considered dependent variables of $\mathbf{s}$, i.e. $\hat{\mathbf{u}}(\mathbf{s})$. The discretized state equations are described in Section 10.3. The optimization problem is solved by a nonlinear programming (NLP) method, and the design sensitivities are calculated by the adjoint method.

10.3 Physics Model

Static equilibrium of phases Ω^A and Ω^B within the design domain is satisfied by the balance of linear momentum referred to the reference configuration Ω_0^p for $p = A, B$:

$$\nabla \cdot (\mathbf{F}^p \ \mathbf{S}^p) + \mathbf{b}_0^p = \mathbf{0} \quad \text{in } \Omega_0^p \ , \tag{10.4}$$

subject to the Dirichlet boundary conditions:

$$\mathbf{u}^p = \mathbf{U}^p \quad \text{on } \Gamma_U^p \ , \tag{10.5}$$

where $\mathbf{u}^p$ is the displacement vector, $\mathbf{F}^p$ is the deformation gradient tensor, $\mathbf{S}^p$ is the second Piola-Kirchhoff stress tensor, $\mathbf{b}_0^p$ is the reference configuration body force vector, and $\mathbf{U}^p$ is the vector of prescribed displacements at the boundary Γ_U^p. We assume a hyper-elastic neo-Hookean material behavior and a nonlinear kinematic relationship:

$$\mathbf{S}^p = \lambda^p \ \ln(\det \mathbf{F}^p) \ \ (\mathbf{C}^p)^{-1} + \mu^p \left(\mathbf{I} - (\mathbf{C}^p)^{-1}\right), \tag{10.6}$$

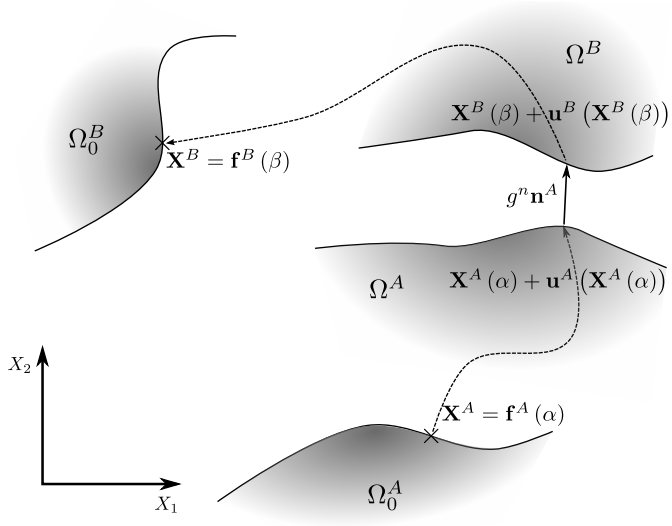

Figure 10.2: Parametric representation of surfaces belonging to materials A and B.

with

$$\mathbf{C}^p = \mathbf{F}^{pT}\,\mathbf{F}^p, \qquad \mathbf{F}^p = \frac{\partial \mathbf{x}^p}{\partial \mathbf{X}^p}, \qquad \mathbf{x}^p = \mathbf{u}^p + \mathbf{X}^p, \tag{10.7}$$

where λ^p and μ^p represent the material Lamé parameters, $\mathbf{C}^p$ is the right Cauchy-Green tensor, $\mathbf{I}$ is the identity matrix, $\mathbf{x}^p$ is the current position, and $\mathbf{X}^p$ is the reference position of phase $p = A, B$.

In the presence of large relative motion between surfaces, the dependence of coincident location along the interface on the displacements of either body needs to be accounted for. To this end, the surfaces of both structural phases are mapped to parametric space. This parametrization simplifies the definition of coincident surface location by describing surface position $\mathbf{X}^p$ and subsequently the displacements $\mathbf{u}^p$ in a reduced dimensional space. The surfaces of phase A and B are parameterized by some functions $\mathbf{f}^A$ and $\mathbf{f}^B$ of the surface parameters α and β respectively, as illustrated in Figure 10.2. The set of parametric functions, $\mathbf{f}^A$ and $\mathbf{f}^B$, used in this chapter are directly related to the method of discretization, and are detailed in Section 5.1.

To provide a continuous representation of coincident surface position, both surface parametrization schemes are coupled through the following relationship:

$$\mathbf{X}^A(\alpha) + \mathbf{u}^A\left(\mathbf{X}^A(\alpha)\right) + g_n \mathbf{n}^A\left(\mathbf{X}^A, \mathbf{u}^A\right) - \mathbf{X}^B(\beta) - \mathbf{u}^B\left(\mathbf{X}^B(\beta)\right) = \mathbf{0}\,, \tag{10.8}$$

where g_n is the magnitude of the gap between both surfaces in the direction of the deformed configuration surface normal $\mathbf{n}^A$; see Figure 10.2. Utilizing a master-slave approach, surface position β and the scalar normal gap g_n are defined through (10.8) for any given surface position α. Qualitatively, this expression states that for any given position along surface $\mathbf{x}^A$ in the current configuration, the coincident position along surface $\mathbf{x}^B$ can be found by a projection in the direction of the deformed surface normal, $\mathbf{n}^A$.

Along either surface in the reference configuration, the following non-penetration conditions apply:

$$g_0^p \ \lambda_0^p = 0, \ g_0^p \geq 0, \ \lambda_0^p \leq 0, \tag{10.9}$$

with

$$\lambda_0^p = (\mathbf{n}_0^p)^T \ \mathbf{S}^p \ \mathbf{n}_0^p, \tag{10.10}$$

$$g_0^p = g^n j^p, \tag{10.11}$$

$$j^p = \det(\mathbf{F}^p) \ \|\mathbf{F}^{p-T} \mathbf{n}_0^p\|, \tag{10.12}$$

where the g_0^p is the normal gap between the bodies pulled back to the reference configuration of material p, g^n is the normal gap between bodies in the deformed configuration, and λ_0^p is the surface traction in normal direction in the reference configuration. The Jacobian of the surface area, j^p, is derived from Nanson's formula, as outlined in [113]. As the bodies cannot interpenetrate, the gap must be greater than or equal to zero. The surface traction is negative when bodies are in contact, but vanishes as they separate. Thus, λ_0^p serves as the Lagrange multiplier of the non-penetration condition. Considering that in the deformed configuration the surface pressures are identical,

$$\lambda_B = \lambda_A \quad \text{and thus} \quad \lambda_0^B j^{B^{-1}} = \lambda_0^A j^{A^{-1}}, \tag{10.13}$$

we express the surface pressure with just λ_0^A, residing within the master reference configuration, $\Gamma_{c,0}^A$. In particular, $\Gamma_{c,0}^A$ is the undeformed contact surface of phase A. To simplify notation, we

drop the superscript and define the Lagrange multiplier as $\lambda_0 \equiv \lambda_0^A$. Provided that in three-phase problems we do not allow the void material interface to directly connect to the contact interface Γ_c , i.e. $\phi^1 = \phi^2 = 0$, both material surfaces are coincident in the reference configuration and the initial gap, g_n, is zero.

The XFEM discretization of the contact problem is based upon the following stabilized weak form of the governing equations:

$$\sum_{p=A,B} \int_{\Omega_0^p} \mathbf{F}(\boldsymbol{\nu}^p) : (\mathbf{F}^p \mathbf{S}^p) \; d\Omega - \sum_{p=A,B} \int_{\Omega_0^p} \boldsymbol{\nu}^p \cdot \mathbf{b}_0^p \; d\Omega \\ - \sum_{p=A,B} \int_{\Gamma_{N,0}^p} \boldsymbol{\nu}^p \cdot \mathbf{T}_0^p \; d\Gamma - \int_{\Gamma_{c,0}^A} \delta g_0^A \; \lambda_0 \; d\Gamma + r^G = 0 \; , \quad (10.14)$$

where $\boldsymbol{\nu}^p$ is an admissible test function, $\mathbf{T}_0^p$ is a prescribed traction at the external boundary $\Gamma_{N,0}^p$, δg_0^A is the variation of the normal gap pulled back to the undeformed surface of phase A, and r^G is a stabilization term discussed in Section 10.4.2. Similar to the augmented Lagrange formulation presented by [113], the Lagrange multiplier is governed by the following constraint equation:

$$\int_{\Gamma_{c,0}^A} \mu \; \left(\lambda_0 - \tilde{\lambda_0} - \gamma \; g_0^A \right) \; d\Gamma = 0, \quad (10.15)$$

with

$$\tilde{\lambda_0} = \kappa^A \mathbf{n}_0^{A^T} \mathbf{S}^A \mathbf{n}_0^A + \kappa^B \mathbf{n}_0^{B^T} \mathbf{S}^B \mathbf{n}_0^B j^{B^{-1}} j^A \quad (10.16)$$

where μ is a test function for the non-penetration condition, $\tilde{\lambda_0}$ is a weighted average of the surface traction in the normal direction and κ^p are weighting factors such that $\kappa^A + \kappa^B = 1$. In our experience, the penalty factor γ discourages penetration during the early stages of convergence, but becomes less significant as equilibrium is achieved and the gap value g_0^A approaches zero. The formulations for κ^p and γ are related to discretization, and are provided in Section 5.1. The constraint equation (10.15) and contact contributions to the weak form of the equilibrium equations (10.14) are integrated over $\Gamma_{c,0}^A$, and an active set strategy is used to handle the inequality constraint regarding surface separation.

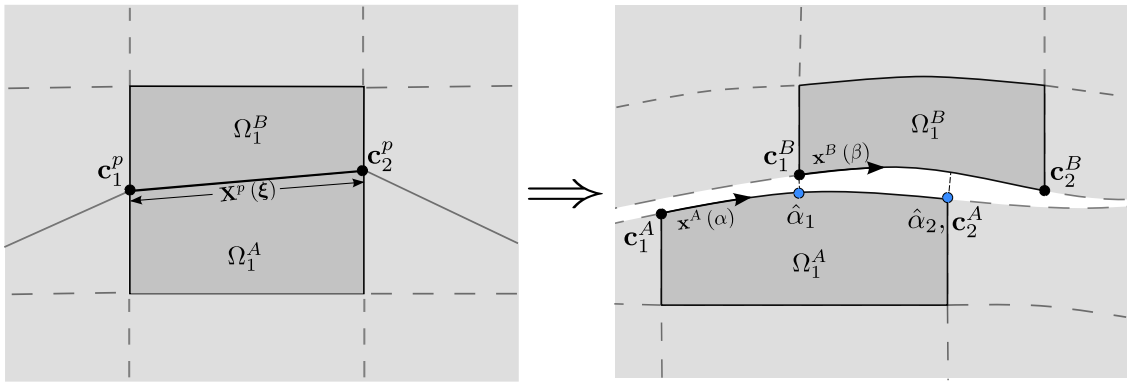

(a) (b)

and current (b) configuration.

Figure 10.3: Element immersed surface parametrization in the undeformed (a)

10.4 Numerical Implementation

10.4.1 Contact Equilibrium Contributions

The XFEM retains a piece-wise continuous definition of the interface geometry subject to the chosen method of LSF interpolation. For STS integration of the contact contributions to the equilibrium equation (10.14), coincident locations at the contact interface must be identified as illustrated in Figure 10.3. Locations $\mathbf{c}_1^p$ and $\mathbf{c}_2^p$ correspond to the interface boundaries for a particular element of phase p, while $\hat{\alpha}_1$ and $\hat{\alpha}_2$ are the limits of integration for this particular element pair. Provided that the coincident surface location is governed by (10.8), element integration limits are deformation dependent. To recover a fully consistent tangent stiffness, which is essential to the accuracy of the adjoint sensitivity analysis, these integration limit dependencies on the solution must be accounted for.

If the integration limit coincides with the element boundary of phase A, i.e. $\mathbf{x}^A(\hat{\alpha}_i) = \mathbf{c}_i^A$, it is solution independent. However, if the integration limit $\hat{\alpha}_i$ does not coincide with the elemental boundary $\mathbf{c}_i^A$, as is the case for $\hat{\alpha}_1$ in Figure 10.3, its position depends on the projection of $\mathbf{c}_1^B$ onto the phase A surface in the deformed configuration. The integration limit $\hat{\alpha}_1$ and its dependencies on the displacement field are defined through (10.8).

In this chapter, the zero level set iso-contour is interpolated linearly within an intersected element and the position of a point on the intersection is parameterized by:

$$\mathbf{X}^p(\xi) = (1-\xi)\,\mathbf{c}_1^p + \xi \mathbf{c}_2^p \ , \tag{10.17}$$

where the local coordinate ξ corresponds to either α or β for phase A or B respectively. The test and trial functions for the normal surface traction, μ and λ_0, are piecewise linear for each STS element pair, but not necessarily continuous across element boundaries. Thus, the associated degree of freedom can be computed for each STS element pair and condensed from the global system of equations.

Following the work of [6], the weighting factors κ^p for computing the average normal traction in (10.16) depend on the elemental intersection configuration as follows:

$$\begin{aligned} \kappa^A &= \frac{|\Omega|^A/E^A}{|\Omega|^A/E^A + |\Omega|^B/E^B} \ , \\ \kappa^B &= \frac{|\Omega|^B/E^B}{|\Omega|^A/E^A + |\Omega|^B/E^B} \ , \end{aligned} \tag{10.18}$$

where $|\Omega|^p$ denotes the elemental volume occupied by phase $p = A, B$ and E^p is the Young's modulus of phase $p = A, B$. The penalty factor in (10.15) depends on the element size h and is set to:

$$\gamma = \frac{E^A + E^B}{h} \ . \tag{10.19}$$

10.4.2 Stabilization

During the design optimization process, the interface of the embedded geometry may produce intersection configurations where certain degrees of freedom interpolate to very small subdomains. This causes an ill-conditioning of the mechanical model system, which may impede the convergence of the nonlinear problem. In the context of contact problems, the vanishing zone of influence of a particular degree-of-freedom may also result in artificially high stress approximations in localized regions near the interface, leading to the erroneous evaluation of the contact pressure. To mitigate ill-conditioning of the system and poor structural response prediction at the interface, we apply a

face-oriented ghost-penalty formulation. Similar to the stabilization method for diffusion problems presented by [17], we penalize the jump in stress across element borders, and define the stabilization term r^G in (10.14) as:

$$r^G = \sum_{p=A,B} \int_{\Gamma_e^0} \gamma^G \left[\!\left[\frac{\partial \boldsymbol{\nu}^p}{\partial \mathbf{X}} \right]\!\right] \mathbf{n}_e^0 \left[\!\left[\mathbf{S}^p \right]\!\right] \mathbf{n}_e^0 \mathrm{d}\Gamma, \tag{10.20}$$

where Γ_e^0 is the reference configuration boundary of intersected elements, γ^G is a penalty parameter, $\boldsymbol{\nu}$ is an admissible test function, $\mathbf{n}_e^0$ is the reference configuration surface normal of the element boundary, and the jump operator,

$$[\![\zeta]\!] = \zeta|_{\Omega_e^1} - \zeta|_{\Omega_e^2}, \tag{10.21}$$

computes the difference of a particular quantity across the facet between two adjacent elements, Ω_e^1 and Ω_e^2. The penalty parameter, γ^G, is defined as:

$$\gamma^G = \epsilon \; h \tag{10.22}$$

where ϵ is a problem-specific scaling factor and h is the element side length. The jump in stress is penalized across the entire element border, irrespective of where the interface intersects it. Face-oriented ghost penalization has been reported as being beneficial to various fluid flow related problems, including fluid-solid interactions [16], high Reynolds number flows [88], and incompressible flows [87]. For more information the reader is referred to Section 7.2.

10.4.3 Dynamic Relaxation

Contact problems often experience moments of neutral equilibrium, and can exhibit snap-through behavior. In this work the discretized mechanical model is solved using a Newton-Raphson iterative procedure, which may suffer from convergence difficulties in such scenarios. To mitigate these issues, we use a Levenberg-Marquardt [71] type method for dynamic relaxation. Initially developed to solve non-linear least square problems, this algorithm has also been reported useful in reducing analysis instabilities caused by element distortion in compliant mechanism optimization problems [48]. We adopt a similar approach by modifying the tangent stiffness matrix:

$$\tilde{\mathbf{J}} = \mathbf{J} + \beta \; \mathrm{diag}\left(\mathbf{J}\right) \;, \tag{10.23}$$

where $\mathbf{J}$ is the original tangent stiffness matrix, β is the damping parameter, and $\tilde{\mathbf{J}}$ is the modified tangent stiffness matrix. The damping parameter is given an initial value, and adaptively increased or decreased by a factor of 10 depending on whether the satisfaction of equilibrium improves or deteriorates throughout the iterative solution procedure. The initial value of the damping parameter is $\beta = 0.01$ for the problems presented in this chapter. For more information, the reader is referred to Section 7.3.

10.5 Numerical Examples

To demonstrate the accuracy of the proposed framework, we first verify both the physical response prediction and adjoint method. Subsequently, a comparative study explores optimal design improvements for large strain theory over small strain theory. Finally, problems with objectives that characterize the structural response during a quasi-static loading process illustrate the main characteristics of the proposed framework.

For all examples, we assume plane strain conditions and a quasi-static response. Finite strain kinematics and large sliding contact are used unless specified otherwise. The mechanical model is discretized with bilinear Quad-4 elements using the framework described in Section 5.1. The nonlinear contact problems are solved by Newton's method with dynamic relaxation, using an active set strategy for the contact conditions. A drop of the residual of 10^{-6} relative to the initial residual is required, unless stated otherwise. Loads are applied incrementally, and a direct solver is used for the linearized sub-problems.

The parameter optimization problems are solved by the Globally Convergent Method of Moving Asymptotes (GCMMA) of [97]. The parameters for the initial, lower, and upper asymptote adaptation are set to 0.5, 0.7, and 1.2, respectively. The relative step size, Δs, is given with each example. The design sensitivities are computed with the adjoint method. The reader is referred to [7], [54] and [53] for an in depth discussion of sensitivity analysis for contact problems. In this work, the partial derivatives of the state equations and objective function with respect to the state variables are evaluated using analytically differentiated formulations. The partial derivatives

of the objective, constraints, and element residuals with respect to the optimization variables are calculated by a finite difference scheme, which is computationally inexpensive as only intersected elements need to be considered.

10.5.1 Mechanical Model Verification: Planar Interface

Consider a rectangular domain with a linear interface shown in Figure 10.4. The rectangular

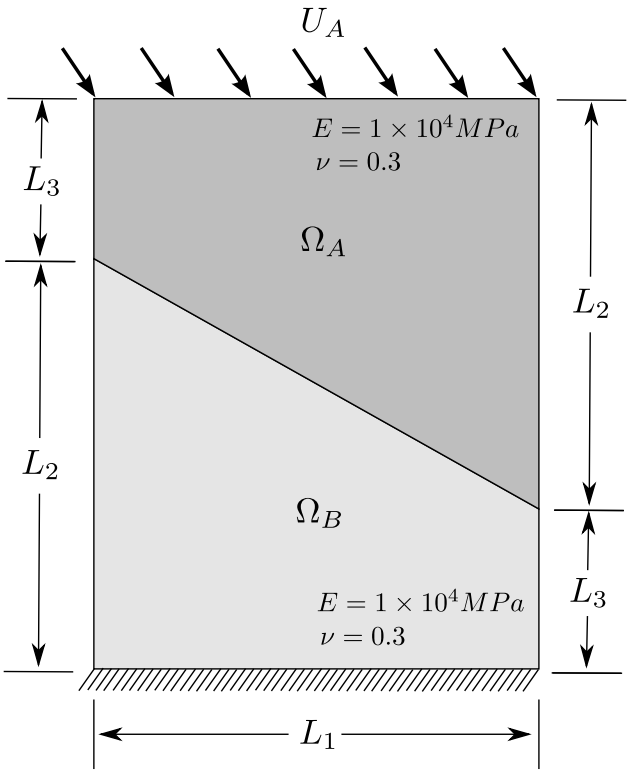

Figure 10.4: Large strain, frictionless contact benchmark setup.

domain is composed of two non-overlapping subdomains Ω_A and Ω_B such that $\Gamma_c = \Omega_A \cap \Omega_B$ is the contact interface. Dimensions for the model are $L_1 = 4m$, $L_2 = 3.9m$, and $L_3 = 2.1m$. Subdomains Ω_A and Ω_B are neo-Hookean materials of the same properties, where frictionless contact is imposed at Γ_c via a stabilized Lagrange method. A contact search algorithm is employed to determine overlapping element segments. Displacements at the top edge of Ω_A are prescribed as $U_x^A = 0.3$ and $U_y^A = -0.3$, whereas the bottom edge of Ω_B is fixed. This example is chosen to demonstrate the convergence behavior of total contact force and penetration error with mesh refinement.

To examine the convergence behavior of the mechanical model, the problem was run for four different mesh sizes: Mesh 1 consists of 7×9 elements, Mesh 2 contains 13×19 elements, Mesh 3 has 21×31 elements, and Mesh 4 consists of 41×61 elements. The consistent tangent stiffness derived in Section 6.2.2.6 results in forward analysis quadratic convergence, requiring on average 4-10 newton iterations to converge to a tolerance of 1×10^{-8}. Surface contact forces and normal penetration errors were extracted at the interface for all models. Figure 10.5 demonstrates the total contact force convergence with mesh refinement.

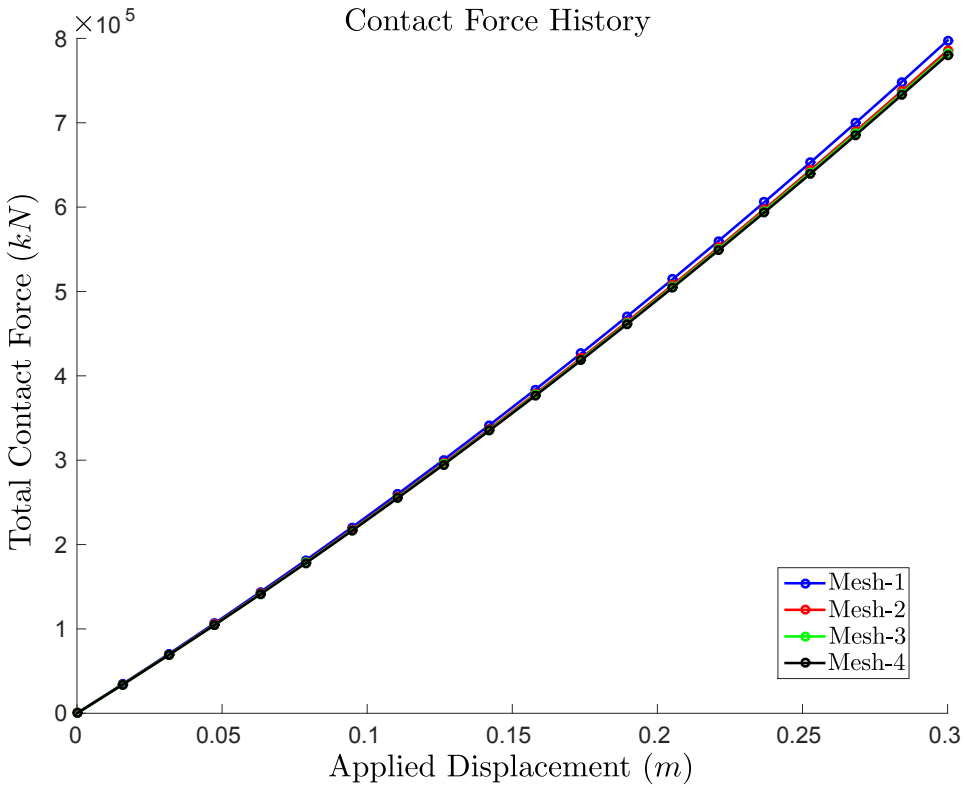

Figure 10.5: Total surface force convergence with Mesh refinement.

For verification, this benchmark problem was modeled in Abaqus using a body-fitted mesh and Quad-4 plain strain elements. Interface conditions were represented using a surface-to-surface, frictionless stabilized Lagrange formulation. All material parameters and model dimensions were kept consistent with Figure 10.4. The accuracy of the stress prediction of the current mechanical model to a body fitted solution produced by Abaqus is illustrated in Figure 10.6. Furthermore, the

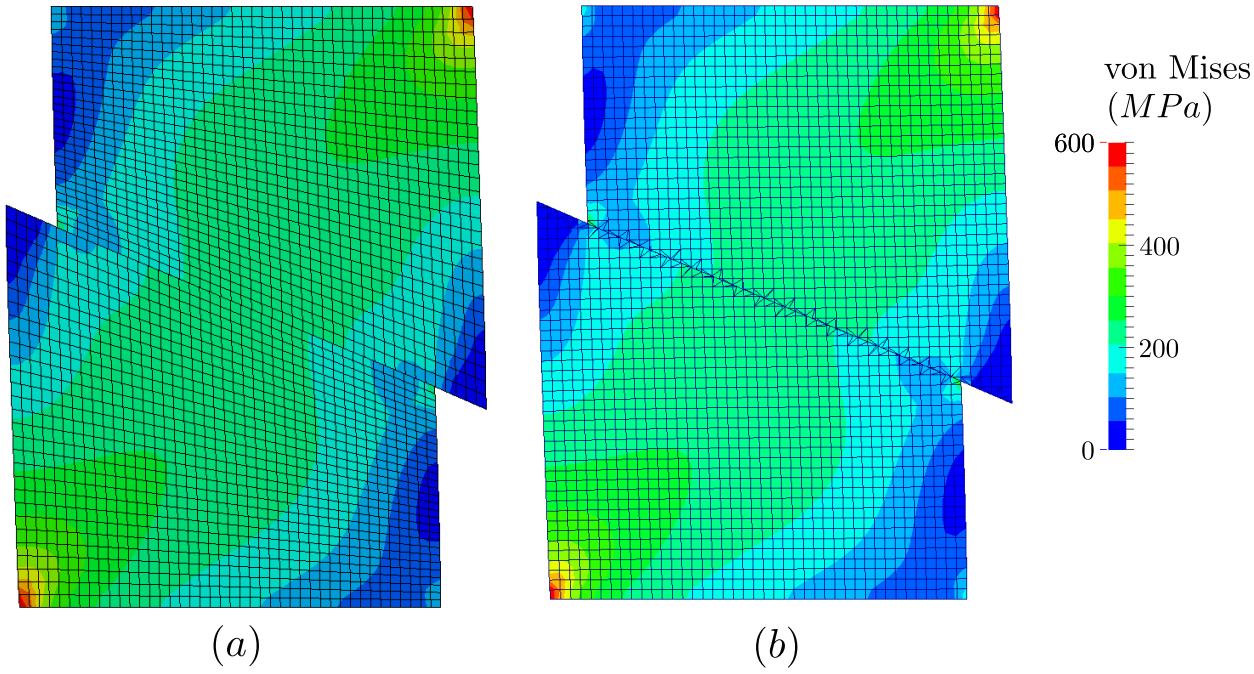

Figure 10.6: Comparison of von Mises stress for (a) Abaqus and (b) current implementation.

total contact force was measured at the interface and plotted as a function of applied displacement. The comparison between the current framework and results produced by Abaqus are illustrated in Figure 10.7.

10.5.2 Mechanical Model Verification: Curved Interface

To verify the accuracy of the XFEM mechanical model, a benchmark example is studied and compared to results produced by Abaqus® using a conformal mesh. We consider a square domain which is composed of two non-overlapping subdomains Ω^A and Ω^B; see Figure 10.8. The contact interface $\Gamma_c = \Omega^A \cap \Omega^B$ is defined by an arc of radius r. The volumes occupied by either phase, Ω^A and Ω^B, are modeled by neo-Hookean materials of the same properties. Displacements at the top edge of Ω_A are prescribed and incrementally increased in 50 load steps to a maximum value of $U_x^A = 0.5$ and $U_y^A = 0.0$. The bottom edge of Ω_B is fixed. Dimensions and material properties for the model are presented in Table 10.1.

To examine the convergence behavior of the mechanical model, the problem is analyzed for

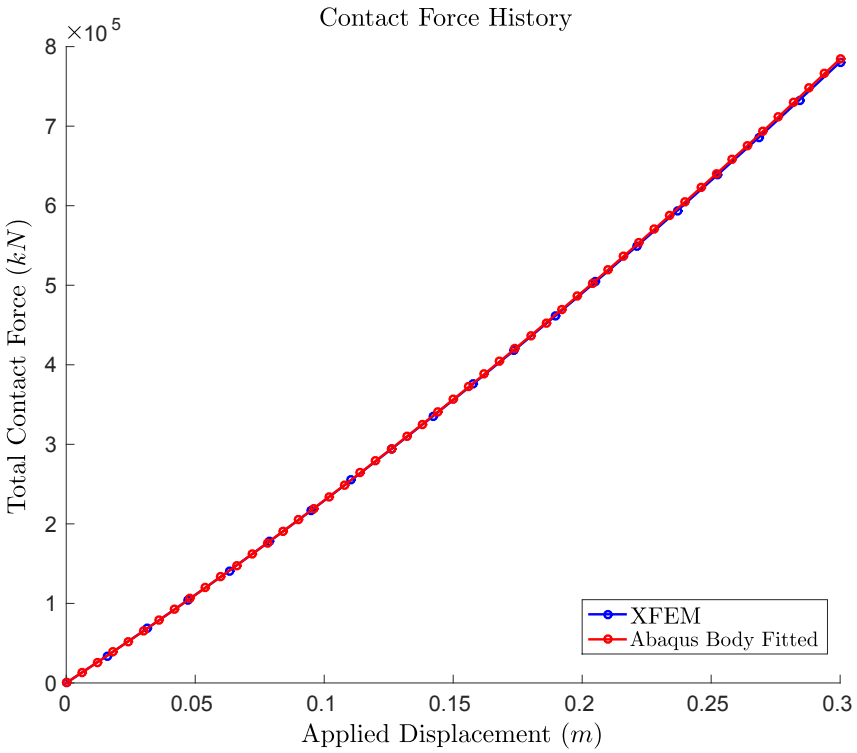

Figure 10.7: Comparison of total contact force as a function of applied displacement.

four different mesh sizes: Mesh 1 consists of 5×5 elements, Mesh 2 contains 11×11 elements, Mesh 3 has 21×21 elements, and Mesh 4 consists of 51×51 elements. The coupled parametric representation

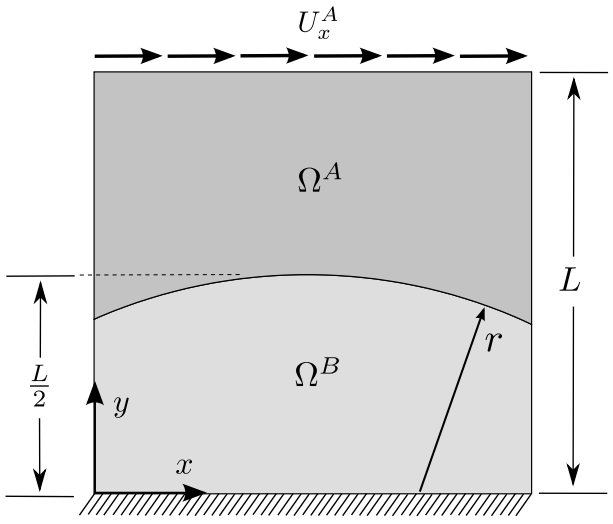

Figure 10.8: Large strain, frictionless contact benchmark setup.

Description	Parameter
domain length	$L = 1.0$ m
interface radius	$r = 1.2$ m
Young's modulus	$E^A = 10$ MPa
Young's modulus	$E^B = 10$ MPa
Poisson's ratio	$\nu^A = 0.3$
Poisson's ratio	$\nu^B = 0.3$
applied displacement	$U_x^A = 0.5$ m

Table 10.1: Benchmark mechanical model parameters.

of coincident surface location facilitates a quadratic convergence, requiring on average 6 Newton iterations to converge to a tolerance criterion of 1×10^{-9}. Surface contact forces and normal penetration errors are extracted at the interface. Figure 10.9 demonstrates the total contact force convergence with mesh refinement.

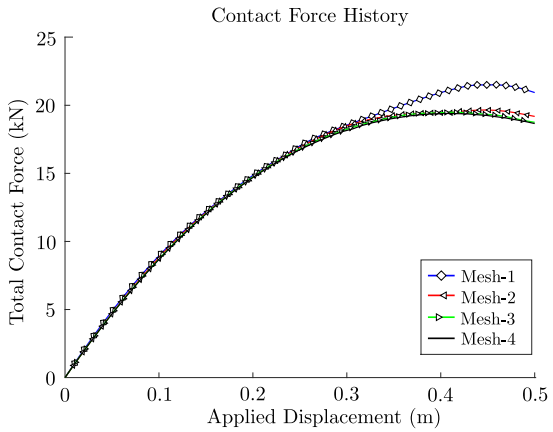

Figure 10.9: Total surface force as a function of applied displacement.

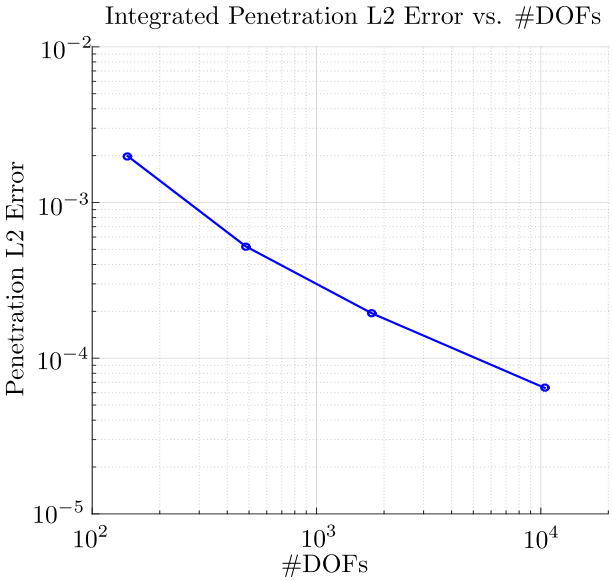

Figure 10.10: Integrated L_2 error with mesh refinement.

Additionally, Figure 10.10 illustrates the integrated penetration L_2 error for each mesh used. The L_2 error is determined as follows:

$$\text{L}_2 \text{ error} = \sqrt{\frac{\int_{\lambda_0<0} \int_{\Gamma_c} g_n^2 \, \mathrm{d}\Gamma \mathrm{d}t}{\int_{\Gamma_c} \mathrm{d}\Gamma}} \,, \tag{10.24}$$

where t is a pseudo-time which describes the loading process, and g_n is the normal gap between surfaces in contact. The normal gap, g_n, is only integrated across contact element pairs when they are in an active state of contact, i.e. $\lambda_0 < 0$. The curved interface is described by a linearly interpolated LSF. This approach leads to a segmented interface that may yield poor response predictions at low levels of mesh discretization. As the mesh is refined, the force profile converges; see Figure 10.9. Considering the non-penetration condition is enforced weakly at the interface, surface penetration error diminishes with mesh refinement; see Figure 10.10. While the general rate of convergence appears to be linear, the author notes that due to the coarseness of the first

two meshes some deviation could be due to pre-asymptotic behavior.

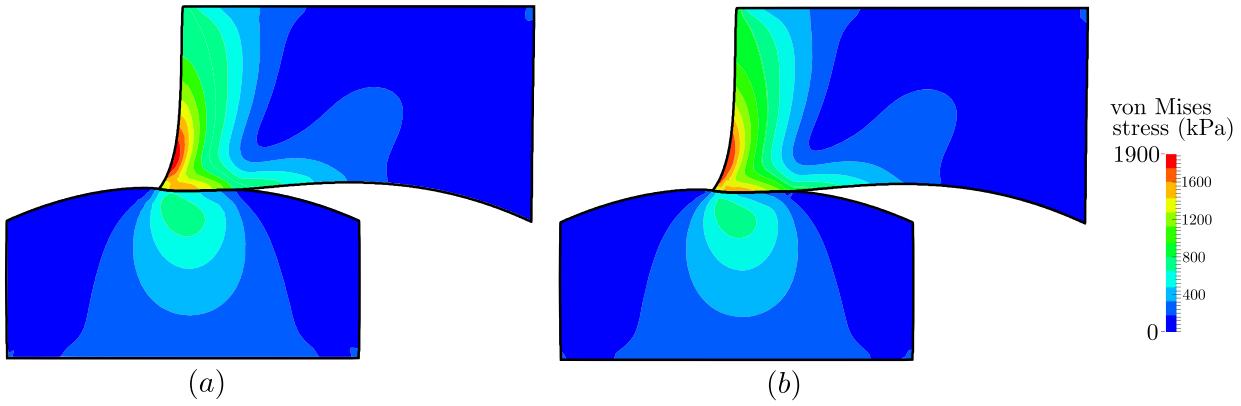

Figure 10.11: Comparison of von Mises stress for (a) Abaqus® and (b) current implementation.

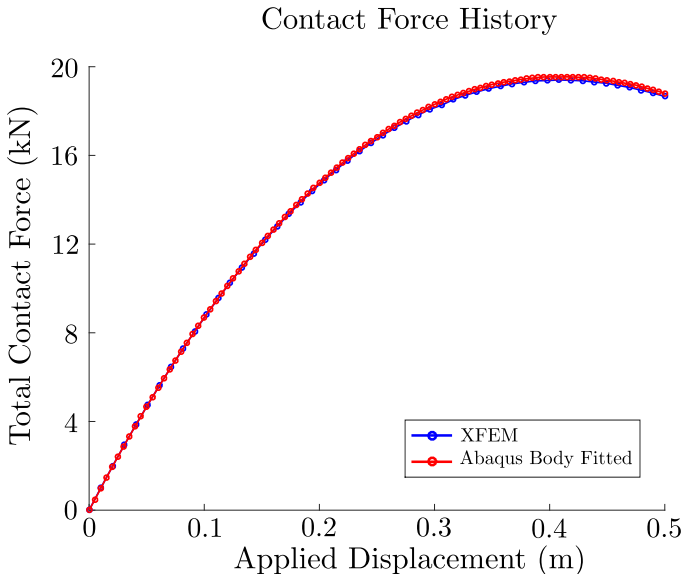

Figure 10.12: Comparison of total contact force as a function of applied displacement.

For verification purposes, this benchmark problem is modeled in Abaqus® using a body-fitted mesh with 50×50 Quad-4 plane strain elements. Interface conditions in Abaqus® are enforced using a surface-to-surface, frictionless augmented Lagrange formulation. All material parameters and model dimensions are kept consistent with Figure 10.8 and Table 10.1. The stress prediction of our XFEM model is compared to the Abaqus® results in Figure 10.11. Furthermore, the results for the total contact force as a function of the applied displacements are shown in Figure 10.12. The

relative difference between the XFEM and Abaqus® force predictions, integrated over the loading process, is 6.5×10^{-4}.

10.5.3 Sensitivity Analysis Verification

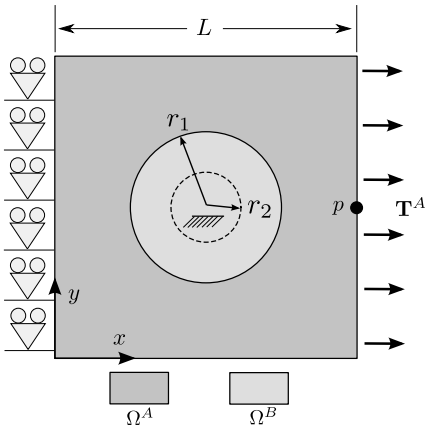

Figure 10.13: Sensitivity verification model setup.

Description	Parameter
domain length	$L = 1.0$ m
interface radius	$r_1 = 1.2$ m
fixed radius	$r_2 = 0.125$ m
Young's modulus	$E^A = 10$ MPa
Young's modulus	$E^B = 10$ MPa
Poisson's ratio	$\nu^A = 0.3$
Poisson's ratio	$\nu^B = 0.3$
applied load	$\mathbf{T}^A = (10, 0)$ kPa/m
observation point	p

Table 10.2: Sensitivity verification model parameters.

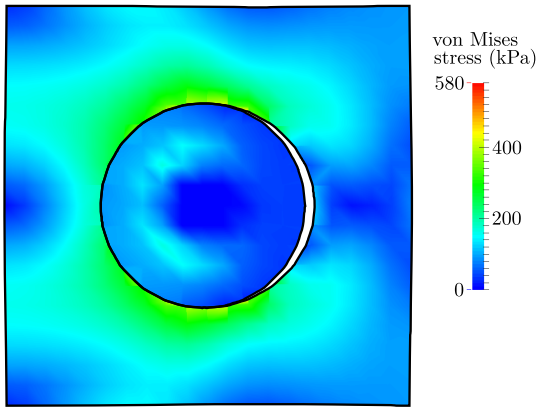

Figure 10.14: Von Mises stress distribution for $r_1 = 0.275$ m.

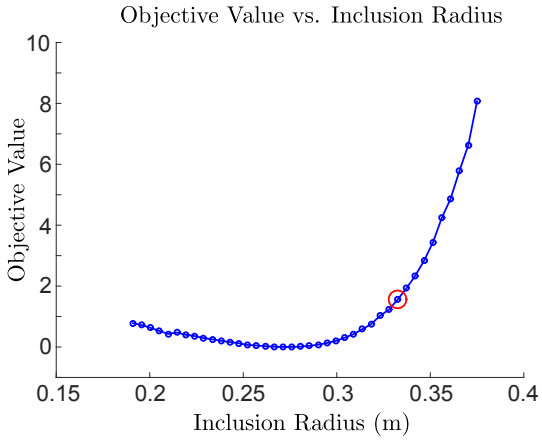

Figure 10.15: Objective value as a function of material interface radius; sensitivity evaluated for range of radii highlighted in red.

To verify the accuracy of the design sensitivities evaluated by the adjoint method for problems involving large sliding contact, we consider the optimization problem illustrated in Figure 10.13. The square design domain of length L is held in place by a circular inclusion of radius r_1, fixed

within radius r_2. In addition, the left hand edge of the design domain is constrained in the y-direction. An external traction $\mathbf{T}^A$ is distributed along the right hand edge and applied in two load steps. Frictionless contact is modeled at the material interface. The converge criterion for solving the nonlinear systems in each load step by Newton's method is set to 1×10^{-9}. The XFEM model is discretized with 20×20 elements. The model parameters are listed in Table 10.2.

The objective function is defined as:

$$z = 1 \times 10^4 \left(u_x(p) - 2.7731 \times 10^{-2} \right)^2. \tag{10.25}$$

The design variable, s, defines radius of the circular inclusion, i.e. $r_1 = s$. The inclusion is described by the following LSF:

$$\phi = r_1 - \sqrt{(\mathbf{x} - 0.5)^2 + (\mathbf{y} - 0.5)^2}. \tag{10.26}$$

To evaluate the behavior of the objective function with respect to the design variable, the inclusion radius is swept from $0.191 \leq r_1 \leq 0.375$. Figure 10.14 illustrates the mechanical response at $r_1 = 0.275$ m. The objective value over the interface radius is plotted in Figure 10.15. The results show a rather smooth dependency of the objective on the interface radius.

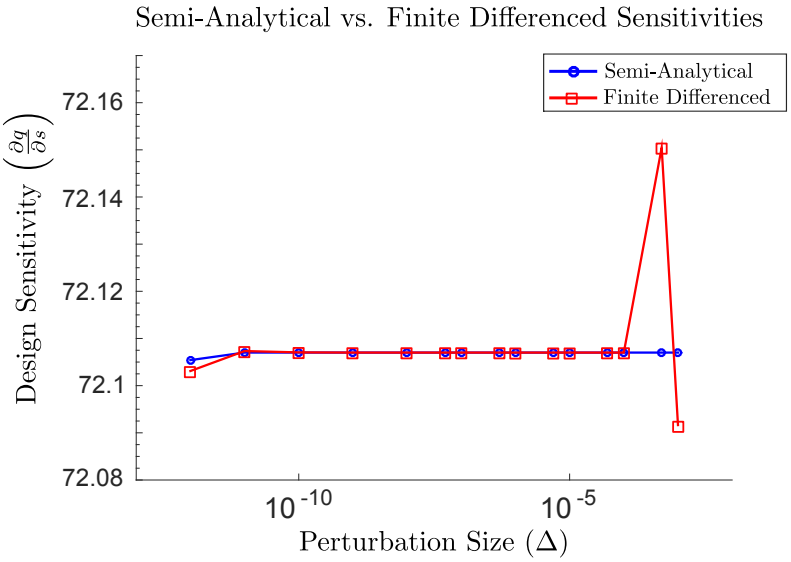

Figure 10.16: Sensitivity of objective value with respect to inclusion radius evaluated by semi-analytical adjoint method and finite differencing over a range of perturbation sizes.

To verify our adjoint sensitivity analysis method, the semi-analytical evaluation of the sensitivities is compared to the results of a central finite differencing scheme. Figure 10.16 plots the semi-analytical and finite differenced sensitivities as a function of the perturbation size. At extremely small perturbation sizes, machine precision round off errors affect the accuracy of the design sensitivities. For this particular problem, perturbation sizes larger than $\Delta s > 10^{-4}$ yield linearization errors when using finite differencing. For perturbations between 10^{-8} and 10^{-5} there is good agreement between both semi-analytical and finite differenced values. The relative error between both methods at a perturbation size of 10^{-8} is 4.62×10^{-10}. However, in addition to being computationally less expensive, the adjoint method is less sensitive to the perturbation size than finite differenced design sensitivities.

10.5.4 Material Anchor Design Problem

To compare designs optimized with finite strain theory to designs optimized with infinitesimal strain theory, we study a material anchor design problem. A structural anchor is embedded within a host material of the same properties, with frictionless contact at the interface to afford resistance to separation. The objective is to find an optimized anchor geometry such that the resistance is maximized. This problem was originally studied under a small strain assumption by [59]. The initial material distribution and boundary conditions are illustrated in Figure 10.17, while model parameters are listed in Table 10.3. The volume occupied by the anchor material, Ω^B, is fixed at Γ_1, while a prescribed displacement, U_x^A, is applied to the volume occupied by the host material, Ω^A, along Γ_{2-4}. Displacements are constrained to zero in the y direction along Γ_{2-4}. To prevent the anchor material from directly connecting boundary Γ_1 to boundaries Γ_{2-4}, they are excluded from the design domain.

For this example, we wish to determine the optimal geometry such that the force at Γ_1 is maximized. The mechanical response contribution to the objective function in Equation (10.1) is

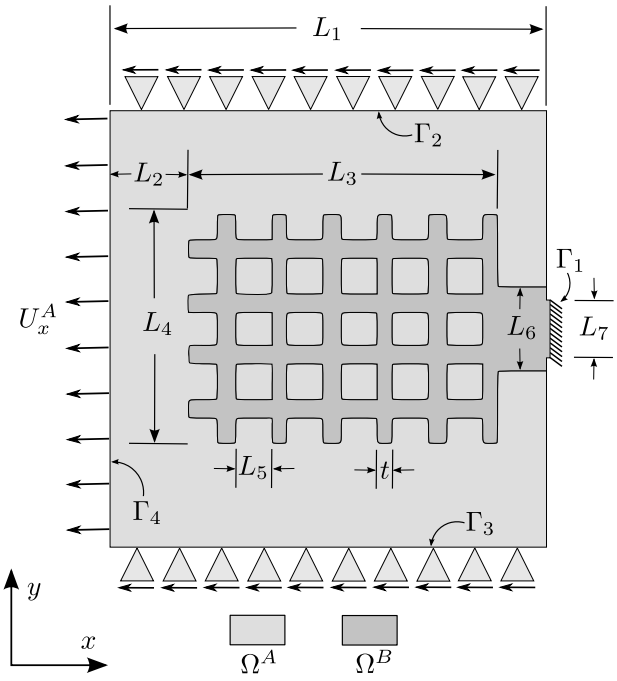

Figure 10.17: Material anchor initial configuration.

Description	Parameter
domain length	$L_1 = 1.0$ m
host depth	$L_2 = 0.175$ m
lattice length	$L_3 = 0.715$ m
lattice width	$L_4 = 0.523$ m
cuboid length	$L_5 = 0.0833$ m
anchor base width	$L_6 = 0.2$ m
fixed support width	$L_7 = 0.133$ m
lattice thickness	$t = 0.038$ m
Young's modulus	$E^A = 10$ MPa
Young's modulus	$E^B = 10$ MPa
Poisson's ratio	$\nu^A = 0.3$
Poisson's ratio	$\nu^B = 0.3$
applied displacement	$U_x^A = 0.01$ m
response weight	$c_u = 75$
penalty weight	$c_p = 25$
volume ratio	$c_v = 0.5$
opt. upper bounds	$s_{max} = 8.33 \times 10^{-3}$
opt. lower bounds	$s_{min} = -8.33 \times 10^{-3}$
rel. step size	$\Delta s = 8 \times 10^{-3}$
smoothing radius	$r_f = 0.0375$ m

Table 10.3: Nominal material anchor model parameters.

defined as:

$$z = 100 - \int_{\Gamma_1} \sigma_{xx} \mathrm{d}\Gamma, \tag{10.27}$$

where σ_{xx} denotes the normal Cauchy stress in the x direction. To regularize the problem, a perimeter penalty of $c_p = 0.25$ is applied. To prevent the anchor material from occupying the majority of the design space, a volume constraint of 50 % is applied to the anchor material, i.e. $c_v = 0.5$. Due to the symmetric nature of the problem, only one half of the domain is analyzed with 120×60 elements. The linear level set filter (2.10) for this problem is set to $r = 4.5h$, where h is the element side length.

10.5.4.1 Nominal Design

We first present the results of the material anchor nominal design, using the design parameters listed in Table 10.3. The magnitude of applied load for this example, $U_x^A = 0.01$ m, was specifically

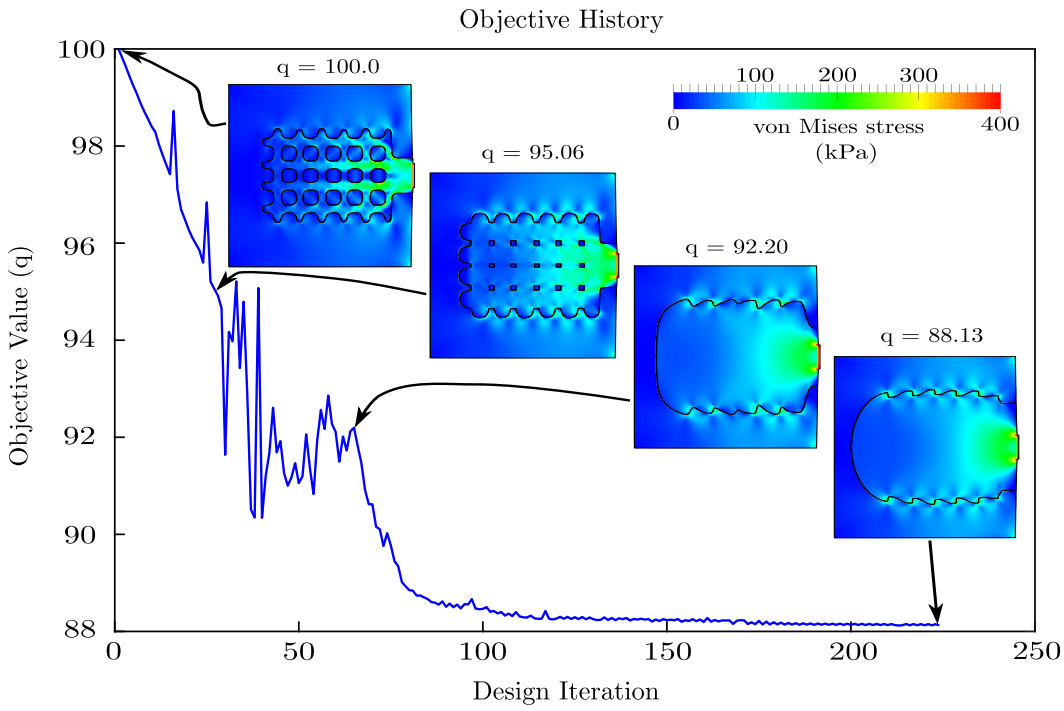

Figure 10.18: Material anchor design objective history with snapshots of specific iterations. Inset depicts the force-displacement curve for specific iterations.

chosen to keep the experienced strain well within the limitations of small strain theory. This allows comparing the results of the proposed optimization method for large strain contact with the results of [59] where infinitesimal strains, a linear elastic response, and negligible sliding between surfaces were assumed. Here, the displacement, U_x^A, is applied in two load steps.

Figure 10.18 illustrates the objective value history during optimization, supported by snapshots of the mechanical response for specific design iterations. The anchor material quickly merges to a uniform body, producing ridges or spines along the outer surface to afford resistance to separation. In the early stages of convergence, topological changes result in an abrupt change in the measured objective value. Once the topology remains unchanged, the optimization process converges smoothly. The optimized geometry closely resembles the small strain theory analog presented by [59].

10.5.4.2 Load Case Study

Even for problems which maintain small relative motion between surfaces in contact, infinitesimal strain theory may still result in mechanical response evaluation inaccuracies. Infinitesimal strain theory assumes that the surface orientation in the current configuration differs insignificantly from that of the undeformed configuration. This assumption may lead to errors in contact pressure estimation and affect the optimized geometry. To illustrate this issue, the applied displacement is increased, and the material anchor problem is optimized for both large and small strain theory. For this load case study, we adopt a continuation approach, where the second load case uses the previous optimized geometry as an initial configuration.

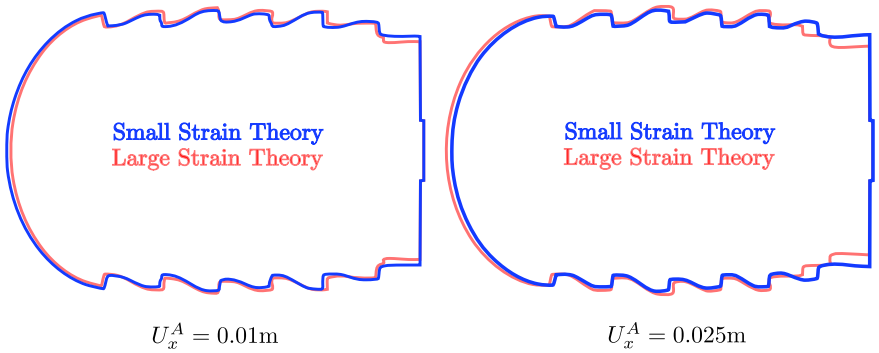

Figure 10.19: Comparison of optimized geometry for small and large strain theory for various applied displacements.

Figure 10.19 compares small and large strain theory optimized geometries for two different magnitudes of applied loads. At the smallest load case, $U_x^A = 0.01$ m, the optimized material anchor profile produced by small strain theory closely resembles that resolved by large strain theory. However, at the higher load case, $U_x^A = 0.025$ m, the discrepancy between the optimized geometries becomes more noticeable, although the conceptual designs differ insignificantly. The close resemblance in geometry can be attributed to similar physical responses. To illustrate these similarities, the optimal geometries for both infinitesimal strain and finite strain theory are incrementally loaded in 15 steps for the larger load case of $U_x^A = 0.025$ m. Figure 10.20 presents the experienced force profile as a function of applied displacement. At this load level, the large strain contact model

displays a rather linear response, similar to the infinitesimal strain contact model.

To cross examine the performance of geometries optimized with infinitesimal strain theory and finite strain theory, the optimized geometries are analyzed with finite strain theory. Table 10.4 compares the holding force of the geometries provided in Figure 10.19 when analyzed strictly with finite strain theory. For the loading cases $U_x^A = 0.01$ m and $U_x^A = 0.025$ m, the optimized geometry produced from small strain theory results in a decrease in holding force of 0.0026% and 0.0081% respectively, when compared to the optimized geometry produced from large strain theory. While the improved performance of optimal geometry from finite strain theory is small, this example demonstrates the limitations of infinitesimal strain theory for these types of optimization problems. To explore optimization problems in which the physical behavior cannot be predicted with any acceptable accuracy using infinitesimal strain theory, the following examples study design problems with highly nonlinear response behavior.

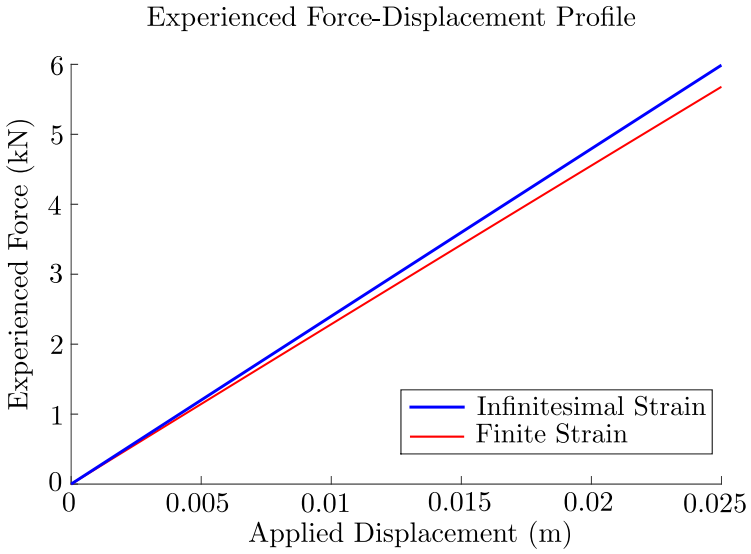

Figure 10.20: Comparison of resistance to separation for incremental loading to the maximum value $U_x^A = 0.025$ m.

Optimized geometry for:	Holding force for load case:	
	$U_x^A = 0.01$ m	$U_x^A = 0.025$ m
Finite strain	2.265 kN	5.679 kN
Infinitesimal strain	2.259 kN	5.633 kN

Table 10.4: Holding force of optimized geometries using finite strain theory.

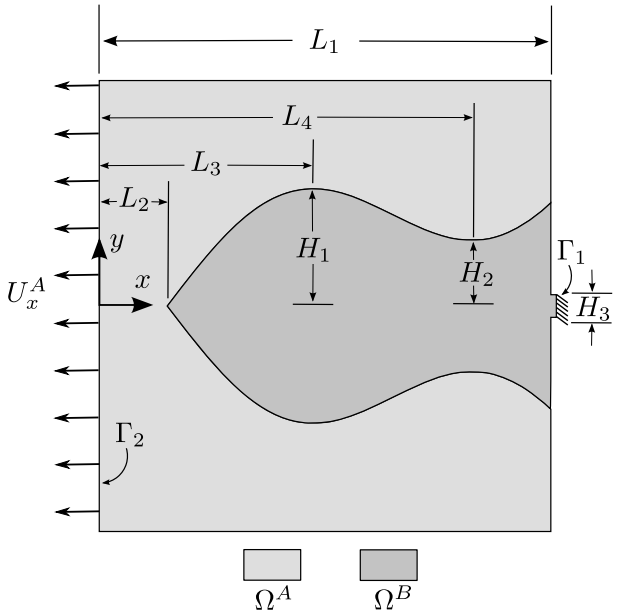

Figure 10.21: Snap-fit design initial configuration.

Description	Parameter
domain length	$L_1 = 1.0$ m
host depth	$L_2 = 0.151$ m
peak width location	$L_3 = 0.4$ m
base width location	$L_4 = 0.9$ m
peak height	$H_1 = 0.2451$ m
base height	$H_2 = 0.16$ m
fixed support height	$H_3 = 0.133$ m
Young's modulus	$E^A = 10$ MPa
Young's modulus	$E^B = 10$ MPa
Poisson's ratio	$\nu^A = 0.3$
Poisson's ratio	$\nu^B = 0.3$
applied load, at $t = 1$	$U_x^A = 0.5$ m
response weight	$c_u = 100.0$
penalty weight	$c_p = 0.0$
volume ratio	$c_v = 1.0$
opt. upper bounds	$s_{max} = 0.0125$
opt. lower bounds	$s_{min} = -0.0125$
rel. step size	$\Delta s = 8 \times 10^{-3}$
smoothing radius	$r_f = 0.0375$ m

Table 10.5: Snap-fit design model parameters.

10.5.5 Snap-Fit Design Problem

Snap-fits remain one of the fastest and cost effective methods of assembly. This simplistic fastener relies on two interlocking components, which if designed properly can be assembled and disassembled numerous times without damaging the components. For applications demanding a high level of precision, the force required to induce separation can be pivotal. Snap-fit designs exhibit a highly nonlinear mechanical response, and during the process of separation the mechanical model can experience moments of neutral and unstable equilibrium. This poses interesting challenges for both the mechanical response prediction, and subsequently the optimization of snap-fit designs.

Here we pose the snap-fit design problem as follows: We wish to find the optimal geometry of a snap-fit mechanism to match a desired load-displacement profile. This problem formulation is explored for two scenarios: the first example is a two phase design in which geometry control is provided by discretized level set nodal variables; the second example is a three-phase design in which geometry control is provided by geometric primitive variables.

10.5.5.1 Two-Phase Example

The initial configuration is illustrated in Figure 10.21, and dimensions and material parameters are listed in Table 10.5. The snap-fit tab, represented by Phase B, is fixed at the boundary Γ_1, whereas the snap-fit container, represented by phase A, is subjected to a prescribed displacement along boundary Γ_2, which is applied in 45 equal load increments.

The objective function is defined as follows:

$$z = \int \left(\int_{\Gamma_1} \sigma_{xx} \mathrm{d}\Gamma - f_t \right)^2 \mathrm{d}t, \tag{10.28}$$

where f_t is a target force profile, and the pseudo-time t represents the incremental loading process. For this particular example, the desired force profile is defined as:

$$f_t = \sin\left(\frac{3\pi}{2}t\right) \text{ kN} \qquad 0 \leq t \leq 1. \tag{10.29}$$

The desired force profile describes a sinusoidal profile with a peak value of 1 kN. This particular force profile was chosen to highlight a design exhibiting a high level of physical response non-linearity.

For geometry control, the nodal level set values are defined in terms of the optimization variables using the linear filter (2.10). The smoothing radius is set to $r = 3h$, where h is the element side length. No perimeter penalty measures or volume constraints are used for this example. The smoothness of the target force-profile causes localized geometry irregularities to be non-beneficial to the design functionality. Due to the symmetric nature of the design, only half of the domain is analyzed with 80×40 elements.

Figure 10.22 shows the convergence profile of the optimization problem, supported by snapshots of the mechanical response at the final time step for select design iterations. The inset of

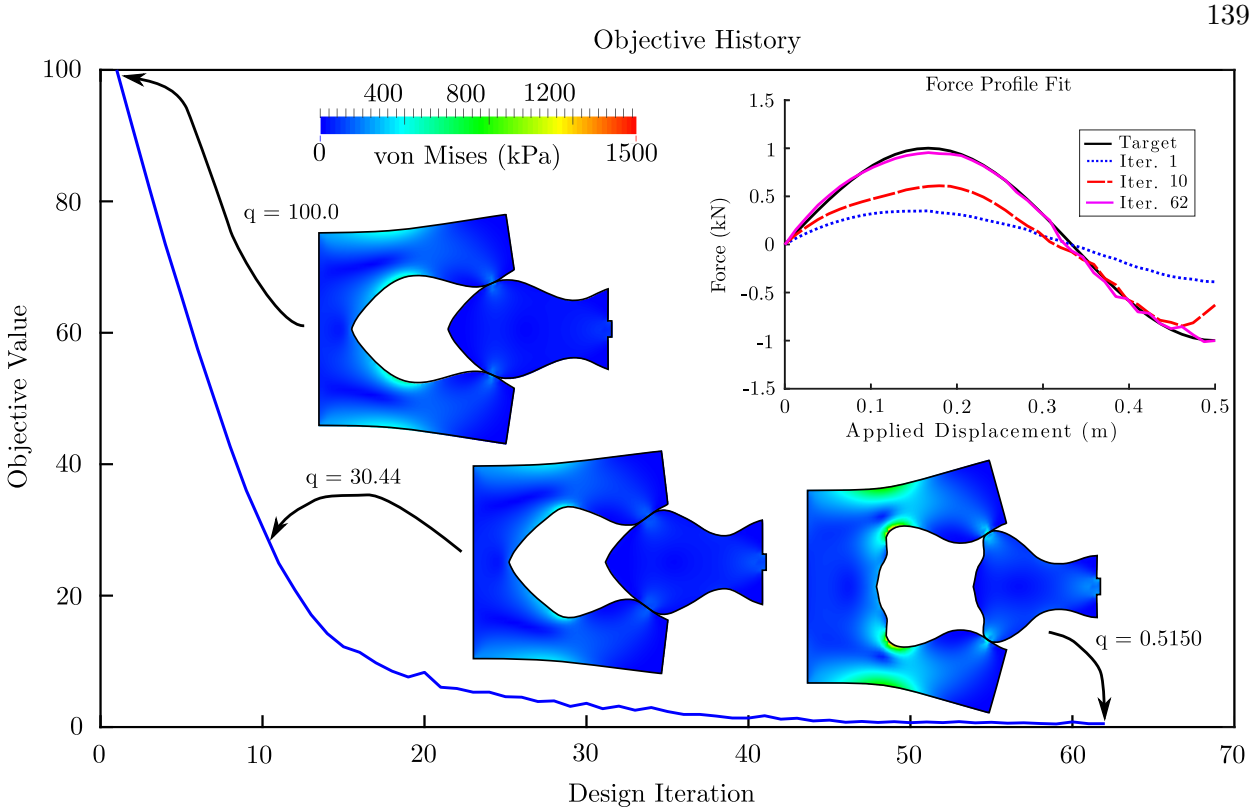

Figure 10.22: Snap-fit design objective history with snapshots of specific iterations. Inset depicts the force-displacement curve for specific iterations.

Figure 10.22 shows the experienced force-displacement profile, compared to the desired profile for specific design iterations. The stem of the tab increases in concavity, increasing the experienced force at the base. The peak width of the tab is increased, whereas the pointed head of the tab flattens out. The geometry evolution observed increases the peak force experienced, and provides a close fit to the desired force-displacement profile. The non-smooth nature of the final design force-displacement curve can be attributed to the piecewise linear interface representation in the XFEM model.

10.5.5.2 Three-Phase Example

The two-phase snap-fit design demonstrated the optimization of a problem experiencing large sliding motion, but with rather small elastic deformations. The three-phase analog explores an optimization problem exhibiting large sliding contact in the presence of large elastic deformation, by

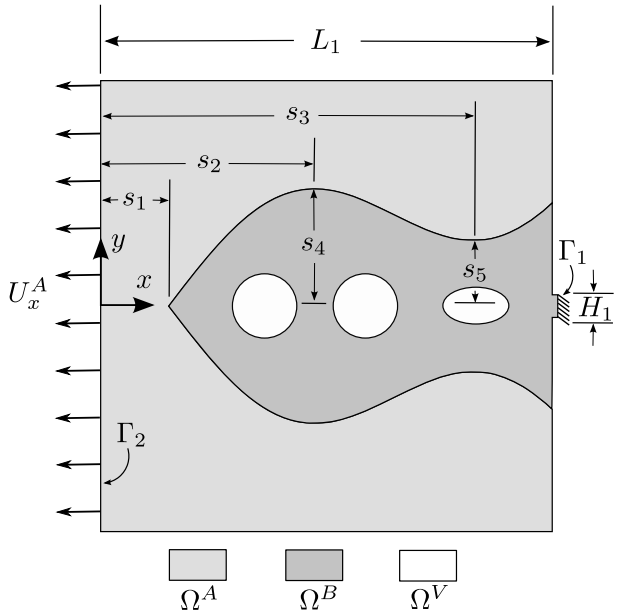

Figure 10.23: Snap-fit design initial configuration.

Description	Parameter
domain length	$L_1 = 1.0$ m
fixed support height	$H_1 = 0.133$ m
host depth	$s_1 = 0.151$ m
peak width location	$s_2 = 0.4$ m
base width location	$s_3 = 0.9$ m
peak height	$s_4 = 0.2451$ m
base height	$s_5 = 0.16$ m
Young's modulus	$E^A = 10$ MPa
Young's modulus	$E^B = 10$ MPa
Poisson's ratio	$\nu^A = 0.3$
Poisson's ratio	$\nu^B = 0.3$
applied displacement	$U_x^A = 0.6$ m
response weight	$c_u = 99.9$
penalty weight	$c_p = 0.1$
volume ratio	$c_v = 0.15$
rel. step size	$\Delta s = 4 \times 10^{-4}$

Table 10.6: Snap-fit design model parameters.

introducing void regions within the tab material. The three-phase snap-fit design problem describes the design domain using a combination of geometric primitives, wherein the variables associated with the geometric primitives are defined as optimization variables. While the design freedom is restricted to the set of shapes that can be produced by the particular geometric primitives, the three-phase example explores a different avenue of complexity by introducing void regions within the tab material, i.e. phase B.

The initial configuration is illustrated in Figure 10.23, and dimensions and material parameters are listed in Table 10.6. Similar to the two-phase snap-fit example, the tab material is fixed at the boundary Γ_1 and a prescribed displacement is applied at boundary Γ_2 in 45 load steps. Provided the same objective of matching a target force displacement profile measured at Γ_1, a new target force displacement curve is defined as:

$$f_t = 0.5 \sin\left(\frac{3\pi}{2} t\right) \text{ kN} \qquad 0 \leq t \leq 1. \tag{10.30}$$

Provided the increased applied displacement value of $U_x^A = 0.6$ m, the target force displacement curve for this example exhibits a delayed peak force value as compared to the two-phase example.

Description	Variable	Initial Value	Upper Bound	Lower Bound
host depth	s_1	0.151 m	0.3 m	0.1 m
peak width location	s_2	0.4 m	0.7 m	0.25 m
base width location	s_3	0.9 m	1.0 m	0.8 m
peak height	s_4	0.2451 m	0.4 m	0.15 m
base height	s_5	0.16 m	0.25 m	0.04 m
$\phi_{c,1}$ x center	$x_{c,1}$	0.4 m	0.85 m	0.25 m
$\phi_{c,2}$ x center	$x_{c,2}$	0.6 m	0.85 m	0.25 m
$\phi_{c,3}$ x center	$x_{c,3}$	0.8 m	0.85 m	0.25 m
$\phi_{c,1-3}$ x radius	$r_{x,1-3}$	0.07 m	0.3 m	0.02 m
$\phi_{c,1-2}$ y radius	$r_{y,1-2}$	0.07 m	0.2 m	0.02 m
$\phi_{c,3}$ y radius	$r_{y,3}$	0.035 m	0.06 m	0.02 m

Table 10.7: Initial value, upper and lower bounds for three-phase snap-fit design problem.

This is done to promote larger deformations prior to exceeding the point of neutral equilibrium.

The design geometry is defined by two LSFs; see Section 2.4.2. The first LSF governs the material interface between subdomains Ω^A and Ω^B and is defined the optimization variables $s_1 - s_5$:

$$\phi^1 = -|Y| + a\ \sin(\theta) + p\ \tilde{X}, \tag{10.31}$$

where

$$a = \frac{s_4}{2} - \frac{p\ s_2}{s_2 + s_3}, \qquad p = \frac{(s_4 + s_5)(s_2 + s_3)}{4s_2 + 2s_3}, \qquad \tilde{X} = \frac{X - s_1}{s_2 + s_3}, \tag{10.32}$$

and the auxiliary coordinates,

$$\theta = \tilde{a}X^2 + \tilde{b}X + \tilde{c}, \tag{10.33}$$

are defined by the following scalar values

$$\tilde{a} = \frac{\pi(2s_2 - s_3)}{2s_2 s_3(s_2 + s_3)}, \tag{10.34}$$

$$\tilde{b} = \frac{\pi\left((s_1 + s_2 + s_3)^2 - 3(s_1 + s_2)^2 + 2s_1^2\right)}{s_2 s_3(2s_2 + 2s_3)}, \tag{10.35}$$

$$\tilde{c} = -\frac{\pi\ s_1\left(-2s_2^2 + 2s_2 s_3 - 2s_1 s_2 + s_3^2 + s_1 s_3\right)}{s_2 s_3(2s_2 + 2s_3)}, \tag{10.36}$$

The geometric primitives chosen for the LSF ϕ^1 conveniently allow control over the length, peak width, and narrow width of the tab material outer geometry, while maintaining a smooth curvature of the profile.

The second LSF distinguishes Ω^V from Ω^B. The geometric primitives chosen for the LSF ϕ^2 define ellipsoidal void regions, shown in Figure 10.23, which can move along the x-axis and grow or shrink in size. The LSF ϕ^2 is defined as a combination of elliptical conical LSFs,

$$\phi_{c,j} = \left(\left(\frac{X - x_{c,j}}{r_{x,j}} \right)^2 + \left(\frac{Y - y_{c,j}}{r_{y,j}} \right)^2 \right)^2 - 1, \tag{10.37}$$

where the jth-elliptical conical field $\phi_{c,j}$ is defined by variables $x_{c,j}$ and $y_{c,j}$ which control the central location of the ellipse, and parameters $r_{x,j}$ and $r_{y,j}$ which control the semi-axis radii of the ellipse. Using three elliptical conical LSFs, the LSF ϕ^2 is defined as:

$$\phi^2 = \min\left(\phi_{c,1}, \phi_{c,2}, \phi_{c,3}\right). \tag{10.38}$$

The y-location of the conical fields are restricted as $y_{c,j} = 0$, and are excluded from geometry control.

The initial values, upper limits, and lower limits for all design variables for this problem are presented in Table 10.7. A volume constraint of $c_v = 0.15$ is enforced to reduce the material of Ω^B, and a perimeter penalty weight of $c_p = 0.1$ used to regularize the void material interface. Due to the symmetric nature of the design, only half of the domain is analyzed with 80×40 elements. No level set smoothing filters are used in this example.

The objective history throughout the optimization process is illustrated in Figure 10.24, supported by snapshots of the physical response of the design at $U_x^A = 0.2133$ m for select iterations. The inset of Figure 10.24 compares the experienced force-displacement of select design iterations to the desired target profile. Throughout the design evolution, the void material expands until the void inclusions coalesce. The snap-fit general profile narrows, while the peak width increases. The combination of these design attributes affords greater elastic stretch in the snap-fit tab, delaying the maximum force value experienced during incremental loading. This example demonstrates that

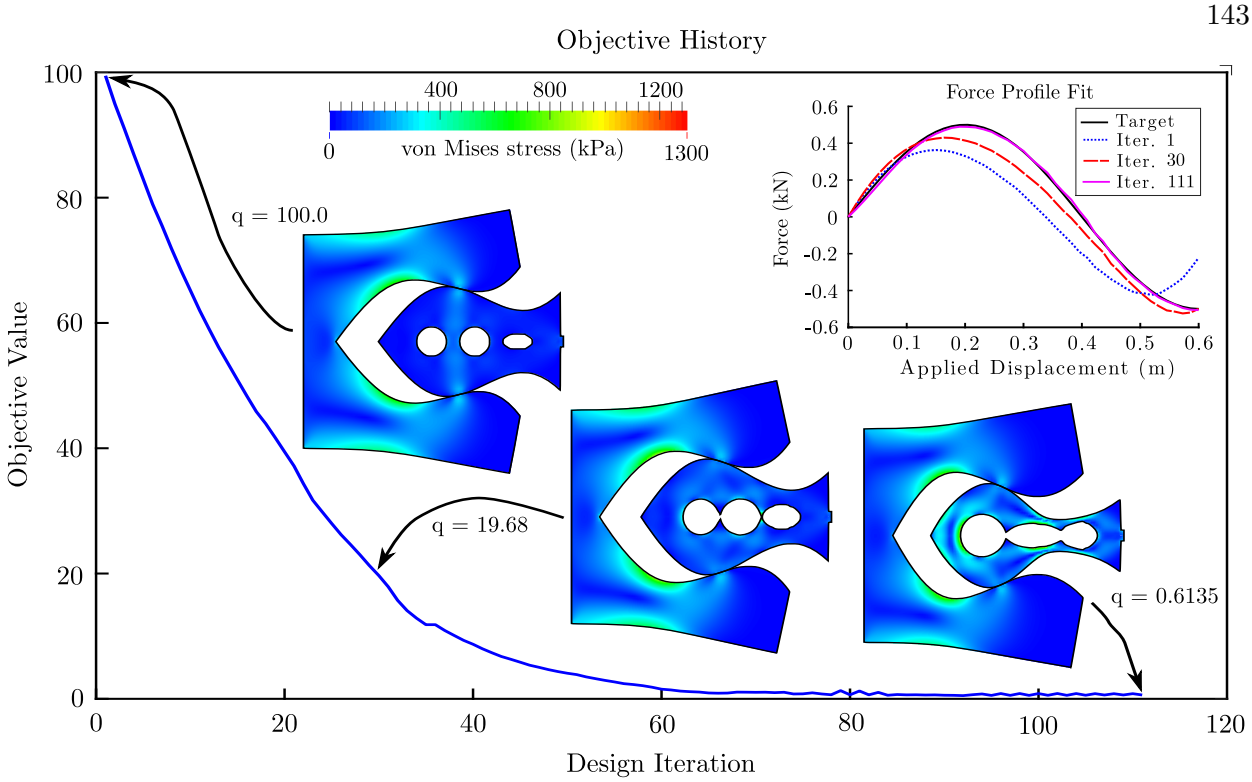

Figure 10.24: Snap fit design objective history with snapshots of specific iterations at applied displacement $U_x^A = 0.213$ m. Inset depicts the force-displacement curve for specific iterations.

the proposed optimization method allows finding non-intuitive optimized designs for frictionless contact problems experiencing large deformations.

10.5.6 Torque Limiter Design Problem

Torque limiters are common devices used in mechanical equipment to prevent damage from overload. Also known as an overload clutch, these devices limit the applied torque to an assembly by slipping or uncoupling the load. Common methods of limiting applied torque by slipping include frictional plates, magnetic clutches, and ball-detent designs. Taking a simpler approach, the torque limiter design problem presented here consists of two pieces; an outer square shaft containing an inner rod with frictionless contact prescribed at the interface. The torque limiter design problem is explored for two scenarios: the first example is a two phase design in which geometry control is provided by discretized level set nodal variables; the second example is a three-phase design in

which geometry control is provided by geometric primitive variables.

10.5.6.1 Two-Phase Example

The torque-limiter design problem consists of an outer shaft, constrained along the outer boundaries, with an internal rod which is rotated as depicted in Figure 10.25. The outer square

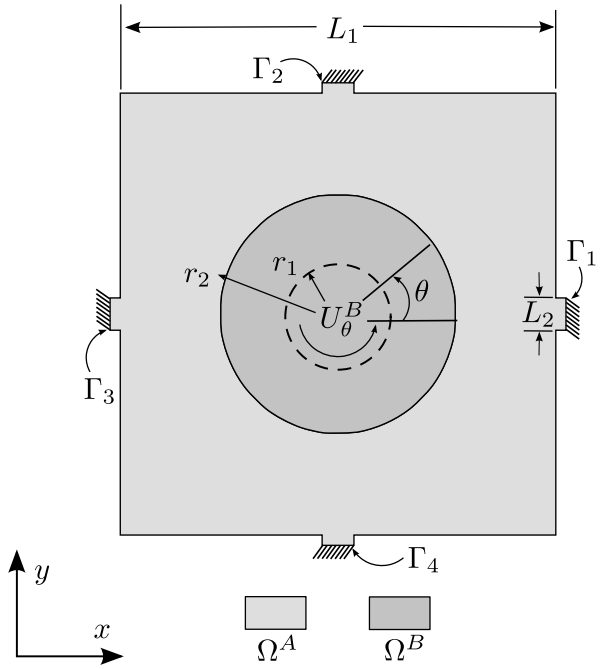

Figure 10.25: Torque limiter initial configuration.

Description	Parameter
domain length	$L_1 = 1.0$ m
fixed support width	$L_2 = 0.0732$ m
loading radius	$r_1 = 0.12$ m
interface radius	$r_2 = 0.2911$ m
Young's modulus	$E^A = 10$ Mpa
Young's modulus	$E^B = 10$ Mpa
Poisson's ratio	$\nu^A = 0.3$
Poisson's ratio	$\nu^B = 0.3$
applied rotation at $t = 1$	$U_\theta^B = \pi/2$ rad
response weight	$c_u = 100.0$
penalty weight	$c_p = 0.01$
volume ratio	$c_v = 1$
opt. upper bounds	$s_{max} = 0.0244$
opt. lower bounds	$s_{min} = -0.0244$
rel. step size	$\Delta s = 1 \times 10^{-2}$

Table 10.8: Torque limiter model parameters.

shaft, represented by phase A, is grounded at boundaries Γ_{1-4}. The inner rod of radius r_2, represented by phase B, is rotated about the centroid with an applied displacement $U_\theta^B(t)$ within radius r_1. The displacement $U_\theta^B(t)$ is applied in 30 equal load increments. Model parameters specific to this problem are listed in Table 10.8. The objective of this study is to find the optimal geometry such that the total torque experienced at boundaries Γ_{1-4} matches a target torque profile. The objective function is defined as follows:

$$z = \int \left(\int_{\Gamma_{1-4}} \sigma_{r\theta}\, r \, \mathrm{d}\Gamma - f_t \right)^2 \mathrm{d}t, \tag{10.39}$$

where $\sigma_{r\theta}$ is the shear component of the Cauchy stress in a polar coordinate system, r is the radial position in a polar coordinate system, and f_t is the desired torque profile. For this particular

example, the desired torque profile is defined as:

$$f_t = 2.5 \ \sin 2\pi t \ \text{kN} \cdot \text{m}, \qquad 0 \leq t \leq 1. \tag{10.40}$$

The chosen target curve describes a load-displacement curve that follows a sinusoidal wave. Pseudo-time t defines the linear increment of applied rotation during the period of $0 \leq t \leq 1$. A sinusoidal target curve provides a gradual transition from experienced torque build-up and decrease, delineated by a peak target value. The entire domain is discretized with 41×41 elements. For geometry control, the nodal level set values are defined as the optimization variables. Numerical experiments showed that while a volume constraint is not necessary for this problem, a perimeter penalty weight of $c_p = 0.01$ is useful to promote a smooth interface profile. Also the smoothing radius of the linear filter (2.10) is set to $r = 1.5\sqrt{2}h$ m, where h is the element side length.

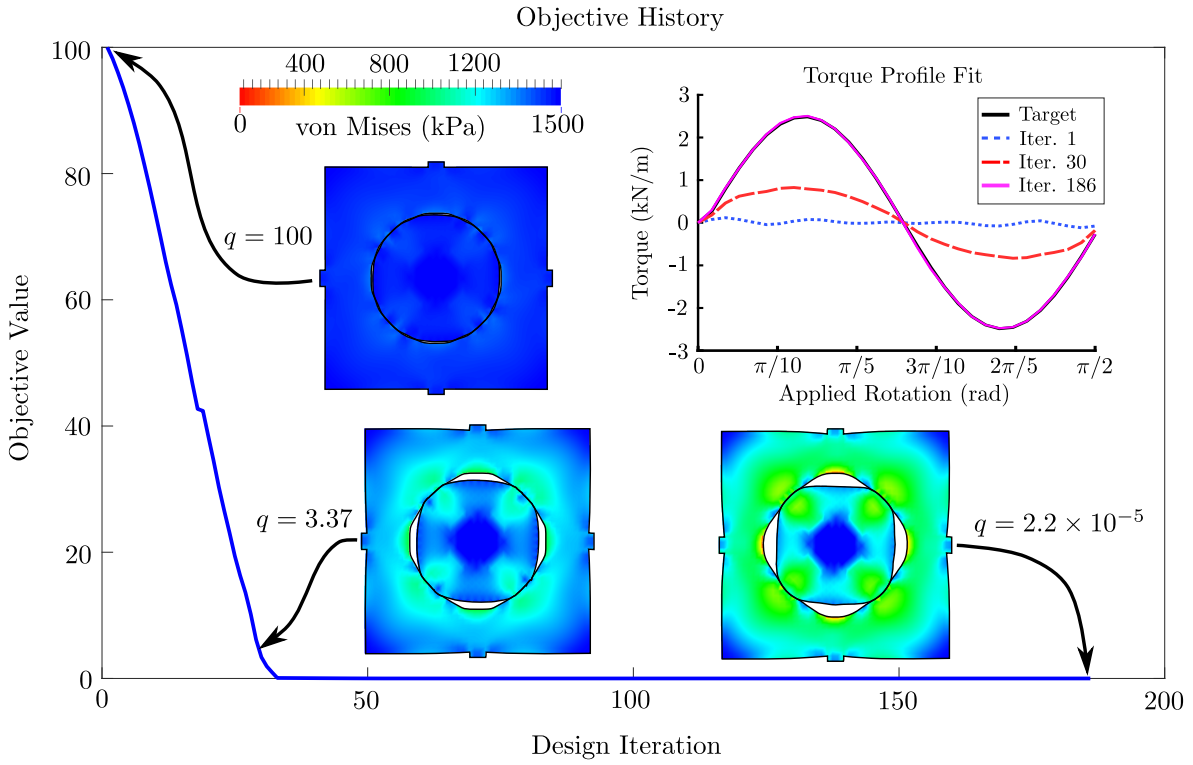

Figure 10.26: Torque limiter design objective history with snapshots of specific iterations. Inset depicts the torque-rotation curve for specific iterations.

Figure 10.26 shows the objective history throughout the optimization process, supported by snapshots of the mechanical response at the final time step for select design iterations. The inset

of Figure 10.26 shows the experienced torque profile, compared to the desired profile for specific design iterations. As expected, the initial circular profile of the inner rod yields no torque as it is rotated. The interface geometry evolves bumps or ridges, providing a torque-rotation profile that closely resembles the desired profile.

10.5.6.2 Three-Phase Example

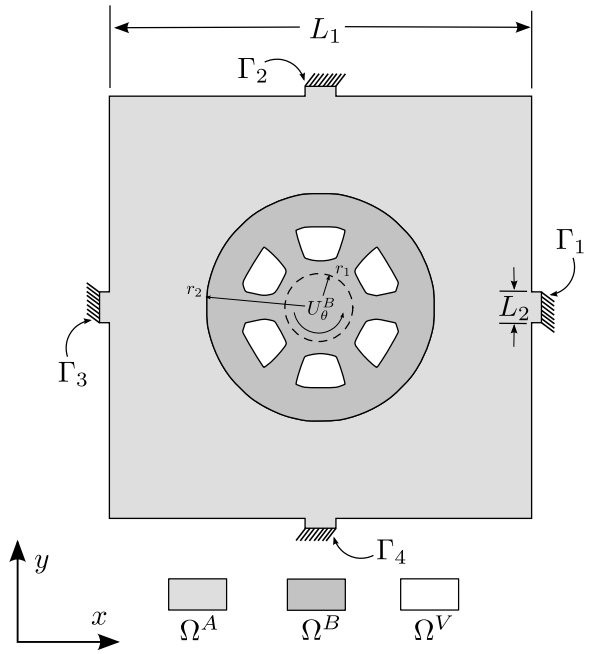

Figure 10.27: Three-phase torque limiter initial configuration.

Description	Parameter
domain length	$L_1 = 1.0$ m
fixed support width	$L_2 = 0.0732$ m
loading radius	$r_1 = 0.06$ m
interface radius	$r_2 = 0.271$ m
Young's modulus	$E^A = 10$ Mpa
Young's modulus	$E^B = 10$ Mpa
Poisson's ratio	$\nu^A = 0.3$
Poisson's ratio	$\nu^B = 0.3$
applied rotation at $t = 1$	$U_\theta^B = \pi/3$ rad
response weight	$c_u = 99.9$
penalty weight	$c_p = 0.1$
volume ratio	$c_v = 0.16$
rel. step size	$\Delta s = 1 \times 10^{-2}$

Table 10.9: Three-phase torque limiter model parameters.

The three-phase torque limiter example explores the buildup of strain energy and abrupt release, also known as 'snap through' behavior, by introducing void material within the rod phase, Ω^B. Similar to the two-phase snap-fit design problem of Section 10.5.5.2, the three-phase torque limiter design problem defines geometry by a set of geometric primitive shapes. The initial configuration is depicted in Figure 10.27, and model parameters are listed in Table 10.9.

The initial design geometry closely resembles that of the two-phase torque limiter problem, however, void regions are introduced radially within phase B. Similarly, we wish to determine the

best arrangement of material to match the desired torque profile:

$$f_t = 5.20\ t(1-t)\left(0.5 - \frac{\tanh(30) + \tanh(60(t-0.5))}{2\tanh(30)}\right)\ \text{kN}\cdot\text{m} \qquad 0 \le t \le 1. \tag{10.41}$$

The torque profile defined for this problem increases to a peak value, then abruptly drops to a minimum value before gradually returning to zero at the final load step. This torque profile encourages a build-up and abrupt release of strain energy. The prescribed displacements are applied in 30 equal load increments.

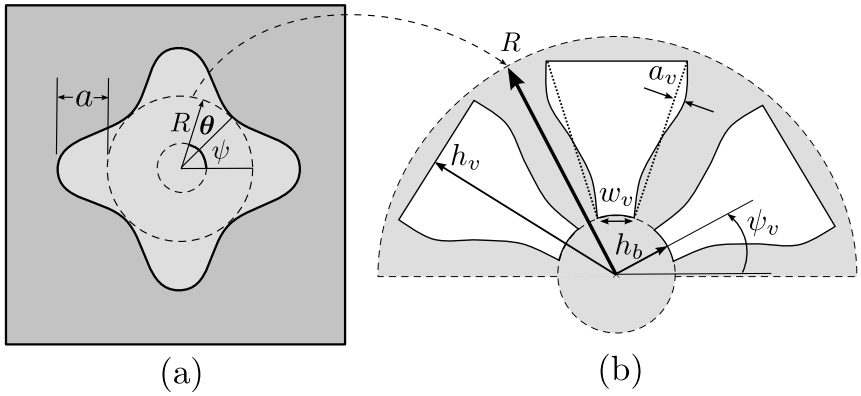

Figure 10.28: Torque limiter geometric primitives for (a) ϕ^1 and (b) ϕ^2.

To afford geometry control, both LSFs define the geometric primitives depicted in Figure 10.28. LSF ϕ^1 describes a circle with a sinusoidally varying radius:

$$\phi^1 = R - \left| \frac{(X - X_c)/L^1}{\cos(n\theta)} - a\sin(n\theta + \psi) \right| \tag{10.42}$$

where R is the base circle radius, a is the amplitude of variations, n is the number of ridges along the outer surface, X_c and Y_c are the center of the design domain, ψ is the phase of variations, and the auxiliary coordinate θ is defined as

$$\theta = \text{atan2}\left((Y - Y_c)/L_1, (X - x^c)/L_1\right), \tag{10.43}$$

where atan2 is the four-quadrant inverse tangent. For LSF ϕ^1, the number of ridges must be a positive integer value, as non-integer values yield a discontinuous zero level-set contour.

The second LSF, ϕ^2, is describes a series of void petals as shown in Figure 10.28(b). The LSF describing the petals is taken from [23]. The jth petal is defined by:

$$\phi_{v,j} = -h_b + \left(\left(\frac{2\tilde{X}_v h_b}{\tilde{w}_v} \right)^{10} + \left(\frac{\tilde{Y}_v h_b}{h_{p,j}} \right)^{10} \right)^{1/10} \tag{10.44}$$

The auxiliary coordinates, $\tilde{X}_v$ and $\tilde{Y}_v$, and pedal width, $\tilde{w}_v$, are defined as

$$\tilde{X}_v = \acute{X} - \text{sign}\left(-\acute{X} a_{v,j} \tilde{w}_v \sin\left(\frac{3\pi\left(\acute{Y} - h_b\right)}{2h_{v,j}} \right) \right), \tag{10.45}$$

$$\tilde{Y}_v = \acute{Y} - h_b, \tag{10.46}$$

$$\tilde{w}_v = w_{v,j} + \pi \frac{\acute{Y} - h_b}{N_p - 1}, \tag{10.47}$$

where the number of petals, N_p, must be a positive integer. Finally, the rotated coordinate system can be expressed as:

$$\acute{X} = \frac{X - X_c}{L_1}\cos(\psi_v) - \frac{Y - Y_c}{L_1}\sin(\psi_v), \qquad \acute{Y} = \frac{X - X_c}{L_1}\sin(\psi_v) + \frac{Y - Y_c}{L^1}\cos(\psi_v) \tag{10.48}$$

LSF ϕ^2 is thus defined as

$$\phi^2 = \min(\phi_{v,j}) \tag{10.49}$$

For this optimization problem, the number of outer ridges, $n = 4$, center location $X_c = 0.5m$ and $Y_c = 0.5m$, and number of void regions, $N_v = 6$, are all held constant. Each void region is distributed radially by increments of $\pi/3$, as shown in Figure 10.27. The 28 design variable initial values, upper and lower bounds are provided in Table 10.10. A volume constraint of $c_v = 0.16$ is applied to reduce the overall volume occupied by the internal rod, and a perimeter penalty weight of $c_p = 0.1$ is applied to regularize model geometry. No smoothing filter is used. The design domain is discretized with 41×41 elements.

Figure 10.29 depicts the objective history of the optimization problem supported by snapshots of select design iterations throughout the optimization process. The inset plot within Figure 10.29

Description	Variable	Initial Value	Upper Bound	Lower Bound
Outer base radius	R	0.271 m	0.4 m	0.1 m
Outer surface amplitude	a	0.0 m	0.05 m	0.0 m
Phase of outer surface	ψ	0.0 rad	$\pi/2$ rad	$-\pi/2$ m
Petal radial location	$\psi_{v,j}$	var.	$+\Delta\pi/4$ m	$-\Delta\pi/4$ m
Petal base	h_b	0.15 m	0.3 m	0.012 m
Petal height	$h_{v,j}$	0.04 m	0.1 m	0.01 m
Petal side variation	$a_{v,j}$	0.0 m	0.1 m	-0.1 m
Petal Width	$w_{v,j}$	0.1 m	0.3 m	0.05 m

Table 10.10: Initial value, upper and lower bounds for three-phase torque limiter problem.

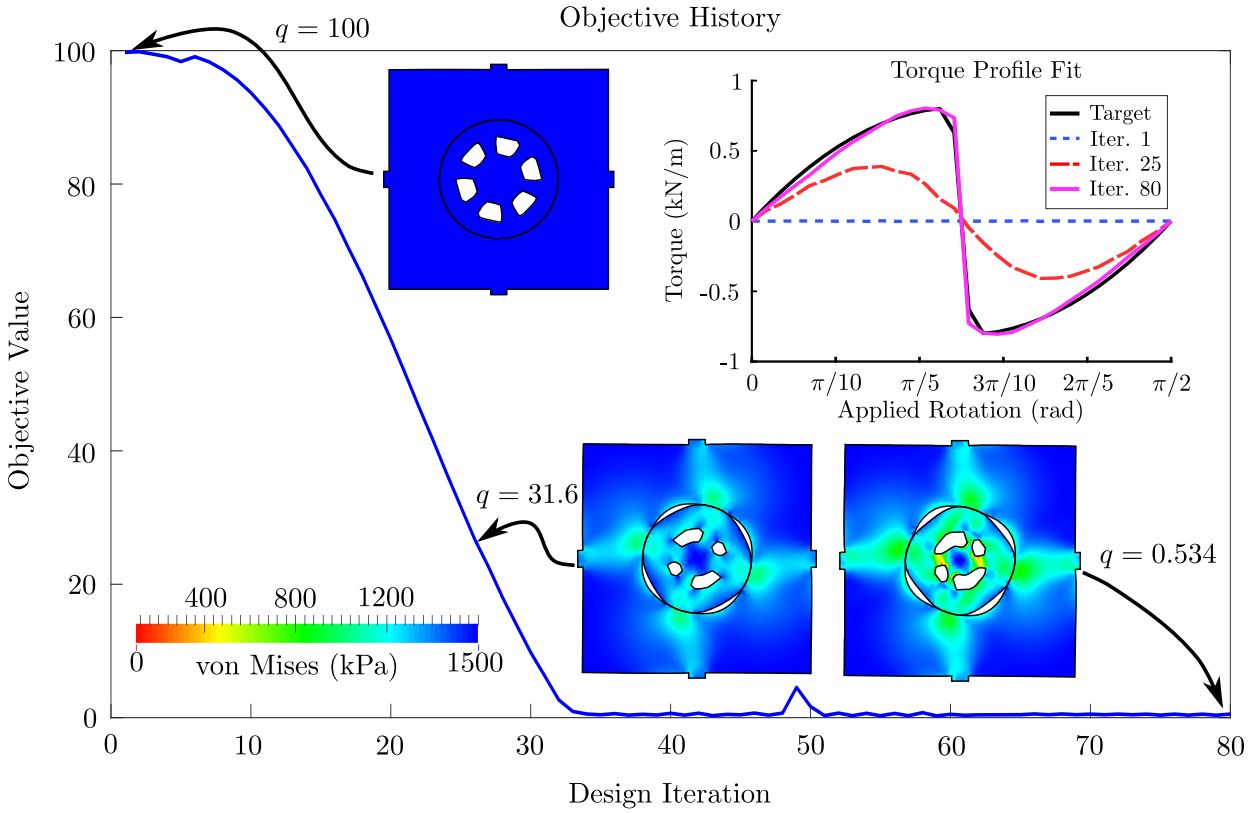

Figure 10.29: Torque limiter design geometry evolution at $U_\theta^B \approx \pi/5$ rad, colored by von Mises stress.

shows the torque-rotation curves for select design iterations compared to the target profile. At early stages of convergence, the contact interface, Γ_c, evolves to exhibit ridges to increase the experienced torque along the boundaries Γ_{1-4}. To match the sudden drop in the target torque-rotation curve, the void regions coalesce to reduce the overall material bridging the area of applied displacement to

the material in the vicinity of the contact interface. This encourages snap-through behavior. The optimized design matches the desired torque profile well, illustrating the ability of the proposed optimization method to find geometries that feature complex mechanical contact behavior.

10.6 Discussion

This chapter presented a shape and topology optimization framework for two- and three-phase problems with finite strain, large sliding bilateral contact phenomena. Coincident surface location was defined by a coupled parametric representation of the surface geometry. The interface condition was described by a stabilized Lagrange formulation with an active-set strategy to allow surface separation. The material behavior of the mechanical model was described by a hyper-elastic isotropic material and finite strains were assumed for the mechanical model. The XFEM was used to discretize and integrate the mechanical model, and a face-oriented ghost penalization model was used to mitigate the ill-conditioning of the physical response prediction. Dynamic relaxation was employed to provide reliable convergence.

Geometry control was provided by an explicit LSM, where single and multiple LSFs were used to describe two- and three-phase geometries, respectively. The optimization problem was solved with a nonlinear programming method, and a perimeter penalty was used to regularize optimized geometry. Material phase volume constraints were imposed, and design sensitivities were evaluated using an adjoint method. The physical response prediction and subsequent design sensitivities were verified with benchmark examples.

The comparative optimization study between small infinitesimal strain theory and finite strain theory demonstrated that within acceptable load limits for linearized strain theory, both physical response models produced similar results. The two-phase snap-fit and torque limiter optimization studies explored physical response behavior that could not be modeled with infinitesimal strain theory. Furthermore, it was demonstrated that reliable convergence behavior, and subsequently, non-intuitive design solutions are feasible for this particular subset of problems. The three-phase design problems explored in this study demonstrated that void regions within components can

contribute to design functionality, specifically by increasing the level of elastic deformation and affording snap through behavior in the snap-fit and torque limiter design problems, respectively.

While this study focused on frictionless and quasi-static contact behavior, the current framework allows for the convenient extension to rate-based interface phenomena such as non-conservative frictional effects. Some of the non-smooth force-displacement behavior may be attributed to the piece-wise linear approximation of interface geometry. Future studies could benefit from C^1 continuous discretization. The current optimization method does not allow for the nucleation of a phase within a volume of another phase. Methods for overcoming this limitation, such as the use of topological derivatives, should be investigated. Extension into three dimensional problems would greatly increase the scope of potential applications, as relatively few real world applications can be reduced into two dimensional space. Additional solution techniques such as arc length methods, and optimization methods should be explored to improve the stability of the physical response prediction and optimization convergence behavior. In future studies, this method needs to be extended to the treatment of triple junction intersections and other considerations for a more generalized multi-phase approach.

Chapter 11

Conclusions

11.1 Summary

This manuscript presented a gradient based optimization method for structural problems whose functionality is dependent on contact behavior. An explicit Level Set Method of geometry control was used, allowing optimization of both shape and topology of the phase boundaries. Accurate evaluation of contact behavior requires precise knowledge of the interface position and orientation, which was provided by the eXtended Finite Element Method numerical model. Linear and nonlinear behavior was employed in the mechanical model, for both geometric and material considerations. Contact contributions were enforced weakly as immersed boundary value problems, with both small and large sliding contact behavior. Ill conditioning caused by thinly cut elements was mitigated by a geometric preconditioner in infinitesimal strain problems, and ghost penalization in finite strain problems. Robust convergence of the mechanical model through neutral instabilities and snap-through behavior was achieved by a dynamic relaxation method. The accuracy of the mechanical model was verified through comparisons to published and analytical examples, and optimization examples explored the defining characteristics of each contact behavior studied.

In two dimensional infinitesimal strain and small sliding frictionless studies, a simple bolted plate example illustrated the convenient use of geometric primitives to define design features. Comparison of optimal designs between perfect bonding and frictionless contact at the interface suggested that different contact behavior may have a noticeable impact on the design, even when the number of design variables is small and the design freedom is limited. A study on perimeter penalty

regularization demonstrated that feature size and irregularity can be reduced at a small cost to the performance of the design. Studies on material properties demonstrated a significant change in optimal designs for contact problems.

In two and three dimensional cohesive interface studies, the interface conditions were shown to have a strong influence on optimized geometry, as various levels of normal and tangential resistance yielded drastically different designs. Gradient measure regularization was shown to be successful at removing small features that are problematic for accurate response prediction and for manufacturing considerations at a minimal cost to design performance. An initial design experiencing total debonding was optimized to recover interface cohesion and a monotonic resistance to separation. An applied load study demonstrated that geometry can be tailored to localized regions where either cohesion or delamination are present. Three dimensional optimization studies revealed design traits that could not deduced from 2D studies, suggesting that care must be taken with reduced dimensionality for particular contact problems.

In two dimensional finite strain and large sliding frictionless studies, the accuracy of the mechanical model was verified through comparison to results produced in Abaqus. Semi-analytical adjoint method sensitivities were validated by finite difference. A load case study comparison between large strain and small strain theory demonstrated that linear kinematic approximations do not correctly capture the mechanical response if the local deformation is comparable to the feature size. The snap-fit design problem demonstrated that geometry can be tailored in situations of prolonged sliding contact behavior to match a desired force-displacement curve. The torque limiter problem demonstrated that a similar geometric tailoring can be achieved where the desired radial force profile is an averaged measure. The three-phase design problems described the design domain using a combination of geometric primitives, wherein the variables associated with the geometric primitives are defined as optimization variables. While the design freedom was restricted to the set of shapes that can be produced by the particular geometric primitives, the three-phase examples explored a different avenue of complexity by introducing void regions within a particular phase.

In summary, the proposed method has shown great promise to achieve optimized geometry for a wide variety of contact behavior. Therefore, applying the proposed optimization method to specific engineering problems seems to be a worthwhile endeavor.

11.2 Future Work

The methodology presented in this thesis has opened many avenues for further research, as the topology optimization of contact problems is still in its early stages of development within the scientific community. Provided in this section is compilation of potential avenues for future work, organized in ascending order of the difficulty of scope.

(1) **Investigation of non-conservative, rate based contact behavior** The framework established in this thesis is readily adaptable to many forms of contact phenomena. A close at hand opportunity is to investigate the optimization of designs in the presence of stiction and sliding friction.

(2) **Optimization of contact interface properties** Cohesive or frictional properties could be tailored locally along the contact interface to attain a desired functionality. To achieve this, elemental design variables could be introduced, providing interface properties for the immersed boundary that resides within a particular element.

(3) **Higher order geometry and displacement field discretization** Parametric representation of immersed boundaries are limited to planar facets in the studies performed thus far. By affording C^1 continuity at the interface, or by increasing the interpolation order of the solution field, one may improve the physical response and convergence behavior during optimization. Additionally, this research avenue would yield a greater resolution of surface geometry for relatively coarse meshes.

(4) **Optimization of contact problems experiencing snap-through or snap-back behavior** In the current framework, dynamic relaxation and scaled solution increment methods allow the physical model to converge around neutral instabilities and 'push through'

mild cases of snap through behavior. A more robust solver method, such as an arc length method, could enable the optimization of designs exhibiting snap-through or snap-back behavior.

(5) **Extension of large sliding contact framework to 3D** The optimization of problems experiencing large sliding contact is currently restricted to two dimensional space. While surface-to-surface integration provides a rich interpolation space for contact traction, it is worth noting that due to the added complexity, many 3D contact solvers rely on a node-to-surface method. Contact search algorithms and boundary value problems must be constructed carefully, as iterative optimization algorithms compound computational expenses.

(6) **Extension to multi-physics problems** To access design problems with more complexity, such as fluid-structure contact problems, the geometry model needs to be extended to a more generalized multi-phase description. Namely, this would require the handling of triple-junction intersections, modification to the way the integration space is determined, and a robust enrichment strategy for multi-phase problems.

Bibliography

[1] Grégoire Allaire, François Jouve, and Anca-Maria Toader. Structural optimization using sensitivity analysis and a level-set method. Journal of computational physics, 194(1):363–393, 2004.

[2] S. Amdouni, P. Hild, V. Lleras, M. Moakher, and Y. Renard. A stabilised lagrange multiplier method for the enriched finite-element approximation of contact problems of cracked elastic bodies. ESAIM: Mathematical Modelling and Numerical Analysis, 46:813–839, 2012.

[3] Ted L Anderson and TL Anderson. Fracture mechanics: fundamentals and applications. CRC press, 2005.

[4] A. Andrade-Campos, A. Ramos, and J. Simões. A model of bone adaptation as a topology optimization process with contact. Journal of Biomedical Science and Engineering, 5:229–244, 2012.

[5] Chandrasekhar Annavarapu, Martin Hautefeuille, and John E Dolbow. A robust nitsche's formulation for interface problems. Computer Methods in Applied Mechanics and Engineering, 225:44–54, 2012.

[6] Chandrasekhar Annavarapu, Martin Hautefeuille, and John E Dolbow. A nitsche stabilized finite element method for frictional sliding on embedded interfaces. part i: Single interface. Computer Methods in Applied Mechanics and Engineering, 268:417–436, 2014.

[7] H.J. Antunez and M. Kleiber. Sensitivity analysis of metal forming process involving frictional contact in steady state. Materials Processing Technology, 60(14):485491, 1996.

[8] Helio J. C. Barbosa and Thomas J. R. Hughes. The finite element method with lagrange multipliers on the boundary: circumventing the babuska-brezzi condition. Computer Methods in Applied Mechanics and Engineering, 85(1):109 – 128, 1991.

[9] R. Behrou, M. Lawry, and K. Maute. Level set topology optimization of structural problems with interface cohesion. International Journal for Numerical Methods in Engineering, 2016 (Submitted).

[10] T. Belytschko, W. K. Liu, and B. Moran. Nonlinear Finite Elements for Continua and Structures. John Wiley & Sons, Ltd, 2005.

[11] T Belytschko, D Organ, and C Gerlach. Element-free galerkin methods for dynamic fracture in concrete. Computer Methods in Applied Mechanics and Engineering, 187(3):385–399, 2000.

[12] Ted Belytschko, Jacob Fish, and Bruce E Engelmann. A finite element with embedded localization zones. Computer methods in applied mechanics and engineering, 70(1):59–89, 1988.

[13] M. P. Bendsøe and O. Sigmund. Topology Optimization: Theory, Methods and Applications. Springer, 2003.

[14] Martin P Bendsøe. Optimal shape design as a material distribution problem. Structural optimization, 1(4):193–202, 1989.

[15] E Biotteau and J. P. Ponthot. Modeling frictional contact conditions with the penalty method in the extended finite element framework. In European Congress on Computational Methods in Applied Sciences and Engineering, 2012.

[16] E. Burman, MA. Fernández, and P. Hansbo. Continuous interior penalty finite element method for oseen's equations. SIAM journal on numerical analysis, 44(3):1248–1274, 2006.

[17] Erik Burman and Peter Hansbo. Fictitious domain finite element methods using cut elements: Ii. a stabilized nitsche method. Applied Numerical Mathematics, 62(4):328–341, 2012.

[18] Erik Burman and Peter Hansbo. Fictitious domain methods using cut elements: Iii. a stabilized nitsche method for stokes problem. ESAIM: Mathematical Modelling and Numerical Analysis, 48(03):859–874, 2014.

[19] Godofredo T Camacho and M Ortiz. Computational modelling of impact damage in brittle materials. International Journal of solids and structures, 33(20):2899–2938, 1996.

[20] S. K. Chan and I. S. Tuba. A finite element method for contact problems of solid bodies - part i. Int. J. Mech. Sci., 13:615–625, 1971.

[21] Peter Coffin and Kurt Maute. A level-set method for steady-state and transient natural convection problems. Structural and Multidisciplinary Optimization, pages 1–21, 2015.

[22] Peter Coffin and Kurt Maute. Level set topology optimization of cooling and heating devices using a simplified convection model. Structural and Multidisciplinary Optimization, pages 1–19, 2015.

[23] Peter Coffin and Kurt Maute. Level set topology optimization of cooling and heating devices using a simplified convection model. Structural and Multidisciplinary Optimization, 53(5):985 – 1003, 2016.

[24] Timothy A Davis. Algorithm 832: UMFPACK V4. 3—an unsymmetric-pattern multifrontal method. ACM Transactions on Mathematical Software (TOMS), 30(2):196–199, 2004.

[25] C. Agelet de Saracibar and M. Chiumenti. On the numerical modeling of frictional wear phenomena. Computer Methods in Applied Mechanics and Engineering, 177(3-4):401–426, 1999.

[26] Joshua D Deaton and Ramana V Grandhi. A survey of structural and multidisciplinary continuum topology optimization: post 2000. Structural and Multidisciplinary Optimization, 49(1):1–38, 2014.

[27] B. V. Derjaguin, V. M. Muller, and Y. P. Toporov. Effect of contact deformations on the adhesion of particles. J. Colloid Interface Sci., 53(2):314, 1975.

[28] E. Dombre, G. Allaire, O. Pantz, and D. Schmitt. Shape optimization of a sodium fast reactor core. ESAIM proceedings, EDP Sciences, 38:319–334, 2012.

[29] D. Dowson. History of Tribology. Longman, New York, 1979.

[30] DS Dugdale. Yielding of steel sheets containing slits. Journal of the Mechanics and Physics of Solids, 8(2):100–104, 1960.

[31] HD Espinosa, S Dwivedi, and H-C Lu. Modeling impact induced delamination of woven fiber reinforced composites with contact/cohesive laws. Computer Methods in Applied Mechanics and Engineering, 183(3):259–290, 2000.

[32] Mehdi Farsad, Franck J Vernerey, and Harold S Park. An extended finite element/level set method to study surface effects on the mechanical behavior and properties of nanomaterials. International Journal for Numerical Methods in Engineering, 84(12):1466–1489, 2010.

[33] Thomas-Peter Fries and Ted Belytschko. The intrinsic XFEM: a method for arbitrary discontinuities without additional unknowns. International journal for numerical methods in engineering, 68(13):1358–1385, 2006.

[34] T.P. Fries and T. Belytschko. The extended/generalized finite element method: an overview of the method and its applications. International Journal for Numerical Methods in Engineering, 84(3):253–304, 2010.

[35] S. Geniaut, P. Massin, and N. Moës. A stable 3D contact formulation using X-FEM. REMN, 16:259–275, 2007.

[36] G. Gilardi and I. Sharf. Literature survey of contact dynamics modelling. Mechanism and Machine Theory, 37(10):1213–1239, 2002.

[37] E. Giner, M. Tur, J. E. Tarancon, and F. J. Fuenmayor. Crack face contact in X-FEM using a segment-to-segment approach. International Journal for Numercial Methods in Engineering, 82:1424–1449, 2010.

[38] Arne S Gullerud, Xiaosheng Gao, Robert H Dodds, and R Haj-Ali. Simulation of ductile crack growth using computational cells: numerical aspects. Engineering Fracture Mechanics, 66(1):65–92, 2000.

[39] V.B. Hammer and N. Olhoff. Topology optimization of continuum structures subjected to pressure loading. Struct. Multidisc. Optim., 19:85–92, 2000.

[40] J. Herskovits, A. Leontiev, G. Dias, and G. Santos. Contact shape optimization: a bilevel programming approach. Struct Multidisc Optim, 20:214–221, 2000.

[41] H. R. Hertz. Ueber die beruehrung elastischer koerper. Gesammelte Werke, 1, 1895.

[42] D. Hilding, A. Klarbring, and J. Petersson. Optimization of structures in unilateral contact. Appl. Mech. Rev., 52(4):139–160, 1999.

[43] D. Hilding, B. Torstenfelt, and A. Klarbring. A computational methodology for shape optimization of structures in frictionless contact. Comput. Methods Appl. Mech. Engrg., 190:4043–4060, 2001.

[44] M. Hirmand, M. Vahab, and A. Khoei. An augented lagrangian contact formulation for frictional discontinuities with the extended finite element method. Finite Elements in Analysis and Design, 107:28–43, 2015.

[45] G.A. Holzapfel. Continuum Mechanics for Engineers. John Wiley & Sons Ltd,, 2000.

[46] Milan Jirásek. Comparative study on finite elements with embedded discontinuities. Computer methods in applied mechanics and engineering, 188(1):307–330, 2000.

[47] K. L. Johnson, K. Kendall, and A. D. Roberts. Surface energy and the contact of elastic solids. Proc. R. Soc. Lond. A., 324:301–313, 1971.

[48] A. Kawamoto. Stabilization of geometrically nonlinear topology optimization by the Levenberg-Marquardt method. Struct. Multidisc. Optim., 37:429–433, 2009.

[49] A. R. Khoei. Extended finite element method: Theory and applications. Wiley, 2015.

[50] AR Khoei and SM Taheri Mousavi. Modeling of large deformation–large sliding contact via the penalty X-FEM technique. Computational Materials Science, 48(3):471–480, 2010.

[51] AR Khoei and M Nikbakht. An enriched finite element algorithm for numerical computation of contact friction problems. International Journal of Mechanical Sciences, 49(2):183–199, 2007.

[52] Noboru Kikuchi and Bing-Chung Chen. Topology optimization with design-dependent loads. Finite Elements in Analysis and Design, 37(1):57–70, 2001.

[53] Nam Ho Kim, Kiyoung Yi, and Kyung Kook Choi. A material derivative approach in design sensitivity analysis of three-dimensional contact problems. International Journal of Solids and Structures, 39(8):2087 – 2108, 2002.

[54] N.H. Kim, Y.H. Park, and K.K. Choi. Optimization of a hyperelastic structure with multi-body contact using continuum-based shape design sensitivity analysis. Struct. Optim., 21(3):196208, 2001.

[55] Sebastian Kreissl and Kurt Maute. Levelset based fluid topology optimization using the extended finite element method. Structural and Multidisciplinary Optimization, pages 1–16, 2012.

[56] Christapher Lang, David Makhija, Alireza Doostan, and Kurt Maute. A simple and efficient preconditioning scheme for xfem with heaviside enrichments. Computational Mechancis, 54(5):1357–1374, 2014.

[57] M. Lawry, R. Behrou, and K. Maute. On the influence of interface models on the optimum layout of multi-component structures and material systems. In 11th World Congress on Structural and Multidisciplinary Optimisation, Sydney Austrailia, June 2015.

[58] M. Lawry and K. Maute. Level set shape and topology optimization of finite strain bilateral contact problems. International Journal for Numerical Methods in Engineering, 2016 (Submitted).

[59] Matthew Lawry and Kurt Maute. Level set topology optimization of problems with sliding contact interfaces. Structural and Multidisciplinary Optimization, 52(6):1107–1119, 2015.

[60] S Li and S Ghosh. Modeling interfacial debonding and matrix cracking in fiber reinforced composites by the extended voronoi cell fem. Finite elements in analysis and design, 43(5):397–410, 2007.

[61] F. Liu and R. Borja. A contact algorithm for frictional crack propagation with the extended finite element method. International Journal For Numerical Methods In Engineering, 76:1489–1512, 2008.

[62] F. Liu and R. I. Borja. Stabilized low-order finite elements for frictional contact with the extended finite element method. Computer Methods in Applied Mechancis and Engineering, 199:2456–2471, 2010.

[63] Pai Liu, Yangjun Luo, and Zhan Kang. Multi-material topology optimization considering interface behavior via XFEM and level set method. Computer Methods in Applied Mechanics and Engineering, 2016.

[64] Y. Luo, M. Li, and Z. Kang. Topology optimization of hyperelastic structures with frictionless contact supports. International Journal of Solids and Structures, 81:373–382, 2015.

[65] Zhen Luo, Liyong Tong, Michael Yu Wang, and Shengyin Wang. Shape and topology optimization of compliant mechanisms using a parameterization level set method. Journal of Computational Physics, 227(1):680–705, 2007.

[66] D. Makhija and K. Maute. Numerical instabilities in level set topology optimization with the extended finite element method. Structural and Multidisciplinary Optimization, 49(2):185–197, 2014.

[67] G.T. Mase, R. Smelser, and G.E. Mase. Continuum Mechanics for Engineers. CRC Press, Taylor & Francis Group, 3rd edition, 2010.

[68] K. Maute, S. Kreissl, D. Makhija, and R. Yang. Topology optimization of heat conduction in nano-composites. In 9^{th} World Congress on Structural and Multidisciplinary Optimization, Shizuoka, Japan, 2011.

[69] N. Moës, J. Dolbow, and T. Belytschko. A finite element method for crack growth without remeshing. International Journal for Numerical Methods in Engineering, 46, 1999.

[70] Nicolas Moës and Ted Belytschko. Extended finite element method for cohesive crack growth. Engineering fracture mechanics, 69(7):813–833, 2002.

[71] JJ. Moré. The Levenberg-Marquardt algorithm: implementation and theory. Numerical Analysis, pages 105–116, 1978.

[72] Jorge J Moré. The Levenberg-Marquardt algorithm: implementation and theory. In Numerical analysis, pages 105–116. Springer, 1978.

[73] D. S. Mueller-Hoeppe, P. Wriggers, and S. Loehnert. Crack face contact for hexahedral-based XFEM formulation. Computational Mechanics, 49:725–734, 2012.

[74] A. Myśliński. Level set method for shape and topology optimization of contact problems. In Adam Korytowski, Kazimierz Malanowski, Wojciech Mitkowski, and Maciej Szymkat, editors, System Modeling and Optimization, volume 312 of IFIP Advances in Information and Communication Technology, pages 397–410. Springer Berlin Heidelberg, 2009.

[75] A. Myśliński. Phase field approach to topology optimization of contact problems. In R. Haftka, editor, Proceedings of the 10th World Congress on Structural and Multidisciplinary Optimization, number paper 233. ISSMO, 2013.

[76] A. Myśliński. Piecewise constant level set method for topology optimization of unilateral contact problems. Advances in Engineering Software, 80:25–32, 2015.

[77] Andrzej A Myśliński and Konrad Koniarski. Sharp interface approach in topology optimization of contact problems. In 11th World congress on computational mechanics, Barcelona, 2014.

[78] A Needleman. A continuum model for void nucleation by inclusion debonding. Journal of applied mechanics, 54(3):525–531, 1987.

[79] I. Nistor, M. L. E. Guiton, P. Massin, N. Moës, and S. Géniaut. An X-FEM approach for large sliding contact along discontinuities. International Journal For Numerical Methods In Engineering, 78:1407–1435, 2009.

[80] Li Pan, Don R Metzger, and Marek Niewczas. The meshless dynamic relaxation techniques for simulating atomic structures of materials. In ASME 2002 Pressure Vessels and Piping Conference, pages 15–26. American Society of Mechanical Engineers, 2002.

[81] Kyoungsoo Park and Glaucio H Paulino. Cohesive zone models: a critical review of traction-separation relationships across fracture surfaces. Applied Mechanics Reviews, 64(6):060802, 2011.

[82] Georg Pingen, Matthias Waidmann, Anton Evgrafov, and Kurt Maute. A parametric level-set approach for topology optimization of flow domains. Structural and Multidisciplinary Optimization, 41(1):117–131, 2010.

[83] G.I.N. Rozvany, M. Zhou, and T. Birker. Generalized shape optimization without homogenization. Structural and Multidisciplinary Optimization, 4(3):250–252, 1992.

[84] Yousef Saad. Ilut: A dual threshold incomplete lu factorization. Numerical Linear Algebra with Applications, 1(4):387–402, 1994.

[85] M Salehi and H Aghaei. Dynamic relaxation large deflection analysis of non-axisymmetric circular viscoelastic plates. Computers & structures, 83(23):1878–1890, 2005.

[86] S. Sathe and T. E. Tezduyar. Modeling of fluidstructure interactions with the spacetime finite elements: contact problems. Computational Mechanics, 43:43:51, 2008.

[87] B Schott, U Rasthofer, V Gravemeier, and WA Wall. A face-oriented stabilized nitsche-type extended variational multiscale method for incompressible two-phase flow. International Journal for Numerical Methods in Engineering, 2014.

[88] B Schott and WA Wall. A new face-oriented stabilized xfem approach for 2d and 3d incompressible navier–stokes equations. Computer Methods in Applied Mechanics and Engineering, 276:233–265, 2014.

[89] M. Siavelis, M. Guiton, P. Massin, and N. Möes. Large sliding contact along branched discontinuities with x-fem. Comput Mech, 52:201–219, 2013.

[90] M. Siavelis, P. Massin, M. L. E. Guiton, S. Mazet, and N. Moës. Robust implementation of contact under friction and large sliding with the extended finite element method. European Journal of Computational Mechanics, 19:189–203, 2010.

[91] Ole Sigmund and Peter Michael Clausen. Topology optimization using a mixed formulation: an alternative way to solve pressure load problems. Computer Methods in Applied Mechanics and Engineering, 196(13):1874–1889, 2007.

[92] Ole Sigmund and Kurt Maute. Topology optimization approaches: A comparative review. Structural and Multidisciplinary Optimization, 48(6):1031–1055, 2013.

[93] Seong Hyeok Song, Glaucio H Paulino, and William G Buttlar. Simulation of crack propagation in asphalt concrete using an intrinsic cohesive zone model. Journal of Engineering Mechanics, 132(11):1215–1223, 2006.

[94] N. Strömberg. The influence of sliding friction in optimal topologies. In G. E. Stravroulakis, editor, Recent Advances in Contact Mechanics, volume 56, pages 327–336. 5th Contact Mechanics International Symposium (CMIS2009), Springer, April 2009.

[95] K. Svanberg. The method of moving asymptotes - a new method for structural optimization. International Journal for Numerical Methods in Engineering, 24(2):359–373, 1987.

[96] K. Svanberg. A globally convergent version of MMA without linesearch. In Proceedings of the First World Congress of Structural and Multidisciplinary Optimization, 28 May - 2 June 1995, pages 9–16, Goslar, Germany, 1995.

[97] Krister Svanberg. A class of globally convergent optimization methods based on conservative convex separable approximations. SIAM J. on Optimization, 12(2):555–573, 2002.

[98] S. M. J. Taheri Mousavi and S. M. Taheri Mousavi. Modeling large sliding frictional contact along non-smooth discontinuities in X-FEM. International Journal of Modeling and Optimization, 1:169–173, 2011.

[99] Kenjiro Terada, Mitsuteru Asai, and Michihiro Yamagishi. Finite cover method for linear and non-linear analyses of heterogeneous solids. International journal for numerical methods in engineering, 58(9):1321–1346, 2003.

[100] Martin GA Tijssens, Bert LJ Sluys, and Erik van der Giessen. Numerical simulation of quasi-brittle fracture using damaging cohesive surfaces. European Journal of Mechanics-A/Solids, 19(5):761–779, 2000.

[101] A. B. Tran, J. Yvonnet, Q-C. He, C. Toulemonde, and J. Sanahuja. A multiple level set approach to prevent numerical artefacts in complex microstructures with nearby inclusions within XFEM. International Journal for Numerical Methods in Engineering, 85(11):1436–1459, 2011.

[102] Viggo Tvergaard. Effect of fibre debonding in a whisker-reinforced metal. Materials science and engineering: A, 125(2):203–213, 1990.

[103] Viggo Tvergaard and John W Hutchinson. The relation between crack growth resistance and fracture process parameters in elastic-plastic solids. Journal of the Mechanics and Physics of Solids, 40(6):1377–1397, 1992.

[104] Nico P van Dijk, K Maute, M Langelaar, and F Van Keulen. Level-set methods for structural topology optimization: a review. Structural and Multidisciplinary Optimization, 48(3):437–472, 2013.

[105] N.P. van Dijk, M. Langelaar, and F. van Keulen. Explicit level-set-based topology optimization using an exact heaviside function and consistent sensitivity analysis. International Journal for Numerical Methods in Engineering, 91(1):67–97, 2012.

[106] L. Vese and T. Chan. A multiphase levelset framework for image segmentation using the mumford and shah model. International Journal of Computer Vision, 50(3):271–293, 2002.

[107] C. H. Villanueva and K. Maute. Density and level set-XFEM schemes for topology optimization of 3-D structures. Computational Mechanics, 54(1):133–150, 2014.

[108] M. Y. Wang, X. Wang, and D. Guo. A level set method for structural topology optimization. Computer Methods in Applied Mechanics and Engineering, 192(1-2):227–246, 2003.

[109] M.Y. Wang and X. Wang. A level-set based variational method for design and optimization of heterogeneous objects. Computer-Aided Design, 37(3):321–337, 2005.

[110] S. Wang and M.Y. Wang. Radial basis functions and level set method for structural topology optimization. International journal for numerical methods in engineering, 65(12):2060–2090, 2006.

[111] M. L. Wilkins. Calculation of elasto-plastic flow. Methods of Computational Physics, 3, 1964.

[112] E. A. Wilson and B. Parsons. Finite element analysis of elastic contact problems using differential displacements. International Journal for Numerical Methods in Engineering, 2(3):387–395, 1970.

[113] Peter Wriggers. Computational Contact Mechanics. Wiley, 2002.

[114] H. L. Xing and A. Makinouchi. Three dimensional finite element modeling of thermomechanical frictional contact between finite deformation bodies using R-minimum strategy. Computer Methods in Applied Mechanics and Engineering, 191(37-38):4193–4214, 2002.

[115] X-P Xu and A Needleman. Void nucleation by inclusion debonding in a crystal matrix. Modelling and Simulation in Materials Science and Engineering, 1(2):111, 1993.

[116] X-P Xu and Alan Needleman. Numerical simulations of fast crack growth in brittle solids. Journal of the Mechanics and Physics of Solids, 42(9):1397–1434, 1994.

[117] B Yang and K Ravi-Chandar. A single-domain dual-boundary-element formulation incorporating a cohesive zone model for elastostatic cracks. International Journal of Fracture, 93(1-4):115–144, 1998.

[118] Gil Ho Yoon. Topology optimization for stationary fluid–structure interaction problems using a new monolithic formulation. International journal for numerical methods in engineering, 82(5):591–616, 2010.

[119] M. Yulin and W. Xiaoming. A level set method for structural topology optimization and its applications. Advances in Engineering Software, 35(7):415–441, 2004.

[120] LG Zhang and TX Yu. Modified adaptive dynamic relaxation method and its application to elastic-plastic bending and wrinkling of circular plates. Computers & structures, 33(2):609–614, 1989.

[121] Zhengyu Jenny Zhang and Glaucio H Paulino. Cohesive zone modeling of dynamic failure in homogeneous and functionally graded materials. International journal of plasticity, 21(6):1195–1254, 2005.

Appendix A

Parametric Representation of Contact Constitutive Relations

This chapter provides examples of various interface constitutive relations, starting from strong form equations and fully deriving coupled parametric weak form equations. Provided are the penalty formulation, Lagrange multiplier method, and a stabilized Lagrange formulation.

A.1 Penalty Formulation

As a purely geometric consideration, we wish to penalize normal penetration between both surfaces. The strong form of the penalty formulation is:

$$\frac{1}{2}\epsilon g_n^2 = 0 \tag{A.1}$$

where ϵ is an arbitrary penalty factor. The penalty factor ensures that the normal gap must be zero to satisfy equilibrium. While this may be an appropriate response for compression, additional conditions must be set to allow surface separation. Surface separation is discussed in Appendix B.

Applying integration over the surface and taking the total variation , the weak form residual contribution from contact becomes:

$$\boldsymbol{r}_c = \int_{\Gamma_c} (\delta g_n \ \epsilon \ g_n) \, \mathrm{d}\Gamma_c \tag{A.2}$$

where the integration domain Γ_c is the contact surface between both structures and δg_n is the variation of the normal gap. After mapping to the master surface parametric configuration, the penalty formulation is as follows.

$$\boldsymbol{r}_c = \int_{\hat{\alpha}^1}^{\hat{\alpha_2}} \left(\delta g_n \left(\alpha\right) \ \epsilon \ g_n \left(\alpha\right)\right) \left| \frac{\partial X_i^m}{\partial \alpha} \right| \mathrm{d}\alpha \tag{A.3}$$

After applying Equation 6.42 the tangent stiffness becomes:

$$\frac{\mathrm{d}\boldsymbol{r}_c}{\mathrm{d}\hat{u}_i^p} = \int_{\hat{\alpha}_1}^{\hat{\alpha}_2} \left(\frac{\partial}{\partial \hat{u}_i^p} \left(\delta g_n\right) \ \epsilon \ g_n + \delta g_n \ \epsilon \ \frac{\partial}{\partial \hat{u}_i^p} \left(g_n\right) \right) \left| \frac{\partial X_i^m}{\partial \alpha} \right| \ \mathrm{d}\alpha + \left(\left(\delta g_n\left(\alpha\right) \ \epsilon \ g_n\left(\alpha\right)\right) \left| \frac{\partial X_i^m}{\partial \alpha} \right| \right) \Big|_{\hat{\alpha_2}} \frac{\partial \hat{\alpha}_2}{\partial \hat{u}_i^p} - \left(\left(\delta g_n\left(\alpha\right) \ \epsilon \ g_n\left(\alpha\right)\right) |\frac{\partial X_i^m}{\partial \alpha}| \right) \Big|_{\hat{\alpha_1}} \frac{\partial \hat{\alpha}_1}{\partial \hat{u}_i^p} \quad \text{(A.4)}$$

Using Equation 6.56, the derivative of residual contributions with respect to parametric control parameters is derived as follows:

$$\frac{\mathrm{d}\boldsymbol{r}_c}{\mathrm{d}c_j^p} = \int_{\hat{\alpha}_1}^{\hat{\alpha}_2} \left(\frac{\partial}{\partial c_j^p} \left(\delta g_n\right) \ \epsilon \ g_n + \delta g_n \ \epsilon \ \frac{\partial}{\partial c_j^p} \left(g_n\right) \right) \left| \frac{\partial X_i^m}{\partial \alpha} \right| \ \mathrm{d}\alpha + \int_{\hat{\alpha}^1}^{\hat{\alpha_2}} \left(\delta g_n\left(\alpha\right) \ \epsilon \ g_n\left(\alpha\right)\right) \frac{\partial}{\partial c_j^p} \left(\left| \frac{\partial X_i^m}{\partial \alpha} \right| \right) \mathrm{d}\alpha + \left(\left(\delta g_n\left(\alpha\right) \ \epsilon \ g_n\left(\alpha\right)\right) \left| \frac{\partial X_i^m}{\partial \alpha} \right| \right) \Big|_{\hat{\alpha_2}} \frac{\partial \hat{\alpha}_2}{\partial c_j^p} - \left(\left(\delta g_n\left(\alpha\right) \ \epsilon \ g_n\left(\alpha\right)\right) |\frac{\partial X_i^m}{\partial \alpha}| \right) \Big|_{\hat{\alpha_1}} \frac{\partial \hat{\alpha}_1}{\partial c_j^p} \quad \text{(A.5)}$$

Although the penalty method of enforcing surface non-penetration is geometrically intuitive and relatively easy to apply, it has its own caveats. The satisfaction of non-penetration is directly tied to the size of penalty parameter ϵ. For larger values of ϵ, penetration error decreases at the cost of the conditioning number of the tangent stiffness matrix. Therefore care must be taken when selecting an appropriate penalty parameter to minimize penetration error without producing an ill conditioned system.

A.2 Lagrange Multiplier Formulation

Instead of relying on purely geometric considerations, a second approach is to begin with the non-penetration inequality condition:

$$g_n \lambda = 0, \qquad \lambda \leq 0, \qquad g_n \geq 0 \quad \text{(A.6)}$$

where λ is the normal pressure at the contact interface. If satisfied, this inequality constraint ensures that the normal gap between surfaces must be greater than or equal to zero. In addition, the normal pressure between surfaces must be compressive. The classical Lagrange Multiplier method can be

derived for surface-to-surface contact by taking the variation of the equality condition integrated over the area of contact:

$$\int_{\Gamma_c} (\delta g_n \lambda + g_n \delta\lambda)\, \mathrm{d}\Gamma = 0 \tag{A.7}$$

where Γ_c is the area of contact. The normal pressure λ can be treated as an independent variable, yielding a residual contribution to displacement equilibrium and a constraint equation.

$$\boldsymbol{r}_c = \int_{\Gamma_c} (\delta g_n \lambda)\, \mathrm{d}\Gamma \tag{A.8}$$

$$\boldsymbol{r}_\lambda = \int_{\Gamma_c} (g_n \delta\lambda)\, \mathrm{d}\Gamma = 0 \tag{A.9}$$

Applying a **push-back** operation and mapping the residual contributions to parametric space,

$$\boldsymbol{r}_c = \int_{\hat{\alpha}^1}^{\hat{\alpha_2}} \left(\delta g_n^0(\alpha)\ \ \lambda^0(\alpha)\right) \left| \frac{\partial X_i^m}{\partial \alpha} \right| \mathrm{d}\alpha \tag{A.10}$$

$$\boldsymbol{r}_c = \int_{\hat{\alpha}^1}^{\hat{\alpha_2}} \left(g_n^0(\alpha)\ \ \delta\lambda^0(\alpha)\right) \left| \frac{\partial X_i^m}{\partial \alpha} \right| \mathrm{d}\alpha \tag{A.11}$$

Here, we interpolate the Lagrange multiplier by some generic test function μ_i, such that $\lambda^0(\alpha) = \mu_i(\alpha)\,\hat{\lambda}_i^0$. Applying Equation 6.42, the tangent stiffness contributions can be expressed as

$$\begin{aligned}\frac{\mathrm{d}\boldsymbol{r}_c}{\mathrm{d}\hat{u}_i^p} = &\int_{\hat{\alpha}_1}^{\hat{\alpha}_2} \left(\frac{\partial}{\partial \hat{u}_i^p} \left(\delta g_n^0(\alpha)\right) \lambda^0(\alpha) + \delta g_n^0(\alpha) \frac{\partial}{\partial \hat{u}_i^p} \left(\lambda^0(\alpha)\right) \right) \left| \frac{\partial X_i^m}{\partial \alpha} \right| \mathrm{d}\alpha + \\ &\left(\left(\delta g_n^0(\alpha)\ \ \lambda^0(\alpha)\right) \left| \frac{\partial X_i^m}{\partial \alpha} \right| \right) \Big|_{\hat{\alpha_2}} \frac{\partial \hat{\alpha}_2}{\partial \hat{u}_i^p} - \left(\left(\delta g_n^0(\alpha)\ \ \lambda^0(\alpha)\right) |\frac{\partial X_i^m}{\partial \alpha}| \right) \Big|_{\hat{\alpha_1}} \frac{\partial \hat{\alpha}_1}{\partial \hat{u}_i^p},\end{aligned} \tag{A.12}$$

$$\begin{aligned}\frac{\mathrm{d}\boldsymbol{r}_\lambda}{\mathrm{d}\hat{u}_i^p} = &\int_{\hat{\alpha}_1}^{\hat{\alpha}_2} \left(\frac{\partial}{\partial \hat{u}_i^p} \left(g_n^0(\alpha)\right) \delta\lambda^0(\alpha) + \delta g_n^0(\alpha) \frac{\partial}{\partial \hat{u}_i^p} \left(\delta\lambda^0(\alpha)\right) \right) \left| \frac{\partial X_i^m}{\partial \alpha} \right| \mathrm{d}\alpha + \\ &\left(\left(g_n^0(\alpha)\ \ \delta\lambda^0(\alpha)\right) \left| \frac{\partial X_i^m}{\partial \alpha} \right| \right) \Big|_{\hat{\alpha_2}} \frac{\partial \hat{\alpha}_2}{\partial \hat{u}_i^p} - \left(\left(g_n^0(\alpha)\ \ \delta\lambda^0(\alpha)\right) |\frac{\partial X_i^m}{\partial \alpha}| \right) \Big|_{\hat{\alpha_1}} \frac{\partial \hat{\alpha}_1}{\partial \hat{u}_i^p}.\end{aligned} \tag{A.13}$$

Applying Equation 6.56, sensitivities are defined as

$$\begin{aligned}\frac{\mathrm{d}\boldsymbol{r}_c}{\mathrm{d}c_j^p} = &\int_{\hat{\alpha}_1}^{\hat{\alpha}_2} \left(\frac{\partial}{\partial c_j^p} \left(\delta g_n^0(\alpha)\right) \lambda^0(\alpha) + \delta g_n^0(\alpha) \frac{\partial}{\partial c_j^p} \left(\lambda^0(\alpha)\right) \right) \left| \frac{\partial X_i^m}{\partial \alpha} \right| \mathrm{d}\alpha + \\ &\int_{\hat{\alpha}_1}^{\hat{\alpha}_2} \left(\delta g_n^0(\alpha)\, \lambda^0(\alpha)\right) \frac{\partial}{\partial c_j^p} \left(\left| \frac{\partial X_i^m}{\partial \alpha} \right| \right) \mathrm{d}\alpha + \\ &\left(\left(\delta g_n^0(\alpha)\ \ \lambda^0(\alpha)\right) \left| \frac{\partial X_i^m}{\partial \alpha} \right| \right) \Big|_{\hat{\alpha_2}} \frac{\partial \hat{\alpha}_2}{\partial c_j^p} - \left(\left(\delta g_n^0(\alpha)\ \ \lambda^0(\alpha)\right) |\frac{\partial X_i^m}{\partial \alpha}| \right) \Big|_{\hat{\alpha_1}} \frac{\partial \hat{\alpha}_1}{\partial c_j^p},\end{aligned} \tag{A.14}$$

$$\frac{\mathrm{d}\boldsymbol{r}_\lambda}{\mathrm{d}c_j^p} = \int_{\hat{\alpha}_1}^{\hat{\alpha}_2} \left(\frac{\partial}{\partial c_j^p} \left(g_n^0 \left(\alpha \right) \right) \delta\lambda^0 \left(\alpha \right) + \delta g_n^0 \left(\alpha \right) \frac{\partial}{\partial c_j^p} \left(\delta\lambda^0 \left(\alpha \right) \right) \right) \left| \frac{\partial X_i^m}{\partial \alpha} \right| \, \mathrm{d}\alpha + \int_{\hat{\alpha}_1}^{\hat{\alpha}_2} \left(\delta g_n^0 \left(\alpha \right) \delta\lambda^0 \left(\alpha \right) \right) \frac{\partial}{\partial c_j^p} \left(\left| \frac{\partial X_i^m}{\partial \alpha} \right| \right) \, \mathrm{d}\alpha + \left(\left(g_n^0 \left(\alpha \right) \ \delta\lambda^0 \left(\alpha \right) \right) \left| \frac{\partial X_i^m}{\partial \alpha} \right| \right) \Big|_{\hat{\alpha_2}} \frac{\partial \hat{\alpha}_2}{\partial c_j^p} - \left(\left(g_n^0 \left(\alpha \right) \ \delta\lambda^0 \left(\alpha \right) \right) |\frac{\partial X_i^m}{\partial \alpha}| \right) \Big|_{\hat{\alpha_1}} \frac{\partial \hat{\alpha}_1}{\partial c_j^p}. \quad \text{(A.15)}$$

A.3 Stabilized Lagrange Multiplier Formulation

The Lagrange multiplier method of satisfying non-penetration can suffer from spurious oscillations of the contact pressure, as there are no requirements that the Lagrange multipliers be positive or negative to satisfy equilibrium. Retaining consistency and convergence of Lagrange multipliers by adding stabilization terms to the classical Galerkin method was introduced by [8]. Here, the stabilized Lagrange method relates the Lagrange multiplier to the surface stresses of either respective body, replacing Equation A.9 with:

$$\boldsymbol{r}_\lambda = \int_{\Gamma_c} \delta\lambda \left(\lambda - n_i^m \left(\kappa^m \sigma_{ij}^m + \kappa^s \sigma_{ij}^s \right) n_j^m + \epsilon g_n \right) \mathrm{d}\Gamma = 0 \quad \text{(A.16)}$$

$$\kappa^m + \kappa^s = 1 \quad \text{(A.17)}$$

where $\delta\lambda$ is the Lagrange multiplier trial function, κ is a stress weighting parameter for material p, and ϵ is a penalty factor. This penalty factor discourages penetration during the early stages of convergence, but becomes insignificant as stress equilibrium is achieved at the converged solution. The most intuitive choice for the stress weighting parameters is $\kappa^p = 0.5$, however within the framework of XFEM, stress predictions can be poor in small fractions of elements. Furthermore, in the context of contact mechanics this choice can cause small fractions of elements to invert under moderate surface pressure. To mitigate this issue, another approach proposed by [5] is to provide a weighting scheme proportional to element fraction volume and inversely proportional to material stiffness:

$$\kappa^m = \frac{\frac{\Omega^m}{E^m}}{\frac{\Omega^m}{E^m} + \frac{\Omega^s}{E^s}}, \qquad \kappa^s = \frac{\frac{\Omega^s}{E^s}}{\frac{\Omega^m}{E^m} + \frac{\Omega^s}{E^s}} \quad \text{(A.18)}$$

where Ω^p and E^p are the element fraction volume and Youngs modulus for material p. This weighting scheme places more emphasis on the predicted surface stress of the greater element fraction.

Here we introduce a generic interpolation space for the Lagrange multiplier μ_i, such that $\lambda^0(\alpha) = \mu_i(\alpha)\hat{\lambda}_i^0$ and $\delta\lambda = \mu_i$. Stresses are derived from objective (frame indifferent) constitutive relations, pushed forward to the deformed configuration for averaging, and mapped to the undeformed master surface for integration:

$$\boldsymbol{r}_\lambda = \int_{\Gamma_m^0} \mu_i \left(\lambda^0 - \kappa^m n_i^{d^m} S_{ij}^m n_j^{d^m} - \kappa^s n_i^{d^m} F_{ij}^s S_{jk}^s F_{lk}^s n_l^{d^m} J^{s-1} \mathcal{J}^m + \epsilon g_n\right) \mathrm{d}\Gamma = 0 \tag{A.19}$$

where Γ_m^0 is the undeformed master surface, F_{ij} is the deformation gradient, $J = \det(F_{ij})$ is the volumetric jacobian, $\mathcal{J} = \frac{\mathrm{d}a}{\mathrm{d}A} = J\|\mathbf{F}^{-T}\cdot\mathbf{n}_0\|$ is the surface jacobian, S_{ij} is the second Piola-Kirchoff stress tensor, and λ^0 denotes the Lagrange multiplier in the master reference configuration. The Lagrange multiplier is condensed out at the elemental level, and the state residual contribution is integrated in the undeformed master configuration.

$$\boldsymbol{r}_c = \int_{\Gamma_m^0} \left(\delta g_n^0 \ \lambda^0\right) \mathrm{d}\Gamma \tag{A.20}$$

Mapping the constraint equation and residual contributions to parametric space:

$$\boldsymbol{r}_\lambda = \int_{\hat{\alpha}^1}^{\hat{\alpha}_2} \mu_p \Big(\lambda^0(\alpha) - \kappa^m n_i^{d^m} S_{ij}^m n_j^{d^m} - \kappa^s n_i^{d^m} F_{ij}^s S_{jk}^s F_{lk}^s n_l^{d^m} J^{s-1} \mathcal{J}^m - \epsilon g_n\Big) \left|\frac{\partial X_i^m}{\partial \alpha}\right| \mathrm{d}\alpha = 0 \tag{A.21}$$

$$\boldsymbol{r}_c = \int_{\hat{\alpha}^1}^{\hat{\alpha}_2} \left(\delta g_n(\alpha) \ \ \lambda(\alpha, \hat{\alpha}_1, \hat{\alpha}_2)\right) \left|\frac{\partial X_i^m}{\partial \alpha}\right| \mathrm{d}\alpha \tag{A.22}$$

The Lagrange multiplier degrees of freedom are condensed at the local level as follows:

$$\hat{\lambda}_q^0 = \left[\int_{\hat{\alpha}^1}^{\hat{\alpha}_2} \mu_p \mu_q \left|\frac{\partial X_i^m}{\partial \alpha}\right| \mathrm{d}\alpha\right]^{-1} \int_{\hat{\alpha}^1}^{\hat{\alpha}_2} \mu_p \Big(\kappa^m n_i^{d^m} S_{ij}^m n_j^{d^m} + \kappa^s n_i^{d^m} F_{ij}^s S_{jk}^s F_{lk}^s n_l^{d^m} J^{s-1} \mathcal{J}^m + \epsilon g_n\Big) \left|\frac{\partial X_i^m}{\partial \alpha}\right| \mathrm{d}\alpha. \tag{A.23}$$

Note that due to condensation, the surface pressure variables $\hat{\lambda}_q^0$ are dependent on the limits of integration. To express this dependency, we begin by taking the derivative of Equation A.23 with respect to $\hat{\alpha}_i$. For brevity, the integrand in Equation A.23 is denoted by $\boldsymbol{f}_\lambda$. Taking the partial derivative with respect to the limit of integration and discrete solution:

$$\frac{\partial \hat{\lambda}_k^0}{\partial \hat{\alpha}_1} = \left[\int_{\hat{\alpha}^1}^{\hat{\alpha}_2} \mu_i \mu_k \left| \frac{\partial X_l^m}{\partial \alpha} \right| \mathrm{d}\alpha\right]^{-1} \left[\mu_i \left(\mu_j \hat{\lambda}_j^0 - \boldsymbol{f}_\lambda\right) \Big|_{\hat{\alpha}_1}\right], \tag{A.24}$$

$$\frac{\partial \hat{\lambda}_k^0}{\partial \hat{\alpha}_2} = -\left[\int_{\hat{\alpha}^1}^{\hat{\alpha}_2} \mu_i \mu_k \left| \frac{\partial X_l^m}{\partial \alpha} \right| \mathrm{d}\alpha\right]^{-1} \left[\mu_i \left(\mu_j \hat{\lambda}_j^0 - \boldsymbol{f}_\lambda\right) \Big|_{\hat{\alpha}_2}\right], \tag{A.25}$$

$$\frac{\partial \hat{\lambda}_k^0}{\partial \hat{u}_q^p} = \left[\int_{\hat{\alpha}^1}^{\hat{\alpha}_2} \mu_i \mu_k \left| \frac{\partial X_l^m}{\partial \alpha} \right| \mathrm{d}\alpha.\right]^{-1} \left[\int_{\hat{\alpha}^1}^{\hat{\alpha}_2} \mu_i \left(\frac{\partial f_\lambda}{\partial \hat{u}_q^p}\right) \mathrm{d}\alpha\right] \tag{A.26}$$

We have derived the necessary relations to evaluate the consistent tangent of our residual contribution. Recalling our residual contribution:

$$\boldsymbol{r}_c = \int_{\hat{\alpha}^1}^{\hat{\alpha_2}} \left(\delta g_n\left(\alpha\right) \;\; \lambda^0\left(\alpha, \hat{\alpha}_1, \hat{\alpha}_2\right)\right) \left| \frac{\partial X_i^m}{\partial \alpha} \right| \mathrm{d}\alpha \tag{A.27}$$

we will abbreviate the integrand as f_u to arrive at a succinct consistent tangent stiffness.

$$\begin{aligned}\frac{\mathrm{d}\boldsymbol{r}_c}{\mathrm{d}\hat{u}_i} = \int_{\hat{\alpha}_1}^{\hat{\alpha}_2} \frac{\partial f_u}{\partial \hat{u}_i} \;\; \mathrm{d}\alpha \;\; + \int_{\hat{\alpha}_1}^{\hat{\alpha}_2} \left(\delta g_n \frac{\partial \lambda^0}{\partial \hat{\alpha}_2}\right) \left| \frac{\partial X_i^m}{\partial \alpha} \right| \mathrm{d}\alpha \;\; \frac{\partial \hat{\alpha}_2}{\partial \hat{u}_i} \;\; + \left(f_u \Big|_{\hat{\alpha_2}}\right) \frac{\partial \hat{\alpha}_2}{\partial \hat{u}_i} \\ - \int_{\hat{\alpha}_1}^{\hat{\alpha}_2} \left(\delta g_n^0 \frac{\partial \lambda}{\partial \hat{a}_1}\right) \left| \frac{\partial X_i^m}{\partial \alpha} \right| \mathrm{d}\alpha \;\; \frac{\partial \hat{\alpha}_1}{\partial \hat{u}_i} \;\; - \left(f_u \Big|_{\hat{\alpha_1}}\right) \frac{\partial \hat{\alpha}_1}{\partial \hat{u}_i}\end{aligned} \tag{A.28}$$

Taking the derivative of the Lagrange multiplier with respect to parametric control variables:

$$\begin{aligned}\frac{\partial \hat{\lambda}_k^0}{\partial c_q^p} = \left[\int_{\hat{\alpha}^1}^{\hat{\alpha}_2} \mu_i \mu_k \left| \frac{\partial X_l^m}{\partial \alpha} \right| \mathrm{d}\alpha\right]^{-1} \left[\int_{\hat{\alpha}^1}^{\hat{\alpha}_2} \left(\frac{\partial \boldsymbol{f}_\lambda}{\partial c_j^p}\right) \mathrm{d}\alpha\right] - \\ \left[\int_{\hat{\alpha}^1}^{\hat{\alpha}_2} \mu_i \mu_k \left| \frac{\partial X_l^m}{\partial \alpha} \right| \mathrm{d}\alpha\right]^{-2} \left[\int_{\hat{\alpha}^1}^{\hat{\alpha}_2} \left(\boldsymbol{f}_\lambda\right) \mathrm{d}\alpha \int_{\hat{\alpha}^1}^{\hat{\alpha}_2} \mu_i \left(\frac{\partial}{\partial c_j^p} \left| \frac{\partial X_l^m}{\partial \alpha} \right|\right) \mathrm{d}\alpha\right]\end{aligned} \tag{A.29}$$

the derivative of residual contributions from contact with respect to parametric control parameters is derived.

$$\begin{aligned}\frac{\mathrm{d}\boldsymbol{r}_c}{\mathrm{d}c_j^p} = \int_{\hat{\alpha}_1}^{\hat{\alpha}_2} \frac{\partial f_u}{\partial c_j^p} \;\; \mathrm{d}\alpha \;\; + \int_{\hat{\alpha}_1}^{\hat{\alpha}_2} \left(\delta g_n \frac{\partial \lambda^0}{\partial \hat{\alpha}_2}\right) \left| \frac{\partial X_i^m}{\partial \alpha} \right| \mathrm{d}\alpha \;\; \frac{\partial \hat{\alpha}_2}{\partial c_j^p} \;\; + \left(f_u \Big|_{\hat{\alpha_2}}\right) \frac{\partial \hat{\alpha}_2}{\partial c_j^p} \\ - \int_{\hat{\alpha}_1}^{\hat{\alpha}_2} \left(\delta g_n^0 \frac{\partial \lambda}{\partial \hat{a}_1}\right) \left| \frac{\partial X_i^m}{\partial \alpha} \right| \mathrm{d}\alpha \;\; \frac{\partial \hat{\alpha}_1}{\partial c_j^p} \;\; - \left(f_u \Big|_{\hat{\alpha_1}}\right) \frac{\partial \hat{\alpha}_1}{\partial c_j^p}\end{aligned} \tag{A.30}$$

Appendix B

Considerations for Mechanical Model Accuracy and Optimization Reliability

The methodology, model verification, and numerical examples provided in this thesis demonstrate that topology optimization shows great promise towards the development of structural designs reliant on contact phenomena. However, throughout the evolution of model geometry, design features and intermediate configurations can arise which pose difficulties to the evaluation of the physical response prediction, and subsequently the determination of design sensitivities. Within the context of XFEM-LSM topology optimization of contact related problems, this chapter provides insight to how various contact assumptions, numerical implementation methods, and XFEM stabilization techniques affect the mechanical model accuracy and optimization reliability of these types of design problems. The studies presented here are specific to large sliding contact behavior in the finite strain regime.

B.1 Contact Behavioral Assumptions

For large deformation contact problems, it can be convenient to integrate contact contributions to equilibrium in an unchanging reference configuration. Non-penetration constitutive relations such as the Stabilized Lagrange formulation or Nitsche's method express contact equilibrium in terms of surface pressure equilibrium. For this work, contact contributions to equilibrium are integrated along the master surface undeformed configuration. This requires mapping surface information from the undeformed slave surface to the undeformed master surface for the evaluation of an averaged interface surface traction. Depending on the assumptions made regarding coinci-

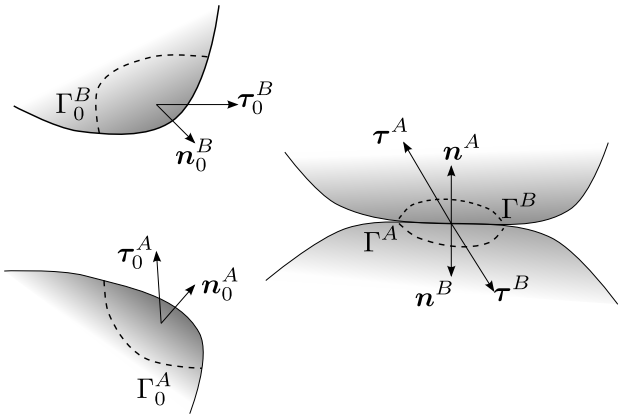

Figure B.1: Continuum bodies 'A' and 'B', which are in contact in the current configuration.

dent surface orientation, the resulting constitutive behavior at the interface may take on slightly different forms.

Consider two elastic continuum bodies with smooth and continuous surface geometry. The continuum bodies are separate in the undeformed configuration, but are in frictionless contact between surface subsets Γ^A and Γ^B in the current configuration, as illustrated in Figure B.1. We wish to evaluate an averaged measure of surface pressure on the undeformed surface Γ_0^A:

$$\bar{p}_0^A = \kappa^A p_0^A + \kappa^B p_0^{B\to A}, \tag{B.1}$$

where $\bar{p}_0^A$ is the averaged measure of surface pressure, κ^A and κ^B are arbitrary weighting terms such that $\kappa^A + \kappa^B = 1$, p_0^A is the surface pressure on the undeformed surface of body 'A', and $p_0^{B\to A}$ is the surface pressure on the undeformed surface of body 'B', mapped to the undeformed surface of body 'A'. The surface pressure p_0^A is determined as:

$$p_0^A = \boldsymbol{n}_0^{A^T} \cdot \boldsymbol{S}^A \cdot \boldsymbol{n}_0^A \tag{B.2}$$

What follows are two different variations for determining $p_0^{B\to A}$.

B.1.1 Orientation Assumption: $\mathbf{n^A = -n^B}$

In a state of perfect frictionless contact within the surface subsets Γ^A and Γ^B, one may assume that the deformed surface normal orientation of each body are equal and opposite:

$$\mathbf{n^A} = -\mathbf{n^B} \ . \tag{B.3}$$

With equal and opposite surface orientation one may directly map surface quantities from one bodies reference configuration to the other, within the area in contact. To define surface pressure on the undeformed surface of body 'B', mapped to the undeformed surface body 'A', pressure is first directly evaluated on the undeformed surface of body 'B:'

$$p_0^B = \mathbf{n}^{B^T}_0 \cdot \mathbf{S}^B \cdot \mathbf{n}_0^B \ . \tag{B.4}$$

Using the surface Jacobian defined in Equation 3.24, surface pressure is scaled to the current configuration:

$$p^B = \mathbf{n}^{B^T}_0 \cdot \mathbf{S}^B \cdot \mathbf{n}_0^B \ \mathcal{J}^{B^{-1}} = \mathbf{n}^{B^T} \cdot \boldsymbol{\sigma}^B \cdot \mathbf{n}^B \ . \tag{B.5}$$

Note that due to the equal and opposite orientation of each surface in contact:

$$p^{B\to A} = \mathbf{n}^{A^T} \cdot \boldsymbol{\sigma}^B \cdot \mathbf{n}^A = \mathbf{n}^{B^T} \cdot \boldsymbol{\sigma}^B \cdot \mathbf{n}^B \ . \tag{B.6}$$

Equation B.6 implies that given the coincident position of either respective surface in the deformed configuration, $p^{B\to A} = p^B$. Using the surface Jacobian of body 'A,' the surface pressure from body 'B' is pulled back to the reference configuration of body 'A.'

$$p_0^{B\to A} = \mathbf{n}^{B^T}_0 \cdot \mathbf{S}^B \cdot \mathbf{n}_0^B \ \mathcal{J}^{B^{-1}} \ \mathcal{J}^A \tag{B.7}$$

This mapping process is illustrated in Figure B.2. Assuming equal and opposite surface orientation leads to a compact and computationally inexpensive mapped pressure term. Surface normals are evaluated in the undeformed configuration only, which are independent of the displacement field. Within the context of weakly enforced immersed boundary conditions, the performance of this mapped pressure term will be compared to one which does not assume both surfaces are equal and opposite in orientation.

B.1.2 Orientation Assumption: $\mathbf{n^A \neq -n^B}$

Although a perfect state of frictionless contact between two smooth elastic continuum bodies indeed yields equal and opposite surface normals in the deformed configuration, numerical approximation of the contact problem can result in non-coincident surface position and orientation. This is especially true for weakly enforced contact equilibrium. This pressure mapping method assumes that surface location is coincident, without making any assumptions of equal and opposite surface orientation. Only the orientation of the master surface (body 'A') is used to evaluate pressure. To define surface pressure from body 'B' mapped to the undeformed surface of body 'A,' the 2nd Piola Kirchhoff stress from body 'B' is first pushed forward to the current configuration:

$$\sigma^B = J^{B^{-1}} \mathbf{F}^B \cdot \mathbf{S}^B \cdot \mathbf{F}^{B^T} \ . \tag{B.8}$$

The deformed normal of body 'A' is then used to determine the resulting pressure on the surface of body 'A:'

$$p^{B\to A} = J^{B^{-1}} \mathbf{n}^{A^T} \cdot \mathbf{F}^B \cdot \mathbf{S}^B \cdot \mathbf{F}^{B^T} \cdot \mathbf{n}^A \ . \tag{B.9}$$

Lastly, the pressure term is pulled back to the reference configuration using the surface Jacobian:

$$p_0^{B\to A} = J^{B^{-1}} \mathbf{n}^{A^T} \cdot \mathbf{F}^B \cdot \mathbf{S}^B \cdot \mathbf{F}^{B^T} \cdot \mathbf{n}^A \ \mathcal{J}^A \tag{B.10}$$

This mapping process without any orientation assumptions is illustrated in Figure B.3. This

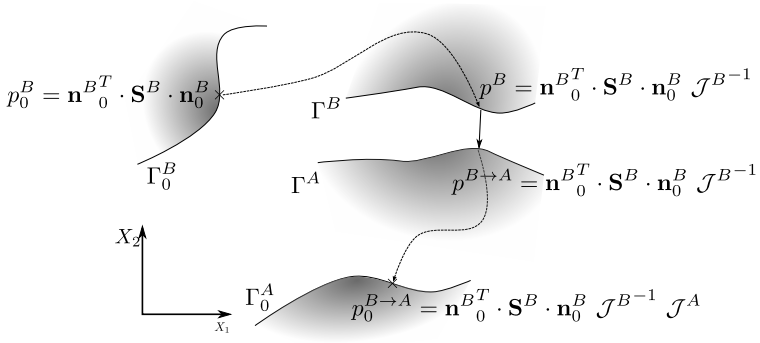

Figure B.2: Mapping surface pressure, orientation assumption: $\mathbf{n^A = -n^B}$.

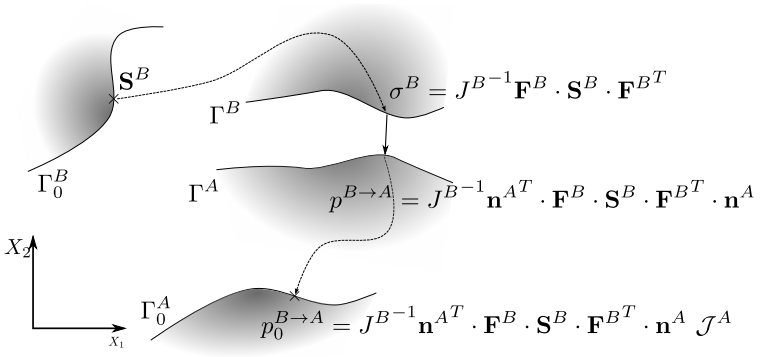

Figure B.3: Mapping surface pressure, orientation assumption: $\mathbf{n^A} \neq -\mathbf{n^B}$.

form of mapped surface pressure does not rely on any orientation assumption, but is computationally more expensive. The deformed surface normals of surface 'A' are dependent on the displacement field, complicating the determination of the tangent stiffness. What follows is a simple example illustrating the difference in predicted model response from either method of mapping surface pressure.

B.1.3 Orientation Assumption: Comparison

For comparison, we revisit the weak form of governing equations:

$$\sum_{p=A,B} \int_{\Omega^{p_0}} \mathbf{C}(\mathbf{v}^p) : (\mathbf{F}^p \mathbf{S}^p) \; d\Omega \; - \sum_{p=A,B} \int_{\Omega^{p_0}} \mathbf{v}^p \cdot \mathbf{f}^p \; d\Omega \\ - \sum_{p=A,B} \int_{\Gamma_N^{p_0}} \mathbf{v}^p \cdot \mathbf{F}^p \; d\Gamma - \int_{\Gamma_0^A} \delta g_0^A \; \lambda_0 \; d\Gamma = 0 \; , \quad \text{(B.11)}$$

where each method of mapping surface pressure from body 'B' to body 'A' are used in the stabilized constraint equation

$$\int_{\Gamma_0^A} \mu \; \left(\lambda_0 - \kappa^A p_0^A - \kappa^B p_0^{B\to A} - \gamma \; g_0^A\right) \; d\Gamma = 0. \quad \text{(B.12)}$$

The same benchmark problem presented in Section 10.5.2 is used with a change to the applied loads. Along the top edge, we will prescribe an applied displacement of $U_x^A = -0.5m$ and $U_y^A = -0.5m$. To compare pressure mapping terms with a coarse model discretization, the mesh is discretized with 15x15 elements. The model is incrementally loaded to the prescribed displacement value, and Figure B.4 illustrates the predicted mechanical response near the area of contact.

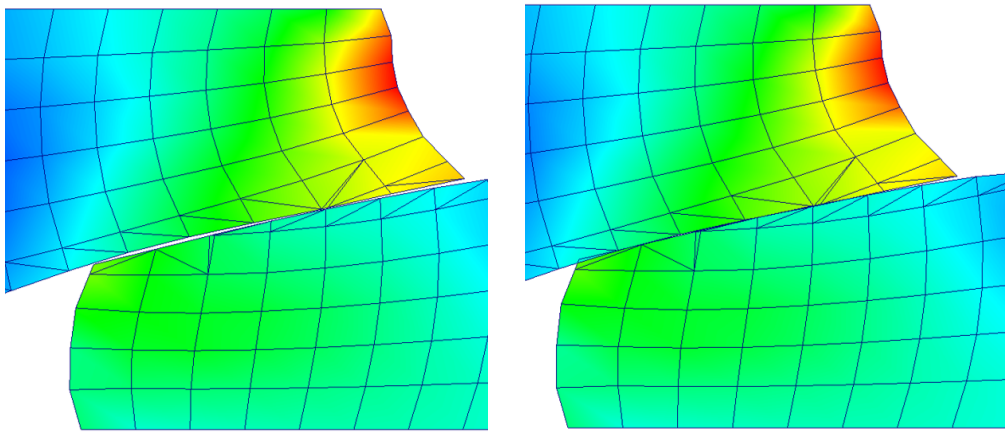

(a) (b)

Figure B.4: Predicted mechanical response for (a) $\mathbf{n^A} = -\mathbf{n^B}$, and (b) $\mathbf{n^A} \neq -\mathbf{n^B}$

While the orientation assumption of $\mathbf{n^A} = -\mathbf{n^B}$ is computationally less expensive, and intuitive to perfectly frictionless contact between smooth elastic bodies, under coarse discretization it over-predicts surface pressure. This over-prediction of contact pressure manifests itself by the small gap between structures in Figure B.4(a). While computationally more expensive, not making any assumptions of orientation yields a more physically accurate response as seen in Figure B.4(b). Although this error in physical response prediction decreases with mesh refinement for both orientation assumptions, topology optimization can result in design features that approach the side-length of an element. In these types of applications mapping option (b) may be preferred, as it provides a better physical response prediction in sub-optimal discretizations.

B.2 XFEM Stabilization Techniques

For topology and shape optimization problems, the XFEM has many advantages compared to more traditional mechanical models which rely on conformal discretization schemes. The XFEM unburdens model geometry and discontinuous displacement fields from being mesh-conforming, provides well-defined material interfaces, eliminates expensive remeshing during design changes, and provides unchanging state and optimization variables throughout the evolution of model geometry.

However, the XFEM can result in an ill-conditioned system of equations when the ratio of volumes on either side of the interface in an element is small. During topological changes on a fixed mesh, this predicament is often unavoidable. For contact related problems, this ill conditioning often results in artificially high stress predictions in thinly intersected elements. This can lead to solution divergence for problems in which the contact constitutive equations rely on stress to satisfy non-penetration conditions.

Chapter 7 presented two stabilization techniques for mitigating ill-conditioning: a geometric preconditioner method and the ghost penalization method. The geometric preconditioner restores the relative influence of the degrees of freedom, and is minimally invasive to the physical response prediction. The ghost penalization method stabilizes the system of equations by penalizing the flux of a state variable across element borders in the vicinity of the material interface. Ghost penalization can be physics related, and requires additional residual contributions to express model equilibrium. Section B.2.1 provides a comparative study of how each stabilization technique performs, compared to a body-fitted Finite Element model solution produced by Abaqus®.

Additionally, Chapter 7 presented two stabilization techniques for encouraging stable convergence of the response prediction through physical behavior such as delamination, neutral instability, and snap-through. Dynamic relaxation augments the global tangent stiffness diagonal, based on the iterative convergence behavior, whereas the solution correction scaling method scales back the iterative solution adjustment to a specified maximum value. Section B.2.2 provides a comparative study of each Newton-Raphson stabilization technique, for an example problem exhibiting snap-through behavior.

B.2.1 Preconditioner vs. Ghost Penalization

Consider the following contact problem illustrated in Figure B.5. The square domain of side length $L = 1.0$ m consists of two continuum bodies, Ω^A and Ω^B, separated by the material interface Γ_c. The shape of the interface is defined by two super-imposed circles of radius $r = \sqrt{2}/2$ m. Both bodies are described as neo-Hookean materials of the same properties, as depicted in

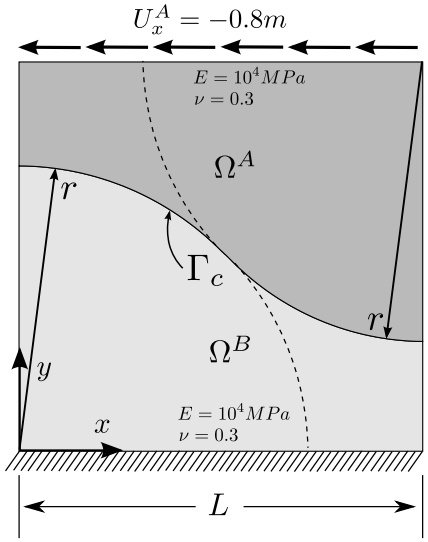

Figure B.5: Stabilization study: model setup

Figure B.5. Frictionless contact is prescribed at the material interface via the stabilized Lagrange formulation defined in Section 10.3. The bottom edge of the design domain is fixed, while an incrementally applied displacement of $U_x^A = -0.8$ m is prescribed along the top edge of the design domain. The domain was discretized with 50×50 quad-4 elements, and incrementally loaded quasi-statically in 50 increments. For both ghost penalization models using locally scaled and globally constant penalties, the global penalty parameter is set to $\gamma^G = 0.01h$. For the locally scaled ghost penalization model, this means that for very small material fractions, the local penalty parameter scales as $0.01h \leq \gamma^L \leq 0.1h$.

This particular model setup was chosen to highlight stabilization performance for a contact problem experiencing large deformation. To verify the response prediction afforded by the XFEM, the same problem was solved using a body-fitted mesh in Abaqus®. The design domain was discretized with 50×50 quad-4 elements, and incrementally loaded quasi-statically in 50 increments. Frictionless contact at the material interface was enforced with a surface-to-surface augmented Lagrange method. The total contact pressure is recorded for each load increment until a loss of convergence is experienced or the simulation is completed. The contact pressure history is plotted for the Abaqus® body fitted solution, XFEM geometric preconditioner solution, and XFEM

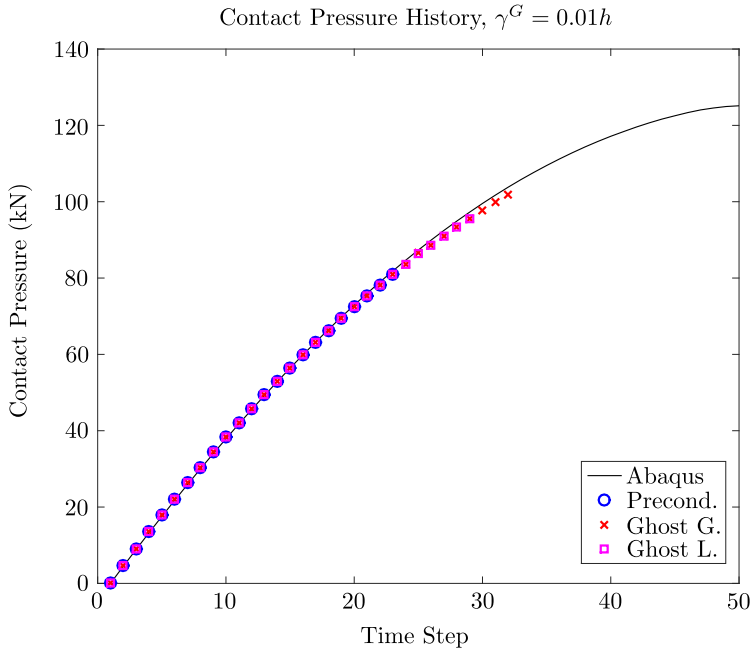

Figure B.6: Comparison of contact pressure history.

ghost penalization solutions in Figure B.6. For ghost penalization, both locally scaled and globally constant penalties are compared as 'Ghost L.' and 'Ghost G.' in the legend of Figure B.6, respectively. For each XFEM model, loss of convergence was experienced at time step 23, 29, and 32 for the global preconditioner, global ghost preconditioner, and local ghost preconditioner models, respectively. Surprisingly, locally scaling the penalty factor up for small volume fractions did not perform as well as maintaining a globally constant value. To gain greater insight to the physical behavior at the interface, the solution predicted by the geometric preconditioner model and that predicted by the globally scaled ghost penalization model are compared at load increment 23 in Figures B.7-B.8. While both the XFEM geometric preconditioner model and the XFEM globally scaled ghost penalty model result in stress approximation errors near the interface, the geometric preconditioner model exhibits an interfacial gap. This gap is a result of over-predicting surface pressure at localized regions along the interface. This suggests that ghost penalization may perform better than geometric preconditioning in reducing erroneous high stress approximations at the interface.

Abandoning geometric preconditioning and locally scaled ghost penalization due to under-performance, the penalty factor of the globally constant ghost penalization model is increased to $\gamma^G = 0.5h$. The higher penalty factor affords the full analysis to be completed. The current configuration of the final load step for both Abaqus® and ghost penalization are illustrated in Figures B.9-B.10. While there is general agreement in the von Mises stress prediction, a high penalty factor for ghost penalization can produce a smearing effect of the stress prediction near the interface. For ghost penalization there is a tradeoff between stability and predicted solution accuracy. The contact pressure history for the Abaqus® model is compared to that produced by the XFEM globally scaled ghost penalty for both penalty factors in Figure B.11. The notable decrease in contact pressure predicted by XFEM could be attributed to the smearing effect caused by high ghost penalization.

B.2.2 Dynamic Relaxation vs. Solution Correction Scaling

Consider the following contact problem illustrated in Figure B.12. The rectangular domain consists of three materials, Ω^A, Ω^B, and Ω^C. Materials Ω^A, and Ω^B are separated by the frictionless contact interface interface Γ_c. Materials Ω^A, and Ω^C are fully bonded at the interface between them. The shape of the contact interface, Γ_c, is defined by a sinusoidal wave offset by $L_2/2$. The sinusoidal wave follows two full periods in the length of L_1, and has an amplitude of $a = 1/30$ m. All bodies are described as neo-Hookean materials, whose properties are listed in Table B.1.

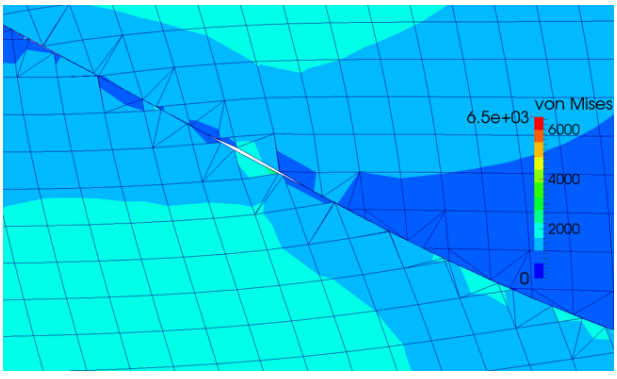

Figure B.7: Physical response, load increment 23, XFEM preconditioner.

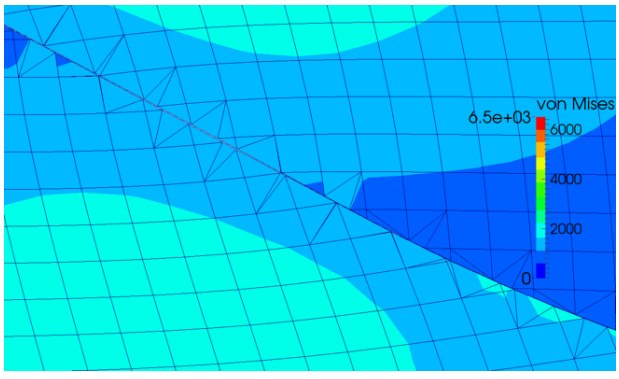

Figure B.8: Physical response, load increment 23, XFEM global scaled ghost penalization.

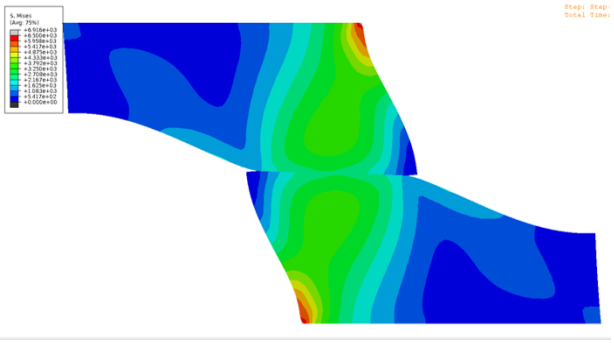

Figure B.9: Physical response, load increment 50, Abaqus®.

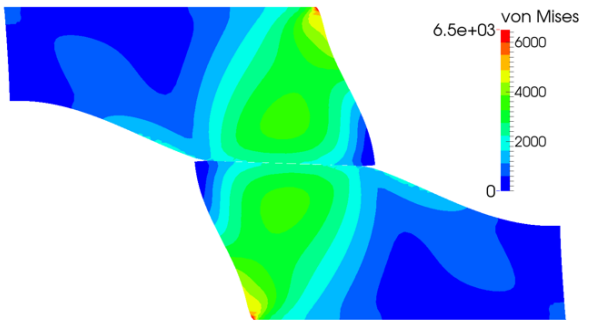

Figure B.10: Physical response, load increment 50, XFEM global scaled ghost penalization.

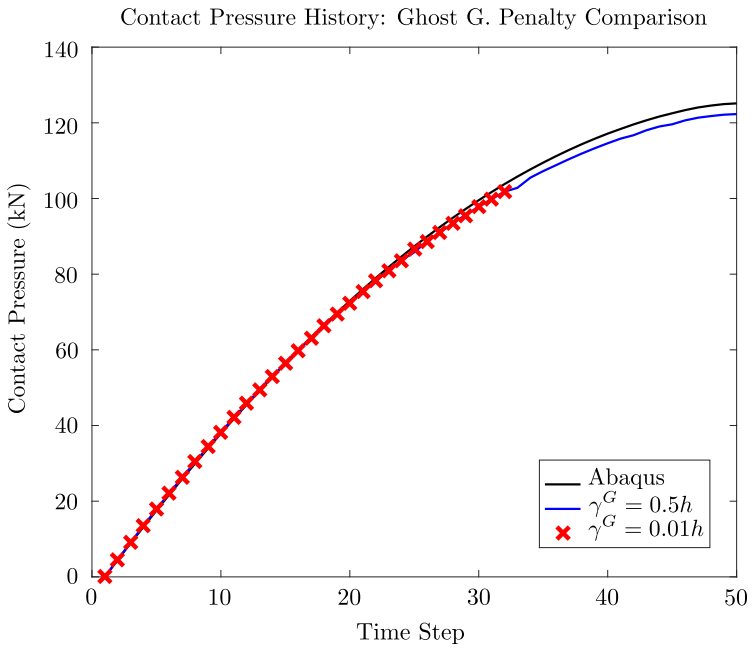

Figure B.11: Comparison of contact pressure history, global scaled penalty.

Frictionless contact is prescribed at the material interface via the stabilized Lagrange formulation defined in Section 10.3. The bottom edge of the design domain is fixed, while an incrementally applied displacement of $U_x^C = 0.5$ m is prescribed along the right hand edge of material Ω_C. The domain was discretized with 30×15 quad-4 elements, and incrementally loaded quasi-statically in 20 increments. For either model using dynamic relaxation or solution correction scaling, Ghost penalization is used with a penalty value of $\gamma^G = 0.01h$.

For the dynamic relaxation model, an initial damping parameter of $\tilde{\beta}_{int} = 0.1$ is applied, the

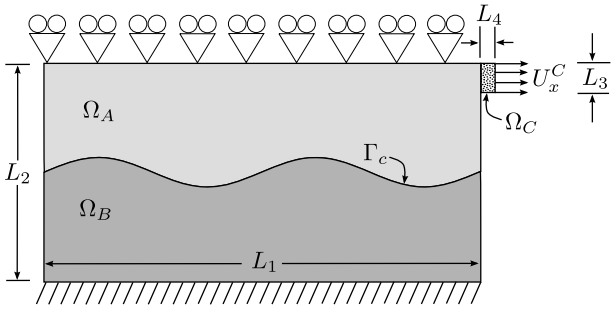

Figure B.12: Stabilization example initial configuration.

Description	Parameter
domain length	$L_1 = 1.0$ m
host depth	$L_2 = 0.5$ m
peak width location	$L_3 = 0.0667$ m
base width location	$L_4 = 0.0333$ m
Young's modulus	$E^A = 10$ MPa
Young's modulus	$E^B = 10$ MPa
Young's modulus	$E^C = 0.4$ MPa
Poisson's ratio	$\nu^A = 0.3$
Poisson's ratio	$\nu^B = 0.3$
Poisson's ratio	$\nu^C = 0.0$
applied load, at $t = 1$	$U_x^C = 0.5$ m

Table B.1: Stabilization example model parameters.

maximum allowable Newton iteration is set to 35, and dynamic relaxation iterations are capped at 1. These parameters were established through trial and error, until the full mechanical response could be achieved. For the scaled solution correction model, the maximum allowable solution correction size is set to $\delta_{max} = h/2$, where h is the element side length, and the maximum allowable Newton iteration is set to 50. To illustrate the snap-through behavior of this problem, Figure B.13 shows the physical response of the system prior and after exceeding the critical applied displacement. During this process, material Ω_A translates a significant distance in the positive x direction in

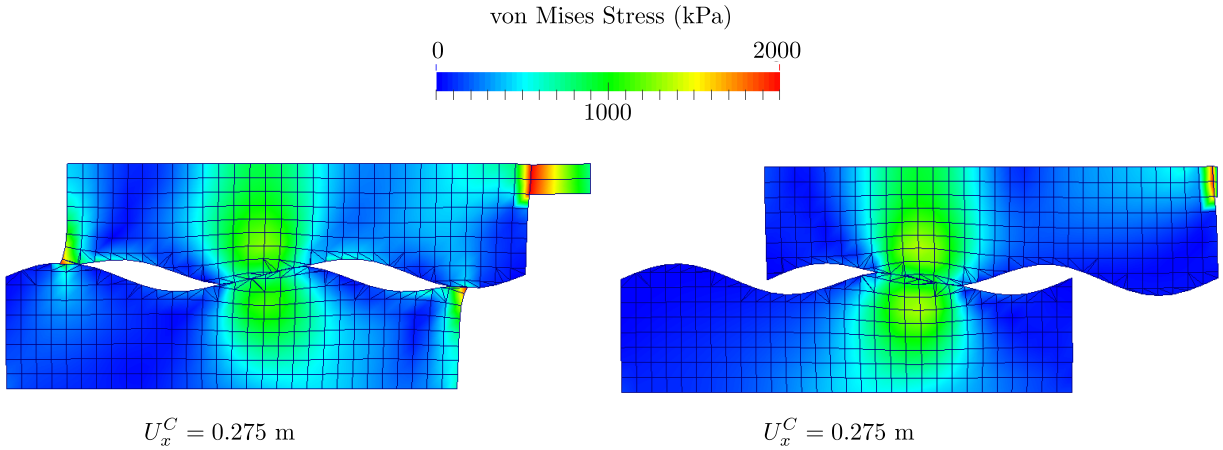

Figure B.13: Physical response at the incremental steps before and after snap-through.

a single load increment. Material Ω_C transitions from large elastic stretch to compression. For

comparison, Figure B.14 depicts the experienced force along the right hand edge of material Ω_C throughout the incremental loading process for dynamic relaxation, scaled solution correction, and unaltered Newton-Raphson models.

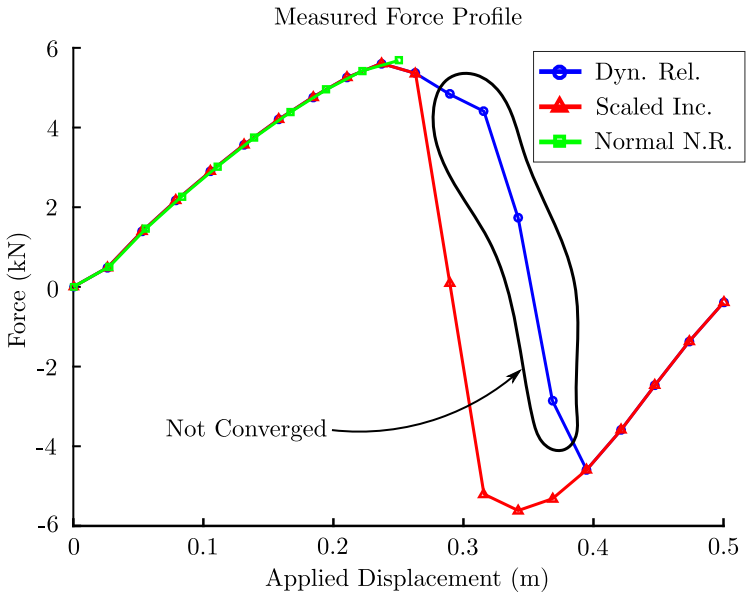

Figure B.14: Force displacement curve for each model.

The unaltered Newton-Raphson model lost convergence after the 11th load increment, and dynamic relaxation predicts an experienced force profile that greatly differs from that produced by the scaled solution correction method. To explore the discrepancy between methods, the relative residual error is plotted for each Newton iteration throughout the duration of load increments; see Figures B.15, B.16, and B.17. The converged solution of each load increment is labeled by s_i, where i corresponds to the particular load increment. The unaltered Newton-Raphson model exhibits quadratic convergence from steps 2 through 11, but diverges at load increment 12 due to the large relative motion caused by the snap-through behavior. The dynamic relaxation model requires on average twice the number of Newton iterations to resolve each load increment, and fails to achieve convergence at increments 11 through 14. This lack of convergence explains the over-predicted reaction force in Figure B.14. The scaled solution correction model converged on all load increments, and out-performed dynamic relaxation for the required number of Newton iterations.

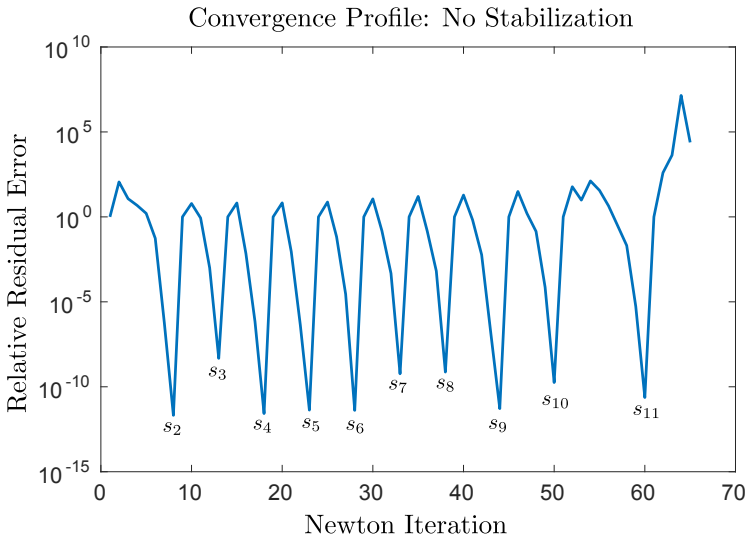

Figure B.15: Convergence behavior for unaltered Newton-Raphson model.

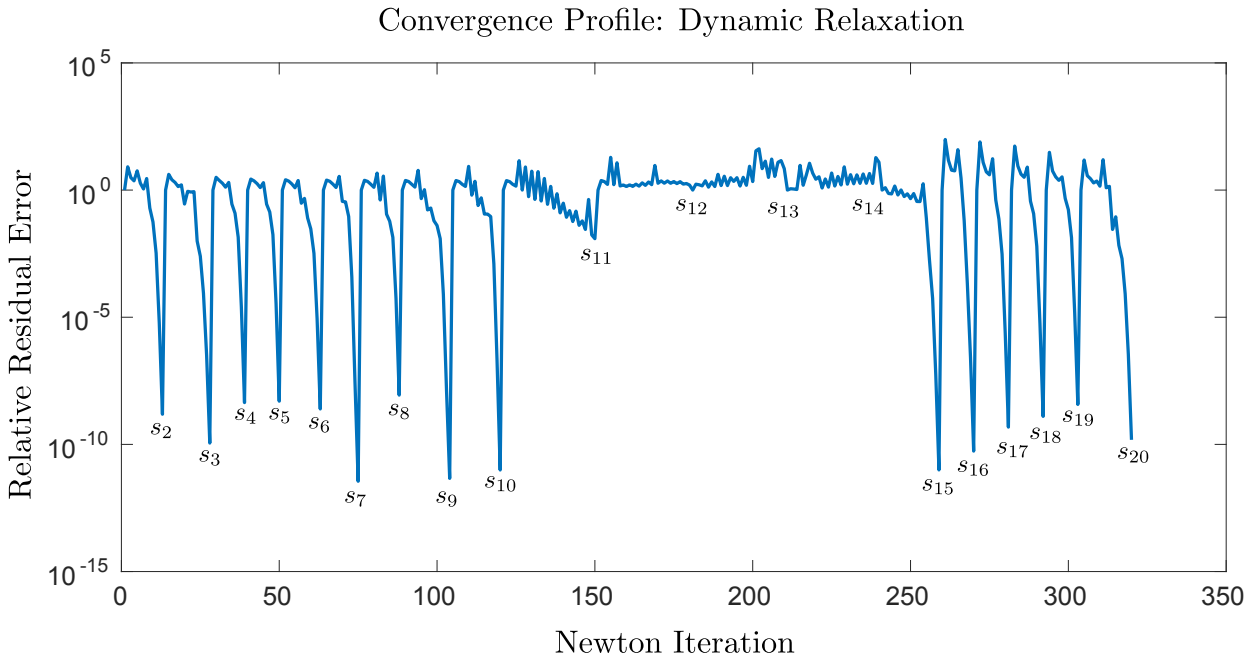

Figure B.16: Convergence behavior for dynamic relaxation model.

While dynamic relaxation has shown very useful to resolving equilibrium around sharp constitutive discontinuities such as material cohesion (see Chapter 9), it does not perform reliably during snap-through behavior in large sliding contact problems. Dynamic relaxation can mitigate total

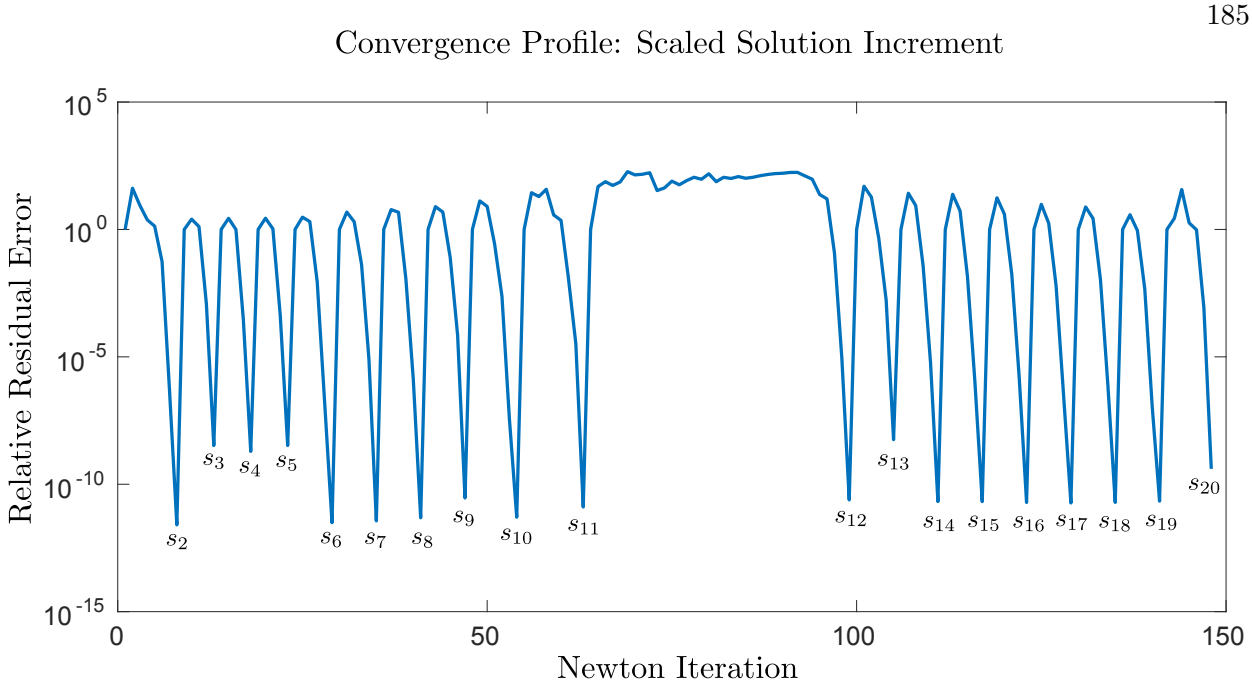

Figure B.17: Convergence behavior for the scaled solution correction model.

solution divergence during snap-through behavior, however it may or may not result in an accurate response prediction. Determining the optimal initial damping parameter and stop criteria is problem dependent, and a daunting endeavor for optimization problems which go through many design changes. In the authors' experience, the scaled solution increment method outperforms dynamic relaxation in many (but not all) large sliding contact problems. The scaled solution increment method is well suited for this subset of problems dealing with mild snap-through behavior, however arc-length methods need to be explored for problems exhibiting greater response nonlinearities.